

Ultrafast Dynamics In Semiconductor Quantum Wells

*A thesis submitted for the degree of
Doctor of Philosophy*

by

Christopher Ronald Hall



Centre for Atom Optics and Ultrafast Spectroscopy

*Faculty of Engineering and Industrial Sciences
Swinburne University of Technology
Melbourne, Australia*

November, 2011

Declaration

I, Christopher Ronald Hall, declare that this thesis entitled:

“Ultrafast Dynamics In Semiconductor Quantum Wells”

contains no material which has been accepted for any other academic award. All the work presented is primarily that of the author. The two-dimensional spectra in Chapter 5 were produced using the 2DFT code developed by Jeffrey Davis.

Christopher Ronald Hall

Centre for Atom Optics and Ultrafast Spectroscopy
Faculty of Engineering and Industrial Sciences
Swinburne University of Technology
Melbourne, Australia

November, 2011

- *To my family*

Abstract

In this thesis, the recombination dynamics within ZnO/MgZnO quantum wells under the influence of the quantum confined Stark effect, and the coherent dynamics of excitons within GaAs/AlGaAs asymmetric double quantum wells, are studied using a wide range of ultrafast spectroscopy techniques. These two topics are presented in two separate and self contained sections.

In the ZnO section, the recombination dynamics within ZnO/Mg_{0.3}Zn_{0.7}O quantum wells under the influence of the quantum confined Stark effect quantum wells are examined from the μ s to the fs timescale. Generating a high density of carriers within these quantum wells screens the internal electric field and reduces the impact of the quantum confined Stark effects. Following excitation, the decay of the excited state population restores the internal electric field. This produces a time varying interband transition energy and a time varying recombination lifetime. The time-dependent properties of the quantum well are revealed by pump-probe, time-resolved photoluminescence and modeling. By combining the measured recombination dynamics and the calculated recombination dynamics it is possible to determine the carrier density, the transition energy, the overlap integral of the electron and hole wavefunctions and the recombination lifetime at any time following excitation.

In a separate investigation a range of graded barrier ZnO/Mg_{0.3}Zn_{0.7}O quantum well samples are examined. Such structured quantum wells may be used to control the electron and hole wavefunction overlap within quantum wells with a built in electric field. In this thesis I report on the first graded barrier quantum wells based on the the ZnO/Mg_{0.3}Zn_{0.7}O

material system. The samples show that the overlap integral of the wavefunctions for the lowest energy electron and hole states may be controlled over a range from 0.25 to 0.86. The capacity to predictably control the transition energy and wavefunction overlap integral in QWs under the influence of the quantum confined Stark effect by using graded barriers adds to the commonly used techniques for tuning quantum well properties, including well width, band gap, and barrier height.

The coherent dynamics of coherently coupled excitons within GaAs/Al_{0.35}Ga_{0.65}As asymmetric double quantum wells are examined in a separate section. The dynamics are measured using four-wave mixing and analysed using two-dimensional Fourier transform spectroscopy. Two sample sets with barrier widths of 2, 4, 6, 20 and 50 nm are examined. The first sample set is designed so that the energy difference between the two lowest energy and bright heavy-hole excitons is equal to the longitudinal optical phonon energy. The purpose of this design is to explore the effect of a longitudinal optical phonon resonance on the coherent dynamics of coherently coupled excitons localised to different quantum wells. The second sample set is designed so that the energy difference between the same two heavy-hole excitons is not equal to the longitudinal optical phonon and may be used for comparison with the coherent dynamics measured in the first sample set. In practice the energy separation between the two heavy-hole transitions vary by up to 25 %, making any association with an optical phonon resonance difficult. Despite this, it is still possible to systematically examine the barrier width dependence of the coherent dynamics and coupling between spatially separated excitons. The calculations and experimental results suggest that the two lowest energy and bright heavy-hole excitons are localised to opposite quantum wells for barrier widths ≥ 4 nm. Using two-dimensional Fourier transform spectroscopy we observe coherent coupling between these excitons for barrier widths of 4, 6 and 20 nm. The possible coupling mechanisms are discussed. Through a process of elimination, dipole-dipole coupling is suggested as being the most likely coupling mechanism. The investigation presented in this thesis provides a first examination of coherently coupled and spatially separated excitons in an asymmetric double quantum well system.

Acknowledgements

There are many people that I would like to thank for making it possible for me to complete this thesis.

First and foremost, I would like to thank Professors Peter Hannaford and Lap Van Dao for giving me the opportunity to work in the ultrafast spectroscopy group at Swinburne. They were able to find a scholarship for me at a time when funding was difficult to come by, and for this I cannot be more appreciative. The resultant scholarship was funded 50 – 50 by the faculty of engineering and industrial sciences (FEIS) and Lastek. I would very much like to thank John Beynon and Alex Stanco for these contributions.

To my co-supervisor, Dr Jeffrey Davis, I give my deepest gratitude. I have learnt an enormous amount from you. Your guidance has been invaluable and your never-ending enthusiasm for high-quality research is contagious. It has been an absolute pleasure working with you.

I am indebted to Hoe Tan and Chennupati Jagadish at the Australian National University for accommodating me for a week to grow the GaAs asymmetric double quantum wells. I would also like to thank Yano's group at the Osaka Institute of Technology for providing the ZnO/MgZnO quantum wells and for spending much time perfecting the growth of the graded barrier samples.

During my time in the ultrafast group I have been fortunate to work with a great group of people; Past students David McDonald and Tra My Do, and new students Evelyn Cannon and Gethin Richards. It has been a fantastic experience working with you all. I would particularly like to thank David for taking the time to show me how to use the system in the early days.

Whilst working in the research center at CAOUS I have enjoyed the company of many people. For borrowing equipment, afternoon “tea time”, general chit-chat and your support, I would like to thank Paul, Evelyn, Eva, Sasani, Gethin, David, Tra My, Daniel and anyone else I may have forgotten.

Finally, I must thank Kylie for her continual support. Your encouragement and patience, particularly during the final months, has been unwavering and has kept me going all the way to the end. Don't worry, I don't plan on writing another thesis any time soon.

Contents

1	Introduction	1
2	Semiconductors	6
2.1	Introduction	6
2.2	Semiconductor materials	6
2.3	Bandstructure of semiconductors	9
2.4	Semiconductor quantum wells	14
2.5	Phonons	20
2.6	Excitons	22
2.7	Semiconductor growth techniques	26
3	Experimental	29
3.1	Introduction	29
3.2	Ultrafast laser system	30
3.3	Time-integrated photoluminescence	33
3.4	Time-resolved photoluminescence (TRPL)	34
3.5	Differential transmission pump-probe	37
3.6	Four-wave mixing spectroscopy	38
3.6.1	Dephasing and decoherence	39

3.6.2	The Bloch sphere	41
3.6.3	Experimental realisation of FWM	48
3.7	Two-dimensional Fourier transform spectroscopy	52
3.7.1	Non-interferometric phase retrieval algorithm	55
4	ZnO/MgZnO quantum wells	58
4.1	Introduction	58
4.2	Review of the development of ZnO/MgZnO quantum wells	62
4.3	Recombination dynamics within ZnO/MgZnO quantum wells	65
4.3.1	Carrier induced screening effect	66
4.3.2	Recombination dynamics - ns to μ s time scale	68
4.3.3	Recombination dynamics - ps time scale	70
4.3.4	Recombination dynamics - simulation	74
4.3.5	Discussion	82
4.3.6	Summary	85
4.4	Graded barrier quantum wells	86
4.4.1	Sample design	87
4.4.2	Sample growth	94
4.4.3	Photoluminescence	95
4.4.4	Time-resolved photoluminescence	99
4.4.5	Summary	103
5	Coupling and coherent dynamics within asymmetric double quantum wells	105
5.1	Introduction	105
5.2	Sample design and characterisation	109
5.2.1	Sample design	110
5.2.2	Photoluminescence	115
5.2.3	Coupled heavy-hole and light-hole excitons	119

5.2.4	Free-carrier continuum contribution to coherent dynamics	123
5.2.5	Peak shift	128
5.2.6	Disorder	133
5.2.7	A note on set 2	140
5.3	Coupling between spatially and energetically separated excitons	142
5.3.1	Three-pulse FWM and 2DFTS	142
5.3.2	Signal for non-rephasing pulse ordering	159
5.3.3	Raman-like coherence	162
5.3.4	Discussion	165
5.3.5	Summary and Outlook	169
6	Conclusions	172
A	Publications of the author	191
B	GaAs ADQW tables	194

Chapter 1

Introduction

Semiconducting materials have been of scientific interest for almost 200 years. The discovery of semiconductors is generally attributed to Michael Faraday, who in 1833 published a description of a material with a resistivity which had the opposite temperature dependence to that typically measured for metals [1]. Forty years later in 1873, Warren Smith observed that the resistivity of a semiconductor reduced when it was illuminated. These phenomena remained misunderstood until the development of the quantum theory of solids in the late 1920's and early 1930's [1]. The use of semiconductors in devices followed the discovery of a preferential direction for current flow through metal contacts made to naturally occurring crystals by Carl Braun in 1874. His work led to the development of the 'cats whisker' radio receiver, for which he shared the 1906 Nobel Prize in physics. The radio receivers, however, proved to be rather finicky and were eventually superseded by Lee De Forest's vacuum tube triode [2].

From the early 1940's the vacuum tube triode found an application in computing. As the need for greater computing power developed, the number of triodes built into newer models was increased. There are, however, several persistent issues with vacuum tube triodes; they are bulky, often leak, require a lot of power to operate, and through continual use will eventually burn out. For computers made up of thousands of triodes, their reliability became

limited by the operational lifetime of the constituent triodes. The need for a more reliable and efficient equivalent to the vacuum tube triode led to the development of a semiconductor based device by William Shockly, John Bardeen and Walter Brattain at Bell Telephone Laboratories, which was called the transistor [3]. The potential applications offered by the transistor generated much interest in semiconductors and subsequently stimulated a multitude of advances in semiconductor physics and technology. The ever growing need for faster computers and the limiting velocity at which electrons can move through electrical circuits drove the development of smaller transistors and the paradigm shifting integrated circuit. A better understanding of semiconductor materials led to new semiconductor based devices which interacted with light, including the light emitting diodes and photodetectors.

The development of molecular beam epitaxy (MBE) and metal-organic chemical vapour deposition (MOCVD) growth processes improved the quality of grown semiconductor materials. In addition, these growth techniques provided better control over the thickness of semiconductor layers and gave researchers the ability to explore quantum confinement effects. These refinements in the growth process allowed the development of quantum well (QW) laser diodes which could operate at room temperature. The ability to generate laser light from a compact solid state device facilitated a new generation of devices. Modern day conveniences stemming from this work include high density data storage (CD and DVD), fast fibre-optic based communications and a myriad of low cost and intense light sources for use in spectroscopy and other research applications. Current research interests involving semiconductors are exceptionally diverse, including significant efforts in photovoltaics, wide bandgap semiconductors for green/blue/UV light generation and detection, sensors (such as chemical, gas and pressure), spintronics, and using semiconductors for efficient lighting.

ZnO is a semiconductor material of significant interest because it has a direct bandgap that is wide at room temperature (3.37 eV) and has the potential to be used in blue/UV light emitting devices. Such device applications are beyond the capabilities of the established semiconducting materials, Si and GaAs. In order to progress to making devices from ZnO which incorporate QW, it is important to characterise the properties of such structures. Two

investigations based on ZnO QWs are presented in this thesis. The first project examines the recombination dynamics of excitons in ZnO/MgZnO QWs which have a built in electric field. The changes induced by the electric field are known as the quantum confined Stark effects and include red-shifting the exciton transition energy, as well as decreasing the exciton oscillator strength and binding energy. These effects are investigated using time-integrated and time-resolved photoluminescence and pump-probe spectroscopy. In the second ZnO project it is shown that ZnO/MgZnO QWs with graded barriers and a built in electric field can be used to predictably control the overlap integral of electron and hole wavefunctions. This is demonstrated through calculations and time-integrated and time-resolved photoluminescence measurements.

With GaAs well established in the electronics industry, its properties are well understood and the techniques used for growing GaAs/AlGaAs QWs are highly optimised. It is for these reasons that GaAs/AlGaAs based QWs make a good platform for exploring phenomena reliant on high quality QW structures. In this thesis, asymmetric double quantum wells made from GaAs/AlGaAs are used to explore the coherent dynamics of excitons localised to separated quantum wells. Four-wave mixing and two-dimensional Fourier transform spectroscopy are used to investigate the coherent coupling dynamics.

Given the diversity of the topics investigated, the three main projects which make up the thesis are divided into two self contained chapters based on the sample material type: ZnO and GaAs. The structure of this thesis is as follows: Chapter 2 introduces the properties of semiconductors. It begins by describing the basic properties of semiconductors (Sec. 2.2) and the semiconductor bandstructure (Sec. 2.3). Semiconductor QWs are then discussed, including how Numerov's method is used to numerically solve Schrödinger's equation to determine the energy and wavefunctions for confined electrons and holes (Sec. 2.4). This is followed by discussions of the general properties of excitons (Sec. 2.6) and phonons (Sec. 2.7).

The experimental apparatus and techniques are described in Chapter 3. The chapter begins by detailing the Swinburne ultrafast laser system in Sec. 3.1. This is followed

by a description of the time-integrated photoluminescence (PL) experiment (Sec. 3.3), which is used to characterise the samples used throughout this thesis. The time-resolved photoluminescence (TRPL) and differential transmission pump-probe (DTPP) experiments, detailed in Sec. 3.4 and Sec. 3.5, respectively, are used to measure the carrier recombination dynamics in the ZnO QWs. The four-wave mixing (FWM) section (Sec. 3.6) consists of several subsections which discuss dephasing of coherent excitons (Sec. 3.6.1), the Bloch sphere concept (Sec. 3.6.2), and the experimental realisation of FWM experiments (Sec. 3.6.3). The FWM section is accompanied by a description of two-dimensional Fourier transform spectroscopy (2DFTS) and the phase retrieval algorithm used to generate 2DFTS spectra (Sec. 3.7). The FWM and 2DFTS experiments are utilised to explore the coherent dynamics of excitons in the GaAs asymmetric double QWs.

The ZnO QW investigation is presented in Chapter 4. The chapter begins with an introduction describing ZnO, its properties and its uses. Sec. 4.2 presents a literature review on the development of ZnO QWs. The first of the two main ZnO investigations, which explores the recombination dynamics within ZnO/ZnMgO QWs under the influence of the quantum confined Stark effect, is presented in Sec. 4.3. Within Sec. 4.3 I examine the carrier induced screening effect (Sec. 4.3.1), the recombination dynamics on the μs - ns timescale (Sec. 4.3.2), the ps timescale (Sec. 4.3.3) and the simulated recombination dynamics (Sec. 4.3.4). A discussion of the carrier recombination dynamics considering the measured and experimental results is given in Sec. 4.3.5.

The second of the two main ZnO investigations is presented in Sec. 4.4. In this section, a first investigation of ZnO/ZnMgO QWs with graded barriers is presented. The sample design is given in Sec. 4.4.1, which includes an analysis of the expected exciton transition energies and wavefunction overlap integrals based on calculations. This is followed by an analysis of the transition energy in the grown graded barrier samples based on PL results (Sec. 4.4.3), and the electron and hole wavefunction overlaps, which is determined from the TRPL results (Sec. 4.4.4).

The coherent dynamics of excitons in GaAs asymmetric double QWs are investigated

in Chapter 5. Asymmetric double QWs provide an ideal platform for studying coherent coupling between spatially separated excitons. The chapter begins by introducing coherent coupling, and discussing previous work where coherent coupling between spatially separated in-plane excitons and excitons in a double QW system has been investigated. Section 5.2 presents the design and characterisation of the samples used in the investigation. PL is used to characterise the transition energies within the grown samples, which are compared with the calculations based on the sample design (Sec 5.2.2). The coherent response of the samples are also characterised, with discussions on the free-carrier continuum contribution to the measured dynamics (Sec. 5.2.4), as well as the effects of peak-shift (Sec. 5.2.5) and disorder (Sec. 5.2.6). In Sec. 5.3, coherent coupling between excitons localised to different QWs is examined. The 2DFTS spectra for a range of samples is shown and analysed in Sec. 5.3.1. A signal which is only observed for non-rephasing pulse ordering is discussed in greater detail in Sec. 5.3.2. The experimental results for a Raman-like coherence between the two bright and lowest energy heavy-hole excitons are shown and discussed in Sec. 5.3.3. Further discussion of the results is given in Sec. 5.3.4, including the mechanisms mediating coupling between the separated excitons.

Chapter 2

Semiconductors

2.1 Introduction

This thesis examines the recombination and coherent dynamics of excited carriers within semiconductor quantum wells (QW). Two different semiconductor materials are examined; ZnO/Mg_xZn_{1-x}O and GaAs/Al_xGa_{1-x}As. The optical and electrical properties of these materials are determined by their band structure, composition and the interaction of excited carriers to their environment. This section describes the general properties of semiconductors, semiconductor quantum structures and how such materials are grown.

2.2 Semiconductor materials

A semiconductor is a solid material with a crystalline structure that is electrically insulating whilst at absolute zero, but is conductive for temperatures below its melting point. As the temperature is increased from absolute zero the resistivity of the material decreases, which is the opposite response measured for metals. The resistivity of the material depends on the occupation of the conduction band (CB) and valence bands (VB). Electrons may be excited

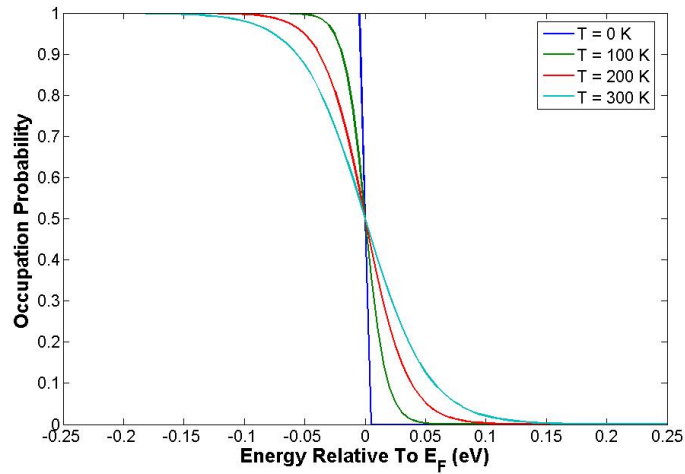


Figure 2.2.1: The Fermi-Dirac distribution relative to the Fermi level, E_F , for temperatures of 0 K, 100 K, 200 K and 300 K.

from the VB to the CB either by thermal energy or electromagnetic radiation. The energy difference between the CB and VB is generally known as the bandgap. Exciting an electron from the VB to the CB produces a vacancy in the VB called a hole. The hole is a quasi-particle with an effective mass that is determined by the bandstructure of the material and a positive charge exactly opposite the charge of an electron. Both electrons and holes can contribute to charge conduction in semiconductors.

The probability of thermally exciting an electron from the VB to the CB is governed by Fermi-Dirac statistics relative to the Fermi level [4]. The probability, $P(E)$, of an energy level, E , being occupied by an electron is given by

$$P(E) = \frac{1}{1 + \exp\left[\frac{(E-E_F)}{kT}\right]} \quad (2.2.1)$$

where E_F is the Fermi level. The Fermi level defines the energy where the probability of occupation by an electron for a given temperature is 0.5. For an undoped semiconductor at 0 K and in thermal equilibrium, the Fermi level is located half way between the CB and VB. This is also the case for intrinsic insulators, however, due to the large bandgap of insulators, the probability of an electron being excited from the VB to the CB thermally is very low.

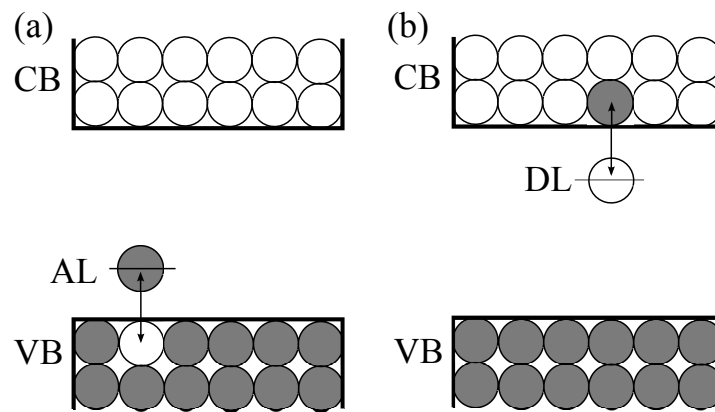


Figure 2.2.2: A semiconductor doped with (a) acceptor atoms and (b) donor atoms. The CB, VB, acceptor energy level (AL) and donor energy level (DL) are labeled. An ideal acceptor atom will have an unoccupied electron level with energy that is slightly higher than the VB of the material it replaces. In this case thermal energy can efficiently excite electrons from the VB to the acceptor dopant level and make the VB conductive. Similarly, an ideal donor atom will have an occupied electron energy level that is slightly less than the CB of the material it replaces. In this case thermal energy can efficiently excite electrons from the donor energy level to the CB, partially filling the CB and making it conductive.

The Fermi-Dirac distribution is shown in Fig. 2.2.1. At 0 K, the probability of occupation of a state by an electron above the Fermi level is zero, and below the Fermi level is equal to one. As the temperature is increased, the probability of occupation of states above the Fermi level by electrons increases. At the same time, to conserve the total electron population, the probability of occupation of states below the Fermi level decreases.

An undoped semiconductor may also be made conductive by doping it with an element that has additional or fewer valence electrons than the material it is replacing. The role of ‘acceptor’ and ‘donor’ dopants is illustrated in Fig. 2.2.2. Dopant atoms that make good ‘acceptors’ have an unoccupied electron level slightly higher in energy than the VB of the host semiconductor material, as shown in Fig. 2.2.2(a). The smaller the energy difference between the acceptor level and the top of the VB, the larger the probability for the thermal excitation of electrons to the acceptor energy level. The holes that are subsequently left in the VB are free to move, making this material conductive for holes at room temperature. This is called *p*-type doping and has the effect of shifting the Fermi level towards the VB.

Atoms which make good ‘donors’ have an occupied electron level that is just below the

CB, as shown in Fig. 2.2.2(b). Ideally, the energy difference between the CB and the donor energy level is sufficiently small so that electrons may be efficiently excited from the donor energy level to the CB by thermal energy. Exciting electrons from the donor energy level to the CB produces a material that is conductive for electrons at room temperature and is called *n*-type. For *n*-type semiconductors, the Fermi level is shifted towards the CB.

2.3 Bandstructure of semiconductors

The crystalline structure of semiconductors is highly symmetric. This allows one to define a unit cell which is repeated throughout the bulk material and may be used to describe the entire crystal lattice. It also permits one to define a reciprocal lattice, which provides a description of the relative angles between planes within the real semiconductor lattice and the thicknesses of the planes. Just as the unit cell is used to completely define the crystal lattice, the Brillouin zone is used to define the reciprocal lattice. The first Brillouin zone for a face centred cubic (f.c.c.) crystal is shown in Fig. 2.3.1 and the points of high symmetry, Γ , X , K and L , are labeled. Γ indicates the zone centre. The lines joining the points Γ and X , Γ and L and Γ and K are labeled Δ , Λ and Σ respectively. This figure is taken from Yu and Cardona [5].

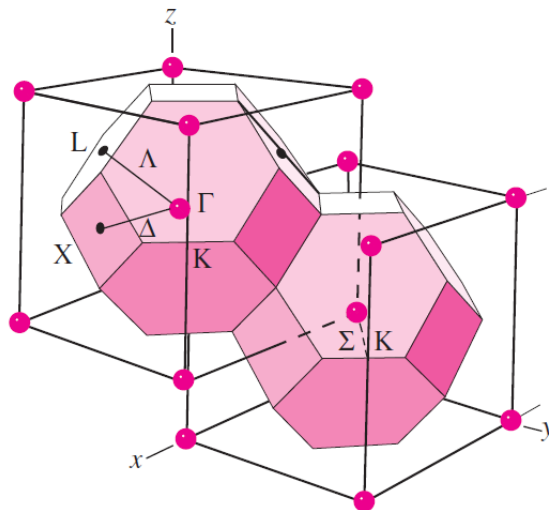


Figure 2.3.1: A portion of the reciprocal lattice for a face centered cubic crystal (f.c.c.) with the first Brillouin zone shown. The points of high symmetry, L , X , K and Γ , are labeled. Γ indicates the zone centre. The lines joining the points Γ and X , Γ and L and Γ and K are labeled Δ , Λ and Σ respectively. This figure is taken from Yu and Cardona [5].

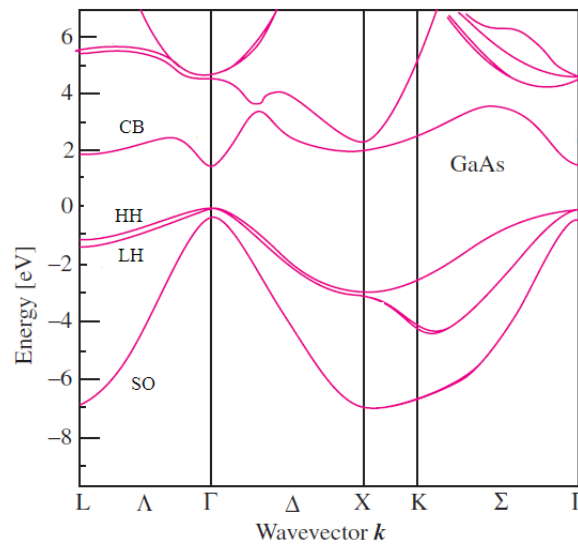


Figure 2.3.2: The dispersion curve for GaAs. The bands corresponding to the CB and the VB HH, LH and SO bands are labeled. From Yu and Cardona [5].

Γ , L, X and K are labeled. Γ indicates the zone centre. The lines joining the points Γ and X, Γ and L, and Γ and K are labeled Δ , Λ and Σ respectively. Points in reciprocal space correspond to wave vectors in the real space lattice. At the zone centre the wavevector, and hence momentum, is zero. The points along the vector from Γ to L, for example, represent a linear increase in momentum in the direction defined by L.

The energy of a non-stationary electron within a lattice is dependent on the direction of motion of the electron through the lattice. The points of high symmetry within the reciprocal lattice provide a convenient reference when plotting the electron energy as a function electron momentum. Plotting the electron energy this way is called a dispersion relation. The dispersion plot for GaAs is shown in Fig. 2.3.2. The bands corresponding to the CB and the VB HH, LH and SO bands are labeled. The origin of the HH, LH and SO bands will be discussed later in this section.

The relationship between kinetic energy, momentum and mass of a particle in free space is given by

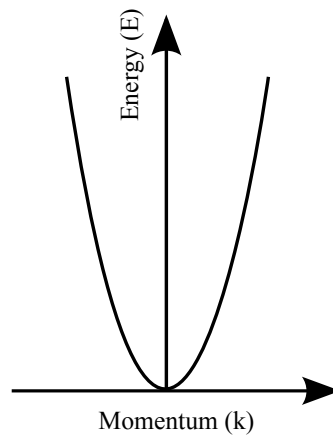


Figure 2.3.3: The energy-momentum diagram for a free electron.

$$E = \frac{\hbar^2 k^2}{2m} \quad (2.3.1)$$

where E is the particle kinetic energy, k is the particle momentum and m is the mass of the particle. The energy defined by Eq. 2.3.1 is plotted as a function of momentum in Fig. 2.3.3. In a crystal lattice, however, electrons and holes are not ‘free’, but interact with the lattice, leading to a complex dispersion relation such as that plotted in Fig. 2.3.2. At the CB minimum and the VB maximum, the curve can be approximated as parabolic. From Eq. 2.3.1, and the band structure, an effective mass can then be defined,

$$m^* = \frac{\hbar^2}{\frac{d^2 E}{dk^2}} \quad (2.3.2)$$

where $\frac{d^2 E}{dk^2}$ defines the local curvature of the dispersion curve. The effective mass of electrons and holes varies between materials due to variations in their bandstructure. In GaAs and ZnO for example, CB electrons have an effective mass of $0.067m_0$ and $0.28m_0$, respectively, where m_0 is the free electron mass.

Returning to Fig. 2.3.2, the bands labeled HH and LH overlap at the Brillouin zone centre. The HH and LH are so named because of their relative curvature and hence their effective mass. A schematic of the VB around Γ is shown in Fig. 2.3.4. The HH and LH

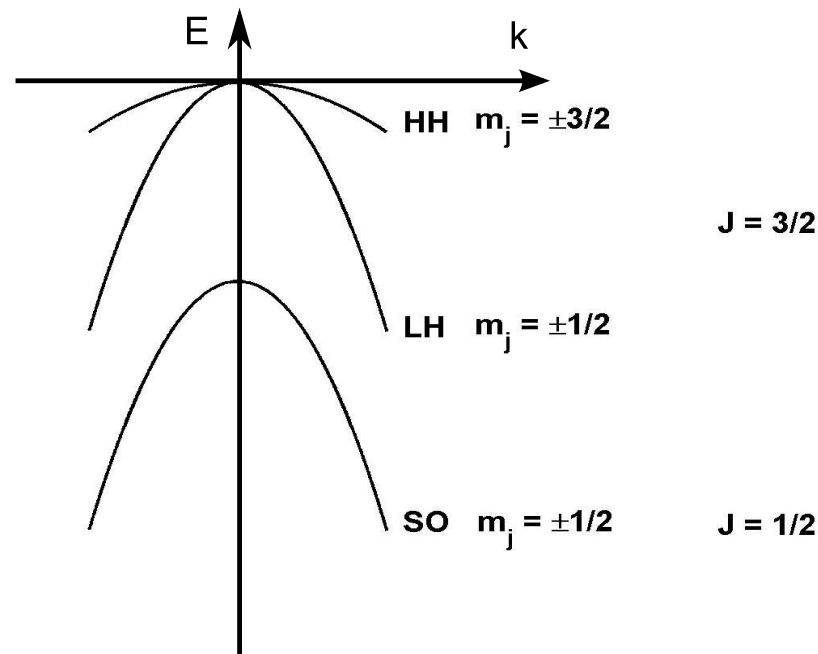


Figure 2.3.4: The bandstructure of the HH, LH and SO bands at the top of the VB at the Brillouin zone centre. The quantum numbers for each of these bands are also included.

states share the same total angular momentum quantum number, $J = 3/2$, but have different angular momentum projections of $m_j = \pm 3/2$ and $m_j = \pm 1/2$. The split-off (SO) band has a total angular momentum quantum number of $J = 1/2$. In most cases, because of the large energy difference between the SO band and the other VB, the SO band does not contribute to the optical properties of the semiconductor. Electrons in the CB have no orbital angular momentum, leaving the angular momentum completely determined by the electron spin. The CB states therefore have angular momentum projections of $m_j = \pm 1/2$. A photon carries one unit of angular momentum, meaning that only transitions which involve a change of one unit of angular momentum are allowed. Based on this selection rule, circularly polarized light may be used to select specific transitions and explore the spin properties of semiconductors.

The overlap of the CB minimum energy and the VB maximum energy in the dispersion plot defines whether the bandgap is direct or indirect and has significant implications on the optical properties of semiconductors. In the case of a direct bandgap semiconductor, where no change in momentum is required for an electron to be excited from the top of the VB to the bottom of the CB, such as GaAs (Fig. 2.3.2), a photon with energy larger than the bandgap

can excite an electron from the VB to the CB. In the case of silicon, which is an indirect bandgap semiconductor, the VB maximum is located at the Brillouin zone centre, Γ and the CB minimum is located near the symmetry point X. A change of momentum is therefore required for an electron with an energy equal to the difference between the VB maximum and the CB minimum to be excited across this energy gap. The required momentum cannot be obtained from the exciting photon because photons only have a small amount of momentum. The additional momentum can, however, be supplied by a phonon, which are discussed in more detail in Sec. 2.5. In GaAs for example, a photon with energy equal to the GaAs bandgap of 1.43 eV has a momentum of $7.53 \times 10^{-28} \text{ kg m s}^{-1}$, which is significantly less than a phonon of energy 0.037 eV which has a momentum of $1.17 \times 10^{-24} \text{ kg m s}^{-1}$. For a band-edge transition to occur in an indirect bandgap material, a phonon and a photon must be simultaneously absorbed or emitted. This leads to a strong temperature dependence of the absorption coefficient of silicon. The differences between the absorption coefficients for direct and indirect bandgap materials can be significant. The absorption coefficients for GaAs and Si at room temperature, for example, are $8 \times 10^3 \text{ cm}^{-1}$ and $1 \times 10^1 \text{ cm}^{-1}$ respectively [6, 7]. The probability of photon absorption, and hence the absorption coefficient, is increased when higher energy photons are used to excite electrons directly across the bandgap to available states that do not require additional momentum.

Whether the material has a direct or indirect bandgap has further implications for light emission and device efficiency. Excited electrons in direct bandgap materials are able to recombine radiatively to the CB without changing momentum. This process can generally occur quickly and efficiently. The recombination of an excited electron in an indirect bandgap material, however, needs to conserve momentum and emit or absorb a phonon. This process is less probable than recombination in direct bandgap semiconductors, leading to much longer recombination lifetimes in indirect bandgap semiconductors. Consequently, the longer the electron remains in the CB, the larger the chance of non-radiative recombination of excited carriers. For light emitting devices, this can lead to reduced device efficiencies.

For intrinsic group IV semiconductors, such as Si, Ge, and C, the bandgap of the material

is fixed, and hence so are the absorption and emission energies of the material. Binary and ternary compound semiconductors based on group III-V or group II-VI semiconductors provide a number of bandgap tuning options. For both of these material types, the total number of valence electrons remains the same as semiconductors based entirely on group IV elements, and the material remains neutral (neither n nor p type). GaAs is a III-V semiconductor with a bandgap of 1.43 eV. By introducing Al and forming the ternary alloy AlGaAs, the bandgap increases, for example, with 35% Al the bandgap is 1.85 eV. Adding Al also produces subtle changes in the band structure of GaAs. For Al > 35%, the L valley (refer to Fig. 2.3.1) becomes the lowest point on the CB and the bandgap becomes indirect.

2.4 Semiconductor quantum wells

A semiconductor QW is a two dimensional structure where electrons or holes or both may be confined. A QW is formed by growing a thin layer of a semiconductor material between two layers of another semiconductor material with a larger bandgap. An example of two materials that may be used to make a semiconductor QW is GaAs/Al_xGa_{1-x}As, where GaAs has a bandgap of 1.43 eV and Al_xGa_{1-x}As has a bandgap of $1.43 + 1.2475x$ eV [8] at room temperature. The QW barrier height is controlled by varying the Al composition in the Al_xGa_{1-x}As material. The difference in the bandgaps of GaAs and Al_{0.35}Ga_{0.65}As is split 60/40 between the CB and VB [5]. This energy difference is called the band offset.

When the width of the well approaches the de Broglie wavelength of electrons and holes, confinement effects are observed. Specifically, the allowed energy levels the electrons and holes can take are no longer continuous, but are semi-discrete. The discretisation of the electron and hole energies in the confinement direction of the QW are derived from the well known ‘particle in a box’ model. In the simplest case of this model, the Schrödinger equation, Eq. 2.4.1, is applied to a one dimensional well with infinitely high barriers,

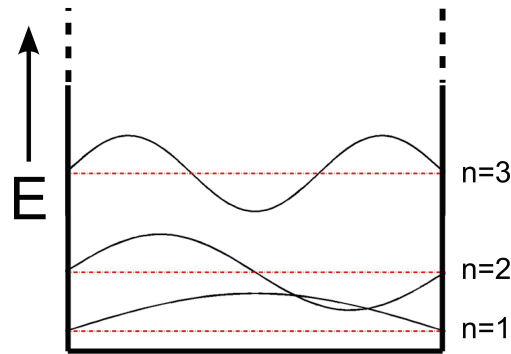


Figure 2.4.1: The first three energy levels and wavefunctions as described by the solutions to the ‘particle in a box’ model.

$$\frac{\hbar^2}{2m} \frac{d^2 \phi_n(z)}{dz^2} + V(z) \phi_n(z) = E_n \phi_n(z) \quad (2.4.1)$$

where $V(z)$ is the spatially dependent potential, m is the effective mass of the particle and E_n and $\phi_n(z)$ are the eigenenergies and eigenfunctions for each integer value of n , the principal quantum number. The solutions for the eigenenergy and eigenfunction are

$$E_n = \frac{\hbar^2}{2m} \left[\frac{n\pi}{L_z} \right]^2 \quad (2.4.2)$$

$$\phi_n(z) = A \sin\left(\frac{n\pi z}{L_z}\right) \quad (2.4.3)$$

where L_z is the width of the well. The solutions to the particle in a box model are plotted in Fig. 2.4.1. From Eq. 2.4.2, it is evident that the energy of the quantised states increases with a quadratic dependence on the principal quantum number, n , and is inversely dependent on the well width. The electrons and holes are, however, only confined in the direction perpendicular to the QW; the electrons and holes are free to move in the 2D plane of the QW, and the dispersion curve and the energy of the electrons and holes in this plane remains continuous. These semi-discrete energy levels of the QW are larger in energy than the bandgap of the material which makes up the well layer in the QW and are referred to as

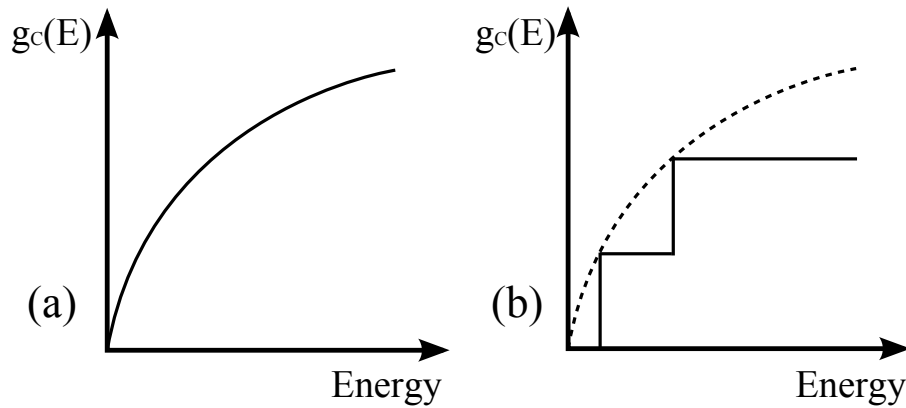


Figure 2.4.2: The density of states for (a) a bulk semiconductor and (b) a QW as a function of energy.

QW subbands. By controlling the width of the well, it is possible to control the energy of the QW subbands, and hence control the interband transition energy. Confining the electrons and holes to a quasi-2D plane also increases the overlap of the electron and hole wavefunctions. According to Fermi's golden rule, this increases the probability of radiative recombination [4]. Such structures are of considerable interest because of the benefits they offer to semiconductor light emitting devices over bulk semiconductor materials. Of particular interest are the associated improvements in radiative efficiency and the tunability of interband transitions.

Confining electrons and holes in one direction significantly alters the density of states for a bulk semiconductor and a semiconductor QW. A schematic representing the energy dependence of the density of states for bulk semiconductors and QWs is shown in Fig. 2.4.2. In a bulk semiconductor, the density of states, $\rho^{3D}(E)$, in the CB as a function of energy is given by [9]

$$\rho^{3D}(E) = \frac{1}{2\pi^2} \left(\frac{2m^*}{\hbar^2} \right)^{3/2} (E - E_c)^{1/2} \quad (2.4.4)$$

for $E \geq E_c$, where E_c is the energy at the bottom of the CB and m^* is the effective mass of an electron. The density of states equals zero for $E < E_c$ as there are no allowed electron states between the CB and VB. The density of states for a 3D material as a function of E is shown

in Fig. 2.4.2(a). The density of states varies continuously as a function of E . The density of states for a QW is given by [9]

$$\rho^{2D}(E) = \sum_{i=1}^n \frac{m^*}{\pi\hbar^2} \Theta(E - E_i) \quad (2.4.5)$$

where Θ is a unit step function, which originates from the quantisation perpendicular to the plane and $\frac{m^*}{\pi\hbar^2}$ is the contribution from the 2D in plane density of states. The density of states for a QW as a function of E for the first two eigenstates of the QW is plotted in Fig. 2.4.2(b). The density of states increments at values of E equal to eigenenergies of the QW. Each incremental step of the density of states is equal.

In some cases it is not so straight forward to solve the Schrödinger equation analytically, for example, for arbitrarily shaped QWs. In such cases it is convenient to derive solutions to the Schrödinger equation numerically. A method commonly used to solve the Schrödinger equation numerically for a potential with any shape is by using the general solution to Numerov's method. Numerov's method is used to solve ordinary differential equations of the form $d^2y/dx^2 = U(x) + Z(x)y$. The time-independent Schrödinger equation is of this form. The general solution to Numerov's method is given by [10, 11]

$$y_{n+1} = \frac{2y_n - y_{n-1} + \frac{h^2}{12}(U_{n+1} + 10F_n + F_{n-1})}{(1 - \frac{Z_{n+1}h^2}{12})} + O(h^6) \quad (2.4.6)$$

where $d^2y/dx^2 = F$, $y_n = y(x_n)$ and x_n are uniformly spaced with a separation of h . For Schrödinger's equation, $U = 0$, $Z(x) = \frac{2m}{\hbar}[V(x) - E]$ and $y = \psi$, therefore $F = \frac{2m}{\hbar}[V(x) - E]y$. The derivation of Numerov's method can be found in Gonzalez et al. [10]. In the calculations presented in this thesis, Eq. 2.4.6 is used to solve Schrödinger's equation for arbitrarily shaped QWs. In essence, it is used determine the wavefunction for a QW profile for a given energy, E . Implementing Eq. 2.4.6 will, however, output an answer for any value of E , which may or may not be a valid solution to Schrödinger's equation. An additional method called the shooting method is used to determine if the wavefunction output by Eq. 2.4.6 is a correct

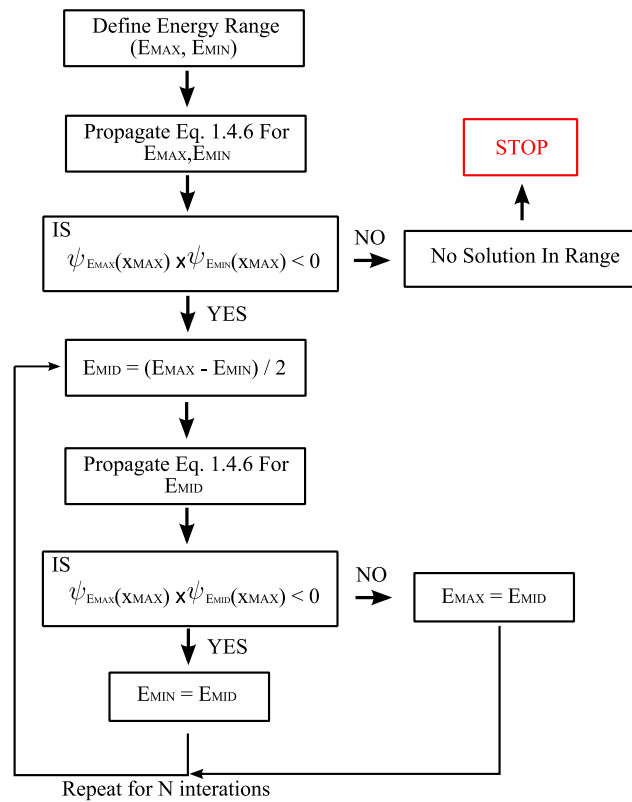


Figure 2.4.3: A flow diagram which represents how the shooting method is used to determine solutions to the Schrödinger equation from Eq. 2.4.6. The details are given in the text.

solution to Schrödinger's equation. To use the shooting method, the relationship between values at the extremities of the calculated range must be known. For valid solutions to the Schrödinger equation, the amplitude of the wavefunction (electron or hole wavefunction) deep into the QW barrier must be zero, or in other words, the boundary conditions are such that

$$\psi(-\infty) - \psi(\infty) = 0 \quad (2.4.7)$$

The shooting method effectively turns the problem into an initial value problem, where solutions to the Schrödinger equation exist when the condition in Eq. 2.4.7 is satisfied. A flow diagram outlining the algorithm that was used to implement the shooting method and determine the correct solutions to Schrödinger's equation for arbitrarily shaped QWs is given in Fig. 2.4.3.

To start with, a guess is made for an energy range, defined by E_{MIN} and E_{MAX} , where a solution to the Schrödinger equation is believed to exist. Eq. 2.4.6 is then used to propagate the wavefunctions across the input QW profile for the energies defined as E_{MIN} and E_{MAX} . An illustration of the wavefunctions returned by Eq. 2.4.6 for two guessed start energies is given in Fig. 2.4.4. For even symmetry wavefunctions, if the starting energy is larger than the solution to the Schrödinger equation, when propagating the wavefunction from the left to the right of the QW profile, the value returned at the far right, $\psi(X_{MAX})$, will be lower than the starting value at $\psi(X_{MIN})$. If the starting energy is lower than the solution, the value returned for $\psi(X_{MAX})$ will be larger than the starting value at $\psi(X_{MIN})$. The deviation from the starting at $\psi(X_{MAX})$ is opposite for odd symmetry wavefunctions. If $\psi_{E_{MAX}}(X_{MAX}) \times \psi_{E_{MIN}}(X_{MAX}) < 0$, at least one solution to the Schrödinger equation exists within the defined energy range. This condition applies to both odd and even symmetry wavefunctions. If this condition is satisfied the algorithm proceeds.

In the next segment of the algorithm, a middle energy, E_{MID} , is defined from the minimum and maximum energies given previously. The wavefunction for the starting energy E_{MID} is then propagated across the QW profile. A solution to the Schrödinger equation exists between E_{MAX} and E_{MIN} if the output of the condition $\psi_{E_{MAX}}(X_{MAX}) \times \psi_{E_{MID}}(X_{MAX}) < 0$ is

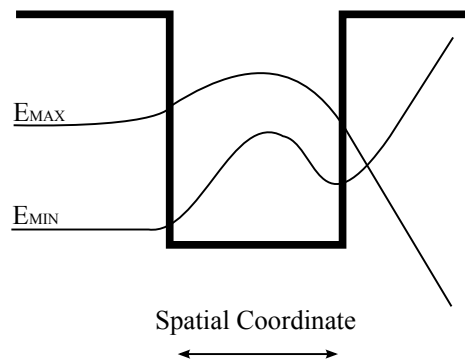


Figure 2.4.4: An example of solutions returned by the algorithm. If the starting energy, E_{MIN} for example, is lower than the correct solution to Schrödinger's equation, when propagating a wavefunction from the left to the right of the QW profile, the value returned at the far right will be higher in energy than the starting energy. If the starting energy is larger than the solution, the value returned at the far right will be lower in energy. A solution to Schrödinger's equation is found if the output energy at the far right is the same as the starting energy.

negative. If this is the case, the energy range is redefined as $E_{MAX} = E_{MAX}$ and $E_{MIN} = E_{MID}$. Otherwise, the solution exists between E_{MID} and E_{MIN} and the energy range is redefined as $E_{MIN} = E_{MIN}$ and $E_{MAX} = E_{MID}$. By repeating this procedure the algorithm hones in on the correct solution.

One case where it is useful to numerically solve the Schrödinger equation is when examining QWs affected by an electric field. In these cases, the QW potential becomes sloped as shown in Fig. 4.1.1. Such conditions cannot be solved analytically and are important in the discussion of ZnO QWs. The numerical method for solving the Schrödinger equation will be used throughout this thesis.

2.5 Phonons

In solid materials it is possible to define quantised vibrational modes that propagate through the lattice with a fixed energy and momentum. These lattice vibrations have particle like properties and are called phonons. The different vibrational modes can be characterised as follows; acoustic phonon modes correspond to atoms within the same unit cell moving in phase relative to each other and optical phonon modes correspond to atoms within the same unit cell moving out of phase. Each of these can be further divided into two transverse and one longitudinal mode, where the vibration is perpendicular or parallel to the direction of propagation, respectively. The phonon dispersion curve for GaAs is shown in Fig. 2.5.1. The dots represent the experimentally measured points and the red line is calculated [5]. As one would expect, the phonon energy varies depending on the direction of propagation through the lattice. The transverse acoustic (TA) and longitudinal acoustic (LA) phonon mode frequencies go to zero at the zone centre, Γ . Away from the zone centre the LA phonon mode has higher energy than the TA mode. From Γ to L the LA and TA mode energies effectively increase linearly from 0 to ~ 26 meV and ~ 8 meV, respectively. Similarly from Γ to X, there is an approximately linear increase in the LA and TA mode energies from 0 to ~ 28 meV and ~ 10 meV, respectively. From L to X the acoustic phonon modes flatten

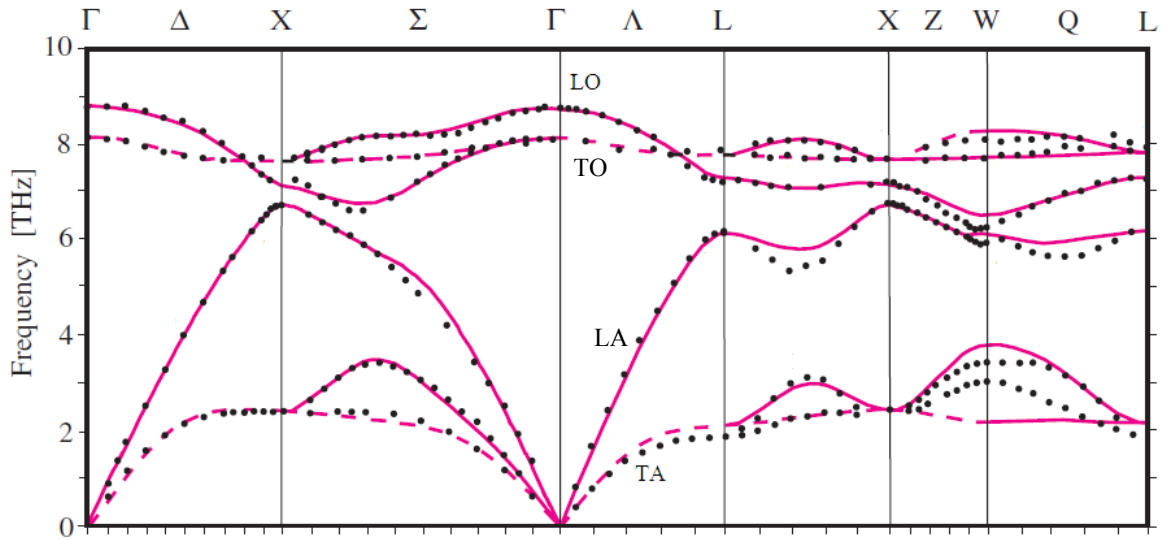


Figure 2.5.1: The phonon dispersion curve for GaAs. This figure has been taken from Yu and Cardona [5]. The points of symmetry from the first Brillouin zone are labeled. The LO, LA, TA and TO phonon modes are labeled at the zone centre.

out, and the LA phonon mode energy is 26 meV, which is much larger than the energy of the TA modes. The longitudinal optical (LO) and transverse optical (TO) modes are relatively flat, regardless of propagation direction, and have energies of ~ 35 meV and ~ 33 meV at Γ , respectively, which is much larger than the acoustic phonons, especially near the zone centre. Such dispersion curves can be measured using inelastic neutron scattering or high resolution inelastic x-ray scattering [5].

The average occupation number for a phonon mode is given by

$$n(T) = \frac{1}{\left[\exp\left(\frac{\hbar\omega}{k_B T}\right) - 1 \right]} \quad (2.5.1)$$

where n is the average number of phonons per phonon mode as a function of temperature, T , $\hbar\omega$ is the phonon energy, and k_B is Boltmann's constant [12]. From the relation given in Eq. 2.5.1 and the dispersion curve given in Fig. 2.5.1, several of the key temperature dependent phonon properties are immediately evident. With the energy of LO and TO modes in the vicinity of 30 - 35 meV, reducing the temperature of the semiconductor will reduce

the average occupation number of these phonon modes and lower the probability of LO and TO phonon interaction. At low temperatures, LO and TO phonon interaction can essentially be ignored. In addition, since the TA and LA phonon frequencies go to zero at the zone centre, acoustic phonon interactions will still be present within the semiconductor, even at low temperature.

The phonon density is reflected in the temperature dependent homogeneous linewidth (Γ_h) of excitons (excitons are discussed in Sec. 2.6). The homogeneous linewidth follows the relation [12, 13]

$$\Gamma_h(T) = \Gamma_h(0) + aT + bn(T) \quad (2.5.2)$$

where $\Gamma_h(0)$ is the temperature independent homogeneous linewidth, or the zero-phonon linewidth, which is due to properties such as impurity scattering and exciton-exciton scattering, a is the temperature dependent acoustic phonon contribution which varies linearly with T and $b_n(T)$ is the optical phonon scattering contribution which is a function of optical phonon occupation.

2.6 Excitons

Following the excitation of an electron from the VB to the CB in a semiconductor, the electron and hole can bind to each other through the Coulomb interaction to form a quasi-particle called an exciton. Conceptually this system is similar to the hydrogen atom and also has discrete eigen-energies. Unlike the hydrogen atom, which consists of a proton and electron with vastly different masses (1.672×10^{-27} kg and 9.109×10^{-31} kg, respectively) the exciton is made up of an electron and a hole with more closely matched effective masses (in GaAs, the effective masses of the electron, HH and LH are $0.063m_0$, $0.51m_0$ and $0.082m_0$, respectively). The equations which are used to determine the binding energy and Bohr radius of the hydrogen atom may also be used for an exciton. The binding energy and the radius of

the ground state exciton are given by [14]

$$E_b = \frac{-m_r^* R_y}{m_0 \epsilon_r^2} \quad (2.6.1)$$

$$a_{ex} = \frac{\epsilon_r m_0 a_0}{m_r^*} \quad (2.6.2)$$

where $m_r^* = \frac{m_e^* m_h^*}{m_e^* + m_h^*}$ is the reduced mass of the electron and hole pair, m_0 is the rest mass of the electron, ϵ_r is the dielectric constant, a_0 is the Bohr radius for a hydrogen atom (0.52 Å) and R_y is the Rydberg energy (13.6 eV).

An electron may bind with either a HH or a LH to form an exciton. HH and LH excitons for bulk GaAs have binding energies of 4.3 meV and 2.7 meV respectively and Bohr radii of 123 Å and 194 Å respectively. Due to the large dielectric constant of semiconductors, the electron and hole Coulomb interaction is screened, leading to the Bohr radius of both HH and LH excitons being much larger than the width of a GaAs unit cell (5.65 Å for GaAs) [8]. A high quality material with few defects and impurities is therefore crucial for creating excitons in semiconductors. Due to the small binding energy of excitons in GaAs, the thermal energy at room temperature ($k_B T \approx 25$ meV) is sufficient to break the exciton bond. Excitons, therefore, are only observed in GaAs at low temperatures. Such excitons with Bohr radii much larger than the lattice constant of the material and weak binding energy are called Wannier-Mott excitons.

In bulk materials, the exciton transition energy is lower than the bandgap of the bulk material by an amount equal to the exciton binding energy. An energy level diagram showing the exciton and the unbound electron and hole continuum states as a function of the centre of mass wavevector is shown in Fig. 2.6.1(a). In Fig. 2.6.1(b), the absorption spectrum expected from the exciton and unbound continuum states is shown. Excitons can either form directly by the absorption of a photon with energy equal to the electron and hole bound state, or through excitation of the unbound continuum states and Coulomb attraction of an electron

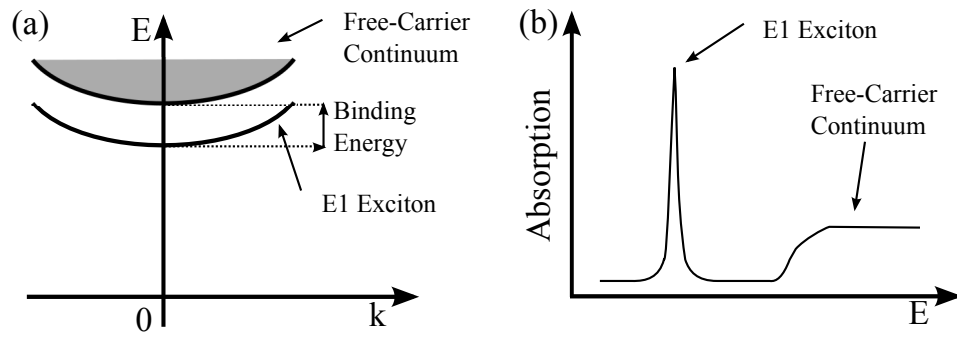


Figure 2.6.1: (a) A schematic comparing the energy of bound and unbound electron and hole states as a function of the centre of mass wavevector. (b) The absorption spectrum expected from the exciton and free-carrier continuum states [12].

and hole. The relative absorption strengths at the exciton and unbound continuum energies shown in Fig. 2.6.1(b) are typical of absorption spectra near the bandgap of semiconductors. As is shown in this case, the exciton absorption line usually dominates as a result of the larger oscillator strength of the exciton transition.

In QWs, the confinement of excitons leads to a reduction in the Bohr radius and an increase in the binding energy. For a 2D exciton, the binding energy is given by [12]

$$E_{b,2D} = \frac{-R_y m_r^*}{[m_0 \epsilon_r^2 (n - 1/2)^2]} \quad (2.6.3)$$

For $n = 1$, the 2D exciton binding energy is four times larger than the binding energy of a 3D exciton. In addition to this, the 2D Bohr radius is reduced by a factor of 2 compared to the 3D Bohr radius [12]. If the binding energy can be increased to values larger than the thermal energy at room temperature, devices based on excitons can operate at room temperature [15, 16]. The oscillator strength for the n^{th} state of an unconfined exciton is proportional to [12]

$$f_{n,3D} \propto \frac{1}{n^3} \quad (2.6.4)$$

For 2D excitons, the n^{th} state dependence of the oscillator strength is proportional to [12]

$$f_{n,2D} \propto \frac{1}{(n - 1/2)^3} \quad (2.6.5)$$

For the first exciton state in a 2D system the oscillator strength of the exciton is a factor of 8 larger than within bulk semiconductors. Within QW based light emitting devices there is, therefore, an increased probability of radiative recombination compared to devices based on bulk semiconductors of the same material, leading to enhanced efficiencies for light generation.

Phonon-exciton scattering processes have significant consequences for the properties of excitons in semiconductors. This is reflected in the temperature dependence of the exciton homogeneous linewidth, recombination lifetime and dephasing lifetime. The temperature dependence of phonon interactions arises because the phonon occupation number is temperature dependent, as discussed in Sec. 2.5. Coupling between excitons and optical phonons can also lead to phonon replica signals, where phonon replicas appear as peaks separated from exciton emission lines in a photoluminescence spectrum by an energy equal to the optical phonon energy. Such coupling is mediated by the Fröhlich interaction [5]. The strength of the interaction is dependent on the polarity of the semiconductor material. Fröhlich coupling therefore can be significant in very polar semiconductors, such as ZnO and GaN.

The scattering of excitons with other excitons or with free carriers is dependent on carrier density and is mediated through the Coulomb interaction. The scattering of excitons again has implications for exciton linewidth, recombination lifetime and dephasing lifetime. Free unbound carriers have been found to be eight times more effective at dephasing excitons than exciton-exciton scattering. In QWs, the scattering rates between these particles are even higher [12]. In cases where very high carrier densities are present, the Coulomb interaction that binds electrons and holes can be screened, preventing excitons from forming. This is known as the Mott density.

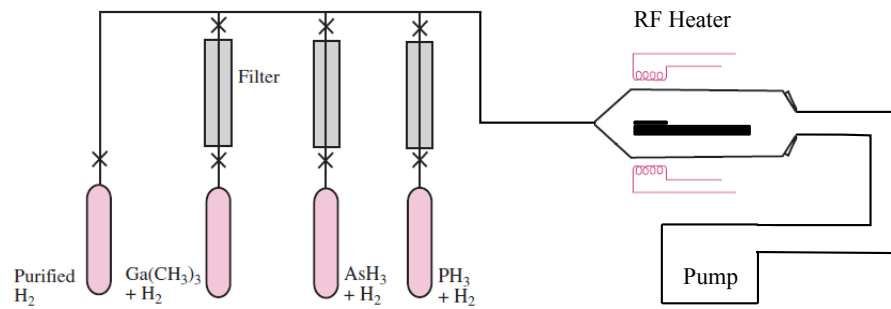


Figure 2.7.1: A schematic of a horizontal MOCVD system. This figure is modified from Yu and Cardona [5].

2.7 Semiconductor growth techniques

Molecular beam epitaxy (MBE) and metal-organic chemical vapour deposition (MOCVD) are methods used to grow semiconductor thin films and semiconductor QWs. In essence, the growth of a semiconductor material by the MOCVD process is by a precisely controlled pyrolysis reaction, where metal-organic (MO) compounds, metal atoms with alkyl radicals attached, decompose when making contact with a heated substrate. After breaking down, the metal atoms are left behind and the residual organic gaseous molecule is carried off. The pyrolysis reaction in the case of GaAs, grown using trimethylgallium (TMGa) and arsine, (AsH_3) is given by



where, in the presence of heat, GaAs attaches to the substrate and methane is carried off. A schematic of a MOCVD system with a horizontal reactor is presented in Fig. 2.7.1. Growth typically takes place in a low pressure atmosphere (0.1 atm), which offers two key benefits; Firstly, the reaction rate at the substrate is low, allowing formation of high quality crystalline structures and, secondly, the reduced gas density prevents the MO compounds from reacting before reaching the substrate.

With the presence of other elements/molecules in the reactor during the growth process,

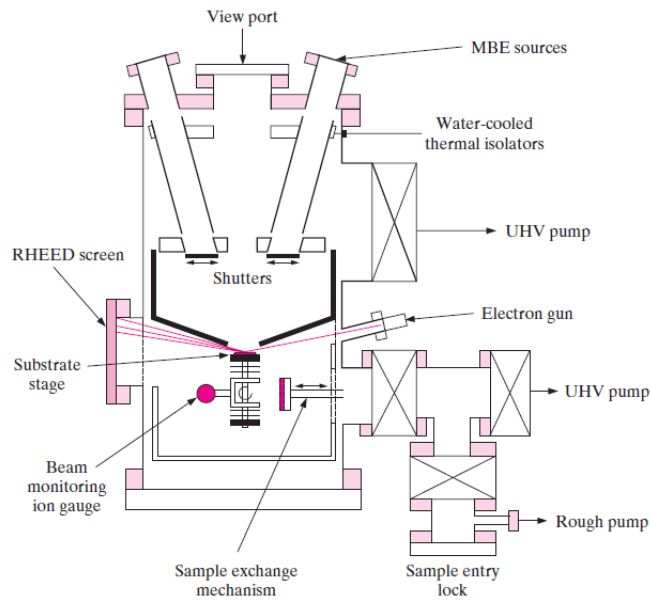


Figure 2.7.2: A schematic of a MBE system. This figure is taken from Yu and Cardona [5].

it is reasonable to expect that they too may be incorporated into the sample structure. This is indeed the case, and can lead to interstitials and unintentional doping. Such issues can be resolved by optimising the growth conditions. For example, in the case of GaAs growth, residual carbon from TMGa can be incorporated into the sample structure. To an extent, this can be compensated for by including additional atomic hydrogen in the growth region, which can be achieved by having an excess of AsH_3 in the system [17].

The MOCVD growth process has been up-scaled in order to produce many wafers simultaneously. Increasing the reactor size, however, leads to a range of engineering issues. In order to repeatably produce homogeneous wafers, the temperature distribution within the reactor needs to be uniform, the samples are usually rotated in order to account for reagent depletion in the carrier gas, the gas flow rate over all samples needs to be matched and the relative reagent density also needs to be uniform throughout the reactor.

Whilst MOCVD growth is achieved by passing a gas over a material in a low pressure environment, MBE takes place in an ultrahigh vacuum environment (1×10^{-14} atm). Under these high vacuum conditions, a thermally evaporated elemental source with a small aperture produces a ballistic beam of atoms which is incident on a substrate. As only the constituent

elemental materials are present within the MBE chamber, impurity concentrations are limited by the purity of the elemental source materials. When binary and ternary alloys are being grown, several molecular beams are incident on a substrate simultaneously. Low incident rates allow thin films to grow epitaxially, with growth rates in the order of a few Å/s. A schematic of a typical MBE system is shown in Fig. 2.7.2.

It is often difficult to precisely control the incident atom rate at the substrate [5]. For this reason, a number of techniques are used to monitor the sample growth rate. Some examples are reflection high energy electron diffraction (RHEED), low energy electron diffraction (LEED), X-ray and ultraviolet photoemission spectroscopy (XPS and UPS). These monitoring methods may also be used to determine the substrate temperature and examine the changing surface morphology. As these methods require an ultrahigh vacuum they cannot be used in MOCVD systems.

The requirement of an ultrahigh vacuum for MBE is rather prohibitive with regard to semiconductor mass production, where high vacuum levels can be difficult to achieve on large scales, leading to slow sample production rates. Large scale commercial production of semiconductor materials is therefore usually by the MOCVD process. MBE systems are, however, particularly useful for small scale production of high quality materials and for research applications.

Chapter 3

Experimental

3.1 Introduction

The electronic transitions within ZnO and GaAs QWs are examined in this thesis using a variety of optical spectroscopic techniques. Details of the laser system used in the following experiments are presented in Sec. 3.2. The experimental details for time-integrated photoluminescence (PL), time-resolved photoluminescence (TRPL) and pump-probe (PP) experiments are presented in Sec. 3.3, 3.4 and 3.5. In Sec. 3.6, four-wave mixing (FWM) experiments, including the mechanisms which lead to the dephasing of a macroscopic polarisation, are discussed. Two-dimensional Fourier transform spectroscopy (2DFTS) is used to aid the analysis of FWM signals and is discussed in Sec. 3.7. These experiments may also be used to investigate other optically active systems (for example, polymers, biomolecules) however, the experimental techniques will only be referred to in the context of semiconductors.

3.2 Ultrafast laser system

The experiments detailed in this thesis utilised the output from a fs-pulsed laser system, as shown in Fig. 3.2.1. This system may be broken down into three stages: femtosecond pulse generation, amplification, and spectral customisation by parametric amplification and frequency mixing.

Pulsed laser light is generated by a mode-locked Ti:sapphire laser oscillator (Spectra-Physics Tsunami) which is pumped by a frequency doubled NdYVO₄ continuous wave (cw) laser (Spectra-Physics Millennia). The oscillator outputs pulses with a pulse duration that may be varied from 60 - 150 fs at a repetition rate of 82 MHz, with an average pulse energy of 8.5 nJ and a photon energy that is tuneable from 1.15 eV to 1.8 eV (690 to 1080 nm). The laboratory is designed so that, depending on the experiment being performed, the oscillator output may be used directly in experiments, for example, for use with a streak camera. Without a pulse picker, the high repetition rate limits the use of this laser to experiments studying dynamics on timescales shorter than 12 ns.

Optical parametric amplifiers (OPA's) are used to tune the photon energy of the laser, covering the range from 4.95 eV to 0.6 eV (250 to 2000 nm). These are based on 2nd and 3rd order non-linear processes (parametric downconversion, second harmonic generation and sum frequency generation) and generally require a pump laser with peak pulse energies greater than 100 μ J. The Swinburne laser system generates such pulses with a femtosecond chirped-pulse regenerative amplifier (Spectra-Physics Spitfire). Amplification achieves a gain of $\sim 10^5$, producing pulses with an energy of 1 mJ and duration ~ 100 fs. The repetition rate is reduced from 82 MHz to 1 kHz, as determined by the repetition rate of the amplifier pump source (Q-switched Nd:YLF, Coherent Evolution-30). The slower repetition rate allows dynamics on timescales up to 1 ms to be investigated.

A schematic of the OPA is shown in Fig. 3.2.2. At the location labelled 1, a broad continuum extending into the infrared spectrum is generated by focusing 5 % of the OPA

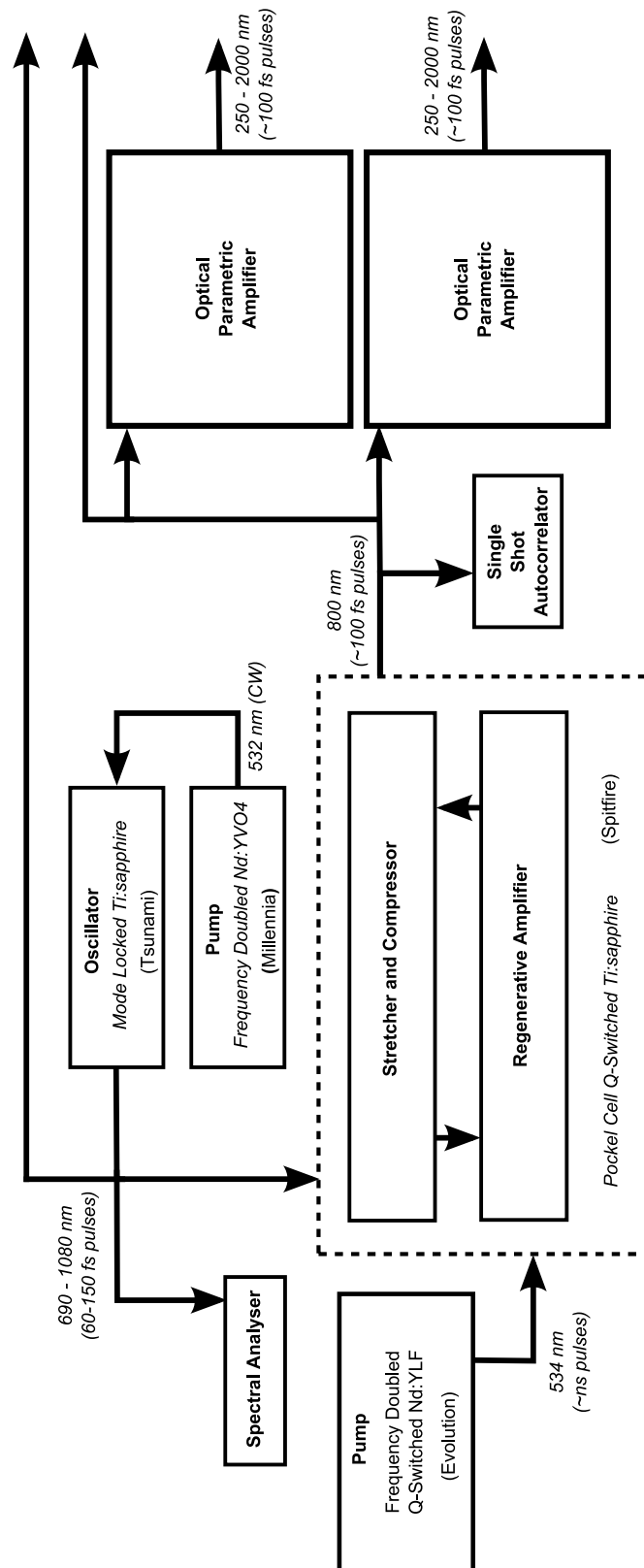


Figure 3.2.1: A schematic of the ultrafast laser system. The details are given in the text.

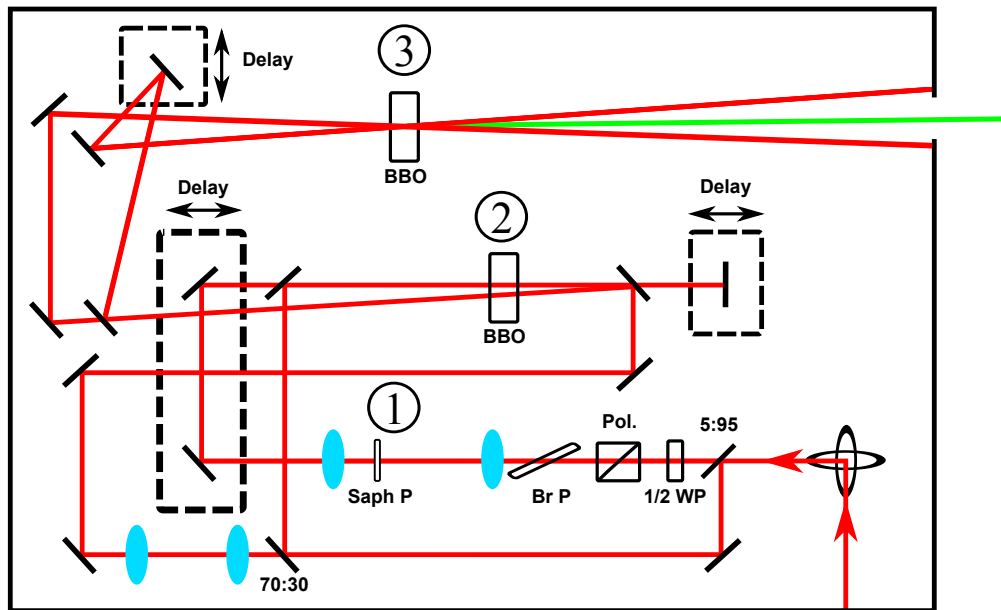


Figure 3.2.2: The optical parametric amplifier, with labels 1, 2 and 3 indicating where white light generation, optical parametric amplification and sum frequency generation occur.

pump beam onto a sapphire crystal. The continuum is used to seed optical parametric amplification for a broad range of photon energies at point 2. The amplification of specific photon energies is determined by the phase matching angle of the type II beta barium borate (BBO) crystal at location 2. The seed stimulates the parametric down conversion of 1.55 eV pump photons (E_p) into signal (E_s , which has the same energy as the seed) and idler (E_i) photons while conserving energy ($E_p = E_s + E_i$). The signal and idler intensities increase exponentially as the signal, idler and pump propagate through the crystal [18]. The design of this OPA utilises two passes through the optical parametric amplification stage (location 2). This system may produce pulses with photon energies in the range 1.1 - 0.62 eV (1100 nm to 2000 nm) and pulse energies of $\sim 100 \mu\text{J}$. At location 3 in Fig. 3.2.2, the signal or idler may be mixed with the residual pump beam from location 2 for sum frequency generation, or alternatively, second and/or third harmonic generation performed on the signal or idler. Further second harmonic generation of the sum frequency generated signal can extend the output range to 4.95 eV. Discussion of optical parametric amplification and sum frequency generation techniques can be found in *Ultrafast Laser Pulses and Applications*, edited by W. Kaiser [18].

3.3 Time-integrated photoluminescence

Time-integrated photoluminescence (PL) is the simplest spectroscopic technique used in this thesis. It is also quite informative, revealing much about the sample under investigation. For these reasons, PL is usually the first characterisation method used to examine new samples. In the simplest of PL experiments, the sample is illuminated by laser light with a photon energy greater than the material bandgap. Under these conditions, electrons will be excited across the bandgap, relax to the local conduction band minimum, and eventually recombine with a hole through radiative or non-radiative processes. The excitation and relaxation of carriers in a QW sample is represented in the diagram in Fig. 3.3.1(a). In this figure an electron and hole are excited in the barrier material, captured by the QW and radiatively recombine whilst occupying the lowest QW subband states.

A typical PL experiment may look like the schematic in Fig. 3.3.1(b). In this setup the radiative emission from the sample is collected and spectrally analysed by a spectrometer. The spectrum of the emitted light reveals the energy of the radiative interband electronic

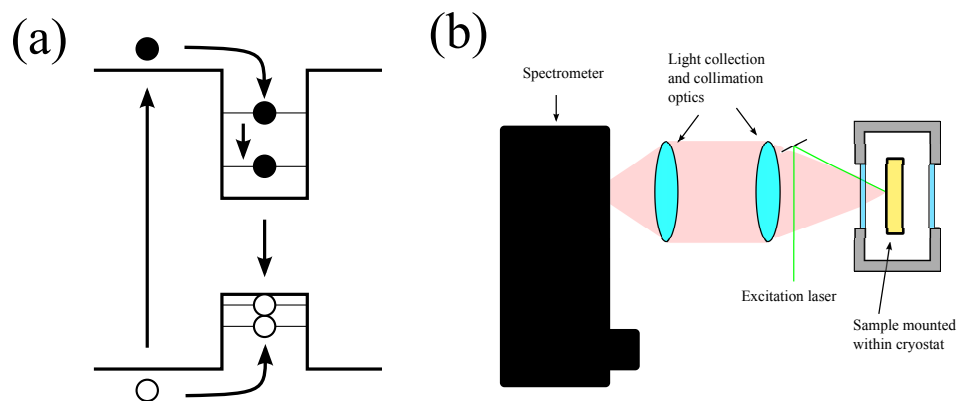


Figure 3.3.1: (a) A schematic representing the excitation of an electron from the valence band to the conduction band in the barrier for a QW sample. The electron relaxes to the lowest subband level of a QW before radiatively recombining with a hole in the valence band, which has also relaxed to the lowest energy subband level. (b) A schematic of the time-integrated photoluminescence setup. A laser excites the sample mounted within the He cryostat. The photoluminescence is collected, collimated and then imaged onto the entrance slit of the spectrometer for spectral analysis.

transitions. In addition to determining the bandgap of semiconductors and the lowest interband transitions in QWs, the emission spectrum may also be used to identify the presence of impurities and defects, and the intensity can provide details of their densities. The shape and width of the emission lines can reveal if transitions are homogeneously or inhomogeneously broadened and the extent to which they are broadened. Temperature and excitation intensity dependent photoluminescence may be used to elucidate the mechanisms responsible for carrier recombination. From the PL spectra alone, an assessment of the quality of the sample being examined may be made. The PL technique, however, is limited to observing the emission from radiative interband transitions. Intraband transitions are generally not radiative and can be identified using other techniques, for example, photoluminescent excitation or spectrally resolved absorption measurements. A comprehensive review of photoluminescence spectroscopy in semiconductors can be found in the review *Photoluminescence Spectroscopy of Crystalline Semiconductors* by G. D. Gilliland [19].

3.4 Time-resolved photoluminescence (TRPL)

The excited carrier recombination dynamics can be examined by time resolving the photoluminescence. This measurement can be made by either directly detecting the decay of the photoluminescence signal using a fast detector and some time resolving electronics, or by correlating the emission signal with a pulse of light that is much shorter in duration than the emission. Pulse correlation techniques achieve the highest time resolution and are usually reserved for measuring dynamics on the femtosecond/picosecond time scale. In most cases the time resolution is limited by the width of both the excitation and measuring pulses. Directly time resolving the photoluminescence with a photomultiplier tube (PMT) attached to an oscilloscope can typically achieve a time resolution on the order of 10 ns. Time-correlated single photon counting, also a direct detection method, can achieve time resolution on the order of 10 ps. New direct detection devices are now becoming available which approach the resolution offered by pulse correlation techniques. One example of this is

a streak camera by Hamamatsu with better than 200 fs resolution [20]. Besides such devices being available, the simplicity and relative cost of setting up pulse correlation experiments make the pulse correlation technique tremendously useful.

The most common pulse correlation methods are upconversion, which is a variation of the sum frequency generation process used in the OPAs, and Kerr gating. In an upconversion measurement, the sample is excited with a pulsed laser and the emission is focused onto a BBO crystal. The signal is mixed with a gating pulse, where by the signal and the gate must be overlapped in space and in time. Typically, the gating pulse only overlaps with the signal over a small temporal window. The gating pulse should be taken from the same laser system which is used to excite the sample to avoid pulse to pulse jitter. When the BBO crystal is at the correct phase-matching angle, a signal is generated at a frequency corresponding to the sum of the gating pulse and sample emission frequencies. The intensity of the upconversion signal is proportional to the intensities of the PL and the gating pulse. The time resolution of upconversion is defined by the temporal overlap of the gate pulse and the PL signals. By varying the delay of the gating pulse relative to the excitation pulse the overlap region is shifted in time, allowing the intensity of the PL to be measured any time after excitation, thereby time resolving the emission. The spectral width of the upconverted signal is limited by the bandwidth of the phase matching conditions within the crystal. By rotating the crystal angle, and therefore changing which wavelengths are phase matched for sum frequency generation, PL with a broad spectrum may be time resolved. A Kerr gate on the other hand is able to gate the entire spectrum of the PL by making use of birefringence induced by a strong electric field, such as a focused high energy laser pulse in a Kerr medium. This effectively acts as a switchable wave plate, which when combined with a linear polariser, creates a gate for a broad spectrum. In the experimental setup for the Kerr gate, the sample photoluminescence is passed through two crossed polarisers with the Kerr medium in between. When a portion of the sample photoluminescence and the gating beam are overlapped in the Kerr medium, the polarisation of that portion of the photoluminescence is rotated and isolated from the rest of the sample emission by the second polariser. The decay of the photoluminescence is again measured by delaying the gating pulse relative to

the sample excitation. Whilst the time resolution of this pulse correlation technique has the potential to be limited by the pulse width, in most cases the time resolution is limited by the response of the Kerr medium and can typically vary from 200 fs to 1 ps [21].

Direct detection methods are typically easier to implement experimentally than pulse correlation methods, and provided the same information can be obtained, are used whenever possible. Of the direct detection devices mentioned, streak cameras achieve the shortest time resolution. Light that enters the streak camera is incident on a photocathode and stimulates the release of electrons. The number of electrons produced is proportional to the intensity of the incident light. The electrons are accelerated across the streak tube and pass between a pair of plates. A time-varying voltage is applied to the plates as the electrons pass between them, deflecting the electrons at angles depending on the voltage across the plates. By timing the voltage change across the plates with the moment that the electrons pass between the plates, the angle of deflection is a function time. The deflected electrons are incident on a micro-channel plate for amplification and are finally incident on a phosphor screen, which emits light on the arrival of an electron. This light may then be easily detected and spatially resolved with a CCD camera. As the electrons are deflected into different angles as a function of time, the spatial dimension along which the electrons are deflected and detected may be calibrated for time. If for example two pulses of light 100 fs in duration and separated by 10 ps entered the streak camera, the pulse of light that arrived first would generate a signal on one edge of the phosphor screen. The electrons generated from the pulse of light that entered second would be deflected at a different angle and would generate a signal at another point on the phosphor screen along the deflection axis. If the streak camera is coupled to the output of a spectrometer, the axis perpendicular to the electron deflection direction may be used to resolve spectral information.

In this thesis two direct detection methods are used to time-resolve photoluminescence. The first is with a Hamamatsu IP28 GaAs PMT connected to a fast oscilloscope with data storage capability. The time resolution of this setup is 10 ns and the PMT is connected to a scanning monochromator to provide spectral resolution. For shorter time resolution,

and access to the UV range where upconversion techniques are not convenient, a streak camera with a time resolution of 20 ps is used. The streak camera is coupled to an imaging spectrometer, allowing the emission energy to be simultaneously resolved.

3.5 Differential transmission pump-probe

The pump-probe technique is perhaps the most widely used technique in ultrafast spectroscopy. In general, the sample is excited by a laser pulse, and the induced changes are probed by a second pulse overlapping the excited region of the sample. By controlling the delay between the two pulses, one may time-resolve the dynamics of interest within the sample. The simplest case for DTPP is when the pump and probe photon energies are equal and are equal to the sample bandgap. The pump pulse will excite electrons from the valence band to the conduction band, partially filling the conduction band and partially emptying the valence band. If the probe pulse is incident on the sample immediately following the pump pulse, the probability for absorption of probe photons is reduced because the valence band is partially empty and the conduction band is partially full. Consequently, the intensity of the transmitted probe beam is larger than when the pump pulse is not incident on the sample. Plotting the differential transmission of the probe beam as a function of the delay between the pump and probe pulses provides a measure of the population recombination dynamics. The time resolution in a DTPP experiment is typically limited by the pulse duration. For very short pulses (< 10 fs), the physical stability of the experiment and the resolution of the delay stage can become limiting parameters.

There are many variations of the DTPP technique which can be used to explore carrier dynamics. These include two-colour DTPP experiments, where pumping and probing at different photon energies allows one to measure the dynamics of carrier relaxation to a different excited state in samples with multiple energy levels. By using a broad spectrum probe and spectrally resolving the differential transmission, the dynamics over a wide range of photon energies may be resolved simultaneously.

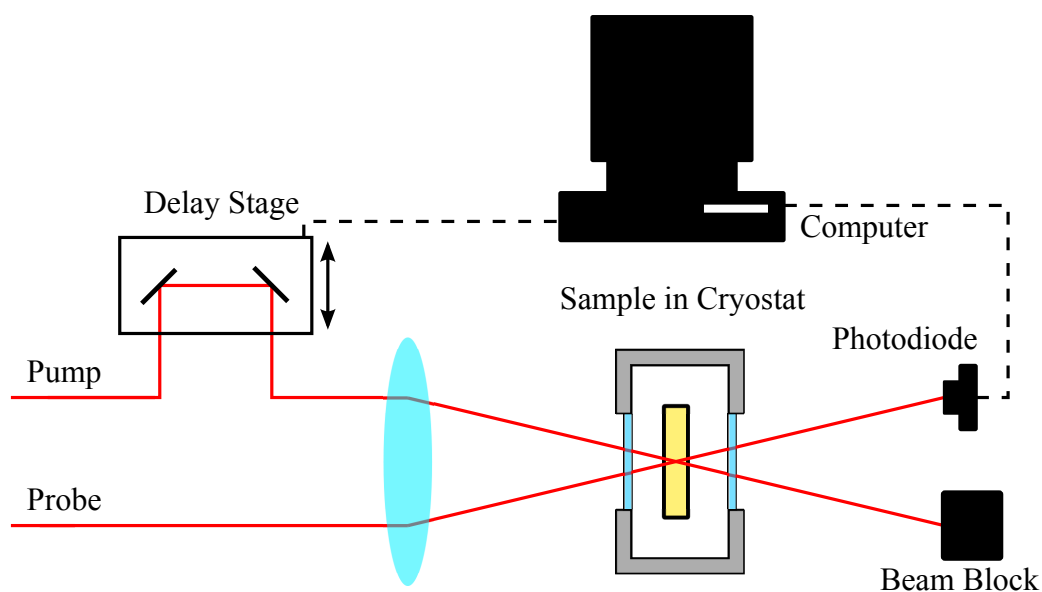


Figure 3.5.1: The experimental setup for DTPP used in this thesis. The pump and probe beams are focused onto the sample, which is mounted within a circulating He cryostat. The probe intensity is monitored as a function of pump-probe pulse separation.

A schematic of the DTPP experiment used in this thesis is shown in Fig. 3.5.1. As shown by the figure the sample is mounted within a He cryostat which is used to control the sample temperature from 20 - 300 K. The time delay between the pump and probe pulses is varied by using a computer controlled delay stage. After passing through the sample, the probe beam is incident on a photodiode. The pump and probe beams are modulated at different frequencies by an optical chopper, which modulates the signal of interest at the difference between the chopping frequencies. A lock-in amplifier is used to detect the DTPP signal at the modulated frequency. This detection setup is essential in order to detect the small changes in the probe transmission on top of the background signal from the transmitted probe and any scattered light from the pump beam.

3.6 Four-wave mixing spectroscopy

Four-wave mixing (FWM) is an extremely versatile tool for examining the coherent dynamics within an excited system. Measurements of the coherent dynamics of excitons within

semiconductor materials can provide valuable insight into the structure and composition of the material. Such information is useful for determining the viability for the use of that material in semiconductor based devices. The coherence lifetime of excitons is particularly sensitive to the presence of defects and impurities, therefore measurements of the coherence lifetime can be used to examine the sample quality. Varying experimental parameters such as temperature, sample composition, size and shape of the nanostructure or the excitation conditions allows one to explore the interactions which contribute to the loss of coherence, and therefore the interactions which are influencing the optical and electrical properties of the material. FWM may also be used to explore coherent coupling phenomena, such as heavy-hole light-hole beating in semiconductors [22, 23], beating between excitons localised to monolayer fluctuations in QWs [24, 25], and exciton-continuum interactions [26–28]. In this thesis, FWM is used to explore the coherent dynamics of excitons in asymmetric double QWs.

3.6.1 Dephasing and decoherence

Exciting a semiconductor with a short pulse of coherent light generates a coherent superposition of the ground and excited states. In the case of excitons, the pulse generates a coherent superposition of the bound electron and hole states. The probability of electron occupancy of the two states oscillate at the frequency of the transition with an initial phase determined by the excitation pulse. After a period of time, a scattering event will cause the loss of the phase set by the excitation pulse. The probability for the loss of the definite phase relationship between the superposition and the excitation source can be defined by a phenomenological lifetime, T_2^* , which is called the pure decoherence time. If the time for such a scattering event to occur is much longer than the lifetime of the exciton, T_1 , the lifetime then becomes the limiting factor for the loss of the initial phase. The decoherence time, T_2 , is given by Eq. 3.6.1.

$$\frac{1}{T_2} = \frac{1}{2T_1} + \frac{1}{T_2^*} \quad (3.6.1)$$

Exciting a region within a sample with a short pulse of light, however, does not excite a single exciton, but an ensemble of excitons which all initially have a phase given by the excitation source. An ensemble of in-phase superposition states is called a macroscopic polarisation, and it is the dynamics of this which are measured by a FWM experiment. The intensity of the radiation emitted by the macroscopic polarisation depends on the phase coherence within the ensemble. As excitons within the ensemble lose their definite phase relationship with the excitation source, the phase coherence within the ensemble decreases. When the phases become evenly distributed between 0 and 2π , the phase coherence within the ensemble is zero and the emission from the ensemble ceases. The decay of the macroscopic polarisation is known as a free polarisation decay (FPD).

For a homogeneously broadened sample the decay of the macroscopic polarisation is proportional to $\exp(-2t/T_2)$, where $T_2 = 2\hbar/\Gamma_H$ and where Γ_H is the homogeneous linewidth [12]. If the sample is inhomogeneously broadened, the different transition frequencies within the ensemble lead to an additional damping of the macroscopic polarisation. If the inhomogeneous linewidth is narrower than the spectral width of the laser, the macroscopic polarisation decays with a time constant proportional to $1/\Gamma_{InH}$, where Γ_{InH} is the inhomogeneous linewidth [12]. If the inhomogeneous linewidth is larger than the spectral width of the laser, the macroscopic polarisation decays within the duration of the excitation pulse. If $\Gamma_{InH} \gg \Gamma_H$, individual excitons may remain in phase with the excitation source well beyond the time where the coherence within the ensemble is lost. As long as the excitons have remained in phase with the excitation source, that is, they have not experienced an event which has caused a jump in their phase, the loss of coherence within the ensemble due to inhomogeneous broadening can be reversed. The macroscopic polarisation can be temporarily restored by reversing the evolution of the different frequency components by the application of an additional pulse (see Sec. 3.6.2). The rephasing of the macroscopic polarisation and temporary emission of light is called a photon echo. Generating photon

echoes subsequently provide a means to measure the decoherence time, T_2 , and therefore the homogeneous linewidth for an inhomogeneously broadened transition. The Bloch sphere concept in the following section will be used to explain the interactions responsible for generating a photon echo.

3.6.2 The Bloch sphere

The Bloch spin-vector formalism, which was developed to interpret magnetic resonance experiments on spin-half particles, may also be applied to an electronic transition for a hypothetical two-level atom undergoing a light induced excitation [29]. There are many instances where the interaction between two energy levels can be approximated as a two-level atom. The interaction between the lowest energy conduction and valence band sublevels of a QW can be considered to be a closed two-level system (TLS) if the two levels are well separated from and do not interact with all other energy levels in the system.

The pseudo polarisation vector, V_{ps} , is a unit vector in three-dimensions that describes the quantum state of a TLS and is confined within the Bloch sphere. A representation of the Bloch sphere is shown in Fig. 3.6.1. V_{ps} is defined by cartesian coordinates R_1 and R_2 , which define the phase of a coherent superposition state, and R_3 , which defines the probability of finding an electron in the excited state minus the probability of finding it in the ground state [29]. If V_{ps} is aligned parallel to the R_3 axis ($R_1=0, R_2=0$) and $R_3 = -1$, this case represents the TLS being in the ground state. If $R_3 = 1$, V_{ps} represents the TLS in the excited state. In the R_1 - R_2 plane, where $R_3 = 0$, the TLS is an even superposition of the ground and excited states. The motion of R_1 and R_2 are defined by

$$R_1(t) = S_1 \cos(\omega t) - S_2 \sin(\omega t) \quad (3.6.2)$$

$$R_2(t) = S_1 \sin(\omega t) + S_2 \cos(\omega t) \quad (3.6.3)$$

where $\hbar\omega$ is the energy required to make a transition from the ground state to the excited

state in the TLS, and S_1 and S_2 define the starting values for R_1 and R_2 , respectively. To simplify this picture, we use the rotating wave approximation (RWA) and choose a frame of reference where V_{ps} is rotating about R_3 at a frequency ω_0 , equal to the angular frequency of the TLS transition. Under the RWA, the frequencies oscillating at twice the frequency of interest are discarded and only the variables changing slowly with time are considered [29]. By using the RWA, the optical frequencies are removed from the problem. Eq. 3.6.2 and Eq. 3.6.3 then become

$$R_1(t) = S_1 \cos(\delta t) - S_2 \sin(\delta t) \quad (3.6.4)$$

$$R_2(t) = S_1 \sin(\delta t) + S_2 \cos(\delta t) \quad (3.6.5)$$

where δ is the detuned angular frequency ($\delta = \omega - \omega_0$). In this picture, V_{ps} will remain

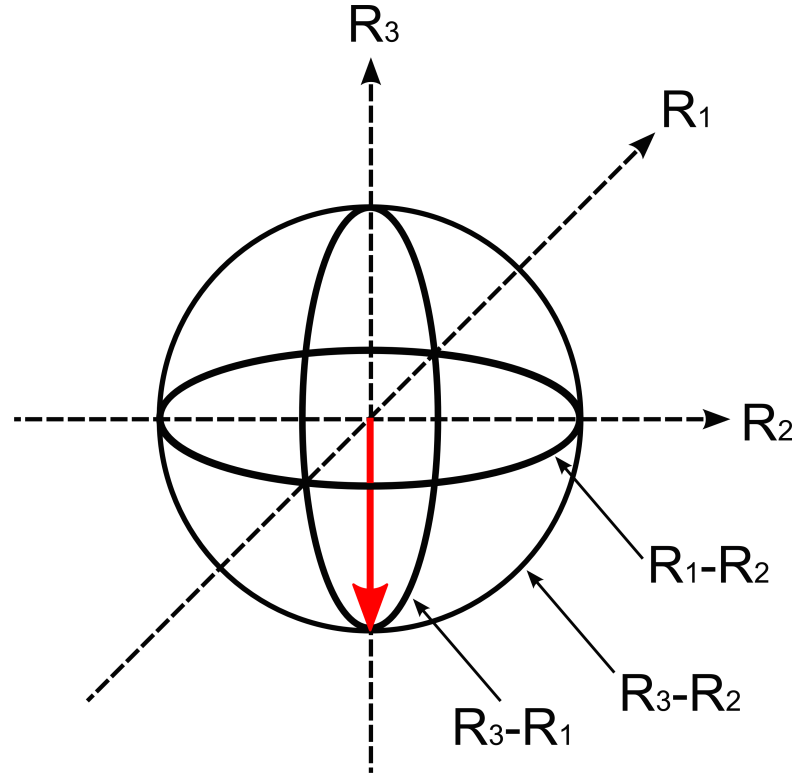


Figure 3.6.1: The Bloch sphere with the pseudo polarisation vector, V_{ps} , representing the two-level atom in the ground state. The R_3 - R_2 , R_3 - R_1 and R_1 - R_2 planes are indicated.

stationary in the R_1 - R_2 plane at $R_1 = S_1$ and $R_2 = S_2$.

The following description of the evolution of V_{ps} follows the notation used by Klingshirn in 'Semiconductor Optics' [30]. The relations given by Eq. 3.6.6 - 3.6.8 are derived from the optical Bloch equations, which come from Schrödinger's time dependent equation. The derivation of these relations is not necessary for the discussion in this section, however, if required it can be found in 'Optical resonance and two-level atoms' by L. Eberly and J. H. Allen or 'Semiconductor Optics' by C. Klingshirn [29, 30].

The equations of motion for the components of V_{ps} , whilst ignoring damping, are given by

$$\dot{R}_1(t) = -\delta R_2(t) \quad (3.6.6)$$

$$\dot{R}_2(t) = \delta R_1(t) + \omega_R R_3(t) \quad (3.6.7)$$

$$\dot{R}_3(t) = -\omega_R R_2(t) \quad (3.6.8)$$

where $\omega_R = \frac{\mu_{ge} E_0}{\hbar}$ is the Rabi flopping frequency, the frequency at which the population of a two level atom cycles from the ground state to the excited state whilst excited by a light field, μ_{ge} is the dipole matrix element relating to the transition, and E_0 is the amplitude of the electric field.

At first the case where a TLS is resonantly excited and $\delta = 0$ is considered. The solutions to the equations of motion for V_{ps} are given by

$$R_1(t) = R_1(t_0) \quad (3.6.9)$$

$$R_2(t) = R_2(t_0) \cos(\omega_R t) + R_3(t_0) \sin(\omega_R t) \quad (3.6.10)$$

$$R_3(t) = -R_2(t_0) \sin(\omega_R t) + R_3(t_0) \cos(\omega_R t) \quad (3.6.11)$$

During excitation, V_{ps} precesses around R_1 at the Rabi flopping frequency ω_R . Equations 3.6.9, 3.6.10 and 3.6.11 suggest that by controlling the excitation pulse area it is possible to control the Bloch vector orientation. If the TLS is initially in the ground state ($R_1(0)=0, R_2(0)=0, R_3(0)=-1$), when $\omega_R t = \pi$ (i.e., the excitation pulse area = π), V_{ps} will have shifted from $R_3(0)=-1$ to $R_3(0)=1$. This special case is known as a ‘ π -pulse’ excitation. By exciting the TLS so that $\omega_R t = \pi/2$, one can shift V_{ps} from ($R_1(0)=0, R_2(0)=0, R_3(0)=-1$) to ($R_1(\pi/\omega_R)=0, R_2(\pi/\omega_R)=1, R_3(\pi/\omega_R)=0$). Similarly, this case is known as using a ‘ $\pi/2$ -pulse’. These pulse area definitions allow one to define interactions in the Bloch sphere picture in a convenient manor.

The generation of photon echo can be described using the Bloch sphere. In the following discussion an ensemble of TLSs which are resonantly excited by delta pulses will be considered. Damping due to decoherence will again be ignored, though the effects inhomogeneous broadening will now be included. In this example ω_0 is equal to the central frequency of the inhomogeneously broadened exciton line. The pulse ordering given in Fig. 3.6.2 is used. The points in time labeled t_0 and t_1 correspond to the incidence a $\pi/2$ -pulse and π -pulse and t_2 corresponds to the emission of a photon echo. The time periods defined as τ correspond to the intervals between t_0 and t_1 , and t_1 and t_2 , respectively. The ensemble is initially in the ground state with the V_{ps} for each TLS defined by the coordinates $R_1=0, R_2=0$ and $R_3=-1$ as shown in Fig. 3.6.3(a). The application of a $\pi/2$ -pulse at t_0 places V_{ps} in the R_1, R_2 plane (Fig. 3.6.3(b)). In the R_1, R_2 plane and during the time period τ , the Bloch vector for each individual TLS is free to precess around the R_3 axis as given by

$$R_1(t) = R_1(t_0)\cos(\delta t) - R_2(t_0)\sin(\delta t) \quad (3.6.12)$$

$$R_2(t) = R_1(t_0)\sin(\delta t) + R_2(t_0)\cos(\delta t) \quad (3.6.13)$$

$$R_3(t) = R_3(t_0) \quad (3.6.14)$$

where $R_1(t_0) = 0, R_2(t_0) = 1$ and $R_3(t_0) = 0$. If the ensemble was homogeneously broadened, $\delta = 0$ and the V_{ps} for each TLS would remain stationary at $R_1 = 0, R_2 = 1$, representing that the

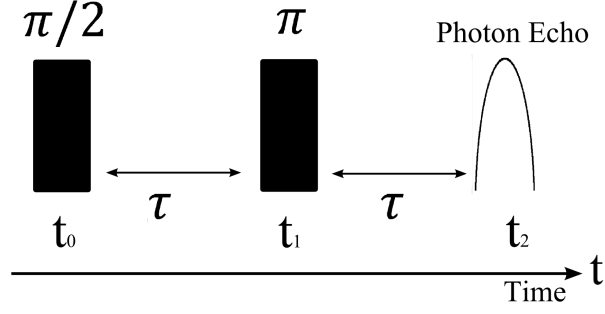


Figure 3.6.2: The pulse ordering (t_0 and t_1), pulse areas and time periods (t_0 to $t_1 = \tau$ and t_1 to $t_2 = \tau$) corresponding to the formation of a photon echo at $t=t_2$. These definitions are used in Fig. 3.6.3

phase coherence within the ensemble is maintained. For an ensemble of inhomogeneously broadened TLSs, a wide range of values for δ will exist. In that case the V_{ps} for each TLS with a transition energy not equal to ω_0 will not remain stationary with the same orientation in the R_1 and R_2 plane, but will precess around R_3 at frequencies given by δ (Fig. 3.6.3(c)). In time, the V_{ps} for each TLS in the ensemble become widely distributed around R_3 on the $R_1 - R_2$ plane, as shown in (Fig. 3.6.3(d)), representing the complete dephasing of a macroscopic polarisation.

The application of a π pulse at time t_1 causes a rotation of V_{ps} for each TLS around the R_1 axis (Fig. 3.6.3(e)-(f)). This is shown by

$$R_1(t_1) = R_1(\tau) \quad (3.6.15)$$

$$R_2(t_1) = R_2(\tau)\cos(\omega_R t) + R_3(\tau)\sin(\omega_R t) = -R_2(\tau) \quad (3.6.16)$$

$$R_3(t_1) = -R_2(\tau)\sin(\omega_R t) + R_3(\tau)\cos(\omega_R t) = 0 \quad (3.6.17)$$

where $\omega_R t = \pi$ and thus $R_3(t_1) = 0$ (as $R_3(\tau) = 0$), $R_1(t_1) = R_1(\tau)$, and $R_2(t_1) = -R_2(\tau)$. The V_{ps} for each TLS continue to precess around R_3 in the same direction as previously, where the sign for R_1 has not changed, however, the sign change in R_2 causes a rephasing of the macroscopic polarisation. This is shown in Fig. 3.6.3(g).

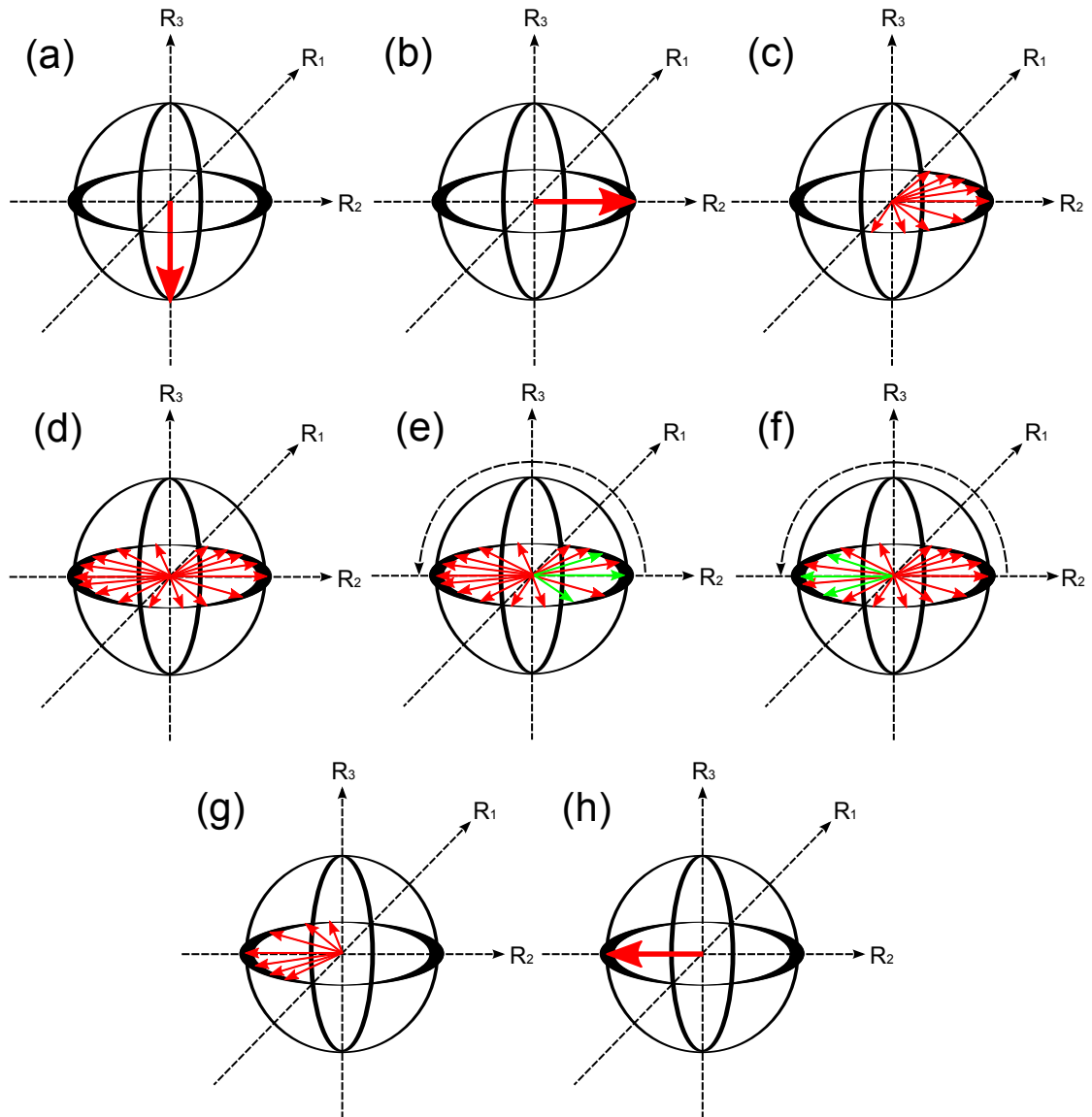


Figure 3.6.3: A slide show of Bloch spheres representing the generation of a photon echo. The time periods discussed in the text correspond to the periods indicated in Fig. 3.6.2. (a) The inhomogeneously broadened ensemble of TLS in the ground state. (b) Following the application of a $\pi/2$ pulse at t_0 , V_{ps} for an ensemble of TLSs is shifted into the R_1 - R_2 plane. (c) The V_{ps} for excitons detuned from the frame of reference (ω_0) precess around R_3 . (d) After a short time the average phase of the ensemble, defined by the sum of the V_{ps} wavevectors in the R_1 - R_2 plane, equals zero. (e)-(f) The application of a π pulse at t_1 after a time τ produces a rotation of the R_1 - R_2 plane about the R_1 axis. (g) Following the application of a π pulse at t_1 , the ensemble begins to rephase. (h) The V_{ps} for each TLS overlap, representing that the macroscopic polarisation has temporarily reformed and a photon echo is emitted at t_2 . The figure is modified from Demtröder [31].

After the interaction at t_1 , the evolution of R_1 , R_2 and R_3 are given by

$$R_1(t) = R_1(t_1)\cos(\delta t) - R_2(t_1)\sin(\delta t) \quad (3.6.18)$$

$$R_2(t) = R_1(t_1)\sin(\delta t) + R_2(t_1)\cos(\delta t) \quad (3.6.19)$$

$$R_3(t) = R_3(t_1) \quad (3.6.20)$$

At $t=t_2=2\tau$

$$R_1(t_2) = -\sin(\delta\tau)\cos(\delta\tau) + \cos(\delta\tau)\sin(\delta\tau) = 0 \quad (3.6.21)$$

$$R_2(t_2) = -\sin(\delta\tau)\sin(\delta\tau) - \cos(\delta\tau)\cos(\delta\tau) = -1 \quad (3.6.22)$$

$$R_3(t_2) = R_3(t_1) = 0 \quad (3.6.23)$$

the V_{ps} for each TLS overlap (as shown in Fig. 3.6.3(h)), independent of the value of δ , and the macroscopic polarisation is re-established. The pulse of emission that occurs whilst the is macroscopic polarisation is restored is called a photon echo.

The application of a $\pi/2$ pulse, followed by a π pulse, represents the interactions responsible for the signal generated by two-pulse FWM experiments. If the π pulse is split into two $\pi/2$ pulses, a three-pulse experiment can be described by this formalism. In that case, following the first excitation by a $\pi/2$ pulse, the second $\pi/2$ pulse converts the coherence to a population where the phases of each TLS within the ensemble are stored. The application of the a third $\pi/2$ pulse converts the population back to a coherence where $R_2 = -R_2$, as was the case in the previous example.

3.6.3 Experimental realisation of FWM

The implementation of the FWM experiment is not too dissimilar to the DTPP experiment. In both cases multiple pulses with different wavevectors, separated by controllable delays, are incident on the sample. Perhaps the most significant difference between DTPP and FWM experiments is that the signal of interest in FWM experiments can be emitted in different directions to the excitation pulses, and is therefore background free. This allows the FWM signals to be detected separate from signals generated as the result of population dynamics. As was shown in Sec. 3.6.2, a $\pi/2$ pulse followed by a π pulse, or alternatively, three ' $\pi/2$ -pulses', are required to generate a FWM signal. In the following discussion, three pulses with wavevectors \mathbf{k}_1 , \mathbf{k}_2 and \mathbf{k}_3 , respectively, will be considered. The incident pulse wavevectors and interpulse timing are depicted in Fig. 3.6.4. Background-free signals are generated in the wavevector conserving directions $-\mathbf{k}_1 + \mathbf{k}_2 + \mathbf{k}_3$, $\mathbf{k}_1 - \mathbf{k}_2 + \mathbf{k}_3$ and $\mathbf{k}_1 + \mathbf{k}_2 - \mathbf{k}_3$, which are given the labels \mathbf{k}_4 , \mathbf{k}_5 and \mathbf{k}_6 , respectively. The discussion will focus on the FWM signal generated in the \mathbf{k}_4 direction. The time delay between the first two incident pulses is given by τ , which is called the coherence time. The delay between the second two pulses is called the waiting time and is given by T . These time definitions will be used throughout the thesis.

Using these time and wavevector definitions, and including the effects of dephasing, the interactions discussed in Sec. 3.6.1 and Sec 3.6.2 will now be briefly summarised. The first pulse with wavevector k_1 excites a region on the sample and generates a macroscopic polarisation. The macroscopic polarisation radiates in the direction k_1 . A second pulse with wavevector k_2 and delayed relative to the first by a delay τ is incident on the same region on the sample. The second $\pi/2$ interaction stores the phase of the polarisation by converting it into a population. A third pulse with a wavevector of k_3 , delayed relative to the second pulse by a delay T , is incident on the same region of the sample and converts the population back to a polarisation. A signal will be generated in the k_4 direction provided some coherence remains. If the case of a homogeneously broadened sample, the signal is a FPD. If the sample is inhomogeneously broadened the signal will be a PE.

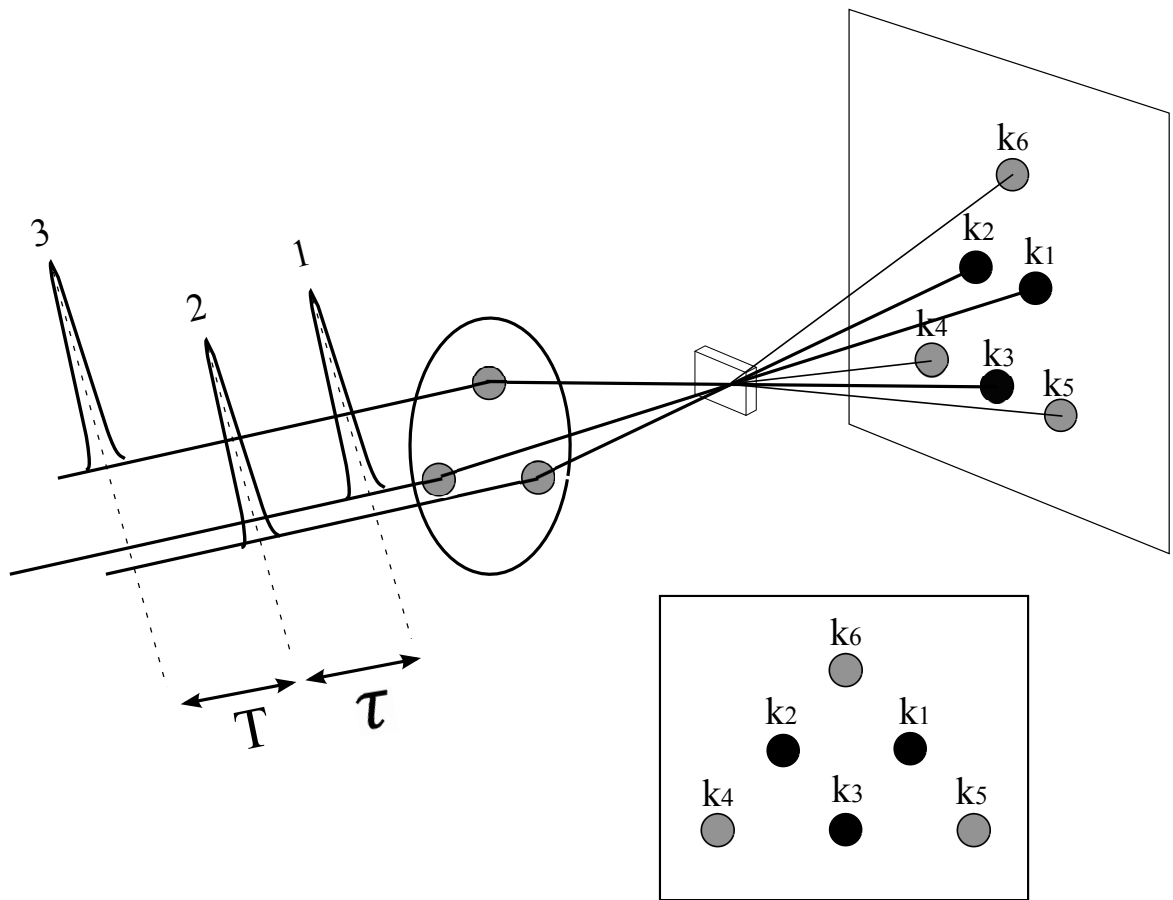


Figure 3.6.4: The pulse ordering and the incident wavevectors in the three-pulse FWM experiment. For pulses with wavevectors k_1 , k_2 and k_3 , signals are generated in the momentum conserving directions k_4 , k_5 and k_6 . The triangle geometry shown here is used in the experiments.

The generation of a photon echo in a given wavevector conserving direction requires the correct excitation pulse sequence. For a given detection direction, the pulse ordering that leads to the rephasing of the coherence within an ensemble requires that the pulse with the negative wavevector is incident on the sample first. The first and third pulses will then induce opposite phase evolutions on the ensemble, causing a rephasing of the ensemble coherence following the third pulse and the generation of a photon echo. This pulse configuration is subsequently called the rephasing pulse ordering. An example of such a case is for the pulse sequence given by pulse 1, pulse 2 and pulse 3 and for signal detection in $\mathbf{k}_4 = -\mathbf{k}_1 + \mathbf{k}_2 + \mathbf{k}_3$. If the pulse with the \mathbf{k}_2 wavevector is incident first, a photon echo is generated in the \mathbf{k}_5 direction. Similarly, if the pulse with the \mathbf{k}_3 wavevector is incident first, a photon echo

is generated in the \mathbf{k}_6 direction. If the ordering of the pulses with wavevectors \mathbf{k}_1 and \mathbf{k}_2 are switched (incident pulse ordering is $\mathbf{k}_2, \mathbf{k}_1, \mathbf{k}_3$) and the signal is still detected in the \mathbf{k}_4 direction, the phase evolution induced on the ensemble phase by the first and third pulses is in the same direction and rephasing does not occur. Rather than a PE, a FPD will be emitted in the \mathbf{k}_4 direction. This pulse configuration is called the non-rephasing pulse ordering.

Different properties of the sample can be measured by detecting the signal as a function of different pulse orderings and interpulse delays. By scanning the delay between pulse 1 and pulse 2, for pulse 1 before pulse 2, whilst pulse 2 and pulse 3 are overlapped ($T = 0$), and detecting the signal emitted in \mathbf{k}_4 , one may examine the coherent dynamics of the system in the absence of population dynamics. Scanning the delay between pulse 1 and 2 for fixed non-zero values of T allows one to examine the effects of the population dynamics on the signal generated. If the stored coherence has not been lost during the waiting time, due to population relaxation for example, a FWM signal is generated. If the first and second pulses are overlapped temporally ($\tau = 0$), a population grating is formed from which the third pulse diffracts. In the regime where the diffusion of the grating is very slow compared to the population lifetime, the transient grating technique may be used as a background free DTPP experiment.

Two-pulse and three-pulse FWM experiments are used in this thesis. In Fig. 3.6.5, the schematic for the two-pulse FWM experiment is shown. The three-pulse experiment can be visualised by adding an additional delay stage and input excitation beam, and considering signals generated with wavevectors of $\mathbf{k}_4, \mathbf{k}_5$ and \mathbf{k}_6 . In the two-pulse case, the two incident pulses have wavevectors \mathbf{k}_1 and \mathbf{k}_2 and generate signals in the momentum conserving directions $2\mathbf{k}_2 - \mathbf{k}_1$ and $2\mathbf{k}_1 - \mathbf{k}_2$. When examining QW samples, signals are also emitted in the directions $-2\mathbf{k}_2 + \mathbf{k}_1$ and $-2\mathbf{k}_1 + \mathbf{k}_2$ as a result of the uncertainty principle. In this very specific case, the position of emitting particles (ie. excitons) is well defined perpendicular to the QW plane, resulting in an uncertainty in the momentum, and hence the emission direction along this axis [32]. The forward and reverse signals carry the same information. This configuration is useful for examining QWs grown on substrates which absorb light

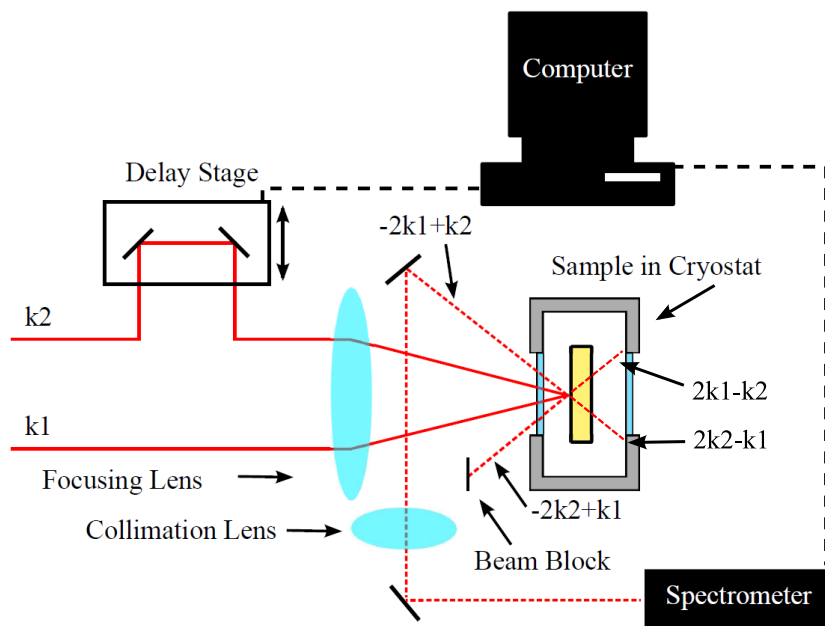


Figure 3.6.5: The beam geometry of the two pulse four-wave mixing setup. In this case, the signal in the $-2\mathbf{k}_1+\mathbf{k}_2$ phase-matching direction (the reverse emission direction) is picked off, collimated, and then directed into a spectrometer to be spectrally resolved as a function of the pulse delay between \mathbf{k}_1 and \mathbf{k}_2 .

at energies equal to the photon energy of the FWM signal, as is the case for the samples examined in Chap. 5.

The signals emitted in FWM experiments can either be time and spectrally integrated, time-integrated and spectrally resolved, or time-resolved. Time-integrated detection is the easiest detection method to implement, however the spectral information is lost. By spectrally resolving the FWM (SR-FWM) signal, one can acquire significantly more information. If, for example, a broad excitation source is used and multiple exciton states are excited simultaneously, SR-FWM can differentiate the FWM signals originating from different states based on their emission energy. These time-integrated signals from homogeneously and inhomogeneously broadened samples decay proportional to $\exp(-2\tau/T_2)$ and $\exp(-4\tau/T_2)$, as shown by Yajima and Taira [12, 33]. The decay of the TI-FWM signal from inhomogeneously broadened samples is a factor of two faster than for homogeneously broadened samples. This is due to the phase coherence within the ensemble dephasing over a period of 2τ before the photon echo is generated (duration τ

between the first two pulses, and duration τ after the third pulse). It is therefore necessary to know whether the sample is homogeneously or inhomogeneously broadened in order to accurately determine T_2 . Time-integrated two-pulse FWM experiments are not able to determine explicitly if the FWM signal is a FPD or a PE, therefore resulting in an uncertainty in the value of T_2 by a factor of 2 [12]. In three-pulse FWM experiments it is possible to estimate whether the signal generated for rephasing pulse ordering is a photon echo when the signals for rephasing and non-rephasing pulse ordering are compared [34] (if the sample is inhomogeneously broadened, the signal generated for non-rephasing pulse ordering will decay at a much faster rate than the signal generated for rephasing pulse ordering). If the FWM signal is time-resolved, it is reasonably straight forward to determine whether the signal is a FPD or a photon echo, and therefore remove any ambiguity regarding the value of T_2 .

3.7 Two-dimensional Fourier transform spectroscopy

Optical two-dimensional Fourier transform spectroscopy (2DFTS) is an extension of FWM spectroscopy and is used to explore correlations between electronic transitions [35, 36]. Using 2DFTS, one may produce 2D frequency spectra where the two axes correspond to the frequencies of a coherent polarisation in two different time domains. Such 2D spectra may be used to isolate quantum pathways and identify energy transfer, coherent coupling, excited state absorption, whilst separating the contributions of inhomogeneous and homogeneous broadening to linewidths [35, 37–40]. In condensed matter systems such as semiconductor QWs, many-body reactions may also be resolved [37, 41–45].

In the standard three pulse FWM experiment, the first excitation pulse excites a coherence which evolves during the period τ , as shown in Fig. 3.7.1 [37]. Following the second pulse, the phase is stored in the population of the excited states. After the third pulse the coherence is restored with the same phase as the initial polarisation when the second pulse arrived. The restored polarisation evolves during the period t and radiates in the direction which

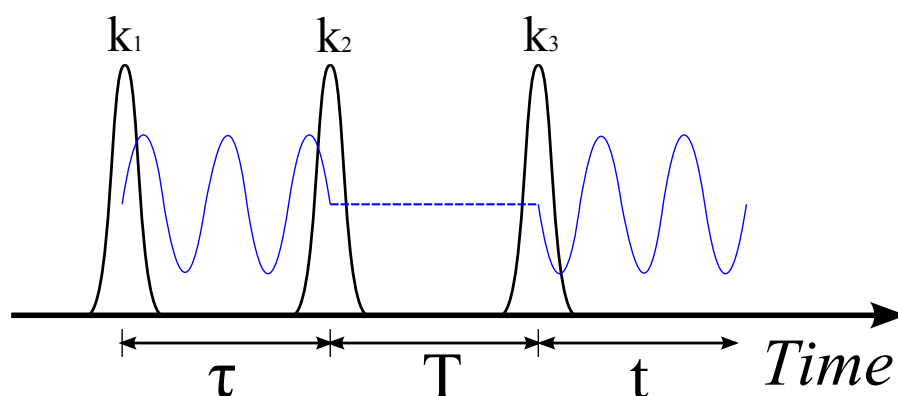


Figure 3.7.1: The evolution of a coherence during a three-pulse FWM experiment [37]. The phase of the coherence generated by a first pulse is stored following the application of a second pulse. The third pulse restores the coherence, which has the same phase as the initial coherence.

conserves the momentum of the incident pulses. The phase of the emitted signal evolves as a function of τ and t . Fourier transforming the signal with respect to τ and t gives the 2D spectrum with the energy in the τ domain correlated to the energy in the t domain. These energies loosely correspond to the absorption and emission energies, respectively. A peak in the 2DFTS spectrum indicates that a coherence oscillating at the energy $\hbar\omega_\tau$ during the period τ and considered to be the absorption energy, leads to an emission during the period t and at the energy $\hbar\omega_t$. A schematic of a 2DFTS spectrum for three example systems is shown in Fig. 3.7.2. In Fig. 3.7.2(a), the system examined is an uncoupled two-level system with transition frequencies ω_1 and ω_2 . Resonantly exciting both transitions with a broadband pulsed laser would produce peaks in the 2DFTS spectrum at the absorption (ω_τ) and emission frequencies (ω_t) of the two transitions. Using a coordinate system (ω_τ, ω_t) , on-diagonal peaks would be observed at (ω_1, ω_1) and (ω_2, ω_2) . In Fig. 3.7.2(b), the excitation of a two level system where electrons can relax from the highest energy transition to the lowest energy transition produces an additional peak at (ω_2, ω_1) . In Fig. 3.7.2(c), quantum beating between coherently coupled two-level systems produces off diagonal peaks in the 2DFTS spectra at (ω_2, ω_1) and (ω_1, ω_2) .

The 2D spectra are generated from the signal measured in FWM experiments. In a typical FWM experiment, the FWM signal is spectrally resolved as a function of τ for fixed

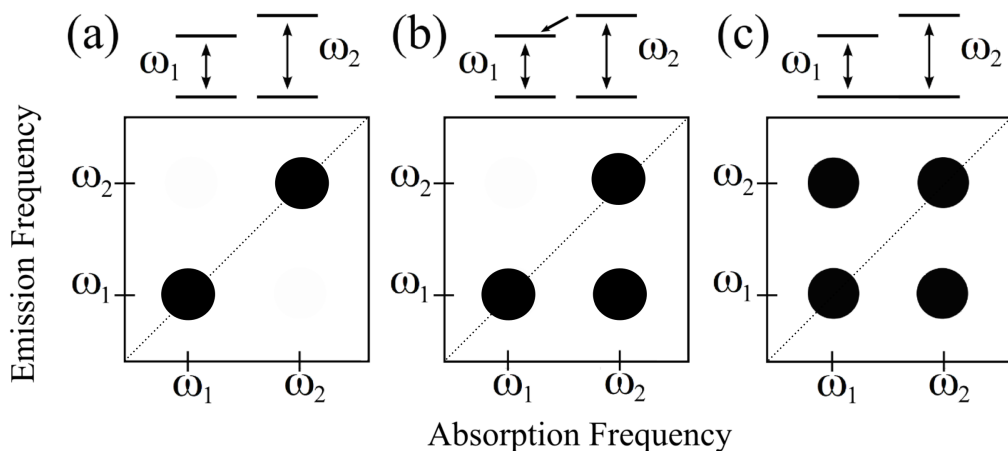


Figure 3.7.2: A schematic of the expected 2DFTS for three different two-level systems. In (a), two uncoupled two-level atoms produce peaks in the 2DFTS along the diagonal at (ω_1, ω_1) and (ω_2, ω_2) , which represent absorption and emission at the same energy. In (b), incoherent relaxation produces a cross-peak at (ω_2, ω_1) , indicating absorption at ω_2 and an emission at ω_1 . In (c), two two-level systems coherently coupled through the ground state produce two cross-peaks at (ω_2, ω_1) and (ω_1, ω_2) in addition to the diagonal peaks (ω_1, ω_1) and (ω_2, ω_2) .

values of T . Usually the intensity of the FWM signal, $I_T(\tau, \omega_t)$ (where $I_T(\tau, \omega_t) = E_T(\tau, \omega_t)^2$), is measured. A Fourier transform of $E_T(\tau, \omega_\tau)$ with respect to τ will give $E_T(\omega_\tau, \omega_t)$ and generate the 2D spectrum. However, since only the intensity was measured and the phase information was lost, a unique solution for the Fourier transform cannot be identified. The phase and amplitude information can be measured using heterodyne detection, where the electric field, $E(\tau, \omega_\tau)$, rather than the intensity of the FWM signal is measured [36, 46]. To perform such measurements in the visible range, the experimental apparatus needs to be phase stable, adding an additional level of complexity to experiments [35]. In a recent publication by Davis et al. [47] it was shown that it is possible to obtain the phase information required to produce the 2DFTS spectra from an intensity measurement of the FWM signal and additional *a priori* information by using a phase retrieval algorithm. This approach negates the requirement for interferometric stability of the experimental apparatus, significantly simplifying the experimental setup required to produce 2DFTS spectra. In addition, a non-interferometric approach allows one to obtain the evolution of the macroscopic polarisation for two-colour FWM experiments, a result which so far has not

been achieved with interferometric based 2DFTS because of the difficulty in obtaining phase stability between pulses with different photon energies.

3.7.1 Non-interferometric phase retrieval algorithm

The method used to determine the phase of the electric field from an intensity measurement is based on iterative algorithms used to resolve the lost phase information in frequency resolved optical gating (FROG) [48] and coherent diffractive imaging (CDI) [49]. Phase retrieval algorithms require an intensity measurement in one Fourier domain and some form of *a priori* information in the conjugate Fourier domain which will reduce the number of possible solutions to the Fourier transform. In the case of the FROG algorithm, the known information is the response function of the system. In the present case, the response function responsible for the emission of the FWM signal is being determined. In the typical CDI problem, the supporting information is based on the known spatial extent of the object being imaged. In the present case, the supporting information is based on known information about the samples transition energies and the excitation conditions, which is used to apply constraints in the time (τ and t) and frequency domains (ω_τ and ω_t).

A flow diagram showing the basic algorithm used is given in Fig. 3.7.3. The algorithm starts with a guess of the electric field, $E_T(\tau, \omega_t)$. This can take the form of a randomized array of complex numbers, however, the algorithm converges significantly faster and more reliably if the guess is closer to the solution. For the cases considered here, the autocorrelation of the measured FWM signal is usually a good start. The first constraint applied to the guess is the amplitude of the measured signal, $|E_T(\tau, \omega_t)| = \sqrt{I_T(\tau, \omega_t)}$. The electric field which propagates through the algorithm must match the measured data. Fourier transforming the solution with respect to τ , the solution is converted to $E_T(\omega_\tau, \omega t)$. $E_T(\omega_\tau, \omega t)$ can be constrained based on what is known about the possible absorption and emission energies within the sample. These parameters may be obtained using a range of additional experiments, for example, photoluminescence, photoluminescence excitation and absorption measurements. The transitions which contribute to the signal will also be limited by the

spectrum of the excitation source.

A 2D inverse Fourier transform with respect to τ and t converts the signal to $E_T(\tau, t)$. $E_T(\tau, t)$ can be constrained by what is known about the processes which generate the FWM signal. Causality requires that the signal cannot exist before all the pulses have reached the sample, therefore, $E_T(\tau, t) = 0$ for $t + \Delta t < 0$, where Δt is the excitation pulse duration. Since the duration of the signal is finite and decays with a decoherence lifetime given by T_2 , one may define an upper limit for t where $E_T(\tau, t) = 0$. These two boundaries in time form the basic constraints applied to the solution in this domain.

A Fourier transform of the resultant solution with respect to t converts the signal back to $E_T(\tau, \omega_t)$. At this position in the algorithm, the answer which has propagated this far may be compared to the signal measured in the experiment and a quantitative difference, or error, between the measured and propagated solution determined. The error metric used to compare the algorithm solution and the measured electric field intensity is defined by the mean-square difference between the measured intensity, $I_T(\tau, \omega_t)$, and the calculated solution, which is given by

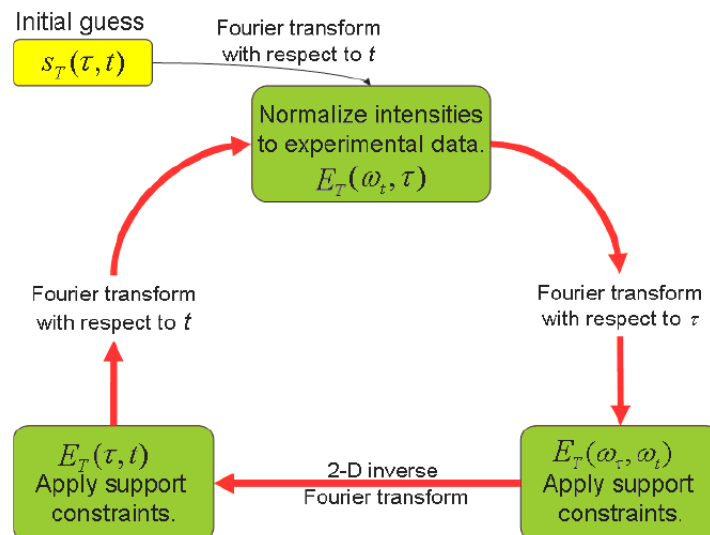


Figure 3.7.3: Flow diagram representing the phase retrieval algorithm. The details are contained in the text.

$$err = \sum (\sqrt{I_T(\tau, \omega_\tau)} - |E_T(\tau, \omega_\tau)|)^2 \quad (3.7.1)$$

The algorithm is cycled until a minimum error can be achieved. The more accurately and tightly the constraints can be defined, the faster the algorithm will converge on a solution.

In addition to the constraints which make up the basic algorithm, other support constraints may be used to assist accurate and efficient retrieval of the phase information and the 2D spectrum. On physical grounds, the FWM signal must be smooth and continuous in both of the time and frequency domains [50]. This *a priori* information regarding the FWM signal may be used to further constrain the solution. The most effective way of ensuring the solution is smooth and continuous is by making an initial guess for the electric field that is smooth and continuous [50]. This support constraint will remove discontinuities in both of the time and frequency domains, improving the quality of the reconstructed electric field. Scatter from sharp discontinuities introduced by the support constraints can also be a problem [50]. The Fourier transform of such edges can lead to artifacts in the conjugate Fourier domain, and in cases where the artifacts in the conjugate Fourier artifact amplitude is significant, can prevent the phase retrieval algorithm from converging. This issue may be overcome by making the signal outside the support constraints decay exponentially [50].

Chapter 4

ZnO/MgZnO quantum wells

4.1 Introduction

Zinc Oxide (ZnO) is a technologically important semiconductor material with many desirable optical and electrical properties, and the potential to be used for a number of device applications [51]. In particular, ZnO has a direct and wide band gap of 3.37 eV [52] at room temperature, thereby being optically active in the UV spectral range. There is currently a demand for cheap and efficient lasers and light emitters in the UV region, with applications that include data storage, sterilisation, lighting, medicinal and a myriad of research and industrial purposes [52–58]. GaN based semiconductor devices are becoming available for such applications, however, there are many compelling reasons why ZnO based devices should be pursued as an alternative. In particular, a number of the optical properties of ZnO are superior to those of GaN. Bulk ZnO has large exciton and biexciton binding energies (60 meV and 15 meV) [52] compared to bulk GaN (25 meV and 5.3 meV) [56, 59]. This will lower the threshold for excitonic stimulated emission and lasing, and allow these processes to occur from low temperatures to well above room temperature [15, 16]. When ZnO is grown as a QW structure, not only is there the opportunity to tune the transition energy, but the exciton and biexciton binding energies will also be further increased.

ZnO has several other properties which interest the semiconductor community. It has a high resistance to radiation damage, suggesting that ZnO devices may be suitable for use in high radiation environments, including space applications[60]. Its low toxicity and biocompatibility make ZnO suitable for use as sensors inside the human body [52, 61, 62]. ZnO is transparent at visible wavelengths, which suggests applications as a transparent conductor, for example, as a potential replacement for ITO (Indium Titanium Oxide), which is expensive and toxic, in the manufacture of LCD screens and solar panels. ZnO is also one of the hardest of the II-VI semiconductors, which is expected to assist device longevity [63]. Depending on the growth conditions, ZnO can readily form a wide range of nanostructures, such as nanocombs, nanorings, nanosprings, nanobelts, nanowires and nanocages, which have potential for use as sensors, transducers and in biomedical sciences [51].

There are, however, a number of inherent properties of ZnO which must be better understood and limitations which must be overcome in order to make the most of the advantages offered by this material system. Perhaps the most significant issue limiting the development of ZnO devices based on *p-n* architecture is the inability to reliably produce high quality *p*-type ZnO. This problem stems from as-grown ZnO being intrinsically *n*-type due to the prevalence of donor-type defects. It has been suggested that this particular problem is caused largely by oxygen vacancies [64]. In order to produce *p*-type ZnO, the density of donor-type defects needs to be reduced by improving growth techniques. In addition, recent work suggests that nitrogen, which is commonly used as an acceptor-type dopant, is too deep to effectively produce *p*-type ZnO, suggesting that appropriate acceptor dopant elements still need to be identified [57, 65]. It has also been suggested that carrier localisation in wide bandgap semiconductors that are doped with a high density of acceptor-type impurities can lead to incorrectly interpreted Hall effect measurements, giving the impression of *p*-type conductivity and therefore inconsistencies in the literature [57]. Resolving these issues would lead to the immediate development of a wide range of light emitting, light sensing and other electronic devices as mentioned above.

Another characteristic of ZnO that can be an advantage or disadvantage is that the unit

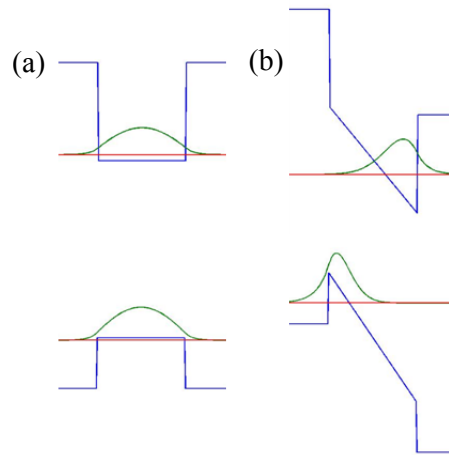


Figure 4.1.1: The CB and VB profiles for a ZnO/Mg_{0.3}Zn_{0.7}O QW plotted (a) not including and (b) including the effects of an internal electric field. The energies and wavefunctions for the first electron and hole subbands have also been plotted. Only the electric field within the QW is considered in this figure.

cell for wurtzite ZnO is polarised along the c -axis [66, 67]. In ZnO/MgZnO QWs grown along the c -axis, the preferential growth direction, there is a mismatch of spontaneous electric fields at the ZnO/MgZnO interfaces. The spontaneous electric field strength across the ZnO and MgZnO unit cells is proportional to the Mg concentration. The difference in polarity is opposite on either side of the QW, resulting in an electric field across the QW [68–70]. A piezoelectric field due to strained ZnO/MgZnO interfaces also contributes to the total electric field across the QW. The strained interfaces are the result of different lattice constants for ZnO and MgZnO. The polarity of the piezoelectric potential is opposite on each side of the QW, therefore also producing an electric field across the QW. The direction of the piezoelectric field, however, is in the opposite direction to the spontaneous electric field. The magnitude of the piezoelectric field is approximately half that of the spontaneous electric field (piezoelectric = $-34x \text{ mC m}^{-2}$, spontaneous = $66x \text{ mC m}^{-2}$, where x = Mg composition), [71–73] giving a total electric field of $32x \text{ mC}^{-2}$.

The electric field produces a slope on the QW potential in both the CB and VB, reducing the energy of the first electron and hole subbands. This is shown in Fig. 4.1.1. For QWs that

are sufficiently wide the transition energy for a transition from the first electron subband to the first heavy-hole subband can be reduced to energies which are less than the bandgap transition for bulk ZnO. The sloping potential also localises the wavefunctions for first electron and hole to opposite sides of the QW. This reduces the overlap integral for the first electron and hole subband wavefunctions and hence reduces the oscillator strength of transitions between the subbands. Consequently, within such a QW, the recombination lifetime for this subband transition is increased and the absorption coefficient reduced. Within a QW which does not have an internal electric field, the first electron and hole wavefunctions are almost perfectly overlapped, with an overlap integral of 0.9998. In a 6 nm wide ZnO/Mg_{0.3}Zn_{0.7}O QW with an electric field of 0.8 MV cm⁻¹ the overlap integral of the wavefunctions for the first electron and hole subbands is reduced significantly to 0.07. Collectively, these effects define what is called the quantum confined Stark effect (QCSE) [74, 75]. If sufficiently large carrier densities can be generated within QWs that have a built in electric field, the electric field may be shielded and its effects reduced. In this chapter the recombination dynamics within QCSEed ZnO QWs, as well as ways of controlling the recombination dynamics, are examined.

In Sec. 4.2, the initial development and characterisation of ZnO/Mg_{0.3}Zn_{0.7}O QWs is briefly reviewed. In Sec. 4.3, the effects of carrier induced shielding of the internal electric field, and the resultant recombination dynamics of excitons in a 6 nm ZnO/Mg_{0.3}Zn_{0.7}O MQW, is studied in detail. The measured recombination dynamics are reproduced by a calculation which self-consistently solves the Schrödinger and Poisson equations. By fitting the calculated population dynamics to the measured TRPL, the transition energy, wavefunction overlap, and carrier density can be determined for any time following excitation. An upper limit to the recombination rate is also calculated, however, pump-probe measurements record an even faster recombination rate, suggesting there are additional recombination processes taking place at early times and high carrier densities. Two-colour pump-probe reveals a strong transient absorption at the blue-shifted transition energy immediately following excitation, providing a measure of the time it takes for the screening of the internal electric field to become established.

In Sec. 4.4 a range of QW structures with stepped barriers are used to control the optical properties of QWs which have a built-in internal electric field. The graded barrier QWs are compared to two square barrier QWs with different well widths. In several of the samples, blue-shifted transition energies and increased recombination rates relative to the square barrier QWs are observed. These QW structures demonstrate that both the inter-band transition energy and transition oscillator strength may be tuned by shaping the barrier of QWs which have a built-in internal electric field.

4.2 Review of the development of ZnO/MgZnO quantum wells

ZnO has been a material of scientific interest for decades, with publications dating back to the 1930s [67, 76]. Currently, most of the ZnO produced annually is used as an additive in concrete and rubber, where its purpose is to improve water resistance and heat conductivity, respectively [67]. The recent interest in ZnO is in its potential for use in a range of electronic and optoelectronic devices. This ‘modern era’ of ZnO was initiated by the work of two Japanese groups in 1997 and 1998 [16, 63, 77], who concurrently demonstrated the growth of high quality thin films of ZnO, a necessary step for making devices. Stimulated emission and optically pumped lasing at room temperature was demonstrated with these samples, verifying the viability of ZnO as a suitable material for UV light emitting devices [16, 63, 77, 78]. In follow-up work by Ohtomo et al. [79], Mg was proposed as an appropriate element for alloying with ZnO to create a material with a larger bandgap for use as a barrier in ZnO based nanostructures. In addition to this, the ionic radius of Mg^{2+} is similar to Zn^{2+} , suggesting the lattice constants for ZnO and MgZnO will be closely matched [79]. Mg was shown to work remarkably well for this purpose and has become the most common material used for alloying with ZnO to form the barriers in ZnO based QWs. In the following year (1999) the first observation of UV emission from ZnO/MgZnO superlattices on sapphire at low temperature was published by the same group [80].

ScAlMgO₄ (SCAM) was introduced by Ohtomo et al. as an alternative substrate to sapphire for ZnO because of near perfect matching of lattice constants [81] (0.08% compared with 18%). This allowed the growth of QW structures directly on the substrate without the need for a buffer layer. Room temperature luminescence of excitons from multiple quantum wells (MQW's) and room temperature stimulated emission of excitons from a superlattice, [82, 83] both on SCAM, and previously not observed with sapphire substrates [81], soon followed. SCAM, however, is expensive and is not widely available, so researchers continued to develop techniques where high quality ZnO could be grown on cheaper substrates. Room temperature emission from ZnO QWs on cheaper Si and sapphire substrates has since been demonstrated [84, 85].

The enhancement of the exciton and biexciton binding energies in narrow ZnO/MgZnO QWs was observed by Sun et al. [15, 86]. This result stimulated much interest because biexcitons have a lower threshold for stimulated emission than excitons and a greater gain coefficient. Continuing this work, Chia et al. determined that in ZnO/MgZnO QWs with widths < 2.5 nm the binding energy of biexcitons increased to values larger than 25 meV, which corresponds to the thermal energy at room temperature. This finding suggested that ultra-low threshold lasers based on biexciton interactions at room temperature may be possible [87]. The presence of coherent biexcitons in ZnO/MgZnO QWs at room temperature was observed by Davis et al. in 2006 using spectrally-resolved one-colour and two-colour four-wave mixing, providing further evidence that biexciton based light emitting devices at room temperature should be possible [88].

In 2004, Gruber et al. demonstrated the first metalorganic vapour phase epitaxy (MOVPE) growth of ZnO QWs [89]. As this is the method usually used for the mass production of opto-electronic devices, this was an important step towards the mass production of ZnO based devices. All growth previous to this was based on molecular beam epitaxy (MBE) or laser assisted MBE (L-MBE).

The presence of the QCSE in ZnO/MgZnO QWs was first mentioned by Makino et al. in 2002 [68]. It is later shown that for a Mg composition of 0.27, the QCSEs only become

noticeable for QWs with widths greater than 4 nm [69]. The absence of the QCSE in work prior to this was because the ZnO/MgZnO QWs studied up to this point in time had been < 4 nm wide.

Morhain et al. [70] soon produced a comprehensive analysis of the QCSE in ZnO. The internal electric field for a ZnO/Mg_{0.22}Zn_{0.78}O system was determined to be 0.9 MV/cm with an interpolation factor of 4.1 x MV/cm, where x is the Mg composition. Very long recombination lifetimes of up to 3 ms were observed for their widest well of 9.5 nm because of the greatly reduced wavefunction overlap integral for the electron and hole. The authors also calculated the effect of the internal electric field on the expected exciton binding energies for different well widths. The exciton binding energy within wide ZnO/MgZnO QWs was found to be much lower than in bulk ZnO because of the QCSE. The interpolation factor was later verified by Davis et al. [90], Bretagnon et al. [91] and by Zhang et al. [92] for a low Mg composition material.

In 2006, Coleman et al. showed the combination of O⁻ ion implantation and rapid thermal annealing may be used as a method for engineering the QW profile of ZnO/MgZnO QWs [93]. This post growth processing smoothed the ZnO/MgZnO QW well/barrier interfaces, slightly narrowing the width of the QW. Large blue shifts of the lowest energy QW transition were observed. In a following paper, Davis et al. [90] showed that the samples also demonstrated shorter recombination lifetimes due to an increase of the electron-hole wavefunction overlap. It was suggested that this method of post growth processing may be used to reduce the effects of the built-in electric field in ZnO/MgZnO QWs.

There is currently much work going into the growth of ZnO/MgZnO QWs which are not c -axis oriented in the growth direction, and hence would not produce an electric field across the QW. Only recently has epitaxial a -axis ZnO with RMS interface roughness suitable for QW growth been demonstrated [94]. ZnO QWs made in this orientation are currently being investigated [95]. There have been other reports of non-polar ZnO/MgZnO QWs [94, 96], however, these results fail to satisfy the appropriate test to prove that a QW is free from an internal electric field. To be confident that such QWs are free from an internal electric field,

one must observe PL emission from a QW with a wide well width (well width > 6 nm) and with a large Mg concentration in the barriers, where the QW emission energy is greater than the bandgap of bulk ZnO.

It is clear that the processes by which high quality ZnO/MgZnO QWs can be grown have advanced significantly since the growth of thin film ZnO was first demonstrated. A range of substrates, including Si, which is important for the incorporation of ZnO devices into existing Si based electronics, have been demonstrated [84, 97]. As soon as reliable *p*-doped ZnO can be demonstrated, there will be an explosion of research on the construction of ZnO based devices and large scale ZnO manufacturing processes, leading to a rapid implementation of ZnO based devices.

4.3 Recombination dynamics within ZnO/MgZnO quantum wells

In this section, the recombination dynamics of a *c*-axis oriented ZnO/Zn_{0.7}Mg_{0.3}O MQW is examined. To date, the work on the QCSE in ZnO QWs has been limited to a small number of photoluminescence measurements [70, 92, 98, 99] and fewer time-resolved measurements [69, 100, 101]. Of the time-resolved measurements, the sub-nanosecond timescale has not been studied in detail. Furthermore, the time dependence of the carrier induced screening has not been investigated. The two most comprehensive investigations, to date, of the well width dependence of the QCSEs in ZnO/MgZnO QWs, are by Davis et al. [90] and Morhain et al. [70]. Both investigations clearly show that the QCSEs dominate the optical properties for QW widths greater than 4 nm. In particular, the lowest energy interband transition, from the lowest energy electron subband to the lowest energy hole subband (which will be called E1-H1 in this chapter), has a transition energy which is significantly lower than the bandgap of bulk ZnO. In addition to this, as the well width is increased from 4 nm to 8 nm, the E1-H1 recombination lifetime increases by 5 orders of magnitude (10 ns to 1 ms) [70].

In the present work, ZnO/MgZnO QWs are investigated with an emphasis placed on carrier induced screening of the internal electric field. If a sufficient density of carriers can be produced in a QW with a built-in electric field, the electric field can be screened and the QCSEs reduced. Screening the internal electric field will result in a blue shift of the transition energy and an increase of the E1-H1 wavefunction overlap integral, which leads to a decrease of the recombination lifetime for the E1-H1 transition. As the excited carriers recombine the internal electric field is gradually restored, producing a time varying E1-H1 transition energy and E1-H1 wavefunction overlap.

The sample under investigation is a MBE grown ZnO/Mg_{0.3}Zn_{0.7}O six well MQW with 6 nm wide QWs and 5.5 nm barriers, on a sapphire substrate. There is a 500 nm ZnO buffer layer between the QWs and the sapphire substrate. A 30% Mg composition was used in the barrier to maximise the strength of the internal electric field without exceeding the solubility of Mg in ZnO [52, 102]. The electric field within this sample has been determined previously to be 0.8 MV cm⁻¹ [90]. Based on earlier investigations of the QCSE [70, 90], the optical properties of the 6 nm wide ZnO/Mg_{0.3}Zn_{0.7}O QW should be dominated by the QCSEs and therefore should make a good choice for the investigation presented in this section.

4.3.1 Carrier induced screening effect

In this sub-section, the carrier density dependence of the carrier induced screening effect is examined by measuring the photoluminescence spectrum as a function of the excitation fluence. Screening the internal electric field will reduce the QCSE and should produce an observable blue shift of the E1-H1 transition energy [70, 103]. In this experiment, the sample was excited by a 1 kHz repetition rate pulsed laser with a pulse width of 100 fs. The excitation pulses were focused to a spot with a diameter of approximately 100 μ m. The laser photon energy is 4.96 eV, which is well above the bandgap of bulk Mg_{0.3}Zn_{0.7}O (4 eV Mg_{0.33}Zn_{0.67}O at RT [52, 79]). A maximum excitation fluence of 4×10^{15} photons cm⁻² per pulse was used. The photoluminescence was spectrally dispersed using a scanning 0.27 m spectrometer with a spectral resolution of 10 meV.

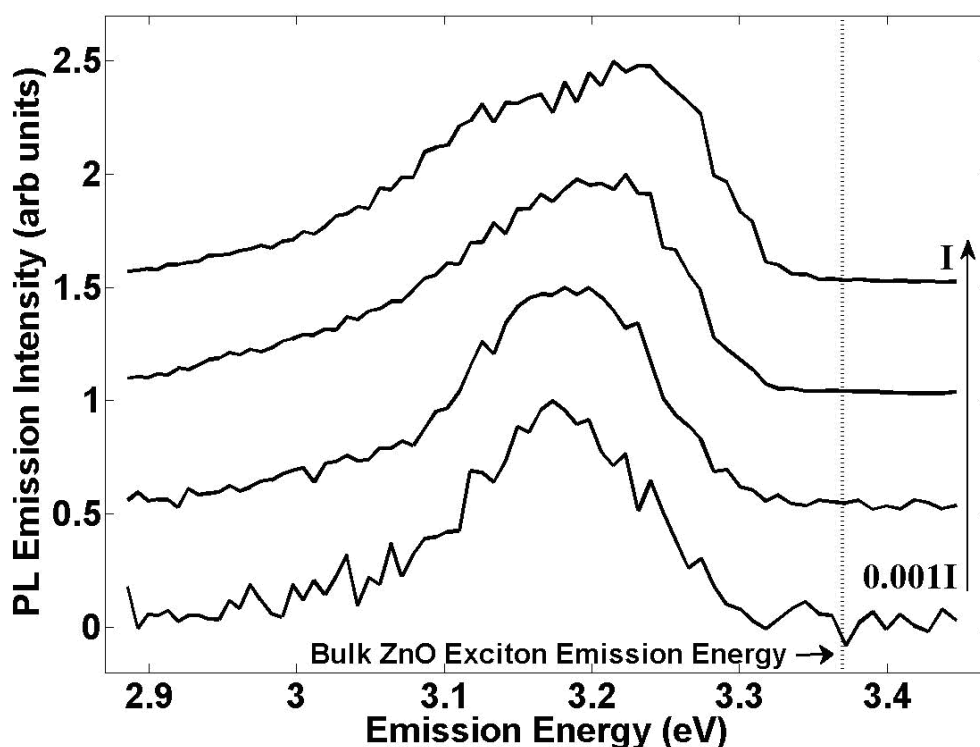


Figure 4.3.1: Intensity dependent PL at 20 K for excitation intensities of I , $0.1I$, $0.01I$ and $0.001I$. For an increase in excitation intensity of three orders of magnitude, the emission peak blue-shifts 66 meV.

Figure 4.3.1 shows the PL spectra for excitation fluence varied over 3 orders of magnitude. As the excitation fluence is increased, a 66 meV blue shift of the PL maximum is observed. In addition to this, the red side of the PL peak appears to broaden. At first glance the results shown in Fig. 4.3.1 appear somewhat different to those published for cw excitation, such as those by Morhain et al. [70] and Makino et al. [98]. When cw excitation is used, a constant excited state population is sustained within the QW, which in turn screens a constant proportion of the internal electric field. In that case a narrow emission peak is observed in the PL spectrum, where the peak can be blue-shifted by an amount proportional to the excitation fluence. In the present case where pulsed excitation is used, the excited state population decays before the following pulse arrives. The decaying population gradually restores the internal electric field, which in turn produces a time dependent E1-H1 transition energy. Consequently, time-integrated detection records an emission peak that appears broad, where the broadening is proportional to excitation fluence, but the observed

broadening is the sum of emission energies from a shifting transition. The time-integrated PL signal therefore shows the energies emitted from the E1-H1 transition for a continuous range of screening magnitudes. The effect of this in PL experiments is to blur out detail in the emission spectrum. Turchinovich et al. observed a similar response from intensity dependent PL measurements when examining an InGaN/GaN MQW, which also had a built-in electric field [103]. Whilst the shifting of the E1-H1 transition complicates the interpretation of the PL spectra, it is still possible to make some important conclusions. The blue shift observed in the PL spectrum in Fig. 4.3.1 as the fluence was increased is consistent with carrier induced screening of the internal electric field. The broadening on the red side the PL signal in Fig. 4.3.1 is attributed to a combination of two interactions. Firstly, collisional broadening as the result of the increased carrier densities present within the QW will broaden the homogeneous linewidth of the E1-H1 transition. Secondly, coupling between LO-phonons and excitons has been shown to be enhanced within QCSEed QWs due to the spatial separation of the electron-hole pairs [91, 104, 105] and will produce strong LO-phonon replicas on the low energy side of the QW emission peak. Discrete LO-phonon peaks, however, cannot be resolved in this PL spectrum because the E1-H1 transition energy shifts proportional to carrier density.

In an excitation intensity dependent PL experiment by Turchinovich et al. [103] on a QCSEed QW and whilst using pulsed excitation, the authors were able to excite a sufficient density of carriers to completely shield the internal electric field. This was evident by the presence of a strong and relatively narrow emission line at the most blue-shifted E1-H1 transition energy. The narrow emission line dominated the PL spectra and did not blue shift further for increased fluence. In the data presented in Fig. 4.3.1, a response similar that shown by Turchinovich et al. is not observed, suggesting that the internal electric field has not been completely shielded in this case.

4.3.2 Recombination dynamics - ns to μ s time scale

In this section, the recombination dynamics of the 6 nm wide ZnO/MgZnO MQW sample is investigated on the μ s - ns time scale using a TRPL experiment. The sample was again

excited by 100 fs pulses which have a photon energy (4.96 eV) well above the bandgap of the $\text{Zn}_{0.7}\text{Mg}_{0.3}\text{O}$ barrier and at a repetition rate of 1 kHz. The excited state population should decay fully between pulses at this repetition rate, given that the unshielded QW carrier recombination lifetime should be much less than 1 ms [70]. The excitation fluence was 4×10^{15} photons cm^{-2} per pulse for a focal spot diameter of approximately $100 \mu\text{m}$. The TRPL was measured directly with a PMT connected to a 500 MHz oscilloscope. Prior to detection, the PL emission was dispersed by a spectrometer in order to reduce the contribution of scattered laser light to the signal at $t = 0$. Care was taken to keep the signal strength well within the linear response range of the PMT.

The TRPL signal centred at 3.17 eV is shown in Fig. 4.4.6. The decay of the signal is clearly non-exponential. The recombination lifetime continuously increases to a seemingly steady rate of decay with a relatively long lifetime. The changing recombination lifetime with time can be demonstrated by fitting single exponential functions to successive regions of the decay curve in Fig. 4.4.6. The decay time constants for each of these regions are given in Table 4.1.

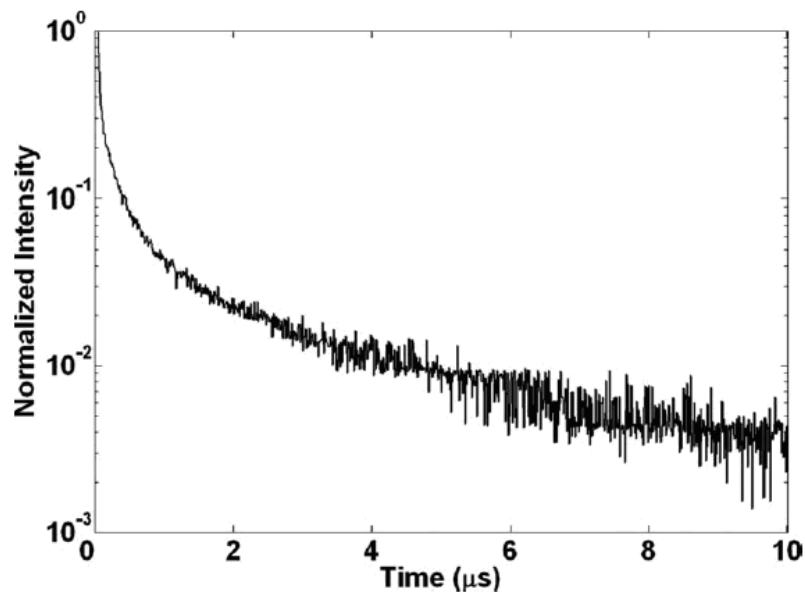


Figure 4.3.2: The time-resolved photoluminescence obtained from the 6 nm wide $\text{ZnO}/\text{Zn}_{0.7}\text{Mg}_{0.3}\text{O}$ MQW sample plotted on a log scale. The signal decays with a continuously increasing lifetime.

Interval (μs)	Decay Time Constant (μs)
0 – 0.04	*
0.04 – 0.14	0.18 ± 0.12
0.14 – 0.24	0.27 ± 0.06
0.24 – 0.34	0.34 ± 0.11
0.34 – 0.44	0.41 ± 0.30
0.44 – 1	0.75 ± 0.10
1 – 2	1.57 ± 0.20
2 – 3	2.30 ± 0.70
3 – 4	3.91 ± 1.20
4 – 5	5.80 ± 2.80

Table 4.1: Decay time constants for single exponential functions fitted to successive regions of the TRPL signal in Fig. 4.4.6. The first interval (0 - 0.04 μs) is excluded because of laser scatter.

The fitted time constants show that the decay time constant decreases from an initial value of 180 ns to 5.8 μs after a period of 5 μs . This is direct evidence of the electron-hole wavefunction overlap decreasing as the excited state population decays. The interval 5 - 10 μs has not been included because of the low signal to noise ratio.

The continuously changing lifetime, dependent on carrier density, is described by the following relationship based on Fermi's golden rule [106]

$$\tau(n) = \tau(0) \left\{ \left[\int_{-\infty}^{\infty} \psi_e(0)\psi_h(0)dz \right]^2 / \left[\int_{-\infty}^{\infty} \psi_e(n)\psi_h(n)dz \right]^2 \right\} \quad (4.3.1)$$

where n is the carrier density, $\tau(0)$ is the lifetime of the unscreened QW and $\left[\int_{-\infty}^{\infty} \psi_e(n)\psi_h(n)dz \right]$ is the electron and hole overlap integral as a function of carrier density.

4.3.3 Recombination dynamics - ps time scale

The direct detection method used to time-resolve the PL in Sec. 4.3.2 cannot resolve decay features which occur faster than about 40 ns. Pump-probe spectroscopy can, however, resolve relaxation processes with resolution limited by the excitation pulse width. In this

section, one and two-colour pump-probe spectroscopy is used to resolve the early time recombination dynamics of excited carriers. The travel range of the delay stage limits the time range which can be examined in this experiment to 300 ps. The sample was mounted in a circulating He cryostat and the probe beam was detected after passing through the sample. As the carrier density is dependent on the excitation fluence, the fluence was varied in order to explore the effect of screening on the recombination lifetime. The maximum excitation fluence in this experiment was 2.5×10^{17} photons cm^{-2} per pulse for an approximate focal spot diameter of approximately $50 \mu\text{m}$. The excitation fluence was varied from the maximum fluence just given to 0.125 the maximum value. For fluences less than this the probe signal could not be resolved. The probe pulses were three orders of magnitude less intense than the pump pulses at the maximum pump pulse fluence. In order to measure the small changes in the probe beam intensity with delay, the pump and probe beams were modulated at different frequencies. The signal of interest was therefore modulated at a frequency equal to the difference between the two chopping frequencies and was extracted by a lock-in amplifier. The pump and probe pulses were generated by two separate OPAs, where the pump and probe pulse photon energies were tuned slightly to the blue side of the PL emission peak; in the high excitation fluence PL experiment the PL peak was measured to be at 3.28 eV with a FWHM of 10 meV. Due to the QCSE, the transition energy is located below the bandgap of bulk ZnO. This is particularly useful in this experiment as it ensures that any dynamics observed following excitation are from the QW and not from the bulk ZnO buffer layer (3.43 eV at 20 K, [52]).

From the data shown in Fig. 4.3.3, it is evident that at early times the decay rate increased as the excitation fluence was increased. This is confirmed by fitting a single exponential function to the interval 0 - 100 ps, which gives decay time constants of 160 ± 20 , 170 ± 20 , 200 ± 30 , and 250 ± 80 ps for fluences I, 0.5I, 0.25I, and 0.125I, respectively. The initial fast decay appears to be on top of a decay with a much longer time constant. Fitting is unable to determine the lifetime of the slow decay component, however, it is reasonable to expect this decay is due to the long lifetimes observed in the TRPL experiment discussed in the previous section. The increased decay rate for increased carrier densities could

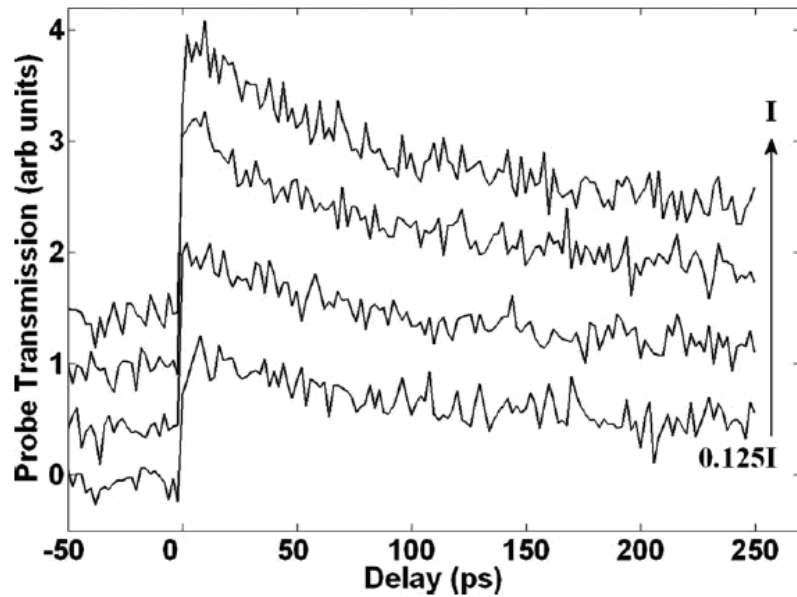


Figure 4.3.3: Fluence dependent one-colour pump-probe. The maximum excitation fluence (I) used in the experiment was 2.5×10^{17} photons cm^{-2} per pulse. The plotted signals are for fluences of $0.125I$, $0.25I$, $0.5I$ and I . The pump and probe pulses have photon energies of 3.28 eV.

ostensibly be attributed to carrier induced screening of the internal electric field, however, the simulation results in Sec. 4.3.4 and the discussion in Sec. 4.3.5 suggest otherwise. The results presented in those two sections suggest that the shortest recombination lifetime, corresponding to complete wavefunction overlap, should be 1-2 ns, which is longer than the recombination lifetimes measured in the one-colour pump-probe experiment. The shorter recombination lifetimes and the observed fluence dependence must therefore be due to either the carrier density within the QWs exceeding the Mott transition density (the changes to the results when excitons are considered in the model are discussed in Sec. 4.3.5), or the enhanced contribution of some other recombination mechanism at high carrier densities. The Mott transition density corresponds to carrier densities sufficient to shield the Coulomb interaction required for an exciton to exist and for carrier densities in excess of this density, the recombination rate is increased [106]. Due to the continuously changing shape of the QW profile, and therefore the continuously changing exciton binding energy and Bohr radius, it is difficult to calculate the carrier density at which the Mott transition will occur. It therefore remains uncertain whether the observed recombination dynamics at early times are due to

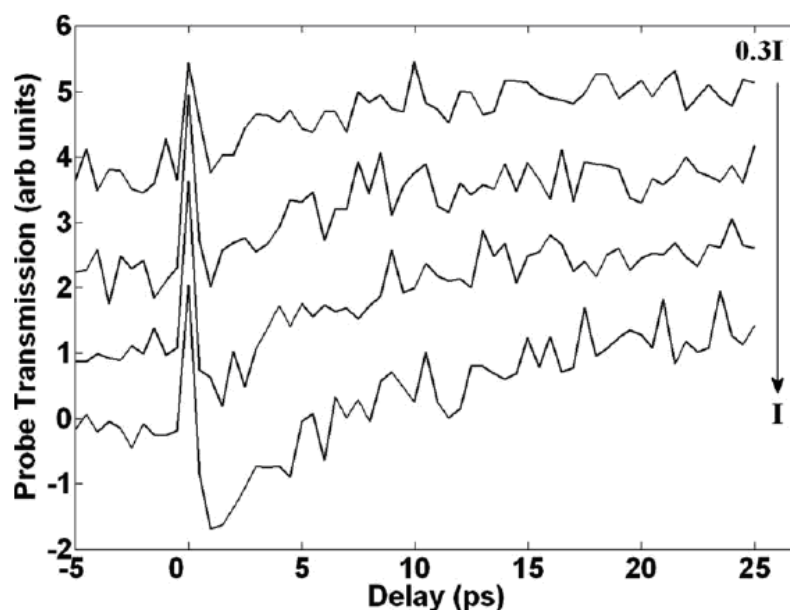


Figure 4.3.4: Fluence dependence of the two-colour pump-probe signal (pump 3.28 eV, probe 3.34 eV) for pump fluences of 0.3I, 0.5I, 0.8I and I.

the Mott transition or the increased role of some other recombination process at high carrier densities. This point will be further discussed in Sec. 4.3.5.

Two-colour pump-probe experiments were used to examine the dynamics of the shifting transition energy observed in the PL results (Sec. 4.3.1). Figure 4.3.4 plots the fluence dependent two-colour pump-probe results, with a probe energy of 3.34 eV and pump energy of 3.28 eV. For high excitation fluence an initial transient absorption is observed which evolves into a transient transmission with a slow decay (not shown). As the fluence was reduced the absorption becomes weaker. The transient absorption is attributed to the QW exciton transition being blue-shifted, becoming resonant with the probe photon energy and increasing the density of available states at this energy. A time constant of 7 ps was measured for the transition from absorption to the long-lived bleach and corresponds to the time taken for the transition energy to shift out of resonance with the probe photon energy. For probe energies greater than 3.34 eV, no signal was observed, suggesting that this is the highest energy to which the transition shifts following excitation. The rapid onset of the transient absorption shows that the screening of the internal electric field by carriers generated within

the QWs is an extremely fast process (< 1 ps).

The rapid onset of screening in QWs with a built-in internal electric field has been modelled by Turchinovich et al. [103, 107, 108] and observed experimentally in GaN QWs by Pinos et al. [109], Chen et al. [110], and others [111, 112]. Turchinovich et al. model the dynamical screening of a QW with a built-in internal electric field based on the theory that the absorption of a photon by such a QW produces an instantaneously polarised electron and hole pair which instantaneously screens a portion of the internal electric field. The probability of absorption for photons which follow is consequently increased with each photon absorbed. If the excitation source is sufficiently intense, the internal electric field may be fully screened in a time less than the duration of the excitation pulses [107]. In a white light continuum pump-probe experiment, Chen et al. [110] resolved the screening establishment time within InGaN/GaN QWs to be less than 1 ps. A similar response is measured by Pinos et al. where they time-resolved the shift in the transition energy of a GaN/AlGaIn QW with a built-in electric field of 0.6 MV cm^{-1} [109]. They observe an instantaneous shift in the transition energy, however, the time resolution is limited by the excitation pulse width which was 20 ps. The rapid screening of the internal electric field revealed in Fig. 4.3.4 is consistent with these previous results.

4.3.4 Recombination dynamics - simulation

In this section, the recombination dynamics for a QW with an internal electric field are calculated. The calculated dynamics are used to verify the interpretation of the results in the previous sections and provide additional insight into the carrier density dependent transition energy and overlap of the E1-H1 wavefunctions. To accurately calculate the carrier recombination dynamics in the presence of carrier induced shielding one must calculate the change in shape of the QW potential profile due to the spatial distribution of charge within the QW [113]. One may determine the carrier density dependent profile of the QW by self-consistently solving the Schrödinger and Poisson equations whilst incrementing the charge density within the QW. By using a simple rate equation and the calculated overlap

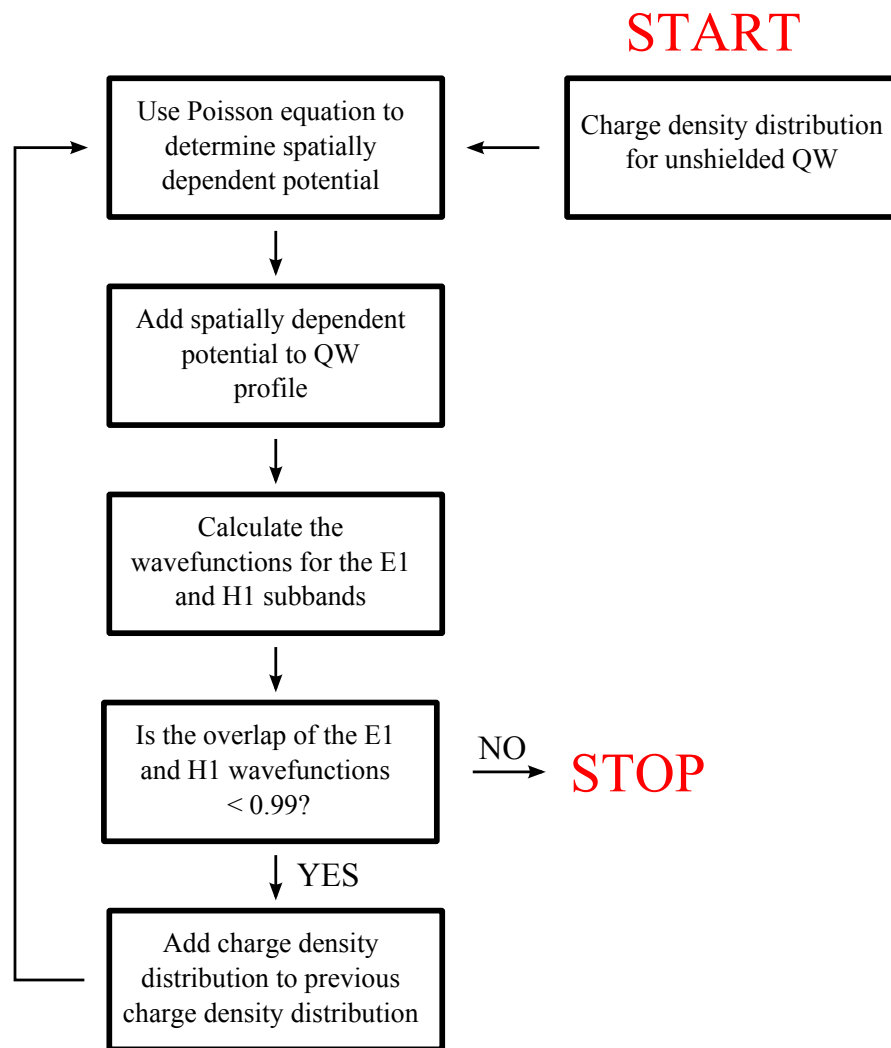


Figure 4.3.5: Flow diagram presenting the general structure of the algorithm used to determine the carrier density dependent E1-H1 transition energy and wavefunctions. The details are given in the text.

of the E1 and H1 wavefunctions in conjunction with Eq. 4.3.1 (modified Fermi's golden rule), the recombination dynamics including the effects of carrier induced shielding may be determined. This method of calculating the recombination dynamics in the presence of carrier shielding is based on the method used by Lefebvre et al. [113]. The calculated recombination dynamics will then be compared to the recombination dynamics measured in Sec. 4.3.2.

The structure of the algorithm is described by the flow diagram in Fig. 4.3.5. The algorithm begins by using the Poisson equation to determine the spatially dependent potential

for the charge distribution in an unshielded 6 nm ZnO/Mg_{0.3}Zn_{0.7}O QW. The following well known equation from electrostatics (Eq. 4.3.2) is typically used to describe the charge density on the two parallel plates of a capacitor for a given electric field between the two plates. It is used here to determine the charge density at the well barrier interfaces of the ZnO/Mg_{0.3}Zn_{0.3}O QW for a given potential difference across the QW

$$p = \frac{V\varepsilon_r\varepsilon_0}{d} \quad (4.3.2)$$

where V is the potential across the QW (0.48 V in this case), ε_0 is the vacuum permittivity (8.854×10^{-14} F cm⁻¹), ε_r is the relative permittivity of the material (6.4 for ZnO [52]), d the QW width (6×10^{-7} cm) and p is the charge density at the QW interfaces which is calculated to be 4.5×10^{-7} C cm⁻². The charge distribution resulting from the charge differential at the well/barrier interfaces for a 6 nm wide ZnO/Mg_{0.3}Zn_{0.7}O QW is shown in Fig. 4.3.6(a).

The Poisson equation is then used to determine the electric field and the spatially dependent potential across the charge distribution. The Poisson equation is given by

$$\frac{d^2V}{dz^2} = -\frac{\rho(z)}{\varepsilon_r\varepsilon_0} \quad (4.3.3)$$

where $\rho(z)$ is the charge distribution. The electric field across the distribution and the spatially dependent potential are plotted in Fig. 4.3.6(b) and Fig. 4.3.6(c) respectively. The spatially dependent potential was added to the QW potential profile to produce the sloped QW profile shown in Fig. 4.1.1.

To determine the energies and wavefunctions for the E1 and H1 subbands of the sloped QW potential the Schrödinger equation was solved numerically using the method described in Chapter 2. The following parameters were used in the calculation: CB/VB offset of 70/30, a ZnO (Mg_{0.3}Zn_{0.7}O) bandgap at 20 K of 3.43 eV (4.06 eV) and electron and heavy-hole effective masses of $0.28m_e$ and $0.78m_e$, respectively, where m_e is the mass of an electron in free-space [52, 114]. If the overlap of the E1 and H1 wavefunctions is less than 0.99, the

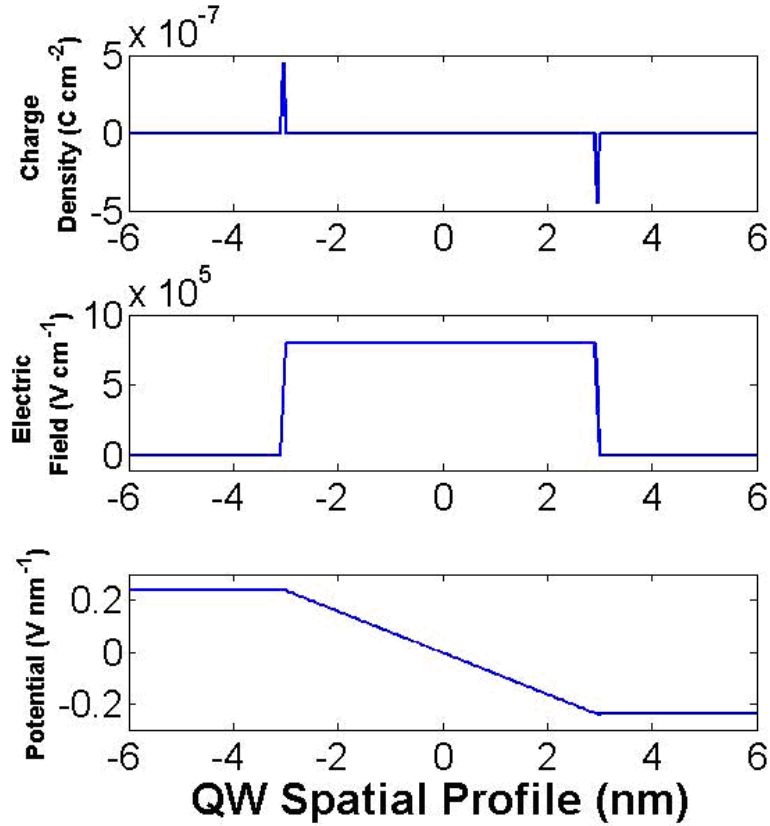


Figure 4.3.6: (a) Charge density (C cm^{-2}) at the well/barrier interfaces of the ZnO/Mg_{0.3}Zn_{0.3}O QW for an internal electric field of 0.8 MV cm^{-1} . (b) Spatially dependent electric field across the QW. (c) Spatially dependent voltage difference across the QW.

QW is not fully shielded and the algorithm continues, otherwise the calculation stops.

The wavefunctions for the E1 and H1 subbands are used to determine the spatial distribution for excited carriers within the QW. The charge distribution is given by

$$\rho(z) = ne \sum [|\psi_{H1}(z)|^2 - |\psi_{E1}(z)|^2] \quad (4.3.4)$$

where ψ_{E1} and ψ_{H1} are the E1 and H1 wavefunctions, respectively, n is the electron and hole density and e is the charge of an electron. Each time the algorithm cycles the charge distribution for 1×10^8 pairs cm^{-2} are added to the charge distribution over the QW. The dipole associated with the spatially separated electrons and holes is opposite to the dipole

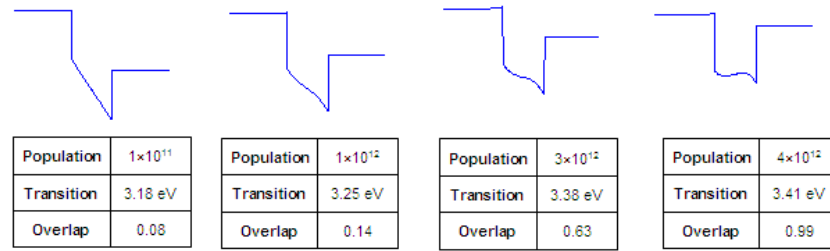


Figure 4.3.7: Plots of the potential profile for the QW CB for a range of carrier densities. The transition energy and wavefunction overlap for each case is also presented.

associated with the built-in electric field and reduces the magnitude of the built-in electric field. The next calculation of the E1 and H1 wavefunctions for the QW potential with the new charge distribution therefore includes the shielding from the first increment of carriers. This process is repeated until the overlap of the wavefunctions for the E1 and H1 subbands is > 0.99 , which corresponds to almost complete shielding of the internal electric field within the QW.

Figure 4.3.7 shows the QW CB for four different carrier densities. In the unshielded QW the E1-H1 transition energy is 3.17 eV and the wavefunction overlap integral is 0.07. At low carrier densities (1×10^{11} electron and hole pairs cm^{-2}) there is no obvious change in the shape of the QW potential profile, however the transition energy is slightly shifted to higher energy and the overlap integral has increased to 0.08. When the carrier density is increased to 1×10^{12} pairs cm^{-2} the QW profile begins to flatten out, pushing the E1 and H1 subbands to higher energy, and the overlap integral of the E1 and H1 wavefunctions increases to 0.14. When the pair density reaches 4×10^{12} pairs cm^{-2} the overlap integral for the E1 and H1 wavefunctions reaches 0.99. The carrier density dependent E1-H1 transition energy and wavefunction overlap integral are plotted in Fig. 4.3.8 and Fig. 4.3.9.

The QW transition energy for the unscreened QW was calculated to be 3.175 eV, which compares well with our experimentally measured value of 3.17 ± 0.01 eV for low excitation fluence. The calculation reveals that for electron and hole pair densities up to 1×10^{11} cm^{-2} there is only a very slight increase in the E1-H1 transition energy. Between 1×10^{11} and 1×10^{12} pairs cm^{-2} an increase in the E1-H1 transition energy from 3.18 eV to 3.25 eV

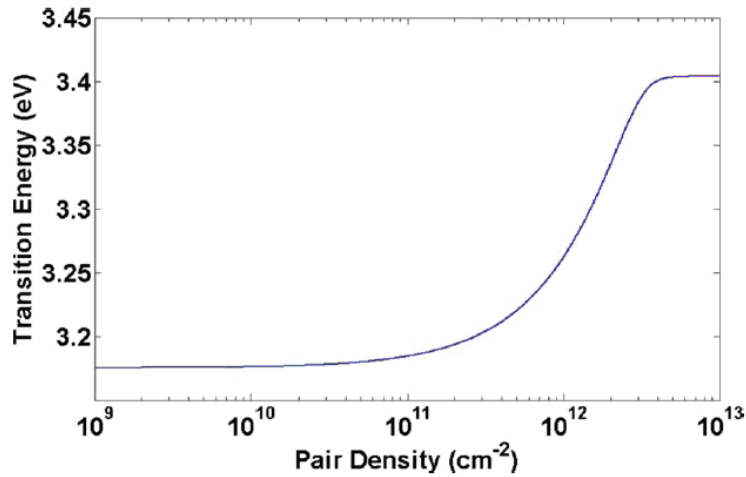


Figure 4.3.8: E1-H1 transition energy as a function of pair density within the QW.

is observed. The most significant increase in the transition energy, however, occurs from 1×10^{12} to 4×10^{12} pairs cm^{-2} , where the transition energy shifts from 3.25 eV to 3.41 eV. As the carrier density is further increased the transition plateaus at 3.41 eV. The plateau appears when additional excited carriers produce no significant change in shape of the potential profile because the wavefunctions of the E1 and H1 subbands overlap and their charge distributions cancel. If the internal electric field was weaker the plateau would occur at lower carrier densities.

The square of the wavefunction overlap for the E1 and H1 subbands as a function of pair density is shown in Fig. 4.3.9. From this, the recombination dynamics as a function of pair density can be determined using the method described by Lefebvre et al. [113]

$$\frac{dn}{dt} = -\frac{n}{\tau_n} \quad (4.3.5)$$

where n is the pair density and τ_n is the density dependent lifetime determined from the E1 and H1 wavefunction overlap integral using Eq. 4.3.1.

In order to compare the calculated recombination dynamics to the recombination dynamics recorded in the TRPL experiment, a reference relevant to both data sets is required. The relation given by Eq. 4.3.1 could be used to link the two data sets, however, it requires

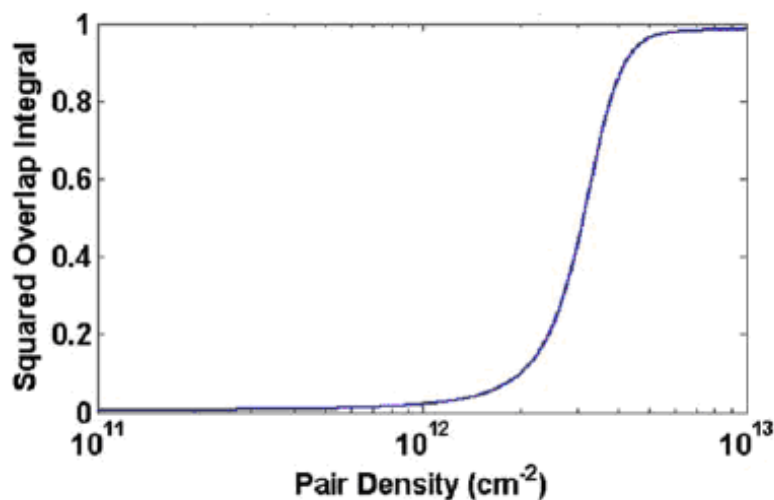


Figure 4.3.9: The calculated overlap integral for the E1 and H1 wavefunctions squared as a function of pair density.

that the recombination lifetime for the unshielded QW is known. It is not reasonable to assume the longest measured decay lifetime corresponds to the unscreened QW lifetime because the measured signal is limited by the sensitivity of the detection arrangement and the decay lifetime may continue to evolve beyond this point. An alternative option would be to approximate the carrier densities present within the QW immediately following excitation and use this to compare with the calculated carrier densities, however, the carrier density cannot be approximated accurately without knowing the QW capture efficiency. The only reasonable method to link the two data sets is to fit the calculated recombination dynamics to the TRPL. This is done using

$$S_{FIT} = A \times S_{CALC}[tT + \tau_0] \quad (4.3.6)$$

where S_{CALC} represents the calculated decay curve as a function of time, t ; A is the amplitude scaling factor; T is the scaling factor for the time axis; and τ_0 is an offset in the calculated decay curve to correct for the initial pair density within the QW immediately following excitation. The relative difference between the calculated and measured curves is used to determine the fitting error.

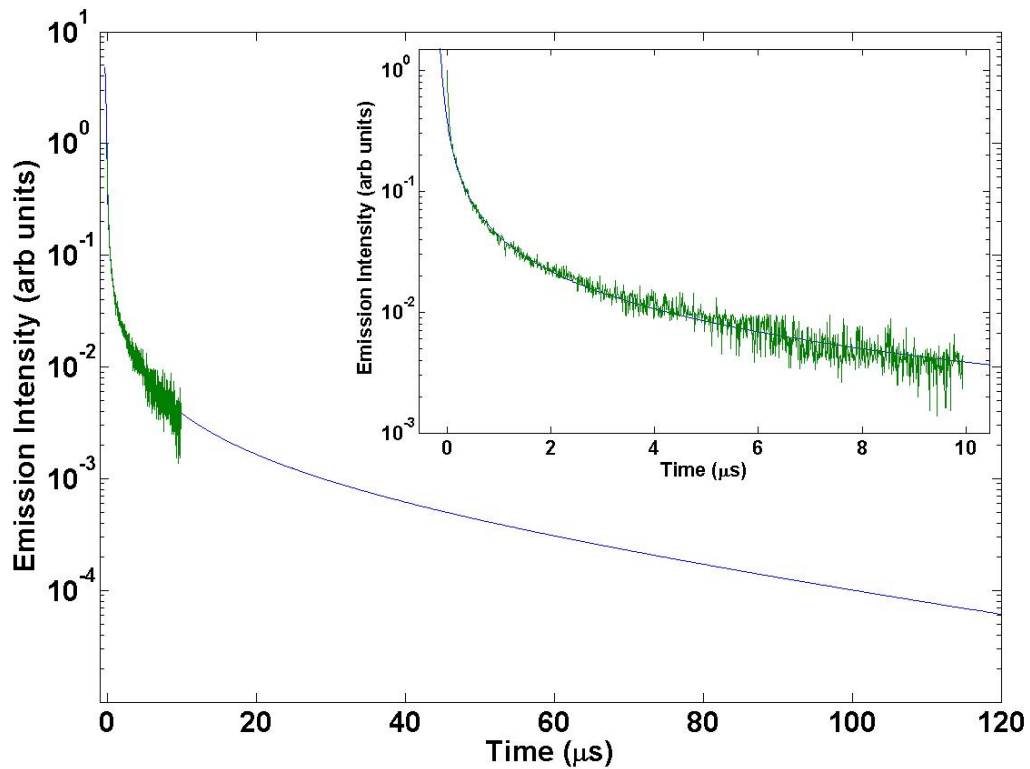


Figure 4.3.10: Calculated recombination dynamics fit to the TRPL from Fig. 4.4.6. The inset provides a zoomed in view of the fit.

The calculated recombination dynamics fit to the measured recombination dynamics is shown in Fig. 4.3.10 and fits remarkably well. For $t > 5 \mu\text{s}$ the measured recombination dynamics was excluded from the fit because of the strong noise on the TRPL. Using this fit, the carrier-density dependent properties of the 6 nm wide ZnO/Mg_{0.3}Zn_{0.3}O QW can be determined for any time following excitation. The only significant discrepancy for the fit occurs at the beginning of the measured decay where there is a fast decay for times < 40 ns. This signal is due to laser scatter, the duration of which is limited by the response time of the detector. This component of the TRPL signal was also excluded from the fitting process.

The fit was able to provide a unique solution with a global minimum in the error metric for different starting guesses of the fitting parameters. The range of values quoted for the carrier density dependent parameters in the following discussion (Sec. 4.3.5) are given for fits within 3% of the error metric global minimum.

4.3.5 Discussion

Extrapolating the fit shown in Fig. 4.3.10 back to the beginning of the measured decay (where $t = 0$) gives an initial pair density of $(2.5 \pm 0.2) \times 10^{12} \text{ cm}^{-2}$. The incident fluence is $4 \times 10^{15} \text{ photons cm}^{-2}$ per pulse, suggesting a combined absorption and QW capture efficiency of $0.067 \pm 0.007 \%$ per well following excitation high into the QW barrier. From the pair density dependent transition energy shown in Fig. 4.3.8, an initial pair density of $(2.5 \pm 0.2) \times 10^{12} \text{ cm}^{-2}$ corresponds to a QW transition energy of $3.364 \pm 0.008 \text{ eV}$. PL emission is therefore expected at this energy. The PL results in Fig. 4.3.1 show emission up to 3.35 eV, although it is not as strong as might be expected. The expected emission intensity for a given E1-H1 transition energy is obtained by evaluating the change in pair density as a function of E1-H1 transition energy. The change in pair density for 0.01 eV steps in transition energy is plotted in Fig. 4.3.11. The carrier density required to shift the E1-H1 transition energy is shown to increase with transition energy. The emission intensities, therefore, should be comparatively larger for higher energy transitions. This is clearly not observed in the PL results.

To explain this discrepancy two possibilities are considered: Firstly, it is reasonable to contemplate that there may be increased non-radiative recombination for large carrier densities. If the non-radiative recombination rate was varying with carrier density within the QW, in addition to the radiative and non-radiative recombination rates being dependent on the overlap of the E1-H1 wavefunctions, this would lead to a decay of the TRPL signal that could not be described by only the change of the overlap of the E1-H1 wavefunctions. The good fit between the calculated and measured recombination dynamics, where the calculated dynamics only take wavefunction overlap into account, suggest that this effect may only be active for early time dynamics immediately following excitation. Another possible explanation is that the effects of bandgap renormalisation, which have not been included in the transition energy calculation, may be significant at the high carrier densities present immediately after excitation. This would red-shift the transition energy and may explain the lack of emission at high energy. If this is the case, then the calculated

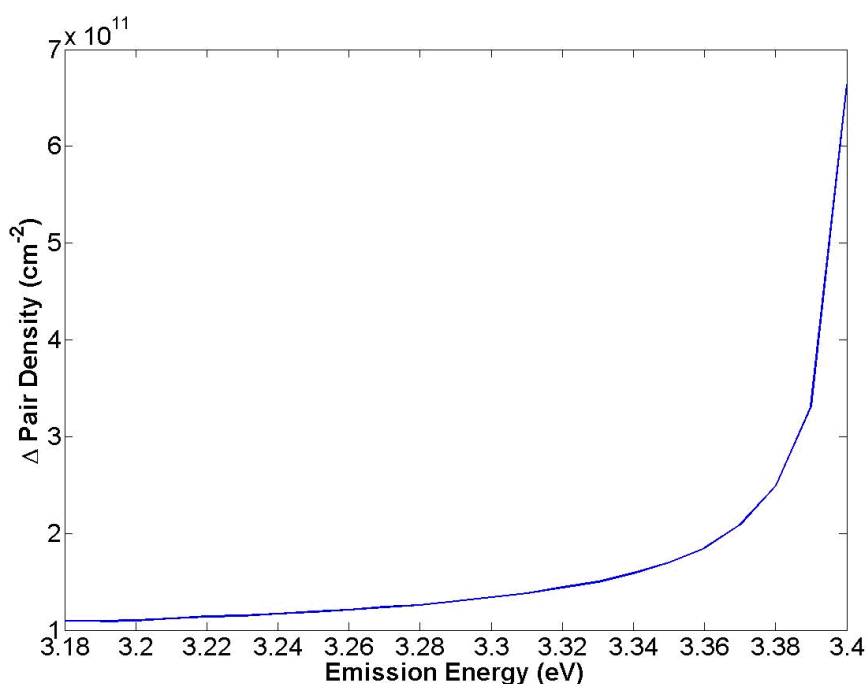


Figure 4.3.11: Change of pair density present in the QW for 0.01 increments in the E1-H1 transition energy. This data provides an indication of the emission intensity expected as the E1-H1 transition energy shifts.

transition energy as a function of pair density would be overestimated, particularly for large densities; the calculated wavefunction overlap and lifetimes, however, would not be affected. Unfortunately, bandgap renormalisation in this case is difficult to calculate because of the continuously changing potential profile. In addition, there are no publications which give typical values for bandgap renormalisation in ZnO/MgZnO QWs.

At a time equal to $5 \mu\text{s}$ following excitation, a pair density of $(8 \pm 1) \times 10^{11} \text{ cm}^{-2}$ remains within each QW giving a transition energy of $3.246 \pm 0.009 \text{ eV}$. The transition energy discrepancy due to bandgap renormalisation at the lower carrier densities will be reduced. As there is still a substantial excited state population within the QWs at this point, it is clear that these values do not represent the lifetime of the unshielded QWs. According to the calculation, the recombination lifetime in the unshielded well, τ_0 , is $34 \pm 9 \mu\text{s}$. Based on this value for τ_0 and using Eq. 4.3.1, the fastest decay time constant for this sample in the event of complete wavefunction overlap should be 1 - 2 ns.

Returning to the pump-probe results in Fig. 4.3.3, the excitation fluence dependent signal decayed with a recombination lifetime which increased from 157 to 245 ps for decreasing excitation fluence. These recombination lifetimes are significantly shorter than the 1 - 2 ns predicted by the calculated recombination dynamics and fitting for complete wavefunction overlap. The exciton recombination lifetime at early times therefore appears to vary at a rate beyond the change of the overlap of the E1-H1 wavefunctions. As discussed in Sec. 4.3.3 the increased rate of decay at early times may be due to the density exceeding the Mott density or the increased contribution from some other recombination mechanism at high carrier densities. It is clear, however, that the density required for this nonlinear behavior to be present is greater than $2.1 \times 10^{12} \text{ cm}^{-2}$, the carrier density from which the calculated and measured recombination dynamics in Fig. 4.3.10 clearly compare well ($t > 40 \text{ ns}$).

It should be mentioned that the model used in this section only considers uncorrelated electron and hole pairs, not excitons. If excitons were to be considered, it is expected that as the internal electric field is shielded, the electrons and holes would become less localized to opposite sides of the QW and the dimensions of the excitons would decrease. The reduction in the size of the excitons would be accompanied by an increase in the binding energy, which will therefore be dependent on the excited pair density. Values for the exciton binding energy, corresponding to no shielding of the internal electric field through to complete shielding, are expected to vary from 20 meV to approximately 80 meV, respectively [70], and are much smaller than the change in the transition energy for uncorrelated electron and hole pairs over the same range, which vary from 3.17 eV to 3.41 eV. The recombination dynamics, for both excitons and uncorrelated electron and hole pairs, will also have a similar dependence on the excited pair density. In the direction perpendicular to the QW plane, the wavefunction overlap integral as a function of the excited pair density will be the same for both correlated and uncorrelated electron and hole pairs. In the plane of the QW the wavefunction overlap integral for excitons is also expected to increase as a function of the excited pair density, leading to faster recombination for a given excited pair density for excitons than for uncorrelated electron and hole pairs. This effect, however, is not anticipated to be significant. It is possible that the excited pair densities used in this experiment exceed

the Mott transition density at pair densities lower than were considered in earlier discussions, and therefore only uncorrelated electron and hole pairs are present within the QW. This could explain the good agreement between the measured and the calculated recombination dynamics in Fig. 4.3.10 where only uncorrelated electrons and holes have been considered. For the time being it is not clear at what density the Mott transition occurs as it is difficult to calculate for a system where the exciton binding energy varies as a function of the pair density.

4.3.6 Summary

To summarise, the carrier induced screening effect in ZnO/MgZnO QWs has been studied in detail. It has been shown that screening the internal electric field in ZnO QWs reduces the QCSE, significantly altering the optical properties of the QW. In the PL experiment, carrier induced screening produced a blue shift of the E1-H1 transition energy. In the TRPL experiment the recombination of excitons was shown to reduce the screening of the internal electric field, which in turn caused the recombination lifetime to be time dependent. One and two-colour pump-probe experiments were used to examine the recombination dynamics on the ps timescale. In the one-colour experiment, the recombination lifetime over the first 100 ps was shown to vary from 160 to 250 ps, dependent on excitation fluence. In the two-colour pump-probe experiment, the rapid onset of a transient absorption showed that the shielding of the internal electric field occurred in less than 1 ps. The simulated recombination dynamics matched the TRPL measurements well, and allowed the QW properties (transition energy, wavefunction overlap and carrier density) to be determined at any time following excitation. The results showed that the expected recombination lifetime for complete overlap of the E1 and H1 wavefunctions was between 1 and 2 ns. The lifetime of the initial decay measured with one-colour pump-probe, however, recorded a value shorter than this. This suggests that at high carrier densities the recombination lifetime varies at a rate beyond the change of the overlap of the E1 and H1 wavefunctions, which is possibly due to the carrier density exceeding the Mott transition density.

4.4 Graded barrier quantum wells

It is well known that applying an electric field over a QW can change the optical properties of the QW [115–119]. Specifically, the electric field produces a slope on the QW profile which red-shifts the E1-H1 transition energy and decreases the overlap of the E1 and H1 wavefunctions. This is similar to what occurs when there is a built-in electric field in the QW, as discussed in the previous section, however, the electric field is applied and controlled externally. Work by Davis et al. [90] and Coleman et al. [93] showed that O⁻ ion implanted ZnO/Mg_{0.3}Zn_{0.7}O QWs, followed by rapid thermal annealing, may induce diffusion of the Mg in the barriers into the well, smoothing the well/barrier interfaces of the QW potential profile. The smoothed interfaces caused the E1-H1 transition energy to blue shift and produced an increase of the E1 and H1 recombination rate, suggesting the overlap of the E1 and H1 wavefunctions had increased. Davis et al. and Coleman et al. showed that this method may be used to control the optical properties of ZnO/MgZnO QWs. The use of ion implantation to control the optical properties of QWs, however, is limited, particularly because it is not possible to produce asymmetric QW profiles using this method. QWs grown with barriers where the barrier energy is stepped allows one to adjust the QW potential profile arbitrarily and without post-growth processing. In these structures, the combination of internal electric field and graded barriers make it possible to create QWs with precisely controlled E1-H1 transition energy and overlap of the E1 and H1 wavefunctions. Such nanostructures will be referred to as graded barrier QWs. The ability to control the overlap of the E1 and H1 wavefunctions allows control of the radiative recombination rate, and hence the radiative recombination efficiency within light emitting devices. Similarly, it is possible to tune the absorption coefficient in light detection devices based on such QW structures.

InGaN/GaN QWs, which are being investigated for use in light emitting devices, also possess an internal electric field. There is currently much research going into InGaN QWs in order to improve the radiative recombination efficiency of InGaN QW based devices

[120–134]. This work is primarily focused around either reducing the magnitude of the internal electric field [122, 131, 132] and, more recently, growing graded/stepped barrier QWs [125–127, 129, 133–135]. Functioning QW LEDs with graded barriers have since been constructed, demonstrating greater radiative efficiency than equivalent wells without graded barriers [127, 128, 132]. It is clear that the optical properties of QWs can be controlled by growing structures with carefully designed graded barriers.

The work in this section will provide a first examination of as-grown ZnO/MgZnO graded barrier QWs. The investigation will determine if the growth method and these QW structures can be used to control the E1-H1 transition energy and the overlap of the E1 and H1 wavefunctions. Section 4.4.1 presents the sample designs which will be used in this investigation. The graded barrier samples will be compared with two square potential QWs, which will be used as references. The sample growth details are given in Sec. 4.4.2. The PL and TRPL results are given and discussed in Sec. 4.4.3 and Sec. 4.4.4, respectively.

4.4.1 Sample design

The structures of each of the graded barrier samples examined are shown in Fig. 4.4.1 and Fig. 4.4.2. The steps in the Mg composition that form the graded barriers are indicated. The potential profile for each of the samples is plotted with and without the effects of the internal electric field in Figs. 4.4.3 and 4.4.4. Also included in Figs. 4.4.3 and 4.4.4 are the energies and the wavefunctions for the E1 and H1 subbands, which were calculated using the method given in Sec. 2.4. Table 4.2 lists the calculated transition energy and overlap of the E1 and H1 wavefunctions for each of the samples. Values are given for each sample with and without the effects of the internal electric field. As there is a variety of QW shapes, in order to compare the QWs the FWHM of the E1 and H1 wavefunctions for all of the samples are listed in Table 4.3.

Samples A and A' are square potential QWs without graded barriers. The electric field produces a slope on the QW potential, which red-shifts the transition energy for samples

A	A'	B	C
Zn _{0.7} Mg _{0.3} O cap 50 nm	Zn _{0.7} Mg _{0.3} O cap 50 nm	Zn _{0.7} Mg _{0.3} O cap 50 nm	Zn _{0.7} Mg _{0.3} O cap 50 nm
ZnO 4 nm	ZnO 2 nm	Zn _{0.85} Mg _{0.15} O 2 nm	Zn _{0.8} Mg _{0.2} O 1 nm
Zn _{0.7} Mg _{0.3} O 400 nm	Zn _{0.7} Mg _{0.3} O 400 nm	ZnO 2 nm	Zn _{0.9} Mg _{0.1} O 1 nm
Zn _{0.9} Mg _{0.1} O 15 nm	Zn _{0.9} Mg _{0.1} O 15 nm	Zn _{0.85} Mg _{0.15} O 2 nm	ZnO 2 nm
Al ₂ O ₃ (1120) sub.	Al ₂ O ₃ (1120) sub.	Zn _{0.7} Mg _{0.3} O 400 nm	Zn _{0.9} Mg _{0.1} O 1 nm
		Zn _{0.9} Mg _{0.1} O 15 nm	Zn _{0.8} Mg _{0.2} O 1 nm
		Al ₂ O ₃ (1120) sub.	Zn _{0.7} Mg _{0.3} O 400 nm
			Zn _{0.9} Mg _{0.1} O 15 nm
			Al ₂ O ₃ (1120) sub.

Figure 4.4.1: ZnO/Mg_{0.3}Zn_{0.3}O samples A, A' B and C. Samples A and A' are square potential QWs with well widths of 4 and 2 nm, respectively. Samples B and C are two symmetrically graded graded-barrier samples, where C has a smaller Mg step size.

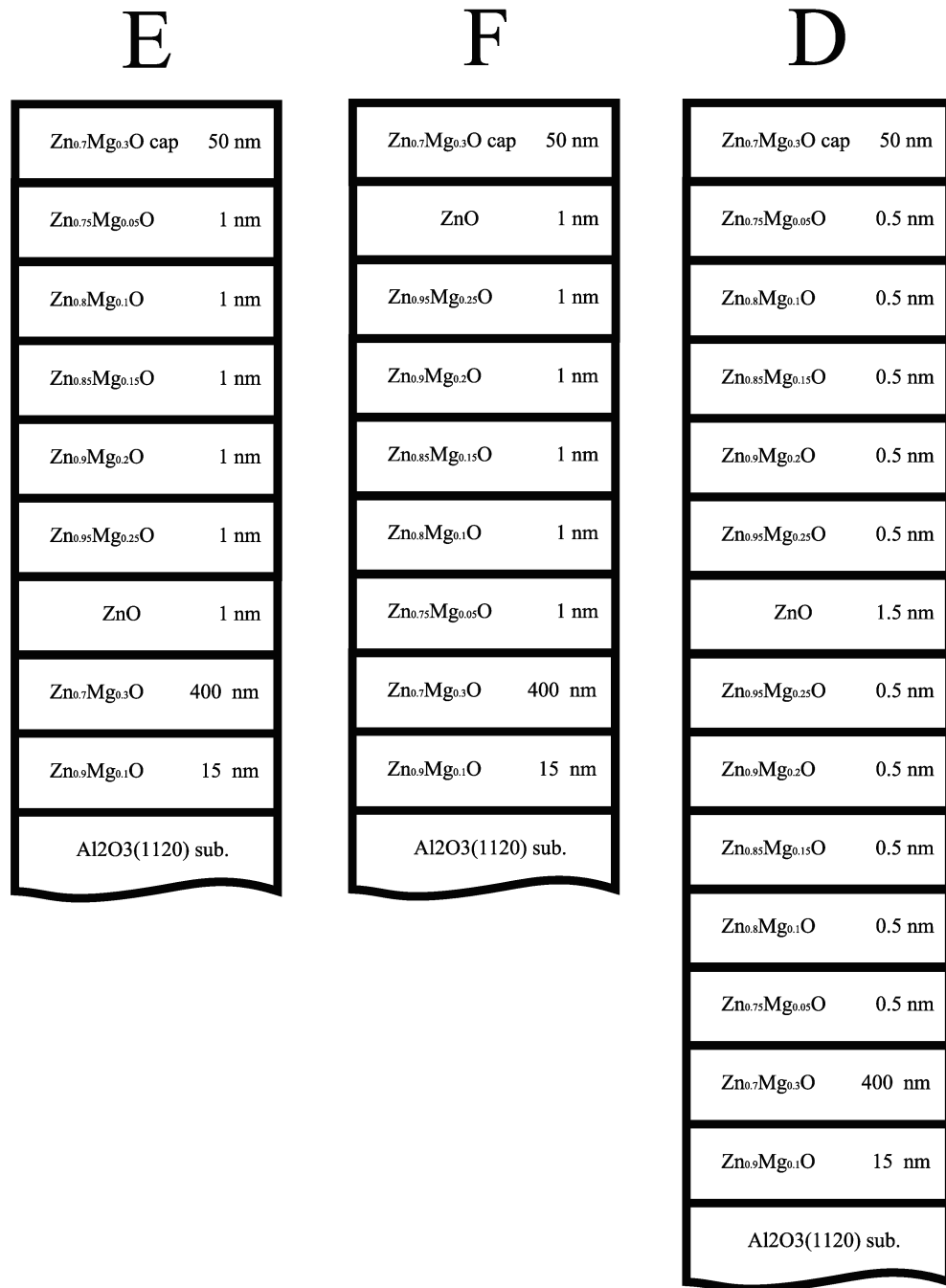


Figure 4.4.2: ZnO/Mg_{0.3}Zn_{0.7}O samples D, E and F. All three samples have graded barriers. Sample D is symmetrically graded, with Mg step sizes than B and C. Samples E and F are asymmetrically graded and graded on opposite sides of the QW.

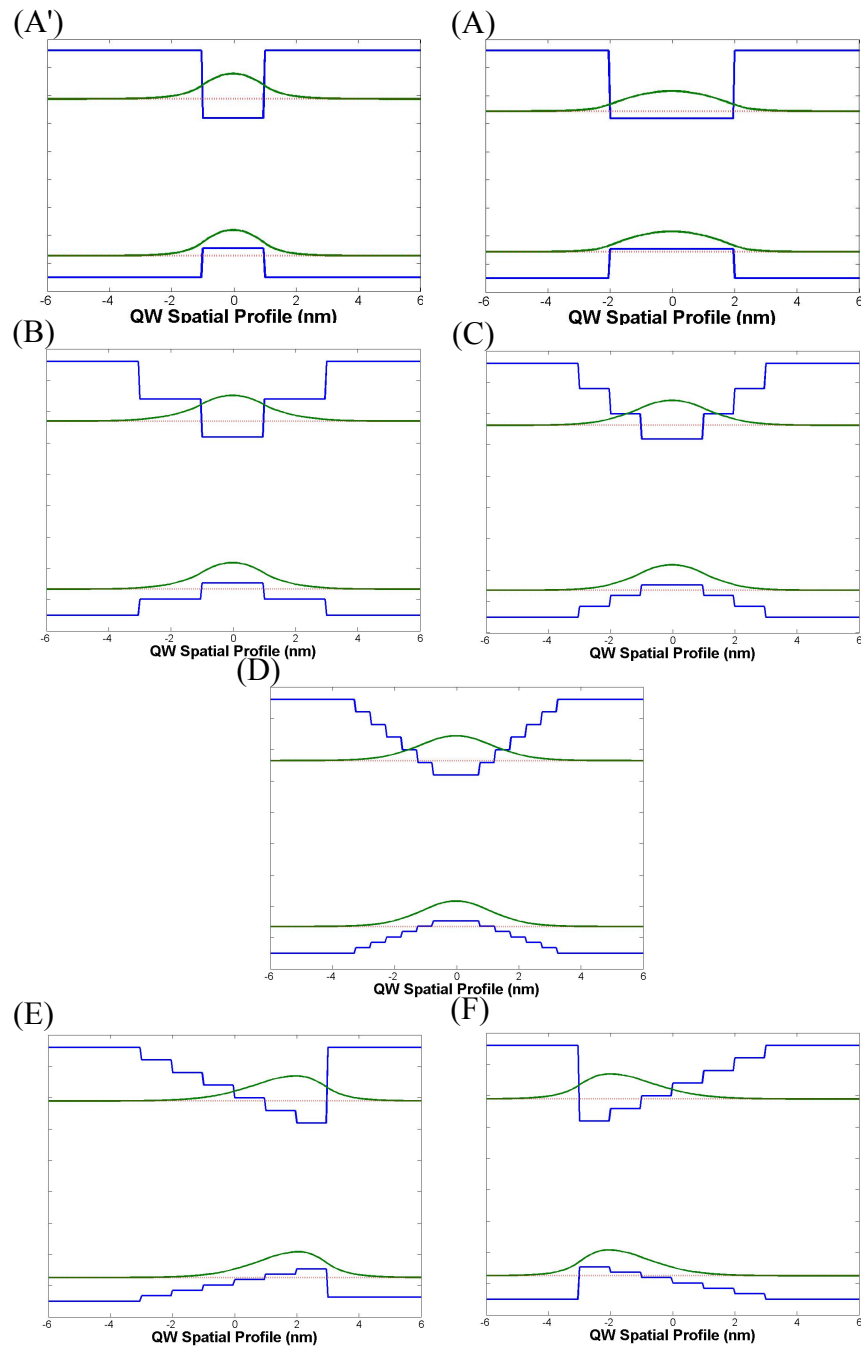


Figure 4.4.3: Potential profiles for each QW sample without the effects of the internal electric field included. The first electron and heavy hole energy and wavefunction are included.

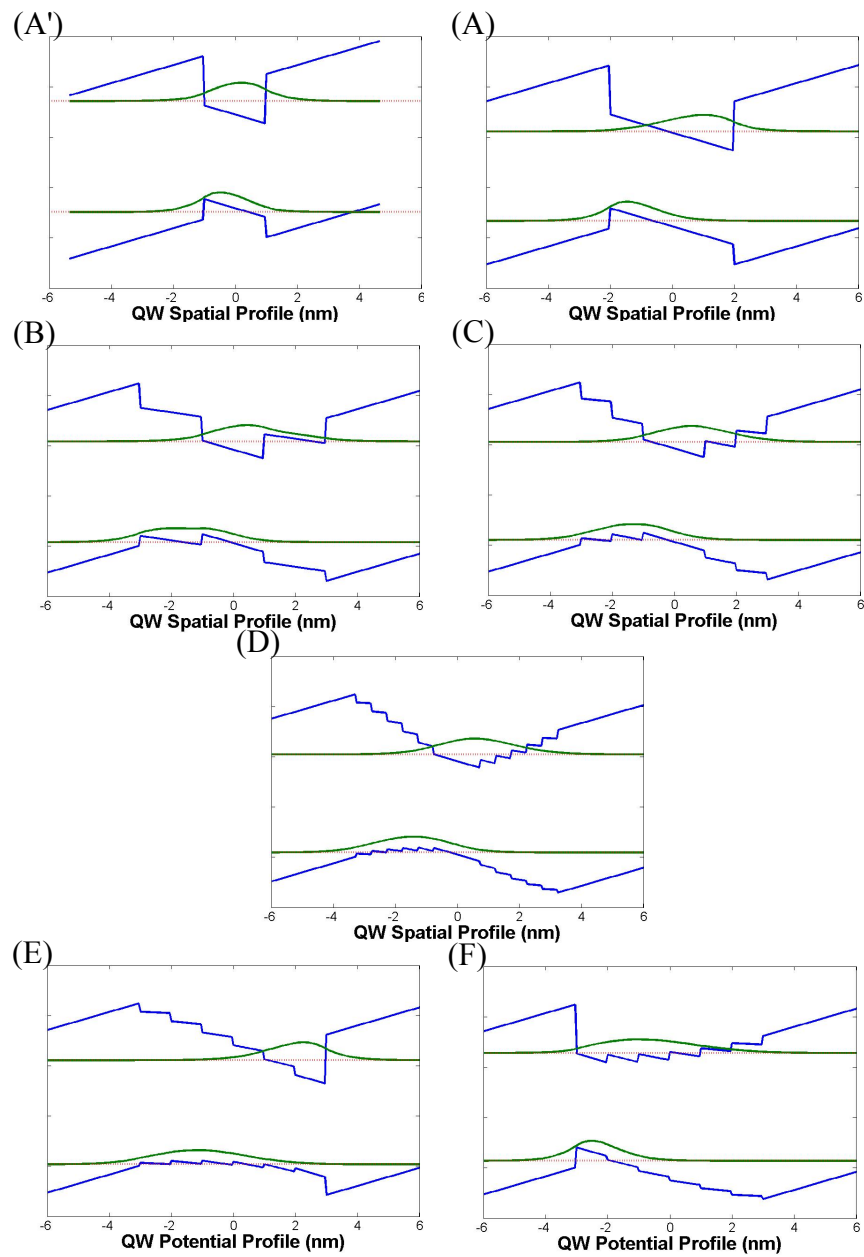


Figure 4.4.4: Potential profiles for each QW sample with the effects of the internal electric field included. The first electron and heavy hole energy and wavefunction are included.

A' and A by 40 and 120 meV, respectively (Table 4.2). The larger red shift for the wider QW is consistent with previous experimental work [70, 90]. Both samples show a decrease in the overlap of the E1-H1 wavefunctions with inclusion of a built-in electric field. The difference is greater for the wider well, sample A, as expected, in agreement with experimental measurements of recombination lifetime in similar samples [70, 90]. Table 4.3 shows that for both A' and A, the FWHMs of the E1 and H1 wavefunctions are reduced when the electric field is included. This effect is again greater for sample A, where the FWHM of the wavefunction in the CB and VB decrease from 3.39 nm to 2.61 nm and from 3.32 nm to 1.91 nm, respectively. This indicates that the electric field enhances the localisation of the E1 and H1 wavefunctions, which further reduces their overlap. The reduction of the wavefunction FWHM is greater in the VB due to the larger effective mass of the hole. In sample A', there is a much smaller change of the FWHMs because the wavefunctions are strongly confined by the barriers in this narrow well and the electric field has little effect.

Samples B, C and D are symmetrically graded QWs which have the same maximum width (6 nm) but different grading step widths and heights (Mg composition). When including the effects of the internal electric field, the calculated E1-H1 transition energies (3.50, 3.47, 3.47 eV) and the overlap of their wavefunctions (0.50, 0.50, 0.47) are approximately the same for each sample. The FWHM of the E1 and H1 wavefunctions

Sample	With E-Field		Without E-Field	
	Transition Energy (eV)	E1-H1 Overlap	Transition Energy (eV)	E1-H1 Overlap
A'	3.58	0.86	3.62	0.99
A	3.38	0.36	3.50	0.99
B	3.50	0.50	3.57	0.99
C	3.47	0.50	3.55	0.99
D	3.47	0.47	3.56	0.99
E	3.52	0.25	3.63	0.99
F	3.57	0.71	3.63	0.99

Table 4.2: Calculated transition energy and wavefunction overlap of the E1 and H1 subbands for all of the samples investigated. Values are given for each sample with and without the effects of the built-in electric field included. The calculated transition energies do not take exciton binding energy into account.

Sample	With E-Field		Without E-Field	
	CB	VB	CB	VB
A'	2.05	1.82	2.09	2.01
A	2.61	1.91	3.39	3.32
B	2.75	3.36	2.52	2.37
C	2.82	2.84	2.76	2.60
D	2.85	2.86	2.80	2.64
E	4.04	1.81	2.73	2.55
F	2.20	3.57	2.73	2.55

Table 4.3: The FWHM of the wavefunction (in nm) for the first CB and VB subband for each sample, respectively. The error for each fit is less than ± 0.02 nm. As the shape of the wavefunctions varies between samples, the FWHM is not obtained through fitting the wavefunctions to a specific function, rather, these values simply define the width at half maximum.

for C and D are essentially the same (CB : 2.82 and 2.85, VB : 2.84 and 2.86), showing little change as the grading step size is reduced from 1 nm to 0.5 nm and the Mg composition step size is reduced from 0.1 to 0.05. The change of the FWHM for the E1 and H1 wavefunctions for C and D, due to the electric field, is much less than occurs in A (C [E1 0.05 nm, H1 0.24 nm], D [E1 0.06 nm, H1 0.22 nm], A [E1 0.78 nm, H1 2.13 nm]). This shows that the localisation of the E1 and H1 wavefunctions observed in A, due to the electric field, is not as significant in C and D. For sample B, the H1 wavefunction extends through the first barrier step (Mg 0.15) and has a two peak structure (Fig. 4.4.4). Because of this, the FWHM of the H1 wavefunction is not a good descriptor for B and therefore the FWHM cannot be used to compare B with C and D. Whilst the wavefunction FWHM cannot be compared in this case, the overlap of the E1 and H1 wavefunctions in B remains similar to C and D. Comparison of the overlap of the E1-H1 wavefunctions of B, C and D with A' and A indicates that the symmetrically graded QWs should have recombination lifetimes in between those of sample A and A'.

Samples E and F are asymmetrically graded QWs, where only one side of the QW is stepped. Both samples have the same maximum width (6 nm) and the same Mg composition step size in the graded barrier (0.05). The only difference between E and F is that they are graded in different directions relative to the growth direction and hence the built-in electric

field. This produces significant differences in the properties of the E1-H1 transition for these two samples. In E, the sloped potential induced by the electric field slopes in the same direction as the stepped CB barrier. In the VB, the sloped potential slopes in the opposite direction to the stepped barrier. In sample F, the stepped barrier is sloped in the opposite direction. In the VB of sample E, the potential difference across each barrier step, induced by the electric field, is approximately the same as the step height, resulting in a somewhat flat potential profile. This leads to a wavefunction for H1 that is wide (FWHM = 4.04 nm) and centred 2 nm from the far left QW barrier. In the CB the E1 wavefunction is centred 0.8 nm from the far right of the QW and is highly localised (FWHM = 1.81). For these reasons the overlap of the E1 and H1 wavefunctions is rather small at 0.25. In the case of F, the barrier step height in the CB is greater than the potential difference due to the electric field, resulting in a potential profile that localises the E1 wavefunction to the same side of the QW as the H1 wavefunction. The result is a larger overlap of E1 and H1 wavefunctions of 0.71. Sample F should therefore produce shorter recombination lifetimes than E. If the band offset ratio for ZnO/MgZnO was 50:50, and the electron and hole effective masses were the same, the E1-H1 transition energy and the wavefunction overlap would be the same in both E and F.

4.4.2 Sample growth

The samples were grown by plasma-assisted molecular beam epitaxy (MBE) by K. Kioke, S. Sasa, M. Inoue and M. Yano at the Osaka Institute of Technology in Japan. The structures were grown on *a*-plane Al₂O₃ and consist of a 15 nm low temperature ZnO/Mg_{0.1}Zn_{0.9}O buffer layer that is followed by a 400 nm Mg_{0.3}Zn_{0.7}O layer, which also forms the barrier on one side of the QW. The growth of the QW was followed by a 50 nm Mg_{0.3}Zn_{0.7}O barrier layer which doubled as the capping layer. All layers were intended to be undoped. The MgZnO layers were grown at 350 °C to avoid phase separation into wurtzite ZnO-rich and rocksalt MgO-rich domains, whereas the ZnO well layer was grown at 500 °C. As the lattice constant along the *c*-axis of a ZnO unit is 5.2 Å [136], the smallest step size is ~ 0.5

Sample	Measured Transition Energy (eV)	FWHM (meV)	Calculated Transition Energy (eV)
A	3.39 ± 0.01	11.6 ± 0.2	3.38
A'	3.58 ± 0.01	15.8 ± 0.2	3.58
B	3.45 ± 0.01	12.7 ± 0.2	3.50
C	3.40 ± 0.01	13.3 ± 0.2	3.47
D	3.42 ± 0.01	11.5 ± 0.1	3.47
E	3.54 ± 0.01	19.5 ± 0.25	3.52
F	3.63 ± 0.01	15.5 ± 0.2	3.57

Table 4.4: PL emission energy obtained from the data in Fig. 4.4.5 and the calculated transition energy for each sample. The calculated transition energies do not include the exciton binding energy.

nm. During the graded barrier growth, a growth interruption of 2 min was introduced at each heterointerface to make the interface abrupt. The Mg composition of each layer was controlled by changing the Mg flux under a Zn-excess condition with constant O₂ and Zn fluxes. Further details of the composition control have been described elsewhere [52, 137].

4.4.3 Photoluminescence

In this section the PL was recorded using a spectrometer coupled to a CCD. The samples were optically excited by 100 fs pulses at a repetition rate of 82 MHz and with a photon energy of 4.66 eV. The excitation density used was $4.5 \mu\text{J cm}^{-2}$ per pulse (6×10^{12} photons cm^{-2} per pulse). For this measurement the sample was mounted in a He cryostat and cooled to 20 K. The PL spectrum for each sample is shown in Fig. 4.4.5. The emission energies are obtained by fitting Gaussian functions to the emission peaks and are given in Table 4.4.

Samples A and A' have PL emission energies of 3.39 ± 0.01 eV and 3.58 ± 0.01 eV respectively. Assuming the exciton binding energies are 40 and 75 meV for samples A and A' respectively [70], the calculated transition energies vary from the measured transition energies by -0.05 eV and -0.075 eV, respectively. This suggests that both QWs may be slightly narrower than they were intended to be. The E1-H1 transition energy for a QW

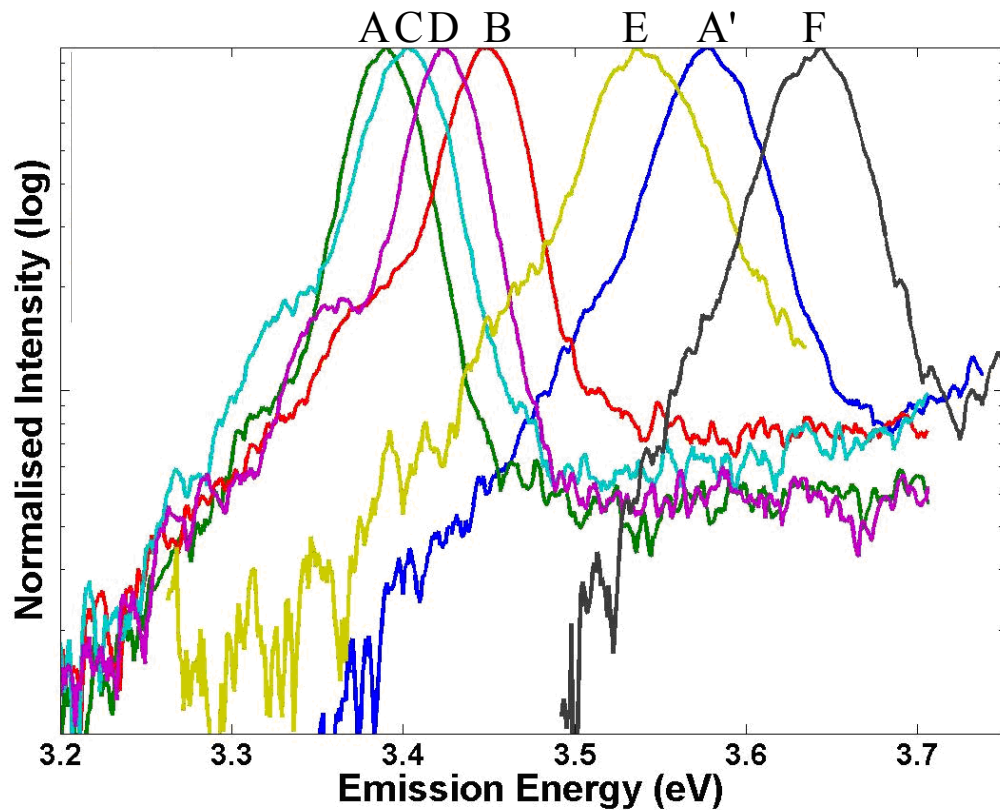


Figure 4.4.5: PL spectrum for each sample. Phonon replicas are observed on the emission from B, C and D. Emission from the barrier tail-states is observed on the high-energy side of each PL peak.

with a width of 1.5 nm, which is equivalent the width for A' minus one ZnO unit cell along the c -axis [52], is calculated to be 3.69 eV. This transition energy is 110 meV greater than for the 2 nm wide QW. If the exciton binding energy is assumed to be 85 meV [70], a transition energy of 3.605 eV is expected, which is slightly larger than was measured in the PL experiment. This suggests that the width of the QW in A' is on average less than one unit cell narrower than it was intended to be. Similarly for A, reducing the QW width by one unit cell shifts the E1-H1 transition energy to 3.43 eV. When an exciton binding energy of 45 meV is considered [70], the measured and calculated transition energies essentially match. Variation in the width of the QW by one unit cell or less is within the accuracy expected for these structures.

The measured transition energies for samples E and F are also greater than the calculated

values. The difference is even greater when the exciton binding energy is considered, regardless of the value of the binding energy. This again suggests that the QWs in this case are slightly narrower than they were intended to be.

A different result is obtained for samples B, C and D, where the measured transition energies are lower than the calculated transition energies for these samples, and are lower still when an exciton binding energy of 40 meV (based on the binding energy for a 4 nm ZnO QW [70]) is used. This result suggests that the width of these QWs is wider than intended, causing the transition energy to be red-shifted from their intended values. The TRPL results in the following section (Sec. 4.4.4) also suggest that B, C and D are wider than intended. Additionally, it can be seen in the PL spectra in Fig. 4.4.5 that on the low energy side of the emission peaks from C and D, and less obvious in B, there appears to be phonon replica peaks. These peaks are separated from the main emission peaks by 69 ± 4 meV, which matches the LO phonon energy of 72 meV [105]. In QWs where the electrons and holes are spatially separated, the LO phonon couples strongly with excitons, producing strong phonon replicas [70, 105]. Similar shoulders are also observed on the other PL peaks, however, these are not as strong, suggesting the spatial separation of the electrons and holes in these samples is not as significant. This provides further evidence that the QWs in B, C and D are wider than they were intended to be.

Several other possibilities, besides variation in the QW profile, are considered to explain the inconsistency between the measured and calculated E1-H1 transition energies. One possibility is that the parameters used in the calculations are not quite right. The parameters used in the calculations were; CB/VB offset of 70/30 [52, 114], a ZnO ($\text{Mg}_{0.3}\text{Zn}_{0.7}\text{O}$) bandgap at 20 K of 3.43 eV (4.06 eV) [52] and electron and heavy-hole effective masses of $0.28m_e$ [46, 52, 90] and $0.78m_e$ [46, 52, 70, 90, 96], respectively, where m_e is the mass of an electron in free-space. In the literature, the CB/VB offset varies from 50/50 to 90/10 [70, 96, 100], however, values within the range 60/40 - 70/30 are generally used [52, 114]. Chauveau et al. [96] showed that varying the CB/VB offset from 50/50 to 90/10 has little effect (~ 0.01 eV) on the calculated E1-H1 transition energy in $\text{ZnO}/\text{Mg}_{0.2}\text{Zn}_{0.8}\text{O}$

QWs, suggesting that this parameter is not responsible for the inconsistencies observed in the present experiment. The heavy-hole effective mass of $0.78m_e$, as suggested by Coli and Bajaj [114], is used consistently throughout the literature [46, 52, 70, 90, 94, 96] and is therefore not considered to be a contributing factor here as there are few other options. An alternative electron effective mass of $0.24m_e$ is regularly used in calculations [70, 96, 114], however, repeating the calculations with this mass typically produces only a small increase in the E1-H1 transition energy (~ 0.01 eV), which does not change any of the conclusions given. In the analysis it was assumed that the values for the exciton binding energy as a function of QW width given by Morhain et al. [70] are transferable to the samples examined in this work. If these values were incorrect, regardless of their values, this would not account for the measured E1-H1 transition energies for A', A, E and F being greater than the calculated values. If the electric field within the QWs was weaker than the value used in the calculations (0.9 MV cm⁻¹), one would expect the measured E1-H1 transition energies to be blue shifted. It is plausible that the strength of the internal electric field within the QWs could be weaker than intended due to a larger than expected strain induced piezoelectric field. Given that the measured transition energies for sample F and A' are even larger than the calculated values for when there is no electric field, it is unlikely that a greater than expected piezoelectric field is responsible for these inconsistencies. The results, therefore, strongly suggest that the dominant source of variation between the measured and the calculated transition energies is due to variations in the QW profile.

Further insight into the nature of the well-barrier interfaces may be gained by examining the FWHM of the PL signal. The sample order for decreasing FWHM for the emission peak is E, A', F, C, B, A, D. One might expect that the FWHM of the emission spectrum would be largest in the samples with the most barrier interfaces, where there is the greatest possibility for fluctuations in the width of the QW or the Mg composition. Sample D has the most barrier grading steps, but has the narrowest FWHM in the emission peak. Sample B has the same number of well/barrier interfaces as E and F, but has the third narrowest FWHM of the PL peak. This suggests that a larger number of well/barrier interfaces doesn't necessarily lead to significantly greater broadening of the E1-H1 transition linewidth. The FWHM of the

PL peak is largest for the samples which have the narrowest wavefunction in either the CB or VB. In these samples, slight changes in the QW profile cause a large relative change of the FWHM of the E1 and H1 wavefunctions, leading to a larger shift in the E1-H1 transition energy. The only exception to this trend is A, where the FWHM of the H1 wavefunction is the third narrowest, whilst the FWHM of the PL peak is second narrowest. This exception is possibly due to there being no barrier grading in A, where any variation in the QW structure can only occur at two interfaces.

4.4.4 Time-resolved photoluminescence

The recombination lifetime for electrons in the E1 sublevel and holes in the H1 sublevel is proportional to the inverse of the square of the E1-H1 wavefunction overlap integral,

$$T_1 \propto \frac{1}{|\langle \psi_e | \psi_h \rangle|^2} \quad (4.4.1)$$

where T_1 is the recombination lifetime and $\psi_e(r)$ and $\psi_h(r)$ are the E1 and H1 wavefunctions, respectively. The TRPL measurements were made to compare lifetimes between the samples and relate these values back to the calculated E1 and H1 wavefunction overlap. The measurements were made by a streak camera with a time resolution of 20 ps and coupled to an imaging spectrometer. The samples were again mounted in a He cryostat and maintained at a temperature of 20 K. The measured TRPL for each sample is shown in Fig. 4.4.6. Each TRPL signal has been fit with a single exponential function and the decay lifetimes are listed listed in Table 4.5. The table also includes the calculated overlap of the E1 and H1 wavefunctions for comparison.

As shown in Table 4.5, the decay lifetime for sample A (1041 ps) is longer than for sample A' (781 ps), suggesting that the overlap of the E1 and H1 wavefunctions in A' is greater than in A. This is consistent with the calculated overlaps of 0.86 and 0.36 for A' and A, respectively. Similarly, the decay lifetime for F (847 ps) is shorter than that for E (1791

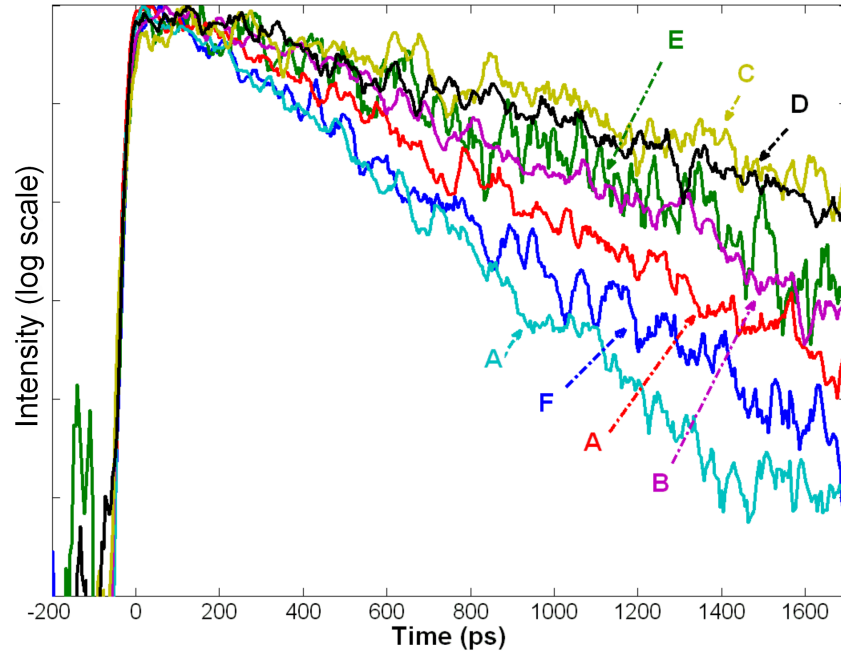


Figure 4.4.6: The normalised TRPL signal from all samples.

Sample	T_1 (ps)	Calculated E1-H1 Overlap
A'	781 ± 10	0.86
A	1041 ± 13	0.36
B	1518 ± 30	0.50
C	2739 ± 170	0.50
D	2809 ± 100	0.47
E	1791 ± 50	0.25
F	847 ± 12	0.71

Table 4.5: Recombination lifetimes obtained by fitting a single exponential function to each of the TRPL signals. The calculated E1-H1 wavefunction overlaps are included for comparison.

ps), which is also consistent with the calculated overlap of the E1 and H1 wavefunctions of 0.71 and 0.25, respectively. These results for A', A, E and F agree qualitatively with Eq. 4.4.1, where the lifetimes increase ($A' < F < A < E$) for decreasing values of the calculated E1-H1 wavefunction overlap.

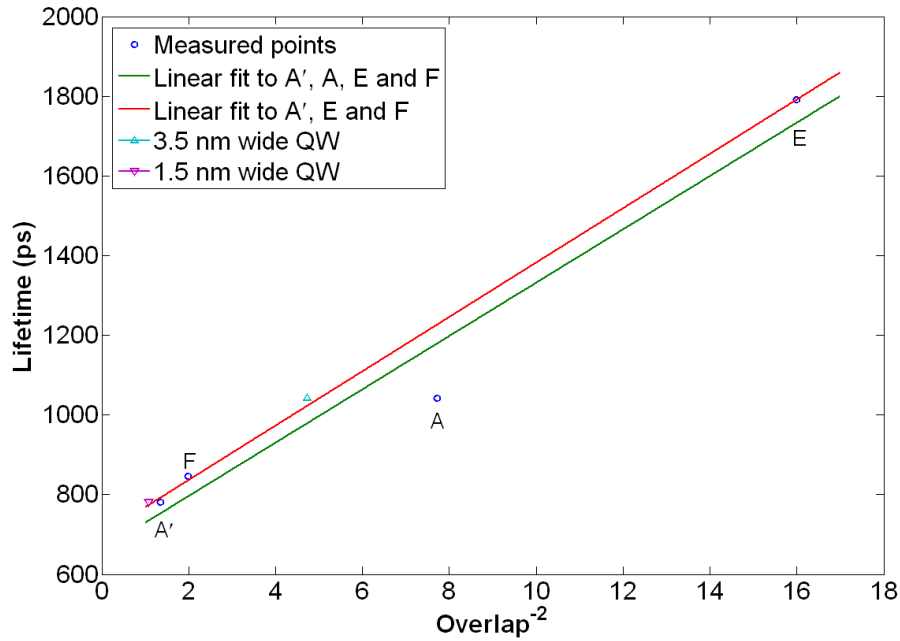


Figure 4.4.7: Using the relation given in Eq. 4.4.1, the overlap of the calculated E1-H1 wavefunctions is plotted against the recombination lifetime for samples A', A, E and F. The overlaps are taken from Table 4.5. Two linear fits are given. \triangle corresponds to the recombination lifetime measured from A and the overlap of the E1 and H1 wavefunctions for a 3.5 nm QW. ∇ corresponds to the recombination lifetime measured from A' and the overlap of the E1 and H1 wavefunctions for a 1.5 nm QW.

The measured recombination lifetimes for A', A, E and F, are plotted in Fig. 4.4.7 against $|\langle\psi_e|\psi_h\rangle|^{-2}$ for the calculated wavefunctions. Whilst the data (points marked with \circ) shown in Fig. 4.4.7 has a somewhat linear relationship, it does not fit Eq. 4.4.1 in its current form; the gradient of a linear fit to the points is not equal to $1/|\langle\psi_e|\psi_h\rangle|^{-2}$ and therefore does not intersect the recombination lifetime axis at (0,0). In order to fit the data shown in Fig. 4.4.7 to a linear function, an offset and a gradient constant are required. The points may be fit using

$$T = \frac{c}{|\langle\psi_e|\psi_h\rangle|^2} + T^* \quad (4.4.2)$$

where c is the gradient linking the change in $|\langle\psi_e|\psi_h\rangle|^{-2}$ with recombination lifetime and T^*

is the recombination lifetime offset. Whilst the value of T^* on its own has no physical significance, given that the E1-H1 wavefunction overlap cannot exceed 1 (and therefore $|\langle\psi_e|\psi_h\rangle|^{-2}$ cannot be < 1), the factors T^* and c , together, describe parameters other than wavefunction overlap that contribute to the E1-H1 recombination rate. These parameters include material dependent properties, such as phonon coupling strength, and impurity and defect densities. The fact that the data points can be described by a simple linear fit suggests that these parameters do not vary significantly from sample to sample.

Two linear fits are given in Fig. 4.4.7, one for A', A, E and F, and the second for A', E and F. It is shown that the point corresponding to sample A deviates significantly from both fits, suggesting that the overlap of the E1 and H1 wavefunctions in A is greater than calculated. In Sec. 4.4.3 the width of the QW in A was suggested to be narrower than intended by one ZnO unit cell. Recalculating the E1-H1 transition energy for a QW of width 3.5 nm (A - 0.5 nm) produced a transition energy which closely matched the measured transition energy for A. At the same time, the overlap of the E1 and H1 wavefunctions is increased to 0.46 from 0.36. In Fig. 4.4.7, it is shown that the measured recombination lifetime in A appears to be more consistent with the linear fit to A', E and F if an overlap of 0.46 is used rather than 0.36. The good agreement between the results suggests that sample A is slightly narrower than intended. In the previous section it was also suggested that A' was slightly narrower than intended. The revised QW width of 1.5 nm produced an overlap for the E1 and H1 wavefunctions of 0.96. In Fig. 4.4.7, the 1.5 nm wide QW does not deviate significantly from fit given by A', E and F.

Samples B, C and D, on the other hand, do not follow the same trend as A, A', E and F. Based on the calculated E1-H1 wavefunction overlaps for samples B, C and D, (0.50, 0.50 and 0.46, respectively), the recombination lifetimes were expected to be faster than A. The measured recombination lifetimes for B, C and D are, however, much longer than measured for A, with lifetimes of 1518 ± 30 ps, 2739 ± 170 ps and 2809 ± 100 ps respectively. Referring back to the PL results in Sec. 4.4.3, it appeared that the QWs in samples B, C and D were slightly wider than they were intended to be. This was evident by the emission

energy from these samples being lower in energy than expected and by the strong phonon replicas present in the PL signal from these samples. This is consistent with the measured TRPL signals from these samples, where wider QWs would allow a larger separation of the E1 and H1 wavefunctions. In Fig. 4.4.5 the phonon replicas were strongest for C and D. This is consistent with the recombination lifetime from these samples being the largest of the sample set. It appears that the QW structures for B, C and D vary significantly from what they were intended to be. Why this is the case for these samples and not for A', A, E and F cannot be explained from these results. Growth studies on this sample design will need to be carried out to determine why this is the case.

4.4.5 Summary

In summary, a range of ZnO/MgZnO QWs were designed to see if the combination of internal electric field and graded barriers could be used to predictably control the E1-H1 transition energy and wavefunction overlap. Two square barrier QWs (A' and A), three symmetric graded barrier QWs (B, C and D) and two asymmetric QWs (E and F) were examined. Samples A' and A have the least complex structure of the sample set, and therefore the grown samples should closely match their calculated values. The calculations also suggested there would be very little variation in the optical properties between B, C and D. For E and F, there is a large difference in the calculated E1 and H1 wavefunction overlaps (0.25 and 0.71, respectively), therefore very different recombination lifetimes are expected for these samples. PL measurements revealed that the E1-H1 transition energy for each sample varied from their calculated values; A', A, E and F had higher transition energies than calculated, whilst B, C and D had lower transition energies than calculated. It was suggested that A', A, E and F were all narrower than expected. For A' and A, recalculating the transition energy for a QW width narrower by one ZnO unit cell produced transition energies which closely matched the measured energies. Clear LO-phonon replicas were observed in the PL spectra for B, C and D, and not so for A', A, E and F, which is consistent with these samples being wider than they were intended to be and wider than A', A, E and F.

The same trends were observed in the TRPL results, where B, C and D had recombination lifetimes that were longer than for the other samples. The reason why B, C and D vary significantly from the other samples is unclear. Samples A', A, E and F on the other hand clearly follow the trend given by the calculations, where the recombination lifetime increases in order of increasing overlap of the E1 and H1 wavefunctions. This ability to predictably control the wave function overlap and transition energy using graded barriers in QWs under the influence of the QCSE adds to the commonly used techniques for tuning QW properties, including well width, band gap, and barrier height.

Chapter 5

Coupling and coherent dynamics within asymmetric double quantum wells

5.1 Introduction

Coherent and resonant excitation of a two-level system generates a coherent superposition of the ground and excited state. The probability of electron occupancy of the two states oscillates at the frequency of the transition with an initial phase determined by the excitation pulse. If two two-level systems with well defined and different transition energies are coherently and resonantly excited, a range of coherent phenomena may be observed. One well known effect is polarisation interference, which describes the situation where the emission from the two coherent two-level systems interfere at the detector. In FWM experiments, this can give a beating signal as a function of interpulse delay [138, 139]. A more interesting effect occurs when the two two-level systems are coherently coupled. When such systems are coherently and resonantly excited, a coherent superposition of the two systems is established. Since the transition energies of the two two-level systems are different, their phases evolve at different rates and interfere. This interference also produces a beating signal in FWM experiments, however, in this case it is the result of

interference within the sample. Such a beating signal is generally known as quantum beating [12, 24, 25, 37]. The characterisation of coherent coupling mechanisms and dynamics in condensed matter systems is of great interest to the semiconductor community. Furthering our understanding of such processes will advance the use of condensed matter systems for quantum information processing and instigate the development of new devices. Characterisation of the coherent dynamics and the mechanisms responsible for coherent coupling between spatially separated excitons in double QWs is the focus of the investigation in this chapter.

Göbel et al. [24] made the first observation of coherent coupling between excitons in GaAs QWs back in 1990. The authors observed beating on a two-pulse FWM signal with a beat period equal to the energy difference between excitons localised to so called ‘excitonic islands’, which form as a result of monolayer fluctuations in the width of the QW. The observed beating was attributed to quantum beating between spatially separated excitons. This interpretation was controversial at the time because quantum beating was not expected between a pair of two-level systems with no shared state. In such cases beating is usually expected to be the result of polarisation interference [12, 138]. Theoretical work by Bastch et al. [140] showed that dipole-dipole coupling between localised excitons could cause quantum beats. Further investigation by Koch et al. [25] on similar samples revealed beating in the TR-FWM signal with characteristics matching those expected for quantum beats and not polarisation interference [141]. These results were later refuted by Euteneuer et al. [142] because the authors did not observe a beating signal in similar samples. Finger et al. [143] were similarly unconvinced and suggested that such a signal could be due to beating between excitons and bi-excitons. Davis et al. [144] investigated this effect further and observed a beating signal that was similar to that observed by Koch et al. [25]. The authors showed that the coupling strength is dependent on the in-plane overlap of the exciton wavefunctions. Such parameters may vary from sample to sample and this may explain the discrepancy between the results of Euteneuer et al. [142] and Göbel et al. [24]. The results also suggested that dipole-dipole coupling was not the mechanism responsible for coupling in such cases. In a very recent publication by Kasprzak et al. [145], the authors identified

coherent coupling between excitons localised within the same QW plane and separated by distances up to $1\ \mu\text{m}$. The authors suggest that dipole-dipole coupling is not the mechanism coupling the spatially separated excitons. They propose a mechanism where the excitons couple through extended exciton states in the QW plane. Such states are created by radiative coupling and can be considered as being localised exciton polaritons [145].

In symmetric and asymmetric double QW structures, the coupling strength between states predominantly localised to different wells has been studied extensively [146–153]. Typical investigations make use of a controlled electric field oriented perpendicular to the QW plane to tune the energy difference between the energy levels. The splitting of the energy levels at the anti-crossing provides a measure of the coupling strength. However, these experiments only measure the coupling strength between electrons or holes near resonance in the double QWs, not the coupling strength between excitons. A measure of the coupling strength between excitons can be made in experiments which measure coherent dynamics, such as FWM experiments. One could examine the amplitude of coupling induced signals, such as quantum beats, as a function of a parameter which varies the coupling strength. Kasprzak et al. [145] recently showed that coupling strength can be measured by examining the amplitude of cross-peaks in 2DFTS. Furthermore, FWM experiments also allow exploration of the decoherence processes affecting coherently coupled excitons.

The coherent dynamics and the coupling strength between excitons mostly localised to adjacent QWs in a double QW structure has not been examined in as much detail as coupled excitons localised to monolayer fluctuations within the same QW plane. The only investigation to date which directly examines coupling between excitons in an asymmetric double QW is by Li et al. [36]. The authors use 2DFT spectroscopy to explore the coupling between the two lowest energy and bright heavy-hole (HH) and light-hole (LH) excitons within an asymmetric double QW system for two barrier widths: 1.7 nm and 10 nm. For the sample with a 1.7 nm barrier, a complex 2D spectrum was observed which suggested that all of the bright exciton states were coupled with each other. However, due to the small energy difference between the two heavy-hole subbands, the authors were not able to determine

which signal corresponded to which heavy-hole, making analysis difficult. Zhang [92] and Li et al. [36] suggested that valance band mixing, as a result of the narrow barrier, would be responsible for the observed signal. For the sample with the 10 nm barrier, the 2D spectrum was much less complex due to the reduced coherent interactions between the exciton states as a result of the increased separation of the QWs. Only the bright HH and LH excitons localised to the same QW were found to be coherently coupled. A cross-peak corresponding to absorption at the higher energy LH bright exciton and emission at the lowest energy LH bright exciton, exciton states which were considered to be localised to separate QWs, was observed. The authors suggested that incoherent relaxation was the most likely source of the cross-peak signal in this case.

The aim of the work in this thesis is to examine the coherent dynamics of coupled and spatially separated excitons which do not share a common state. Asymmetric double quantum wells (ADQW) provide an ideal platform for studying spatially separated excitons under controlled conditions. By varying the QW width, the exciton transition energies of single QWs and the relative difference in transition energy between the two wells can be controlled. Varying the barrier width separating the two wells controls the spatial separation between the localised states. With current growth techniques QW structures can be produced with monolayer accuracy, allowing the optical properties of such structures to be controlled with high precision.

Using such QW structures also allows one to explore the effect of particular resonances on the coherent and energy transfer dynamics of spatially separated excitons. In a theoretical investigation, Batsch et al. [140] suggested that spatially separated excitons that are dipole-dipole coupled and have an energy difference equal to the longitudinal-optical (LO) phonon energy should experience efficient transport through the barrier separating the two excitons. Such an energy transfer process is considered to be an analogue to Förster-type energy transfer in molecules. This energy transfer process has still not been demonstrated experimentally in semiconductors.

In the investigation presented in this Chapter, two asymmetric double QW sample sets

are examined. Sample set 1 has been grown to examine the interaction of LO-phonons with coherently coupled excitons. The sample set is designed so that the energy difference between the two lowest energy bright HH excitons of the ADQW system are separated by the LO phonon energy. Samples with a range of barrier widths are grown to explore the effect of spatial separation, whilst preserving the energy difference between the two HH excitons of interest. The set is made up of asymmetric double QWs with barrier separations of 2, 4, 6, 20 and 50 nm. The second set is designed so that these two HH excitons are not separated by the LO-phonon energy. By comparing the two sample sets, it may be possible to determine the role played by LO phonons on the observed dynamics.

The structure of this Chapter is as follows. In Sec. 5.2.1, the design of the double QW system in each sample set is discussed. In Sec. 5.2.2, the samples are characterised at low temperature using a photoluminescence experiment and the transition energies are compared to those calculated in Sec. 5.2.1. In Sec. 5.2.3 - 5.2.7 the coherent response of these samples is characterised, discussing heavy-hole light-hole beating, exciton dephasing due to coupling to the free-carrier continuum, peak-shift and disorder, before proceeding to the main experimental results of this chapter. In Sec. 5.3, experimental results which demonstrate coupling between spatially and energetically separated excitons are presented and discussed.

5.2 Sample design and characterisation

In this section the sample design is discussed. The samples are characterised using photoluminescence experiments and compared to the intended design using the calculated and measured emission energies. This is followed by the characterisation of the coherent dynamics.

5.2.1 Sample design

The samples have been designed so that the energy difference between the two lowest energy HH exciton transitions of the ADQW system are separated by the LO-phonon energy. The sublevel energies of the ADQW system have been calculated using the method described in Chap. 2. The QWs will be made from GaAs/Al_{0.35}Ga_{0.65}As, where the LO phonon energy is taken to be 35 meV [8]. In the calculations the following effective masses were used; $m_e = 0.067m_0$ [154, 155], $m_{hh} = 0.51m_0$ [156], $m_{th} = 0.082m_0$ [156]. A bandgap of 1.51 eV for GaAs and 1.93 eV for Al_{0.35}Ga_{0.65}As at 20 K was used [157, 158]. The band offset was 67/33 (CB/VB) [8, 159]. The sample dimensions which give the desired relative transition energy differences are given in Table 5.1 and 5.2.

Set 1 - WW = 8 nm, NW = 5.7 nm					
Barrier Width (nm)	2	4	6	20	50
Sample Name	S1-2	S1-4	S1-6	S1-20	S1-50

Table 5.1: The wide well (WW) and narrow well (NW) dimensions for sample set 1.

Set 2 - WW = 6.7 nm, NW = 5.7 nm					
Barrier Width (nm)	2	4	6	20	50
Sample Name	S2-2	S2-4	S2-6	S2-20	S2-50

Table 5.2: The wide well (WW) and narrow well (NW) dimensions for sample set 2.

The variation of the exciton binding energy with barrier width is ignored when determining the exciton transition energies and is assumed to be the same, ~ 10 meV [160–162], for all excitons. It is anticipated that the variation of the exciton binding energy as a function of barrier width will be less than the variation of the exciton transition energy due to sample inhomogeneities. Based on this assumption, correcting for these differences will have no meaningful effect. In addition to this, the energy difference between the exciton transitions will vary with barrier width due to the energy splitting between the conduction band states and the valence band states for narrow barrier widths. The effect of this on the transition energy of excitons is also expected to be much less than the variation of the exciton transition energy due to inhomogeneities and is not accounted for in the sample design. For

an initial investigation into coupling phenomena, these samples will nonetheless provide valuable insight.

The ADQW profiles perpendicular to the QW plane for samples S1-2, S1-4, S1-6 and S1-20, as defined in Table 5.1, are shown in Fig. 5.2.1. The calculated energies and wavefunctions for the first two electron (E), heavy-hole (HH) and light-hole (LH) are included. In S1-20, the 20 nm wide barrier separating the WW and NW localises the E1, HH1 and LH1 wavefunctions to the wide QW and the E2, HH2 and LH2 wavefunctions to the narrow QW. When the barrier width is reduced to 6 nm, HH1 and HH2 remain localised to the WW and NW respectively. Similarly, the E1 and E2 wavefunctions also remain highly

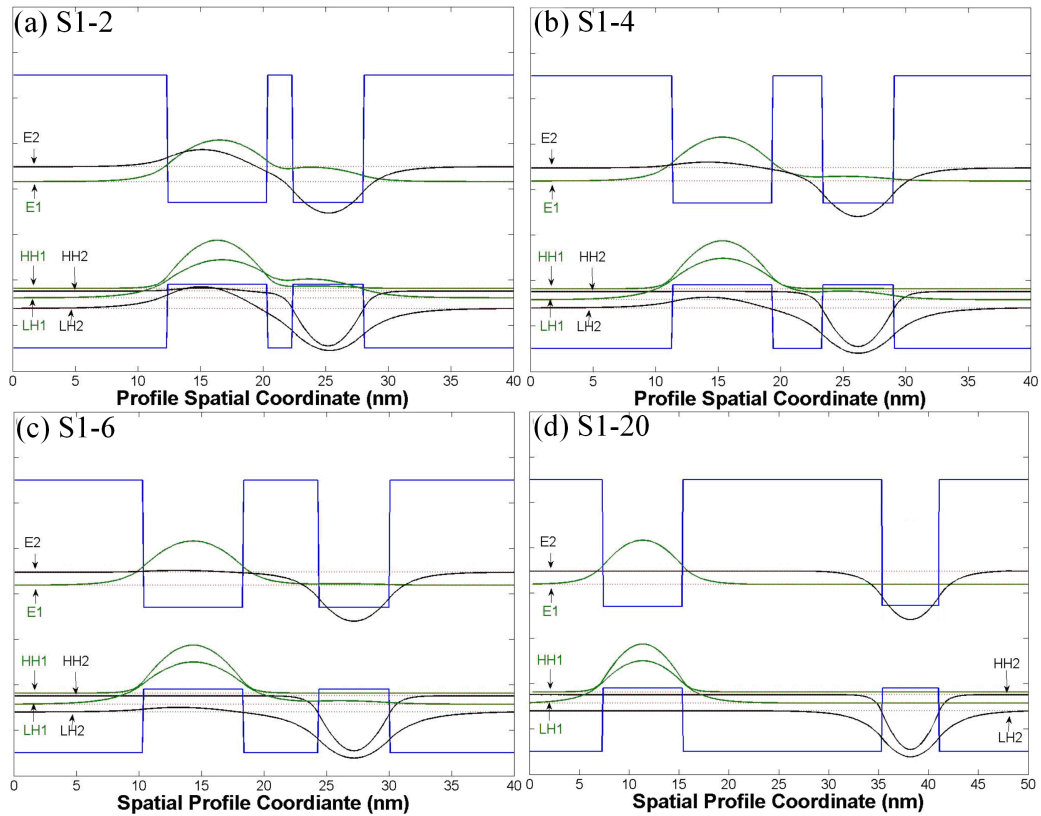


Figure 5.2.1: The profiles, wavefunctions and energies for the first two electron (E), heavy-hole (HH) and light-hole (LH) states of samples (a) S1-2, (b) S1-4, (c) S1-6 and (d) S1-20. In (a), the wavefunction for each E, HH and LH subband extends through the barrier separating the two wells. As the barrier width is increased the wavefunctions become more localised. In (d), where there is a wide barrier separating the two QWs, each of the E, HH and LH wavefunctions can be considered to be completely localised to the wide and narrow QWs.

localised. The LH1 and LH2 wavefunctions, however, show some extension through the barrier separating the QWs due to their lighter effective mass. Whilst the effective masses of the E ($0.067m_0$) and LH ($0.082m_0$) are comparable, the conduction and valence band band-offset allows greater extension of the LH1 and LH2 wavefunctions through the barrier separating the QWs. As the barrier width is reduced to 4 nm in S1-4, each of the E, HH and LH wavefunctions become less localised. In S1-2, the extension of the E, HH and LH wavefunctions through the barrier is further enhanced and each of the E, HH and LH wavefunctions have significant wavefunction amplitudes in both QWs. The barrier width dependent localisation of each of the E, HH and LH wavefunctions has implications for the wavefunction overlap of different QW states. This variation from sample to sample is important when comparing coupled excitons in the experimental results presented in this chapter.

The calculated transition energy for the four so called ‘bright transitions’, the interband transitions between electrons and holes which have the greatest wavefunction overlap, are given in Table 5.3 and are plotted as a function of barrier width in Fig. 5.2.2. The bright transitions in both sample sets are the transitions labeled E1HH1, E1LH1, E2HH2 and E2LH2, representing transitions between E1 and HH1, E1 and LH1, E2 and HH2, and E2 and LH2 respectively. In Fig. 5.2.2 the transition energy for a double QW with a barrier

Sample	E1HH1	E1LH1	E2HH2	E2LH2	E2HH2-E1HH1
S1-2	1.572	1.593	1.611	1.649	0.039
S1-4	1.575	1.599	1.610	1.646	0.035
S1-6	1.575	1.600	1.609	1.645	0.034
S1-20	1.575	1.600	1.609	1.645	0.034
S1-50	1.575	1.600	1.609	1.645	0.034
S2-2	1.585	1.609	1.615	1.657	0.030
S2-4	1.591	1.619	1.610	1.647	0.019
S2-6	1.592	1.621	1.610	1.645	0.018
S2-20	1.592	1.622	1.609	1.645	0.018
S2-50	1.592	1.622	1.609	1.645	0.018

Table 5.3: The calculated transition energies, in eV, for the so called ‘bright excitons’ for each of the grown samples. The transition energy difference between the E1HH1 and E2HH2 excitons is also given.

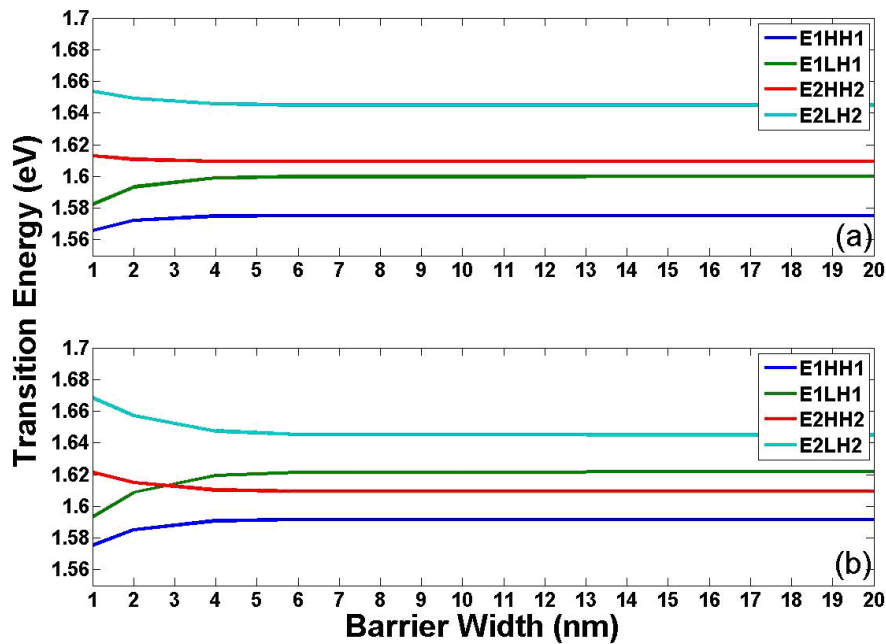


Figure 5.2.2: The transition energy for the E1HH1, E1LH1, E2HH2 and E2LH2 transitions plotted as a function of the barrier width separating the wide and narrow wells for sample sets: (a) 1 and (b) 2. As the width of the barrier separating the two QWs is increased from 1 nm to 20 nm, the double QW system shifts from a coupled to an uncoupled system. This is apparent from the splitting between the E1HH1 and E2HH2, and the E1LH1 and E2LH2 transitions for increasing barrier width. For barrier widths greater than 6 nm, there is no shift in each of the transition energies.

width of 1 nm, which was not grown, is also plotted.

In double QW systems, the interaction between electrons and between holes in adjacent QWs can lead to a splitting of their energy levels [9]. The strength of the interaction, and therefore the splitting in the energy between these subbands, is proportional to the ir coupling strength. The subband splitting results in an energy separation between the E1HH1 and E2HH2 excitons that is greatest at narrow barrier widths. The subband splitting similarly affects the E1LH1 and E2LH2 exciton transition energies. This is evident in Fig. 5.2.2, where the transition energy for E1HH1, E1LH1, E2HH2 and E2LH2 are plotted dependent on the width of the barrier separating the two QWs. For barrier widths greater than 6 nm, the effect of the subband splitting on the bright transition energies is insignificant.

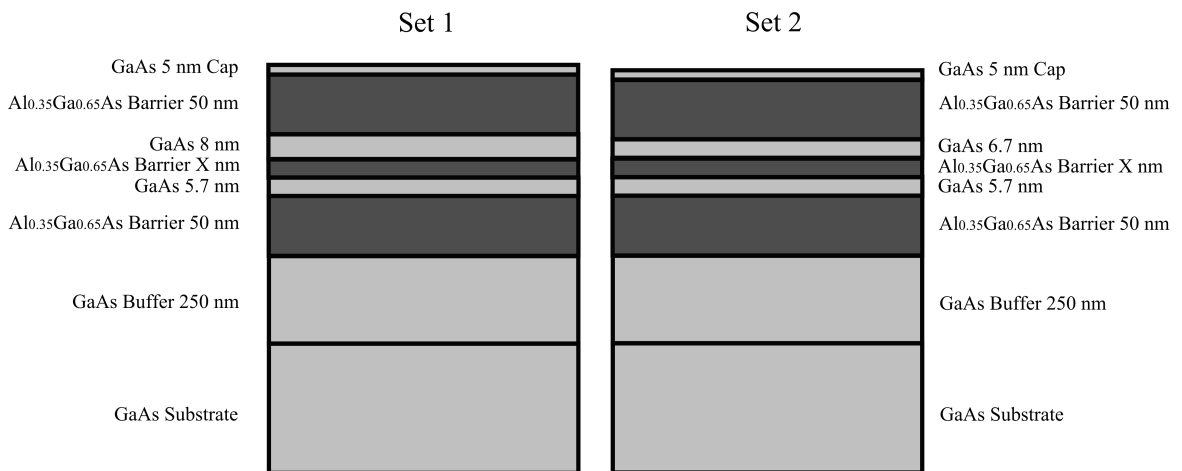


Figure 5.2.3: The structure of sample set 1 and 2. In each set, the barrier separating the two QWs has values 2, 4, 6, 20 and 50 nm. The GaAs buffer layer and substrate below the QWs prevents FWM experiments being carried out in the transmission geometry.

In addition to calculating the E1HH1, E1LH1, E2HH2 and E2LH2 transition energies for the given well dimensions and for each barrier width, the E1LH2, E1HH2, E2LH1 and E2HH2 transition energies have also been calculated. The difference in transition energy between each of these possible QW transitions has been determined and is listed for each sample in Appendix B. Also included in the tables for each transition is the overlap integral for the electron and hole wavefunctions, which may be used as an indication of the transition oscillator strength. The tables are used to help identify which transitions are observed in the FWM experiments.

The GaAs/Al_{0.35}Ga_{0.65}As asymmetric double QW samples were grown by our collaborators in the Department for Electronic Materials Engineering (EME) at The Australian National University (ANU). The samples were grown using the Metal Organic Chemical Vapor Deposition (MOCVD) process, which is briefly described in Chap. 2.

The sample structure is shown in Fig. 5.2.3. All of the QW samples were grown on top of a semi-insulating (100) GaAs substrate. Prior to growth, the substrate was annealed in the reactor for 10 mins at 750 °C in order to ensure a high quality substrate surface. Immediately on top of the substrate a 250 nm GaAs buffer layer was grown, followed by a 50 nm Al_{0.35}Ga_{0.65}As layer, which forms the barrier on one side of the first QW. In both

sample sets, the 5.7 nm QW was grown first, followed by the $\text{Al}_{0.35}\text{Ga}_{0.65}\text{As}$ barrier, the width of which is varied from sample to sample. The second GaAs QW layer was then grown. For sample set 1 and 2, this layer is 8 nm and 6.7 nm wide, respectively. Another 50 nm $\text{Al}_{0.35}\text{Ga}_{0.65}\text{As}$ layer was grown on top, which forms the barrier layer for the second QW. The growth was finished off with a 5 nm GaAs capping layer to avoid Al oxidation in atmosphere, preserving the sample surface quality.

The GaAs buffer layer and GaAs substrate located beneath the QWs prevents FWM experiments from being carried out in the transmission geometry. This is because these layers will absorb the FWM signal emitted from the QWs and the excitation laser. As described in the experimental chapter, the FWM signals emitted in the reverse direction are detected to overcome this issue.

5.2.2 Photoluminescence

The initial characterisation of these samples was carried out by photoluminescence (PL) experiments. Low temperature (20 K) PL measurements used optical excitation at 2.484 eV from an OPA (1 kHz, 100 fs \sim 20 nJ pulses). The excitation pulses were focused to a diameter of approximately 100 μm with an excitation fluence of 2.5×10^{13} photons cm^{-2} per pulse. The emission spectra for all samples, plotted on a log scale, are shown in Fig. 5.2.4.

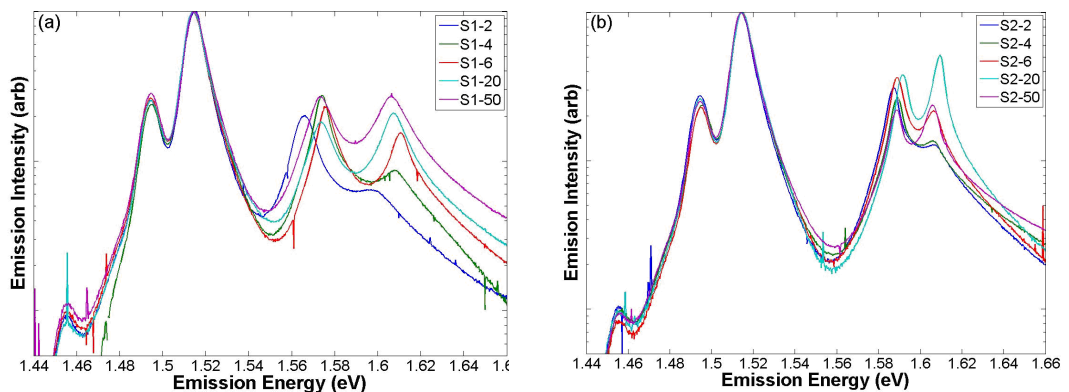


Figure 5.2.4: Low temperature (20 K) PL for sample set (a) 1 and (b) 2 plotted on a log scale.

Sample	E1HH1	E2HH2	E2HH2 - E1HH1
S1-2	1.566 ± 0.001	1.598 ± 0.002	0.032
S1-4	1.574 ± 0.001	1.608 ± 0.001	0.034
S1-6	1.576 ± 0.001	1.611 ± 0.001	0.035
S1-20	1.576 ± 0.001	1.607 ± 0.001	0.031
S1-50	1.573 ± 0.001	1.606 ± 0.001	0.033
S2-2	1.587 ± 0.001	1.607 ± 0.002	0.02
S2-4	1.589 ± 0.001	1.606 ± 0.002	0.017
S2-6	1.589 ± 0.001	1.607 ± 0.001	0.018
S2-20	1.592 ± 0.001	1.610 ± 0.001	0.018
S2-50	1.589 ± 0.001	1.606 ± 0.001	0.017

Table 5.4: The low temperature emission energies for the E1HH1 and E2HH2 transitions shown in Fig. 5.2.4 for all samples. The emission energies are obtained by fitting a Lorentzian function to each PL peak.

The peak at 1.49 eV (0.0217 eV on the low energy side of the bulk GaAs emission peak at 1.512 eV) is attributed to a carbon impurity [163] and is ignored for the purposes of this thesis. A small unidentified peak at 1.456 eV (0.057 eV lower in energy than the bulk GaAs emission) is observed and is also assumed to originate from defects in the GaAs bulk layer and is also ignored.

The peaks at ~ 1.57 eV and ~ 1.61 eV in set 1, and the peaks at ~ 1.59 eV and ~ 1.61 eV in set 2 are attributed to the E1HH1 and E2HH2 transitions based on the calculated values in Table 5.3. The emission energies for the E1HH1 and E1HH2 transitions for each sample are tabulated in Table 5.4 and plotted as a function of barrier width in Fig. 5.2.5. In Fig. 5.2.2, calculations showed that as the barrier width increased from 1 nm to 6 nm, the difference between E1HH1 and E2HH2 transition energies decreased. As the barrier width was increased further, from 6 nm to 20 nm, there was no additional change in the difference between the E1HH1 and E2HH2 transition energies. These trends are not observed in the measured results presented in Table 5.4 and Fig. 5.2.5. In set 1, the E1HH1 and E2HH2 transitions in samples S1-4, S1-6, S1-20 and S1-50, are essentially constant with an average energy of 1.575 ± 0.001 eV (E1HH1) and 1.608 ± 0.001 eV (E2HH2). In sample S1-2, the E1HH1 and E2HH2 transitions are both red-shifted relative to this with energies of 1.566 ± 0.001 eV and 1.598 ± 0.002 eV, respectively. The energy difference between the E1HH1

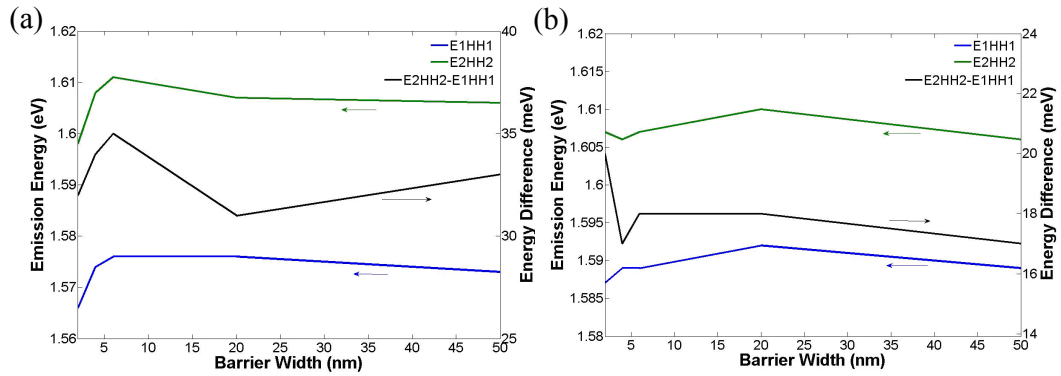


Figure 5.2.5: The E1HH1 and E2HH2 transition energy, and difference in transition energy, as function of barrier width, is plotted for sample set (a) 1 and (b) 2. The data is taken from Table 5.4.

and E2HH2 transitions varies from 31 to 35 meV, following no particular trend as a function of barrier width. In set 2, the transition energies are essentially constant as a function of barrier width with average values of 1.589 ± 0.001 eV (E1HH1) and 1.607 ± 0.001 eV (E2HH2). There is also very little variation in the energy difference between the E1HH1 and E2HH2 transitions between samples in set 2, where the energy difference varies from 17 to 20 meV. For sample set 2 there is no discernable trend for the energy difference as a function of barrier width. It is evident that the variation of the energy difference between the E1HH1 and E2HH2 transitions for both sample sets does not follow the barrier width dependence expected from Fig. 5.2.2. Inhomogeneities, such as monolayer fluctuations within the QW layer and variations in strain, will cause the energy difference between the E1HH1 and E2HH2 transitions to vary from sample to sample in addition to the variation due to splitting of the E, HH and LH subbands. The variation of the energy difference between the E1HH1 and E2HH2 transitions due to inhomogeneities are too great to observe the barrier width dependence expected from Fig. 5.2.2. This result plainly reflects the limitations when growing semiconductor QW structures.

The ratio of the emission intensity of the E1HH1 and E2HH2 transitions in the PL experiment is presented for all samples in Table 5.5. The emission from the E1HH1 transition is much stronger than the emission from the E2HH2 transition for the thinnest barrier widths. As the barrier width is increased the ratio of the emission intensities

Barrier Width (nm)	Set 1	Set 2
2	3.21	2.41
4	3.22	1.95
6	1.51	1.70
20	0.87	0.73
50	1.00	0.92

Table 5.5: The ratio of the emission intensity from E1HH1 and E2HH2 as a function of barrier width. As the barrier width is increased, the relative emission intensity from E2HH2 increases, which reduces the value of the ratio.

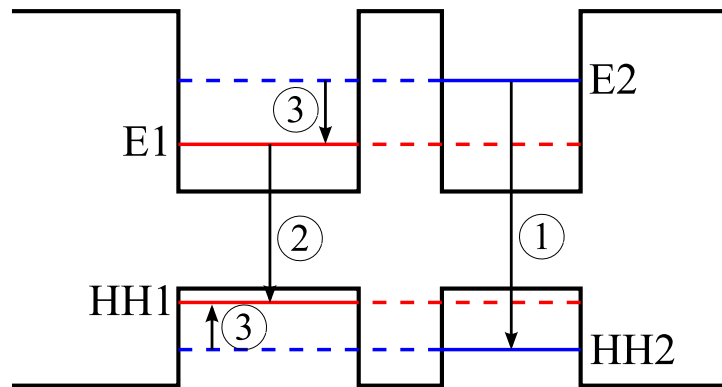


Figure 5.2.6: A simple model representing some of the possible recombination pathways within the asymmetric double QW samples. The dashed lines represent extended wavefunctions.

decreases. This trend can be explained by considering the dominant carrier recombination pathways shown in Fig. 5.2.6. The recombination pathway labelled (1) indicates the radiative recombination of carriers via the E2HH2 transition, where the E2 and HH2 wavefunctions are predominantly localised to the narrow well for barrier widths ≥ 4 nm and (2) indicates the radiative recombination of carriers via the E1HH1 transition, where the E1 and HH1 wavefunctions are mainly localised to the wide well for barrier widths ≥ 4 nm. Pathway (3) indicates intraband relaxation of electrons and holes from E2/H2 to E1/H1, following which the carriers may recombine via (2). For double QW systems at low temperature and with thin barriers, the intraband relaxation rate has been shown to be greater than the interband (E2HH2/E1HH1) recombination rate of carriers [12, 164, 165]. This results in a depletion of carriers radiatively recombining via the E2HH2 transition and an increase in recombination via the E1HH1 transition. The amplitude of the E1 and HH1 wavefunctions in the narrow

QW decreases as the barrier width is increased (likewise, the amplitude of the E2 and HH2 wavefunctions in the wide QW decreases as the barrier width is increased), reducing the overlap integral of the E1 and E2, and the HH1 and HH2 wavefunctions. This subsequently reduces the intraband relaxation rate. Therefore, as one increases the width of the barrier separating the two QWs, the emission from the E2HH2 transition increases. This barrier width dependence of the relative emission intensities is observed in Table 5.5. LO phonon resonances have been shown to increase the intraband relaxation rate [166] which may explain why a greater contrast between the E1HH1/E2HH2 emission intensities is observed in set 1 compared to set 2 in Table 5.5.

5.2.3 Coupled heavy-hole and light-hole excitons

The observation of beating in experiments which probe coherent dynamics can be a clear indication that the excited states are coupled. A three-level system, consisting of two transitions with slightly different energies that share either a common ground or excited state, or consisting of a ground state, a single excited state and a doubly excited state, are such systems which may produce quantum beating. The phase of each transition evolves at different rates due to the difference in their transition energy. Interference between the two evolving phases produces beating in the coherent response of the three-level system with a period given by $h/\Delta E$. In Sec. 5.3 we investigate whether excitons localised to spatially separated QWs may be coherently coupled. The observation of beating in the FWM signal originating from spatially separated exciton states, with a beat frequency equal the energy difference of the two states, would provide strong evidence that the two states are coupled.

Coherently exciting the heavy-hole exciton and light-hole exciton states within the same QW, where the heavy-hole and light-hole excitons are coupled via a common electron state, is known to produce strong beating in FWM experiments [22, 23]. In this section, beating between the E1HH1 and E1LH1 excitons is examined in sample S1-20. As shown by the calculated subband wavefunctions for S1-20 in Fig. 5.2.1(d), the wavefunctions for the E1, HH1 and LH1 states are localised to the wide QW and the E2, HH2 and LH2 states are

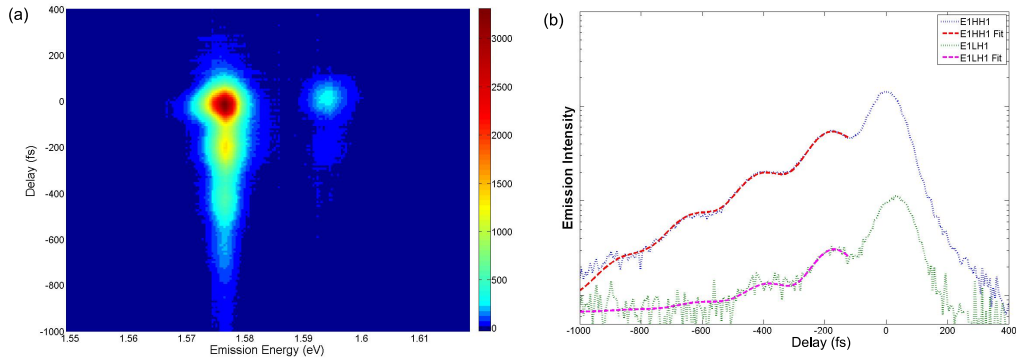


Figure 5.2.7: (a) The SR-FWM signal from the E1HH1 and E1LH1 transitions for sample S1-20 as a function of coherence time, τ . The spectrally-integrated signals are plotted in (b). Beating is observed in the FWM signal from both transitions with a beat period equal to the energy difference between the two transitions. Also included in (b) is a fit using Eq. 5.2.1. The fitting parameters are given in Table 5.6.

localised to the narrow QW, allowing us to treat the two QWs as uncoupled single QWs. The coherent dynamics were measured with a two pulse FWM experiment. In this experiment the laser was centred at 1.577 eV and resonantly excited the E1HH1 transition of the wide QW. The laser had a FWHM of 20 meV and a pulse width of 100 fs. The excitation pulses were focused to a spot with a diameter of approximately 50 μm with a fluence of 1.2×10^{11} photons cm^{-2} per pulse. The sample was maintained at a temperature of 20 K. The higher-energy shoulder of the laser spectrum also resonantly excited the E1LH1 transition of the same QW. The spectrally resolved signal detected as a function of delay between the excitation pulses, τ , is plotted in Fig. 5.2.7(a). A signal is observed from the E1HH1 and E1LH1 excitons at emission energies of 1.575 ± 0.001 eV and 1.593 ± 0.001 eV, respectively, with an energy difference of 17 ± 1 meV. Strong oscillations are observed on the FWM signal from the E1HH1 and E1LH1 transitions. Spectrally-integrated plots of the signal from the E1HH1 and E1LH1 transitions are plotted in Fig. 5.2.7(b).

The following equation was used to fit the signal at the E1HH1 and E1LH1 transition energies

$$S(x) = A \exp\left(\frac{x}{B}\right) \sin\left(\frac{2\pi x}{C} + D\right) + E \exp(xG) + F \quad (5.2.1)$$

Fitting Parameter	E1HH1 Fitting Value	E1LH1 Fitting Value
A	$3.3 \times 10^4 \pm 0.2 \times 10^4$	2584 ± 1800
B	172 ± 8 fs	136 ± 60 fs
C	226 ± 3 fs	223 ± 30 fs
D	2.2 ± 0.8 rad	2.3 ± 0.9 rad
E	$9.5 \times 10^4 \pm 0.1 \times 10^4$	4595 ± 1200
F	74.8 ± 50	65 ± 60
G	241 ± 5 fs	188 ± 40 fs

Table 5.6: The values returned after fitting Eq. 5.2.1 to the FWM signals from the E1HH1 and E1LH1 transitions. The fitting parameters are as follows: A - initial beat amplitude, B - lifetime of the beating signal (fs), C - beat period (fs), D - beat phase offset (rad), E - initial amplitude of the FWM signal, G - lifetime of the FWM signal (fs) and F - offset to the signal background.

where A is the starting beat amplitude, B is the lifetime of the beating, C is the beat period, D is a phase offset, E is the initial amplitude of the FWM signal in the absence of beating, G is the lifetime of the FWM signal, and F is the signal offset relative to any background signal. The delay, x , is negative. The fits for Eq. 5.2.1 to the E1HH1 and E1LH1 signals are included in Fig. 5.2.7(b). The fitting parameters are given in Table 5.6. The data was fit for $\tau \leq -120$ fs so the fit was not be distorted by the coherence spike which occurs whilst the excitation pulses are temporally overlapped. The emission from E1HH1 shows strong oscillations with a beat period of 226 ± 3 fs. The E1LH1 transition is fit with a beat period of 223 ± 30 fs. The large error for the beat period fit to E1LH1 is due to the weak signal from this transition. The beat periods for the E1HH1 and E1LH1 transitions correspond to a difference in transition energy of 18.3 ± 0.3 meV and 18.54 ± 3 meV respectively, which are equal to the energy difference between the two transitions of 17 ± 1 meV, confirming that the beating is the result of the E1HH1 and E1LH1 transitions being coherently coupled.

The FWM signal for E1HH1 decays with a time constant of 241 ± 5 fs. Without time resolving the FWM signal it is uncertain if the FWM signal is a free polarisation decay (FPD) or a photon echo (PE). It is therefore uncertain if the decoherence time (T_2) is 482 fs or 964 fs. It is interesting to note that the amplitude of the beats on the E1HH1 signal decays with a lifetime of 172 ± 8 fs, which is shorter than the decoherence time of the FWM signal. This decay lifetime matches the decoherence time fit to the E1LH1 signal ($188.7 \pm$

40 fs), suggesting that the decoherence time of the E1LH1 exciton is limiting the duration of the beat signal observed on the E1HH1 exciton. This may be due to the larger Bohr radius of the E1LH1 exciton, which would give the E1LH1 exciton an increased probability of interacting with impurities and defects. An alternative explanation for the increased rate of decay of the beat amplitude on E1HH1 is that the inhomogeneous linewidths of the HH and LH excitons are not identical. Whilst the HH and LH will be exposed to the same monolayer fluctuations of the well width, the variation of the LH energy with well width is greater than for the HH due to the differences in their effective masses. A difference in inhomogeneous linewidths has been shown to lead to a damping of the beat amplitude in time-integrated FWM experiments [167]. Furthermore, if the fluctuations in the energy of the E1HH1 and E1LH1 excitons is not correlated, this could also lead to a damping of the beat amplitude [167].

The 2DFT spectrum for the data in Fig. 5.2.7(a) is shown in Fig. 5.2.8. The 2DFT spectrum is plotted for the rephasing portion of the FWM signal, that is, for coherence time signals where \mathbf{k}_2 is incident on the sample first (this signal is detected in the direction $-\mathbf{2k}_1+\mathbf{k}_2$). In this two-pulse FWM experiment and for the timing convention used, the signal components for positive τ do not correspond to coherence and are excluded. In Fig. 5.2.8, two well defined peaks are observed at the emission energy of 1.575 eV and at the absorption energies of 1.575 eV and 1.591 eV. Two weaker peaks are observed at the emission energy of 1.592 eV and absorption energies of 1.578 eV and 1.592 eV. The on-diagonal peaks indicate the absorption and emission of light at the same energy for the E1HH1 and E1LH1 transitions. As only the rephasing portion of the FWM signal is used to generate the 2DFT spectrum, the on-diagonal peaks are not elongated along the diagonal. For this reason the peak shape is not analysed. The off-diagonal peaks, corresponding to absorption and emission at different energies, suggest that the E1HH1 and E1LH1 transitions are coupled. As mentioned in Chap. 3, population transfer may also lead to cross-peaks in 2D spectra. In this case where $T = 0$, it is unlikely that significant population transfer between the E1HH1 and E1LH1 excitons could have occurred within the pulse overlap given that the pulse duration is 60 fs and population transfer, which occurs during the period T , is expected

to occur on a picosecond timescale at these temperatures [168]. It is therefore likely that the cross-peak represents coherent coupling between E1HH1 and E1LH1. Besides the peak shapes not being diagonal, the 2D spectrum in Fig. 5.2.8 is typical of what is expected from coupled E1HH1 and E1LH1 excitons [36, 45].

Clearly present in the 2DFT spectrum is an elongated signal along the absorption energy axis at emission energies equal to the E1HH1 and E1LH1 transitions. The source of this signal is the strong coherence spike in the SR-FWM data which occurs when the excitation pulses are temporally overlapped. The duration of the spike is limited to the autocorrelation of the excitation pulses. This introduces a comparatively short-lived signal at $\tau = 0$ into the $E_T(\omega_t, \tau)$ data. The Fourier transform, with respect to τ , of this signal component in $E_T(\omega_t, \tau)$, effectively reproduces the bandwidth of the excitation laser. As the laser bandwidth is much broader than the linewidth of the exciton transitions, an elongated signal along the ω_τ axis is observed in the 2DFT spectrum. Whilst the presence of the strong elongated signal in this case complicates the 2DFT spectrum, the position of the on and off diagonal peaks is preserved.

The beating between heavy-hole and light-hole excitons in semiconductors has been studied extensively [23, 45, 138, 169]. Due to the large wavefunction overlap of the E1, HH1 and LH1 subbands, the beating signals due to this interaction dominate the FWM signals when both E1HH1 and E1LH1 exciton transitions of the same QW are coherently excited. By selectively exciting exciton transitions it is possible to reduce the occurrence of this interaction, which in some circumstances may simplify the detected FWM signal and allow other more subtle effects to be observed.

5.2.4 Free-carrier continuum contribution to coherent dynamics

In this section, the contribution of the free-carrier continuum to the coherent dynamics of excitons is examined. A diagram representing the transition energies for the E1HH1, E1LH1, E2HH2 and E2LH2 excitons in the set 1 samples is shown in Fig. 5.2.9. If it is assumed that

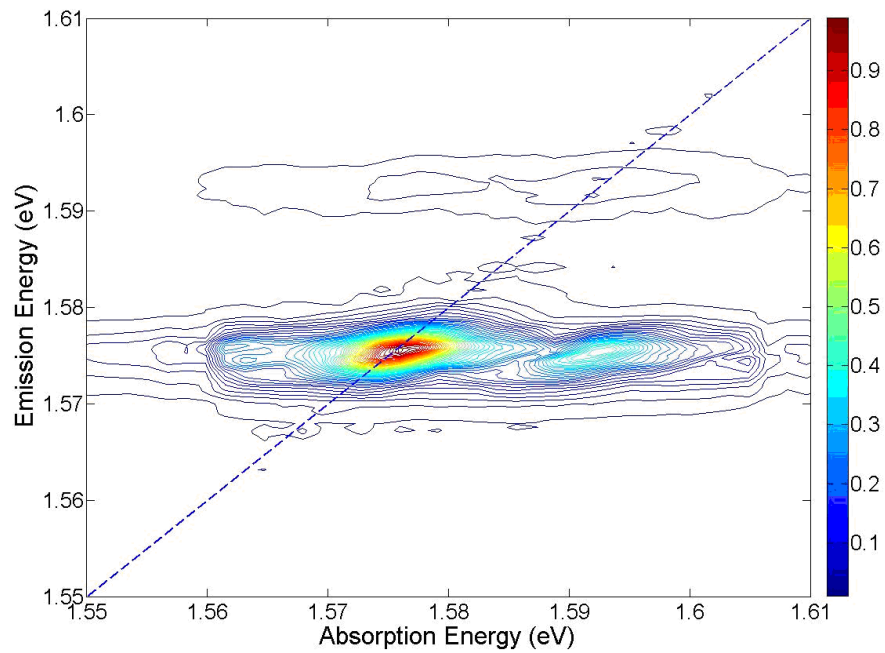


Figure 5.2.8: 2DFT spectra for S1-20 excited at 1.577 eV. Strong cross-peaks are resolved for the E1HH1 and E1LH1 transitions.

the maximum binding energy for each of these excitons will be less than 10 meV [160], given that there is ~ 15 meV separation between the E1HH1 and E1LH1 transitions, the E1LH1, E2HH2 and E2LH2 exciton transitions will all be resonant with the E1HH1 free-carrier continuum. It is therefore reasonable to expect that if the excitation energy is resonant with

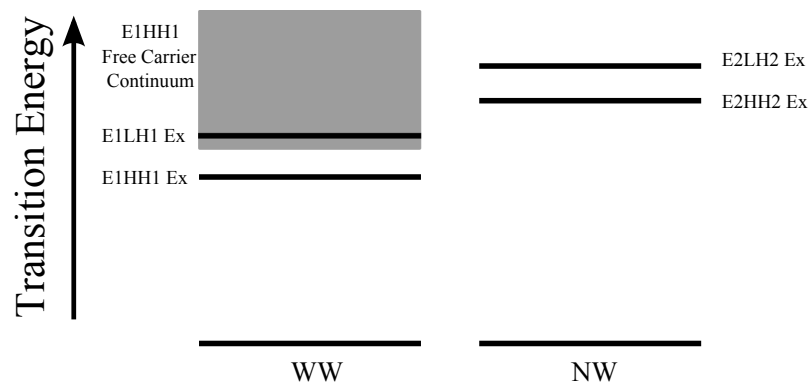


Figure 5.2.9: Comparison of the E1HH1, E1LH1, E2HH2 and E2LH2 transition energies. The E1LH1, E2HH2 and E2LH2 transitions are resonant with the E1HH1 free-carrier continuum.

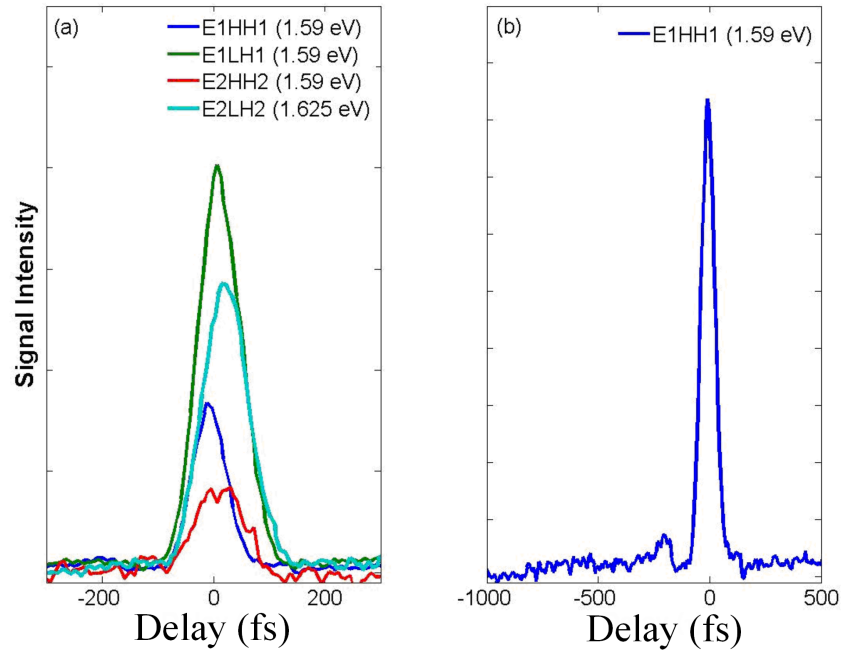


Figure 5.2.10: (a) Spectrally-integrated FWM signal from E1HH1, E1LH1 and E2HH2 for excitation at 1.59 eV, and E2LH2 for excitation at 1.625 eV. Each exciton appears to dephase rapidly. (b) A weak extended signal is observed from the E1HH1 transition in the negative delay direction. In both (a) and (b) the delay corresponds to τ .

the E1LH1 transition, the free-carrier continuum states for the E1HH1 transition are also excited. This has a very dramatic effect on the coherent dynamics of the mentioned excitons.

The free-carrier continuum interaction in sample S1-2 is examined using a two-pulse FWM experiment. The spectrally-integrated FWM signals from the E1HH1, E1LH1, E2HH2 and E2LH2 excitons are plotted in Fig. 5.2.10(a). In these measurements the excitation spectrum had a FWHM of 20 meV. The FWM signals from E1HH1, E1LH1 and E2HH2 were recorded with the excitation centred on the E1LH1 exciton (1.59 eV). The appearance of each FWM signal is much like the autocorrelation of two 100 fs pulses. The FWM signal from the E2LH2 exciton was recorded in a separate measurement with the excitation spectrum centred at 1.625 eV, approximately midway between the E2HH2 and E2LH2 exciton transitions. Similarly, no extended signal was observed from E2LH2 and E2HH2 (E2HH2 FWM signal from the second measurement is not shown).

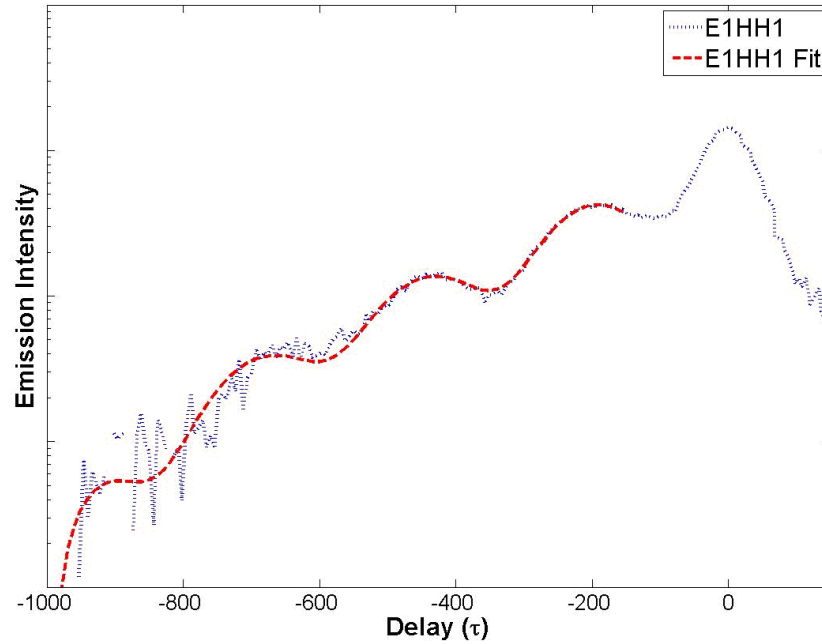


Figure 5.2.11: Beating between the E1HH1 and E1LH1 excitons in sample S1-2.

In contrast to the results shown in Fig. 5.2.10(a), if the E1HH1 and E1LH1 transitions were excited with the excitation spectrum centred on E1HH1, an extended signal was observed from E1HH1. The spectrally-integrated signal from E1HH1 in that case is plotted in Fig. 5.2.11. A fit to this signal using Eq. 5.2.1 is also shown. As was observed from sample S1-20 in Sec. 5.2.3, coherently exciting the E1HH1 and E1LH1 transitions produces a strong beating signal on the E1HH1 transition. In the present case a strong beating signal is also observed. From the fit the beat period is determined to be 244 ± 3 fs, which corresponds to an energy difference of 16.9 ± 0.2 meV. The beat period matches the energy difference of the E1HH1 and E1LH1 transitions (17.1 ± 0.3 meV) and is attributed to HH-LH beating.

There are several interactions which may contribute to this observed behaviour. Honold et al. showed that for carrier densities in the range $1 \times 10^9 - 2 \times 10^{10}$ cm⁻², free carriers are more effective in dephasing coherent excitons than exciton-exciton scattering [170]. The excitation density in the present case is 1×10^{11} photons cm⁻², which should put us near this density range. However, this carrier density is not expected to lead to rapid dephasing and a

FWM signal with a duration limited to the overlap of the excitation laser pulses. Free-carrier scattering alone, at these carrier densities, cannot explain the signal shown in Fig. 5.2.10(a).

It has also been shown that when a E1LH1 exciton is resonant with the E1HH1 free-carrier continuum, the E1LH1 exciton dephases 8 - 20 times faster than when it is not resonant with the continuum [171]. Gopal et al. suggested that this was due to auto-ionisation of the E1LH1 exciton. Again, this did not result in a FWM signal that appeared to be pulse-width limited.

FWM signals essentially limited to the temporal width of the excitation laser, when the exciton and free-carrier continuum states are coherently excited, have been observed in experiments by Cundiff et al. [27], Birkedal et al. [26] and Wehner et al. [28]. Cundiff et al. [27] suggest that this effect is due to quantum interference between exciton and free-carrier continuum states, which leads to the rapid decay of the FWM signal. If the bandwidth of the continuum is larger than the pulse bandwidth, the duration of the FWM signal will be pulse width limited. The calculations for S1-2 in Sec. 5.2.1 showed that the E, HH and LH wavefunctions extend through the barrier separating the two QWs, suggesting that in this case the E1LH1, E2HH2 and E2LH2 excitons are spatially and energetically overlapped with the E1-HH1 continuum. There are no publications that have reported the observation of exciton-continuum interactions within double QW structures; however, one would expect that the strength of this interaction is dependent on the overlap of the E, HH and LH wavefunctions with the free-carrier continuum. This dependence on wavefunction overlap with the E1HH1 continuum is observed in the experimental results. In the previous section (Sec. 5.2.3), an extended FWM signal was observed from the E2HH2 exciton, where the E2HH2 is resonant with the E1HH1 free-carrier continuum. In that experiment the E2HH2 exciton was resonantly excited, meaning that the E1HH1 free-carrier continuum was also resonantly excited. However, the coherent dynamics for the E2HH2 exciton were not noticeably affected. In that case the spatial separation of the E2HH2 exciton from the E1HH1 continuum prevented their interaction. In the present case, the FWM signals for each of the bright excitons decay rapidly, suggesting quantum interference between the bright excitons

and the E1HH1 free-carrier continuum is dominating the coherent response of the bright excitons.

Birkedal et al. [26] showed that in experiments where the E1HH1 exciton and free-carrier continuum are coherently excited, the FWM signal should actually be made up of two components; a prompt component which is pulse-width limited due to interference between excitons and the free-carrier continuum, and a component that has a slower decay lifetime, which decays at the same rate as excitons that are not interacting with the continuum states. On closer inspection of the signals in Fig. 5.2.10(a), a weak signal extended in the negative time direction is observed from E1HH1, which is shown in Fig. 5.2.10(b). No extended signal is observed from the E1LH1, E2HH2 or E2LH2 transitions. Free-carrier scattering will also contribute to the dephasing of all the excitons [170]; however, it does not account for why no extended signal is observed from E1LH1, E2HH2 and E2LH2. As E1LH1, E2HH2 and E2LH2 are resonant with the E1HH1 free-carrier continuum, in addition to dephasing due to free-carrier scattering, they may also be experiencing a dephasing interaction similar to the observations of Gopal et al. [171].

The results in this section indicate that the coherent response of the bright exciton states in these samples will be completely dominated by exciton-continuum interactions when the exciton state wavefunctions overlap with the E1HH1 free-carrier continuum and both are coherently excited. Without further investigation it is uncertain whether free-carrier scattering and auto-ionisation are also contributing to the observed dynamics. Nonetheless, it is clear that the effect of co-exciting exciton and continuum states in these samples needs to be considered when examining experimental results in later sections.

5.2.5 Peak shift

In Sec. 5.2.3 and Sec. 5.2.4, coherently co-exciting the bright HH and LH exciton transitions localised to the same QW was shown to produce strong quantum beating on the HH and LH FWM signals. By exciting the HH exciton without exciting the LH exciton, it is possible to

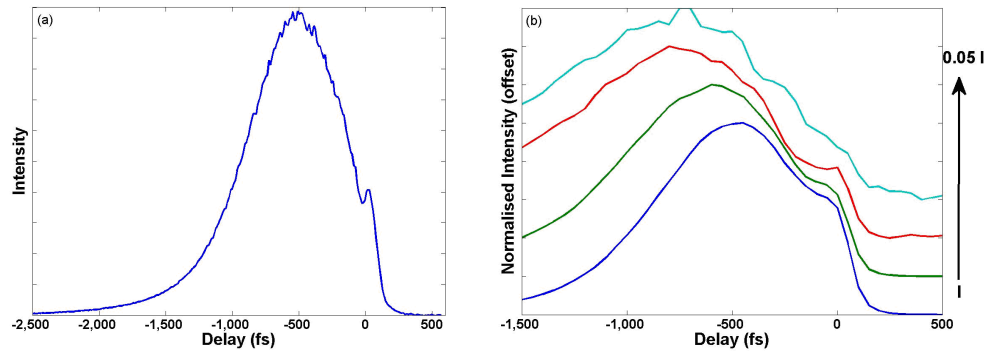


Figure 5.2.12: Peak shift in sample S1-6. Delay corresponds to coherence time, τ . (a) The non-exponential FWM signal observed from the E2HH2 exciton. (b) Fluence dependence shows that for reduced excitation fluences, the delayed maximum shifts further away from $\tau = 0$.

observe the FWM signal from the HH exciton without HH-LH beating contributing to the signal, simplifying the signal dynamics. This is particularly useful when trying to examine subtle features in the FWM signal. In the present experiment, two-pulse FWM is used to examine sample S1-6. The excitation laser was centred on the low energy side of the E2HH2 exciton so as to not co-excite the E2LH2 exciton. The excitation pulses were 100 fs long and had a FWHM of 20 meV. The time-integrated FWM signal from the E2HH2 exciton is plotted in Fig. 5.2.12(a). A strong and extended FWM signal is observed from the E2HH2 exciton. This signal shape is unlike the signal observed for the same transition in sample S1-2, where no extended signal was observed due to the E2HH2 exciton interacting with the E1HH1 free-carrier continuum. The strong and extended FWM signal indicates there is no significant interaction between E2HH2 and the E1HH1 free-carrier continuum in sample S1-6. The absence of this interaction suggests the E2 and HH2 wavefunctions are localised to the narrow QW and the E1 and HH1 free-carrier continuum is localised to the wide QW, which is consistent with the calculations presented earlier in this chapter.

Clearly present in the FWM signal in Fig. 5.2.12(a), following pulse overlap at $\tau = 0$, is a slow rise which reaches a maximum for an inter-pulse delay of 500 fs and decays almost to zero over the following 2 ps. A delayed maximum, known as a peak shift, is expected in the time integrated FWM signal if the FWM emission is a photon echo (PE) [172]. The peak shift

occurs in time-integrated FWM experiments as a result of the real time PE emission being clipped, which in turn reduces the time-integrated PE signal. The peak shift is proportional to the temporal width of the PE, which is inversely proportional to the inhomogeneous linewidth of the transition, and the dephasing time, which is inversely proportional to the homogeneous linewidth.

The excitation fluence dependence of the time integrated signal is shown in Fig. 5.2.12(b). As the fluence is increased, the FWM signal shortens and the position of the delayed maximum shifts towards $\tau = 0$. This response is attributed to the excitation density dependence of the homogeneous linewidth, where, for increased excitation fluence the homogeneous linewidth broadens, resulting in a shorter decoherence time. A similar time integrated FWM signal and fluence dependence has been observed previously by Erland et al. [172, 173]. The authors showed that such a time-integrated FWM signal may be described by the following function,

$$P_{inh}^{(3)}(\tau, \omega) \propto 4iNM_{21}^4 \frac{\sqrt{\pi \ln 2}}{\Gamma} e^{i2\omega\tau} e^{-2\gamma_{21}\tau} \exp\left[-4\ln 2 \frac{(\omega_{21}^c - \omega)^2 - \gamma_{21}^2}{\Gamma^2}\right] \\ \times \exp\left[-i8\ln 2 \frac{(\omega_{21}^c - \omega_{21})\gamma_{21}}{\Gamma^2}\right] \operatorname{erfc}\left[2\sqrt{\ln 2}\left[\frac{\gamma_{21}}{\Gamma} - \frac{\Gamma\tau}{8\ln 2} + i\frac{\omega_{21}^c - \omega}{\Gamma}\right]\right] \quad (5.2.2)$$

where Γ is the inhomogeneous linewidth, γ_{21} is the homogeneous linewidth, ω_{21}^c is the centre frequency of the transition, ω is the frequency detected at the spectrometer, N characterises the excitation density, M_{21} is the dipole matrix element and τ is the delay between the two pulses. The time-integrated FWM signal represented by Eq. 5.2.2 is dominated by two terms; firstly, an exponential decay with a lifetime determined by the homogeneous linewidth, and secondly, a rise given by an error function, which only contributes to the signal significantly for $\tau < 1/\Gamma$ and when the inhomogeneous linewidth closely matches the homogeneous linewidth.

Erland et al. [173] and Hvam et al. [174] suggest that exciting the low energy side of an exciton transition predominantly excites the localised tail of the exciton line profile,

and under these excitation conditions the homogeneous and inhomogeneous linewidths may have similar values. This suggestion is based on the work of several groups that have shown there is a so called ‘mobility edge’ near the centre of the exciton absorption linewidth which separates localised and mobile exciton states [175–177]. In general, excitons are free to move within the plane of the QW; however, small fluctuations in width of the QW can cause excitons to become localised. These localised states have a lower transition energy than mobile exciton states and exist on the low energy side of the exciton line [175]. The homogeneous linewidth of localised excitons has been shown to be much narrower than delocalized excitons, which is due to fewer interactions with their environment [178, 179]. If the photon energy of the excitation source can change the ratio of inhomogeneous to homogeneous linewidth and hence the peak shift in the time integrated FWM signal, as suggested by Erland et al. [173] and Hvam et al. [174], it is important to characterise this effect. In the following experiment the excitation energy dependence of the time-integrated FWM signal was investigated. In this experiment sample S1-6 is again used. The centre photon energy of the exciting laser was tuned from 1.587 eV, well below the E2HH2 transition, to 1.624 eV, which is midway between transition energies for the E2HH2 and E2LH2 excitons. The excitation pulses were 100 fs long with a FWHM of 20 meV. In Fig. 5.2.13(a), the spectrally-integrated signal from the E2HH2 transition is plotted normalised to the signal intensity at the delayed maximum for each excitation energy. In Fig. 5.2.13(b), spectrally-integrated E2HH2 signals are plotted for excitation approximately resonant with the E2HH2 transition, and for excitation centred approximately 10 meV either side of the E2HH2 transition. In Fig. 5.2.13(c), the spectrally resolved FWM signals for the E2HH2 transition are plotted, from which the data in Fig 5.2.13(a) and Fig 5.2.13(b) was taken.

The results in Fig. 5.2.13(a) and Fig. 5.2.13(b) show that as the excitation energy was shifted from 1.587 eV to approximately resonant with the E2HH2 transition (1.612 eV), the delayed maximum shifted towards $\tau = 0$. As the excitation energy was shifted further to the blue of the E2HH2 transition, the delayed maximum continued to shift towards $\tau = 0$. Because the laser also resonantly excited the E2LH2 transition, the bright LH exciton

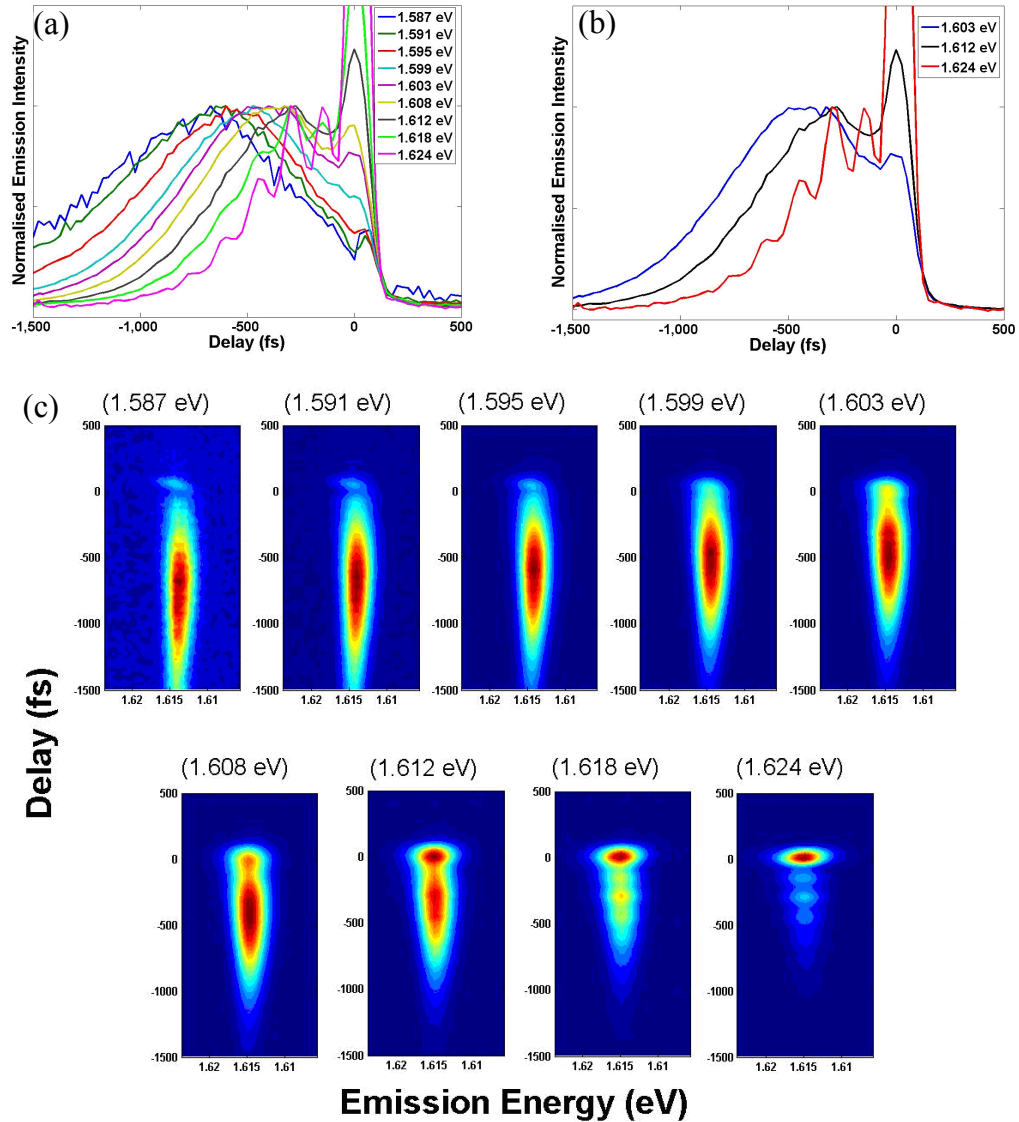


Figure 5.2.13: The excitation photon energy dependence of the FWM signal from the E2HH2 transition for sample S2-6. (a) Plots of the spectrally-integrated FWM signal, normalised to the delayed maximum, for different centre excitation energies. (b) Plots of the spectrally-integrated FWM signal for excitation energies approximately resonant with this transition and approximately 10 meV to the blue and red of this transition. (c) The SR - FWM signals for E2HH2 for each excitation energy from which the data presented in (a) and (b) was taken.

localised to the same QW as the E2HH2 exciton, strong quantum beats are present on the E2HH2 FWM signal. The shift of the delayed maximum suggests a change in the homogeneous and/or the inhomogeneous linewidth/s of the E2HH2 exciton as the excitation energy is tuned across the E2HH2 transition. When the laser is shifted from being off-

resonant to fully resonant with the E2HH2 transition, it is reasonable to suggest that larger carrier densities are generated within the QW, broadening the homogeneous linewidth and reducing the decoherence time. However, at the same time, shifting the excitation energy from the low energy side of the exciton transition to the high energy side will excite more of the delocalised exciton states, increasing the inhomogeneous linewidth of the excited exciton ensemble. The increase in the inhomogeneous linewidth reduces the temporal width of the PE and will shift the peak of the delayed maximum towards $\tau = 0$. If the shift of the delayed maximum was entirely due to changes in the homogeneous linewidth, one would expect that as the excitation energy was shifted from resonant with the E2HH2 exciton to higher energies, the homogeneous linewidth would narrow and the delayed maximum would shift away from $\tau = 0$. This effect is not observed in the results, as shown in Fig. 5.2.13(b), suggesting changes in both the homogeneous and inhomogeneous linewidths are contributing to the observed shifting.

The peak shift appears to varying degrees in the FWM signal from each of the samples. For the same excitation conditions the peak shift is most apparent in S1-6, suggesting that this sample is the most homogeneous. The variation of this effect from sample to sample reflects the limitations of MOCVD semiconductor growth techniques to produce exactly identical samples.

5.2.6 Disorder

In QWs, the width of the well can sporadically fluctuate from its intended design by a single unit cell of the barrier material. In addition to this, composition fluctuations in the well and barrier materials produce deviations in the QW potential profile throughout the QW plane. These effects are usually referred to as disorder and typically determine the inhomogeneous linewidths of excitons. As described previously, variation in the width of the QW leads to localised regions in the QW plane with lower potential energy where excitons can become trapped [37]. A diagram of an exciton localised by monolayer fluctuations is shown in Fig. 5.2.14. Whilst excitons can typically move freely within the QW plane, excitons can

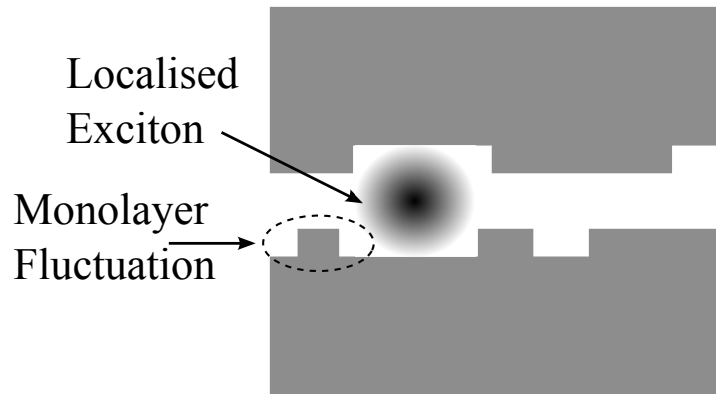


Figure 5.2.14: An exciton localised by monolayer fluctuations within a disordered QW.

become trapped in the lowest energy regions. Localised excitons contribute to the lower energy side of the exciton linewidth, whilst the delocalised excitons contribute to the high energy side, leading to so called ‘mobility edge’ effects [175, 176]. The localisation of excitons reduces the interaction between excitons and their environment, producing narrower homogeneous linewidths, and therefore longer decoherence times, than delocalised excitons.

The coherent response of excitons may be used to explore disorder. In a three-pulse FWM experiment, if during the waiting time (T) the transition energy of excitons change, the ability of the system to form a PE is reduced. The shift in energy is typically known as spectral diffusion. Plotting the peak shift of the FWM signal as a function of waiting time, T , allows one to track the ability of the system to form a PE. It has been shown that spectral diffusion as the result of exciton migration between points of localisation is assisted by acoustic phonons [177, 179, 180]. The rate of spectral diffusion has been shown to exhibit a strong temperature dependence [181]. At higher temperatures, the rate of spectral diffusion is increased due to the thermal excitation of localised excitons to delocalised states. As disorder promotes spectral diffusion, an examination of spectral diffusion allows one to characterise the disorder within QWs.

In this section the coherent response of excitons is used to explore the role of disorder. This investigation will provide further characterisation of the coherent response of the samples used for the investigation presented in Sec 5.3, as well as additional commentary on the effects of disorder on the coherent response of excitons. In the present investigation

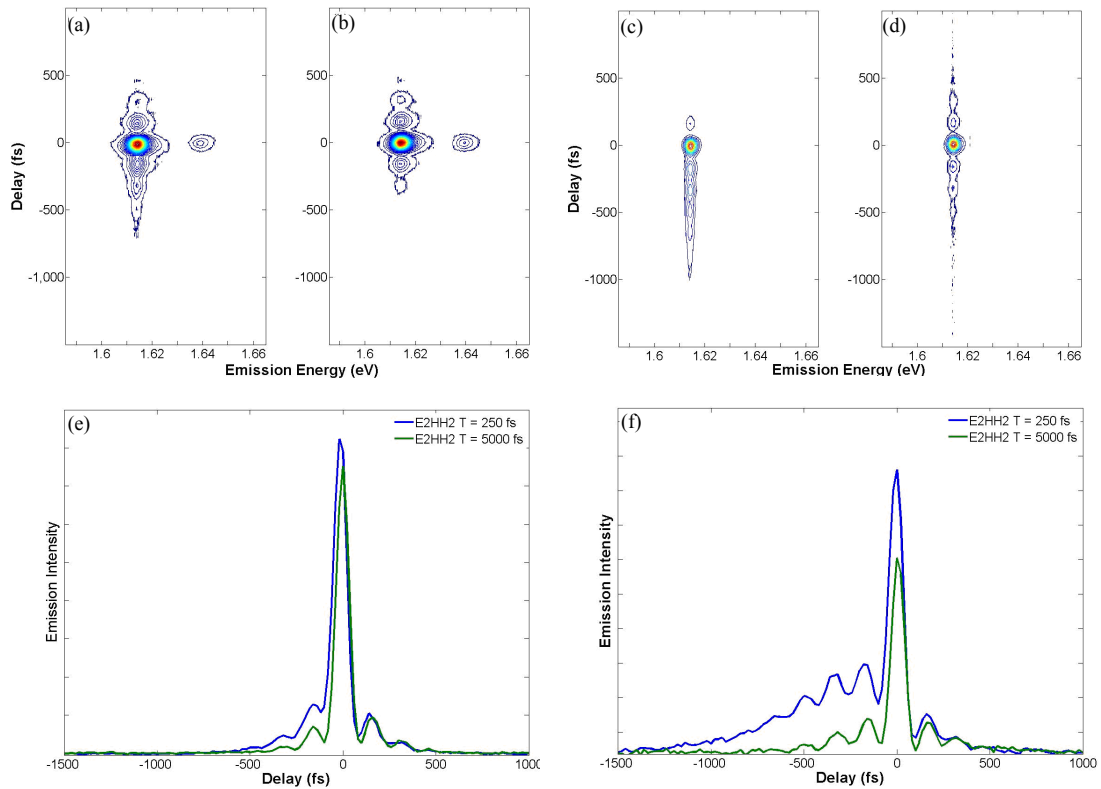


Figure 5.2.15: Spectrally resolved 3-pulse FWM signals from S1-6, for waiting times (T) of 250 fs and 5000 fs and for excitation fluences, I , are shown in (a) and (b), respectively. The signals at 1.612 and 1.638 eV are from the E2HH2 and E2LH2 transitions, respectively. The measurements made in (a) and (b) were repeated with an excitation fluence of $0.25I$ and are shown in (c) and (d). In (e) and (f), the spectrally-integrated E2HH2 signals for fixed waiting times of 250 fs and 5000 fs are shown for excitation fluences I and $0.25I$, respectively.

sample S1-6 is examined. The E2HH2 and E2LH2 excitons, with transition energies of 1.612 eV and 1.638 eV respectively, were coherently excited by a laser centred on the blue side of E2HH2 at 1.615 eV. The FWHM of the excitation spectrum was 20 meV and the pulse duration was 100 fs. Measurements were made with excitation fluences of I , $0.4I$, $0.25I$ and $0.1I$, where $I = 1 \times 10^{11}$ photons cm^{-2} per pulse. The spectrally resolved signals from the three-pulse FWM experiment, for fixed waiting times of 250 fs and 5000 fs and for an excitation fluence I , are shown in Fig. 5.2.15(a) and Fig. 5.2.15(b), respectively. Fig. 5.2.15(c) and Fig. 5.2.15(d) show the spectrally resolved FWM signal for an excitation fluence of $0.25I$ and for fixed waiting times of 250 fs and 5000 fs, respectively. In Fig. 5.2.15(a) and Fig. 5.2.15(b), the signal from the E2HH2 transition is much stronger than

Fluence	Beat Period ($\tau < 0$)		Beat Period ($\tau > 0$)	
	T = 250 fs	T = 5000 fs	T = 250 fs	T = 5000 fs
1	166 ± 4	164 ± 8	165 ± 7	156 ± 4
0.4	163 ± 3	162 ± 6	156 ± 5	166 ± 6
0.2	160 ± 8	174 ± 6	153 ± 12	148 ± 12
0.1	167 ± 3	183 ± 40	176 ± 18	152 ± 6

Table 5.7: The beat periods fit to the E2HH2 FWM signals using Eq. 5.2.1 given for both the rephasing and non-rephasing pulse directions. The beat periods effectively fluctuate from 165 fs to 155 fs, representing a transition energy difference of 25 meV to 26.7 meV. This is equal to the energy difference between the E2HH2 and E2LH2 excitons, which is 26 meV.

that from the E2LH2 transition. This is due to a combination of two factors; firstly because the centre of the excitation spectrum is closer to the E2HH2 transition, and secondly the E2HH2 exciton has a larger oscillator strength than the E2LH2 exciton. When the excitation fluence is reduced to 0.25I the signal from the E2LH2 exciton is too weak to analyse. For this reason the analysis in this section is focused on the coherent dynamics of the E2HH2 exciton. Spectrally-integrated plots of the signal from the E2HH2 transition for both fixed delays are shown in Fig. 5.2.15(e) and Fig. 5.2.15(f) for the excitation fluences I and 0.25I, respectively.

Immediately evident in the spectrally resolved and the spectrally-integrated plots in Fig. 5.2.15 is the beating in the FWM signal. Both the E2HH2 and E2LH2 transitions are coherently excited in this measurement. The beats evident in Fig. 5.2.15 are present for each excitation fluence and waiting time used. The beat periods were fit to the E2HH2 FWM signals using Eq. 5.2.1 and are listed in Table 5.7. The period fit to the observed beats ranges from 165 fs to 155 fs. This corresponds to a transition energy difference of 25 meV to 26.7 meV, which is equal to the energy difference between the E2HH2 and E2LH2 transitions of 26 meV, indicating that these two transitions are coupled, as expected.

The decoherence times, which were fit using Eq. 5.2.1, are given in Table 5.8. Each data set was fit from the first beat maximum in order to exclude any contribution from the coherence spike that occurs whilst the excitation pulses are overlapped. For the signals where the peak shift is clearly present, the fit was made to the region following the delayed

Fluence	Decay Time Constant ($\tau < 0$)		Decay Time Constant ($\tau > 0$)	
	T = 250 fs	T = 5000 fs	T = 250 fs	T = 5000 fs
1	165 ± 6	122 ± 12	135 ± 10	145 ± 15
0.4	279 ± 10	161 ± 15	162 ± 13	155 ± 20
0.2	<i>365 ± 30</i>	236 ± 35	154 ± 25	258 ± 70
0.1	<i>387 ± 20</i>	121 ± 32	150 ± 50	370 ± 200

Table 5.8: The fluence and waiting-time dependent decay time constants fit to the FWM signal of E2HH2 for rephasing ($\tau < 0$) and non-rephasing ($\tau > 0$) pulse ordering. The *italic* values indicate the fit was made to a FWM signal where a delayed maximum was observed. In these cases the decay lifetime is fit to the region following the delayed maximum. All of the remaining fits are made from the first beat maximum in order to exclude any contribution from the coherence spike.

maximum. For measurements where $T = 0$, the decoherence time for rephasing and non-rephasing pulse ordering can provide direct access to the homogeneous and inhomogeneous linewidths. For $T \neq 0$, these values do not directly correspond to the linewidths, but changes to these values will nevertheless provide valuable insight into the coherent dynamics.

A fluence and T dependence of the FWM signal is clearly observed in Fig. 5.2.15(e) and Fig. 5.2.15(f). Most apparent is the extension and the increase in amplitude of the signal for rephasing pulse ordering ($\tau < 0$) as the excitation fluence is reduced. It is also evident that as the waiting time is increased from 250 fs to 5000 fs, the signal for rephasing pulse ordering decreases. The unusual shape of the FWM signal in Fig. 5.2.15(f) for $T = 250$ fs is due to peak shift, which was discussed in detail in Sec. 5.2.5. The decay lifetimes for both the rephasing and non-rephasing directions, as a function of excitation fluence, are shown in Table 5.8. As the excitation fluence was decreased from I to 0.1I for $T = 250$ fs, the decay lifetime of the rephasing FWM signal increased from 165 ± 6 fs to 387 ± 20 fs. This is consistent with a decrease in the homogeneous linewidth due to a decrease in the exciton-exciton and exciton-free carrier scattering rates, which is a well known excitation induced effect within semiconductors [170, 173]. As T was increased from 250 fs to 5000 fs, the decay lifetime in the rephasing direction decreases. Within the experimental uncertainty, the decay lifetime fit to the time period corresponding to rephasing pulse ordering matches the decay lifetime for non-rephasing pulse ordering. This symmetry around $\tau = 0$ after a waiting

time of 5 ps suggests that PEs are no longer able to form due to spectral diffusion [181], and the signal is the result of a free-polarisation decay (FPD) [34]. The loss of the ability of the system to form a PE within a waiting time of 5 ps is significantly shorter than the value recorded by Carter et al. for QW excitons at a temperature of 25 K [181]. In that case, with a three-pulse photon-echo peak-shift measurement, the peak shift was shown to decay with a time constant of 9.7 ps. This suggests that interactions which lead to the loss of a PE within the sample examined in this case are significantly stronger than in the case of Carter et al. [181]. Unfortunately, it is not possible to make specific comparisons between the growth processes used to produce their sample and sample S1-6 because the sample growth method is not given in the publication. The most likely explanation for these observed differences between S1-6 and the sample examined by Carter et al. is that the inhomogeneous linewidth of the E2HH2 exciton within S1-6 is greater than in the sample used by Carter et al. as the result of a higher density of disorder, leading to a faster rate of spectral diffusion.

Within the measured uncertainty, the decay time constant for non-rephasing pulse ordering does not appear to be dependent on the excitation fluence. To observe a fluence dependence for non-rephasing pulse ordering the sample generally needs to be very homogeneous [12, 182]. There is also no T dependence of the decay time constant of the signal in the non-rephasing direction, which is to be expected, since the dynamics of the FPD in the non-rephasing direction are determined by the evolution of the polarisation during the period between the first two excitation pulses.

By plotting the spectrum of the FWM signal from E2HH2 for fixed values of τ in the rephasing direction, one may examine the distribution of homogeneous linewidths within the inhomogeneous linewidth for E2HH2 excitons. The emission spectrum at various coherence time delays for $T = 250$ fs is plotted in Fig. 5.2.16. The fluence in this case is $0.25I$. As the coherence time delay, τ , was increased from 0 to 800 fs in the rephasing direction, the high energy side of the FWM signal disappeared. This indicates that the decoherence time of excitons on the high energy side of the exciton emission spectrum is shorter than excitons on the low energy side of the emission spectrum. This is consistent with previous work

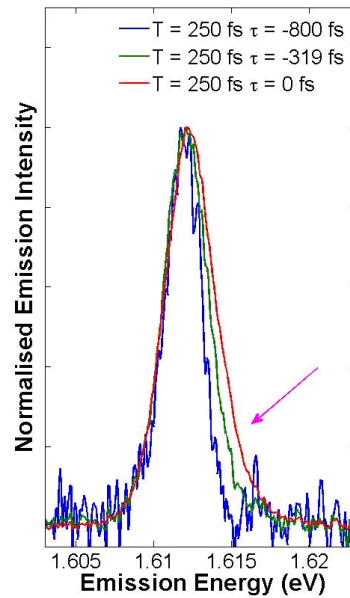


Figure 5.2.16: The FWM spectra for coherence time delays of $\tau = -800$ fs, -319 fs and 0 fs are shown for a waiting time of $T = 250$ fs. The fluence in this case is $0.25I$. At $\tau = -800$ fs, the signal on the high energy side of the E2HH2 signal has decayed much faster than the signal on the low energy side. This is due to the homogeneous linewidth of delocalised excitons being greater than for localised excitons.

by Hegarty et al. [175, 176] which suggests that localised excitons have a much narrower homogeneous linewidth than delocalised excitons and are centred on the low energy side of the exciton transition linewidth. As a result of the different decoherence times across the exciton emission linewidth, the centre frequency of the rephasing FWM signal becomes red-shifted as a function of τ . This may produce a τ dependent energy difference between the E2HH2 and E2LH2 transition energies. Such a shift was recently shown to produce a change in the beat period of HH-LH excitons [183]. In that case, the shift in the beat period suggested that excitons on the low-energy side of the light-hole exciton emission line dephased faster than the excitons on the high energy side, suggesting that the localised LH excitons were higher in energy than the delocalised excitons. Fitting the results in the present experiment with a time dependent beat period could neither convincingly agree or disagree with those conclusions.

The presence and role of disorder within sample S1-6 has been investigated. It was found that spectral diffusion caused the sample to lose the ability to generate a PE within a waiting

time of 5 ps. Given that all of the samples have been grown using the same growth conditions, it is reasonable to expect spectral diffusion will affect the other samples within a similar timeframe. Mobility edge effects were also identified and clearly need to be considered when analysing the decoherence times and linewidths of excitons in later sections.

5.2.7 A note on set 2

As was stated at the beginning of this chapter, two sample sets were designed in order to determine whether coupling between spatially separated states could be mediated by an LO-phonon. The two sets were designed so that in one set the energy difference between the E1HH1 and E2HH2 transitions was equal to the LO-phonon energy, and in the other set the energy difference was not. By determining if the E1HH1 and E2HH2 transitions were coupled in neither, one or both sample sets and how this varied with barrier width, it may be possible to comment on coupling mechanisms within such systems. Unfortunately, in sample set 2, the E1LH1 and E2HH2 transition energies overlap, and consequently are not distinguishable. The overlap of these transitions was not predicted by the calculations, where it was expected that the E1LH1 and E2HH2 transitions would be separated by ~ 11 meV. In the grown samples, the E1LH1 and E2LH2 excitons in set 1 are consistently about 6 - 7 meV lower in energy than their calculated values. The E1HH1 and E2HH2 excitons, however, are much closer to the calculated energies, and are typically within 1-2 meV. In set 2, a red shift of around 7 meV of the E1LH1 would reduce the energy difference between the E2HH2 and E1LH1 states to 4 meV. In addition to this, the oscillator strength of the HH exciton is larger than that for the LH exciton, leading to a stronger signal generated by the E2HH2 exciton. The combination of these two effects makes it difficult to separate the coherent dynamics for these two excitons in spectrally-resolved FWM data.

The issue resolving the E2HH2 and E1LH1 transitions is illustrated by the SR-FWM data presented in Fig. 5.2.17. In this experiment, sample S2-6 is excited by 60 fs pulses with a FWM of 45 meV, centred at 1.612 eV. According to the calculations, peaks are expected at around 1.592 eV, 1.609 eV, 1.622 eV and 1.645 eV, corresponding to E1HH1,

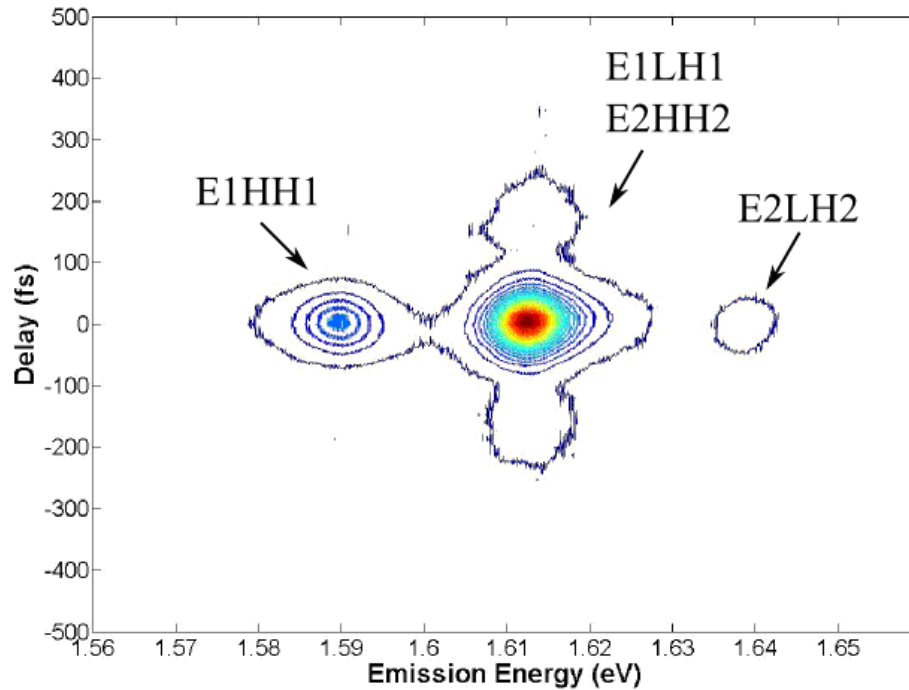


Figure 5.2.17: SR-FWM signal from sample S2-6. The excitation energy is centred at 1.612 eV. The peak centred at 1.589 eV corresponds to the E1HH1 transition, and the peak centred at 1.639 eV is the E2LH2 transition. The emission from the E1LH1 and E2HH2 transitions are overlapped at around 1.612 eV.

E2HH2, E1LH1 and E2LH2. In the measured spectra, the peak at 1.589 eV is attributed to the E1HH1 exciton and the peak at 1.639 eV to the E2LH2 exciton. The FWM signals expected from both of the E1LH1 and E2HH2 transitions are anticipated to occur between the E1HH1 and E2LH2 transitions, however, only one peak can be clearly resolved. No other signals are observed for higher or lower excitation energies, strongly suggesting the above identification of the E1HH1 and E2LH2 transitions is correct and providing further evidence that the E1LH1 and E2HH2 transitions are overlapped at ~ 1.612 eV. On closer inspection in Fig. 5.2.17, there appears to be a shoulder on the high energy side of the peak centred at 1.621 eV, which may be due to the signal from the E1LH1 exciton being slightly higher energy than the E2HH2 exciton, but this is far from clear. As a result, it has not been possible to clearly distinguish signals corresponding to the E1LH1 and E2HH2 excitons, making quantitative analysis difficult and consequently set 2 will not contribute to the discussion later in this section regarding coupling mechanisms.

5.3 Coupling between spatially and energetically separated excitons

In this section, the coherent response of excitons within asymmetric double QWs is examined. The coherent coupling between spatially separated excitons will be the focus of the discussion. Sample set 1 has been designed so that the energy separation between the E1HH1 and E2HH2 excitons is equal to the LO-phonon energy. The coherent dynamics of sample set 1 are examined in Sec. 5.3.1 through the use of a three-pulse FWM experiment. In this experiment the E1HH1 and E2HH2 excitons are coherently and resonantly excited by spectrally broad pulses centred between the two exciton transitions. The SR-FWM signals are analysed using 2DFTS and the results are briefly discussed throughout the section. In Sec. 5.3.3, the Raman-like coherence between the E1HH1 and E2HH2 excitons is examined. The implications of these results will be discussed in detail in Sec. 5.3.4.

5.3.1 Three-pulse FWM and 2DFTS

The first sample examined in this section is S1-4 with the laser centred at 1.595 eV. The excitation pulses were focused to a spot with a diameter of approximately 50 μm with a fluence of 1×10^{11} photons cm^{-2} per pulse. These parameters were constant for all experiments in this section. The excitation pulses had a spectral FWHM of 45 meV and a temporal width of 60 fs. The spectrally resolved FWM signal from this sample is given in Fig. 5.3.1(a). Signals are observed at emission energies of 1.570 ± 0.001 eV, 1.590 ± 0.001 eV and 1.614 ± 0.001 eV, which are attributed to the E1HH1, E1LH1 and E2HH2 excitons, respectively. The energy difference between the E1HH1 and E2HH2 transitions is therefore 44 meV. The emission energies from the E1HH1 and E2HH2 excitons are slightly lower and higher, respectively, than the corresponding values in the low temperature PL measurements (Table 5.4). This is attributed to variations in the sample structure across the GaAs wafer, where different segments of the same wafer have been used in the PL and this

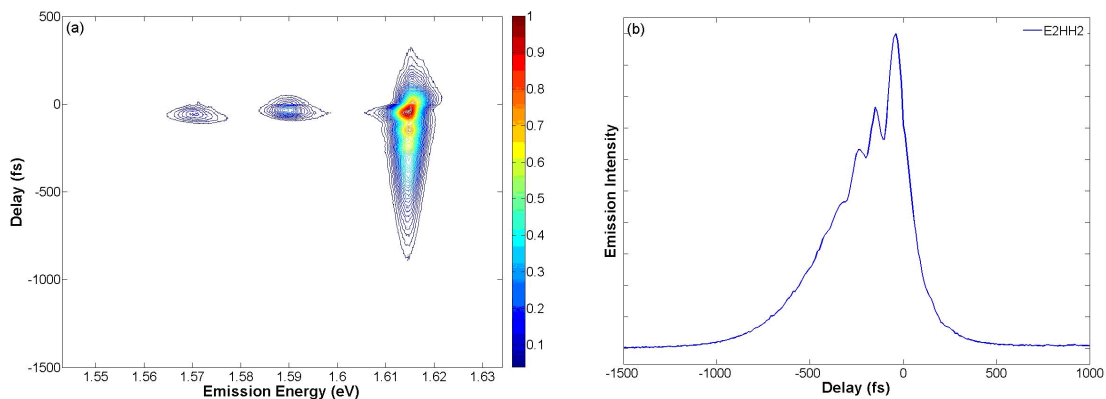


Figure 5.3.1: (a) SR-FWM signal for sample S1-4 as a function of coherence time, τ . The E1HH1, E1LH1 and E2HH2 transitions are coherently excited by broad spectrum pulses centred at 1.595 eV. The waiting time is set to $T = 0$. Strong beating is observed on the emission from the E2HH2 exciton state. (b) Spectrally-integrated (1.604 - 1.624 eV) signal from the E2HH2 exciton state as a function of the interpulse delay, τ .

FWM experiment. Because the energy separation between the E1HH1 and E2HH2 excitons for this sample is greater than planned, it will be difficult to assign any observed dynamics to the involvement of an LO-phonon resonance.

The spectrally-integrated signal from E2HH2 is shown in Fig. 5.3.1(b). The signal corresponding to the rephasing pulse ordering, for $\tau < 0$, is non-exponential and similar in shape to the signals emitted from sample S1-6 in Sec. 5.2.5. This is attributed to peak shift and was discussed in detail in Sec. 5.2.5. Fitting the rephasing signal in Fig. 5.3.1(b) for delay times of $\tau \leq -700$ fs, in order to avoid the contribution from the delayed maximum, gives a decay constant of 180 ± 3 fs and assuming the signal for rephasing pulse ordering is a PE, gives a decoherence time of 720 fs. The signal in the non-rephasing direction decays with a time constant of 102 ± 2 fs. The longer signal decay in the rephasing direction, when compared to the non-rephasing direction, suggests that the signal emitted for $\tau < 0$ is a PE. In addition, the presence of the peak shift requires that the signal emitted for rephasing pulse ordering was a PE.

Beating is observed on the extended signal from the E2HH2 exciton. The beating is clearer on the spectrally-integrated signal shown in Fig. 5.3.1(b). Fitting returns a beat period

of 92 ± 8 fs, which is equal to a transition energy difference of 45 ± 4 meV, suggesting that the beating in this case is due to beating between the E1HH1 and E2HH2 excitons. The amplitude of the beating on the E2HH2 FWM signal ceases well before the extended signal decays to negligible values, suggesting that either the decoherence time of E1HH1 excitons is not the same as E2HH2 excitons, the inhomogeneous linewidths of the E1HH1 and E2HH2 excitons are not the same, the fluctuation in the energy difference between the excitons is not correlated, or a combination of these effects. With E1HH1 and E2HH2 localised to different QWs, it is not unreasonable that the decoherence times of these excitons could be different. In the present case the homogeneous linewidth of the E1HH1 exciton cannot be determined because of the strong free-carrier continuum contribution to the coherent dynamics of the E1HH1 exciton. It is likely that exciting the E1HH1 free-carrier continuum generates free carriers in the wide QW which could scatter with E1HH1 excitons and reduce the E1HH1 decoherence time. The vastly different decay times for the E1HH1 and E2HH2 FWM signals suggests that the E1HH1 free-carrier continuum is either weakly interacting or not-interacting with E2HH2 excitons, implying that the E1HH1 and E2HH2 excitons are highly localised to the wide and narrow QW, respectively, and that the E2HH2 excitons are un-affected by the free carriers. Mismatched inhomogeneous linewidths of the E1HH1 and E2HH2 excitons could also explain the dampening of the beat amplitude [167]. The different inhomogeneous linewidths could arise because the excitons are localised to different QWs of different widths. Alternatively, if the fluctuation of the exciton energies is uncorrelated, a more rapid damping of the beat amplitude, when compared to damping as the result of different inhomogeneous linewidths, is expected [167]. Uncorrelated energies could be expected with E1HH1 and E2HH2 localised to different QWs. Based on the data available, it is unclear which interaction is dominating the observed dynamics.

The 2D spectra for the data shown in Fig. 5.3.1(a) are given in Fig. 5.3.2. The 2D spectrum shown in Fig. 5.3.2(a) includes both the rephasing and non-rephasing components. On-diagonal signals ($\omega_\tau = \omega_t$, where the absorption and emission energies are denoted by ω_τ and ω_t , respectively) are observed for each of the E1HH1, E1LH1 and E2HH2 transitions. The E2HH2 on-diagonal peak is elongated along the diagonal, whilst the E1HH1 and

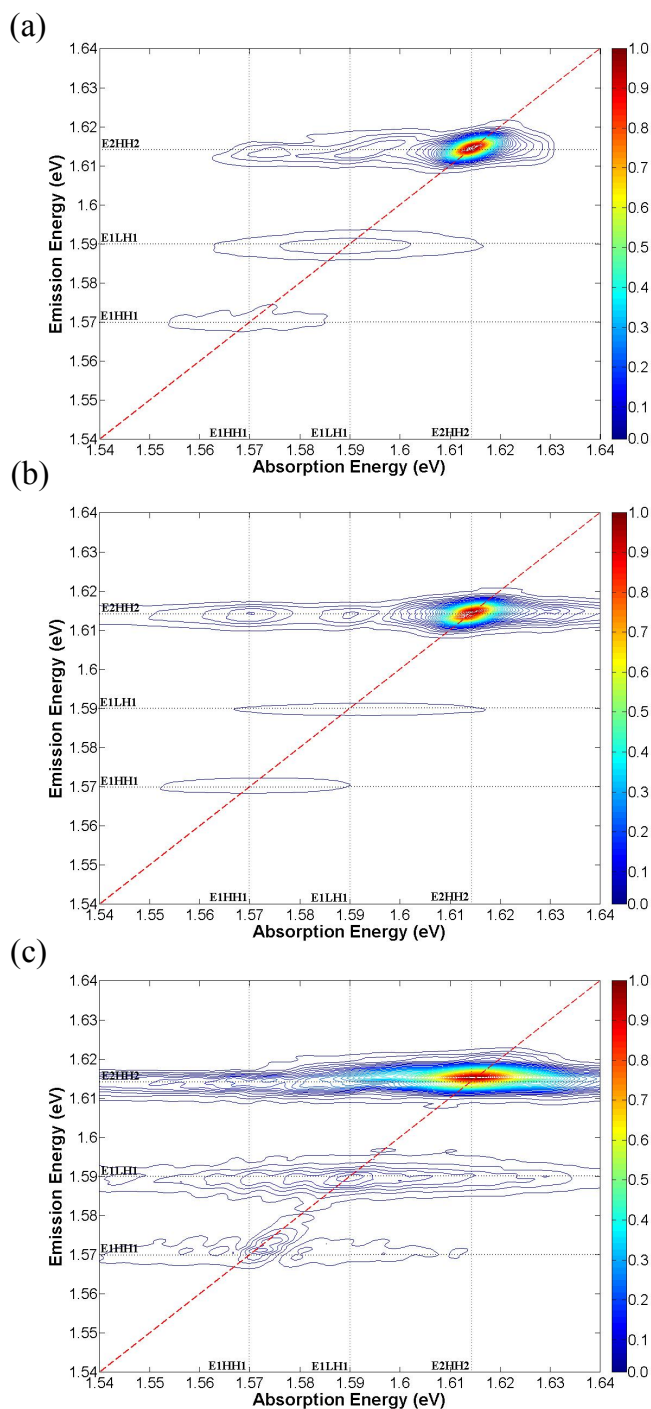


Figure 5.3.2: Total 2DFT spectrum from sample S1-4 for $T = 0$ is shown in (a). Rephasing and non-rephasing signals are presented separately in (b) and (c) to show the contributions of the rephasing and non-rephasing signals on the total 2DFT spectrum presented in (a). Included in the plots are guides at 1.570, 1.590 and 1.614 eV, corresponding to fits of the transition energy to the E1HH1, E1LH1 and E2HH2 excitons.

E1LH1 on-diagonal peaks are elongated along the absorption energy axis. As mentioned in Sec. 5.2.3, the Fourier transform of a rapidly decaying signal can produce a peak that is elongated along the absorption energy axis, ω_τ . In the present case, the decay of the FWM signals from the E1HH1 and E1LH1 excitons is dominated by interference with the E1HH1 free-carrier continuum states. This limits the duration of the FWM signal emitted by the E1HH1 and E1LH1 excitons to a duration equivalent to the autocorrelation of the excitation pulses. In the 2D spectrum, this leads to a signal elongated along the absorption axis with a spectral width approximately equal to the excitation pulse bandwidth. By recording the phase evolution of the FWM signal, Borca et al. were able to resolve the free-carrier continuum in the 2D spectrum [45]. In that case, the free-carrier continuum appeared as peaks elongated along the ω_τ axis with absorption energy equal to the E1HH1 free-carrier continuum, and emission at the E1HH1 and E1LH1 exciton energies. In the present experiment, imperfections in the phase retrieval algorithm prevent the free-carrier continuum from being resolved with the correct absorption energy. Furthermore, the rapid decay of the FWM signal from the E1HH1 and E1LH1 excitons lead to weak signals in the 2D spectra, which makes resolving the signals corresponding to E1HH1, E1LH1 and the free-carrier continuum in the 2D spectrum difficult.

In Fig. 5.3.2, two cross-peaks are observed with emission energies equal to the E2HH2 exciton and absorption energies matching the E1HH1 and E1LH1 excitons. These cross-peaks are designated (E1HH1,E2HH2) and (E1LH1,E2HH2), respectively, where the coordinates are defined as (ω_τ, ω_t) , i.e., by (absorption energy, emission energy). Coherent coupling and population transfer can contribute to the amplitude of cross-peaks. Given that the waiting time in this measurement was fixed at zero, it is unlikely that there is sufficient time for population transfer to occur and significantly contribute to the signal at either cross-peak. The cross-peak fluence at (E1HH1,E2HH2) and (E1LH1,E2HH2) should therefore be proportional to the coupling strength of the coupled excitons. The E1HH1 and E2HH2 coupling was identified in the FWM signal shown in Fig. 5.3.1 by fitting the beat period. Coherent coupling between E1LH1 and E2HH2, however, was not resolved by fitting the time-resolved FWM signal using standard fitting techniques. This is due to the dominance

of the beating signal between E1HH1 and E2HH2. This result illustrates how powerful 2DFTS can be when it comes to analysing FWM signals.

No cross-peak at (E2HH2,E1HH1) is observed in the 2DFT spectra. This is attributed to the free-carrier continuum interaction dominating the coherent response from the E1HH1 excitons and causing the FWM signal from the E1HH1 exciton to decay rapidly. Any signal which follows that quantum pathway (i.e., has an emission at E1HH1) will be very weak in the 2D spectra. Similarly, no cross-peak is observed at (E2HH2,E1LH1) for the same reasons. One may also expect cross-peaks at (E1HH1,E1LH1) and (E1LH1,E1HH1) in Fig. 5.3.2(a) due to coherent coupling between the E1HH1 and E1LH1 excitons, however, these also cannot be resolved due to the free-carrier continuum interaction. It appears that for the excitation conditions used in this experiment, the free-carrier continuum interaction limits our ability to examine quantum pathways that emit signals at energies equal to the E1HH1 and E1LH1 excitons.

In the 2D spectrum shown in Fig. 5.3.2(a), the cross-peak at (E1HH1,E2HH2) is actually centred on the low energy side of the E2HH2 peak on the ω_t axis. In addition, the (E1LH1,E2HH2) cross-peak appears elongated parallel to the diagonal with a peak width along the ω_t axis equivalent to that of the E2HH2 on-diagonal peak. Insight into the origin of these observations is gained by plotting the rephasing and non-rephasing components of the total 2D spectrum separately in Fig. 5.3.2(b) and Fig. 5.3.2(c). In the rephasing component, cross-peaks at (E1HH1,E2HH2) and (E1LH1,E2HH2) are again present. The cross-peaks in this case, however, appear to have a centre emission energy closer in value to the centre emission energy of the on-diagonal E2HH2 peak. In the non-rephasing component shown in Fig. 5.3.2(c), the E2HH2 on-diagonal peak appears elongated along the ω_t axis when compared to Fig. 5.3.2(b). This is due to shorter decay time of the E2HH2 exciton for non-rephasing pulse ordering when compared to rephasing pulse ordering, which occurs when $T = 0$. This will always be the case for the non-rephasing component of the 2DFT spectrum plotted on its own. In addition, the E2HH2 on-diagonal peak is blue-shifted from the rephasing signal by 0.0015 eV to 1.6155 eV. On closer inspection of the spectrally resolved

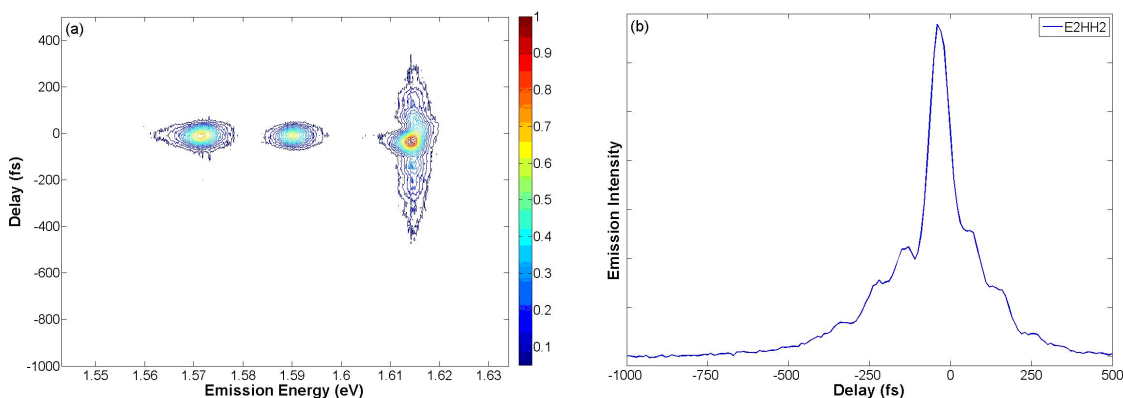


Figure 5.3.3: (a) SR-FWM signal for sample S1-4 as a function of coherence time, τ . The E1HH1 and E2HH2 excitons are coherently excited by broad spectrum pulses centred between the two transitions. In the three-pulse data presented here, the waiting time is set to $T = 5000$ fs. Beating is observed on the emission from the E2HH2 exciton state. Due to spectral diffusion, the signal in the rephasing direction is shortened and the signal almost appears symmetric about $\tau = 0$. (b) Spectrally-integrated signal from the E2HH2 exciton state.

FWM signal in Fig. 5.3.1(a) for non-rephasing pulse ordering, the signal from the E2HH2 exciton appears blue-shifted relative to the rephasing signal. These results suggest there is a quantum pathway for the non-rephasing pulse configuration which leads to the generation of an on-diagonal signal that is larger in energy than the E2HH2 exciton and which is not present for the rephasing pulse configuration. The origin of this signal will be discussed later in Sec. 5.3.2.

The SR-FWM signal for a waiting time of $T = 5000$ fs and with the same excitation conditions is shown in Fig. 5.3.3(a). Emission is again observed from the E1HH1, E1LH1 and E2HH2 excitons, with an extended signal observed from the E2HH2 exciton. The blue-shifted signal observed for non-rephasing pulse ordering in Fig. 5.3.1 is not clearly present in this case. A plot of the spectrally-integrated signal from the E2HH2 exciton transition is given in Fig. 5.3.3(b). A beating signal with a beat period of approximately 90 fs is again observed. The strength of the rephasing signal, relative to the signal for $T = 0$, has reduced considerably, which is consistent with spectral diffusion as discussed in Sec. 5.2.6 and represents the loss of the exciton's ability to form a PE. For non-rephasing

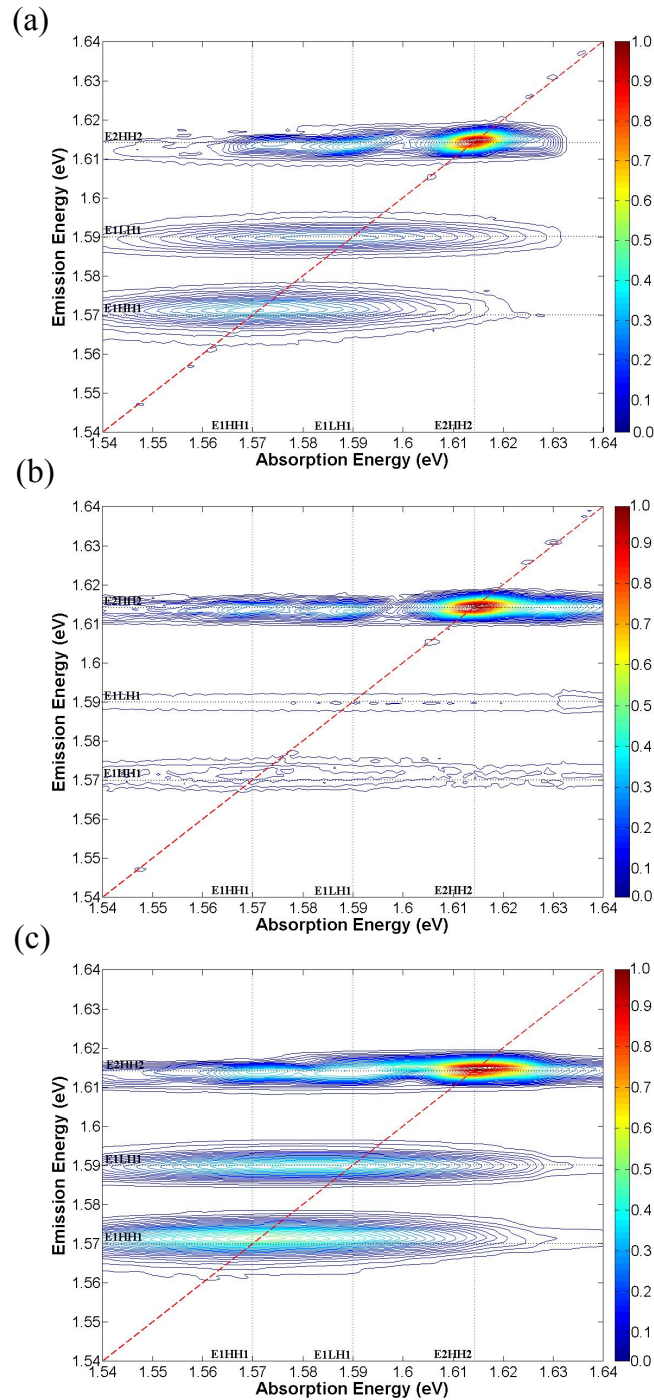


Figure 5.3.4: 2DFT spectra for sample S1-4 with $T = 5000$ fs. In (a), the total 2DFT spectrum is shown. On-diagonal peaks at (E_{1HH1}, E_{1HH1}) , (E_{1LH1}, E_{1LH1}) and (E_{2HH2}, E_{2HH2}) , and off-diagonal peaks at (E_{1HH1}, E_{2HH2}) and (E_{1LH1}, E_{2HH2}) are again observed. (b) and (c) are the 2DFT spectra for rephasing and non-rephasing pulse ordering respectively. The same on-diagonal and cross-peaks are observed.

pulse ordering, the signal decays with a time constant of 115 ± 17 fs, which closely matches the value obtained for a waiting time of 0 fs (102 ± 2 fs).

The total 2DFT spectrum for the data presented in Fig. 5.3.3(a) is shown in Fig. 5.3.4(a). Three on-diagonal peaks corresponding to the E1HH1, E1LH1 and E2HH2 excitons are again present. Furthermore, the off-diagonal peaks at (E1HH1,E2HH2) and (E1LH1,E2HH2) are also evident. The strong beating on the E2HH2 FWM signal in Fig. 5.3.3(b) suggests coherent coupling between E1HH1 and E2HH2 is contributing to the amplitude of the (E1HH1,E2HH2) cross-peak. However, because $T = 5$ ps in this case, population transfer from E1HH1 to E2HH2 cannot be assumed to be insignificant and therefore should also be considered to be contributing to the intensity of the cross-peaks. The relative contributions of the coherent coupling and population transfer pathways to the same peak in the 2DFT spectrum is not clear.

The 2DFT spectra for rephasing and non-rephasing pulse ordering are plotted separately in Fig. 5.3.4(b) and Fig. 5.3.4(c). The (E1HH1,E2HH2) and (E1LH1,E2HH2) cross-peaks are present for both rephasing and non-rephasing pulse ordering. The signal that was observed on the high energy side of the 2D spectra for non-rephasing pulse ordering in Fig. 5.3.2(c), is not clearly observed in Fig. 5.3.4(c), suggesting the quantum pathway leading to the generation of this signal is suppressed with the increase in the waiting time. The E2HH2 on-diagonal peaks in Fig. 5.3.4(b) and Fig. 5.3.4(c) are elongated along the absorption energy axis and have similar dimensions. Due to spectral diffusion, the FWM signals for rephasing and non-rephasing pulse ordering are both due to a FPD, as opposed to the signal in the rephasing direction being a PE, giving the E2HH2 on-diagonal peaks in Fig. 5.3.4(b) and Fig. 5.3.4(c) similar widths in the 2D spectra.

Examining a different sample with a wider barrier between the two QWs allows an investigation of the effects of spatial separation on coupling strength for spatially separated excitons. The SR-FWM signal for S1-6 with $T = 0$ is shown in Fig. 5.3.5. The excitation conditions were the same as those used for S1-4. Signals are observed at emission energies of 1.568 ± 0.001 eV, 1.587 ± 0.001 and 1.611 ± 0.001 eV, which are attributed to the E1HH1,

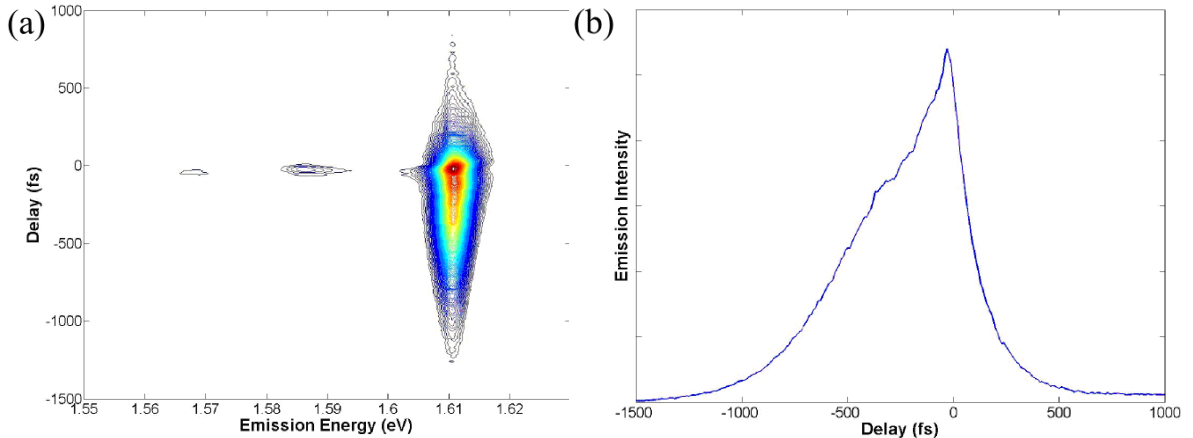


Figure 5.3.5: (a) SR-FWM signal from S1-6 as a function of coherence time, τ , with $T = 0$. Signals are observed for each of the E1HH1, E1LH1 and E2HH2 excitons. Weak beating is observed on the emission from E2HH2. (b) Spectrally-integrated FWM signal for E2HH2.

E1LH1 and E2HH2 excitons, respectively. The change in emission energy between S1-4 and S1-6 is due to variations in the sample structure between samples. The energy difference between the E1HH1 and E2HH2 transitions is 42 meV and is again larger than expected.

The total 2D spectrum for S1-6 with $T = 0$ is shown in Fig. 5.3.6(a). The rephasing and non-rephasing components are plotted in Fig. 5.3.6(b) and Fig. 5.3.6(c), respectively. In each spectrum the (E1HH1,E1HH1), (E1LH1,E1LH1) and (E2HH2,E2HH2) peaks are evident. The E1HH1 and E1LH1 on-diagonal peaks are again elongated along the absorption axis due to coupling with the free-carrier continuum, as discussed earlier. The (E1HH1,E2HH2) and (E1LH1,E2HH2) cross-peaks, which were clearly observed in S1-4, are weaker in the S1-6 sample. The reduced signal strength of these cross-peaks is attributed to the reduced coupling strength between these excitons. This a direct result of the increased spatial separation of the QWs.

The signal that was observed on the high energy side of the E2HH2 on-diagonal peak in S1-4 for $T = 0$ and for non-rephasing pulse ordering is not clearly apparent in S1-6, suggesting that the interaction responsible for this signal is not as strong in S1-6. The weaker signal in S1-6 indicates that this interaction is dependent on the width of the barrier separating the two QWs.

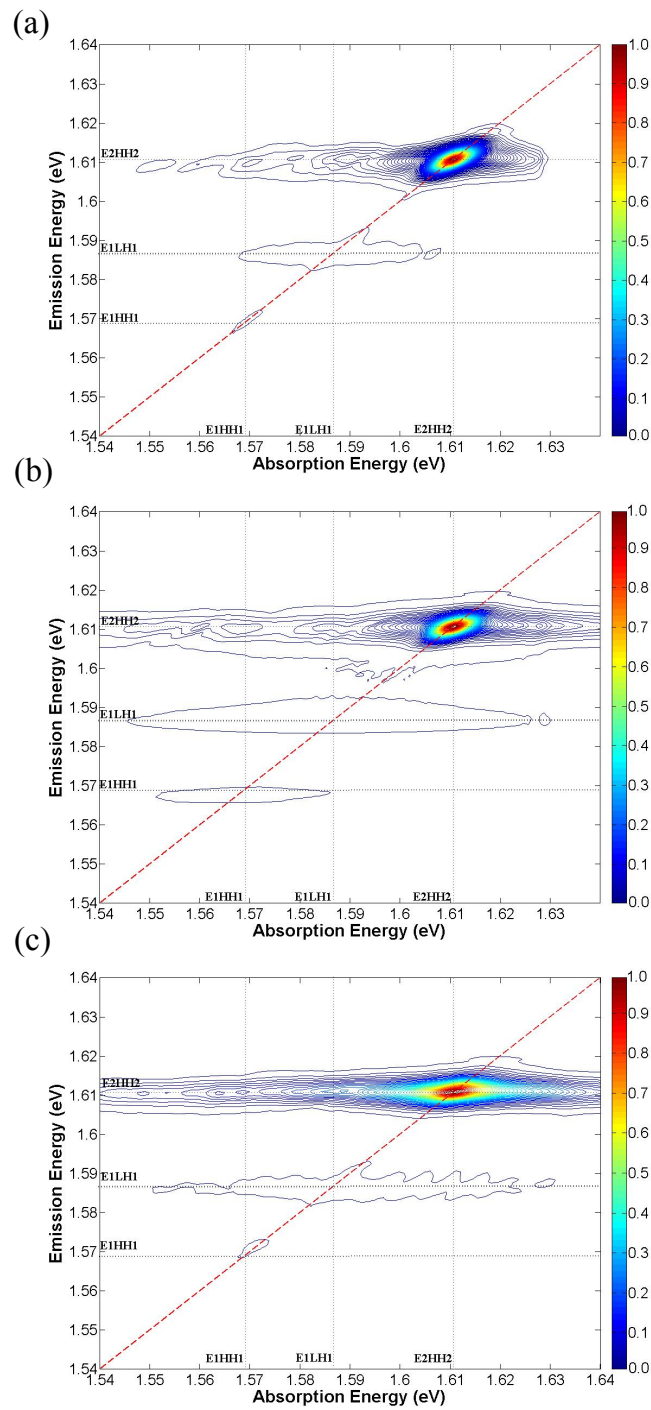


Figure 5.3.6: 2D spectra for S1-6 with $T = 0$. The total 2D spectrum is presented in (a). The 2D spectrum has two cross-peaks with an emission energy equal to the E_{2HH2} exciton and absorption energy equal to E_{1HH1} and E_{1LH1} . In (b), the rephasing component of the total 2D spectrum in (a), the same cross-peaks are observed. In (c), the non-rephasing component of (a), the cross-peaks are not clearly defined.

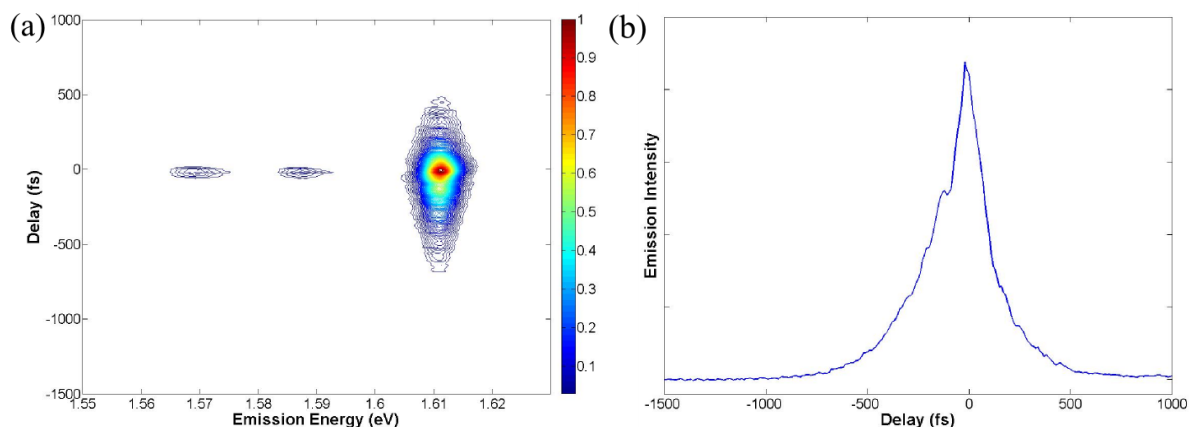


Figure 5.3.7: (a) The SR-FWM signal from S1-6 as a function of delay, τ and with $T = 5000$ fs. Signals are observed for each of the E1HH1, E1LH1 and E2HH2 excitons. There appears to be weak beating on the emission from E2HH2. (b) The spectrally-integrated FWM signal for E2HH2.

With the waiting time increased to 5 ps, the SR-FWM signal is shown in Fig. 5.3.7(a) and the spectrally-integrated signal from E2HH2 is shown in Fig. 5.3.7(b). Beating with a period between 90 - 110 fs is observed on the signal from the E2HH2 exciton. The 2D spectrum is shown in Fig. 5.3.8. Most of the features are the same as when the waiting time was set to 0 fs. The strength of the (E1HH1,E2HH2) and (E1LH1,E2HH2) cross-peaks, relative to the E2HH2 on-diagonal peak, is weaker than shown in Fig. 5.3.4(a) for S1-4. This is further evidence of the coupling strength between the E1HH1 and E2HH2 excitons reducing as the result of increasing the barrier width between the two QWs.

The SR-FWM signal for sample S1-20 with a waiting time of 0 fs is shown in Fig. 5.3.9(a). In this sample the E1HH1, E1LH1 and E2HH2 exciton transitions are measured at 1.562 ± 0.001 eV, 1.581 ± 0.001 eV and 1.602 ± 0.001 eV, well below the values recorded for samples S1-4 and S1-6 and the values from the low temperature PL measurements. For the same excitation conditions used for S1-4 and S1-6, this has resulted in the co-excitation of the E2LH2 transition and reduced the excitation of the E1HH1 transition. The signal from the E2LH2 transition can be seen in Fig. 5.3.9(a) at 1.624 ± 0.001 eV. Because the E2LH2 exciton is excited, coupling between E2HH2 and E2LH2 will also need to be considered. The spectrally-integrated signal for E2HH2 is plotted in Fig. 5.3.9(b).

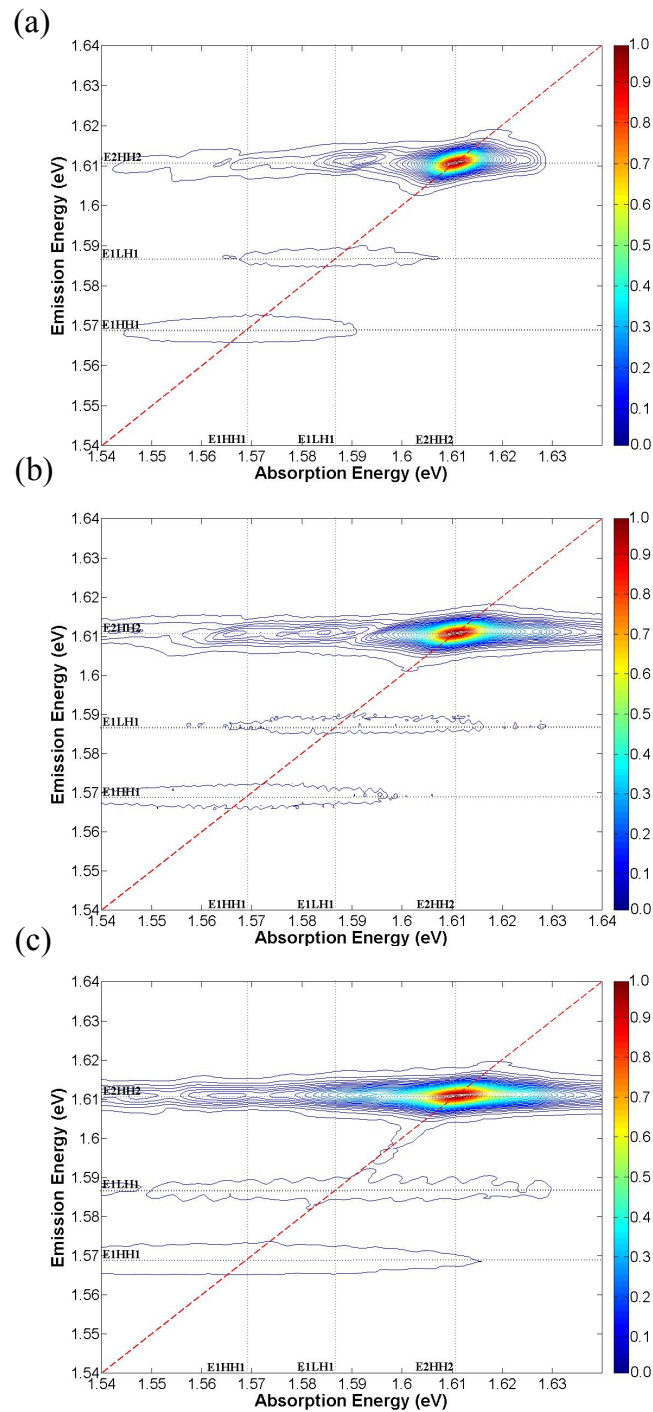


Figure 5.3.8: The 2D spectra for S1-6 with $T = 5000$ fs. The total 2D spectrum is presented in (a). Cross-peaks with emission energy equal to E2HH2 and absorption energies equal to E1HH1 and E1LH1 are evident. In (b), the rephasing component of the total 2D spectrum in (a), cross-peaks with same absorption and emission energies are observed. In (c), the non-rephasing component of (a), the same cross-peaks may also be present, however, this is not as clear as in (b) due to a strong background signal.

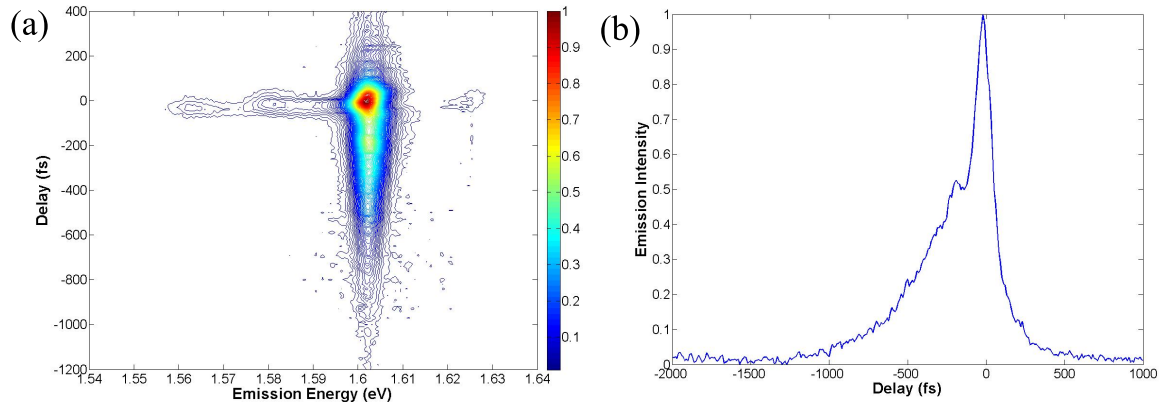


Figure 5.3.9: (a) SR-FWM signal from sample S1-20 for $T = 0$. The spectra is recorded presented as a function of delay, τ . (b) Spectrally-integrated signal for E2HH2.

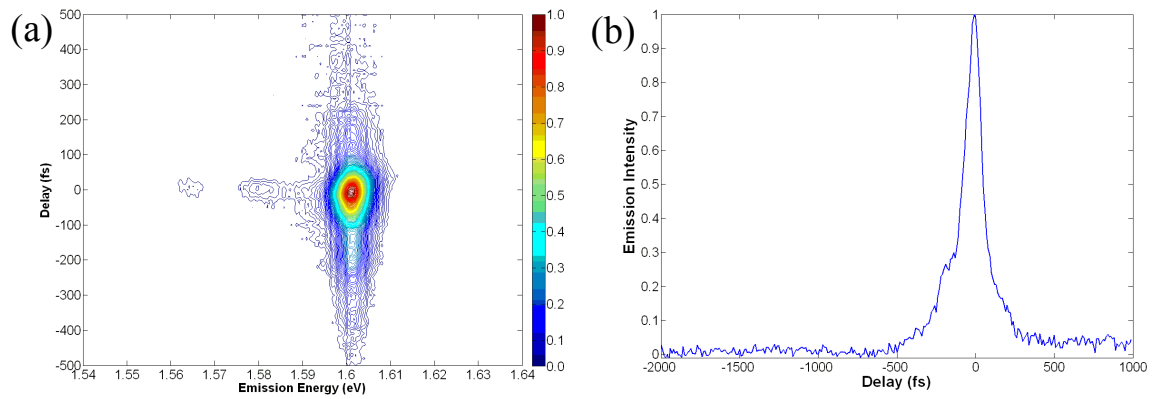


Figure 5.3.10: (a) SR-FWM signal from sample S1-20 as a function of delay, τ , for $T = 5000$. (b) Spectrally-integrated signal for E2HH2.

In this plot there appears to be a single beat around $\tau = -250$ fs, however, the beat period cannot be determined.

The two-dimensional spectra for S1-20 with $T = 0$ fs is shown in Fig. 5.3.11. On-diagonal peaks are observed for each of the E1HH1, E1LH1, E2HH2 and E2LH2 excitons. A rather weak (E1HH1,E2HH2) cross-peak is observed in the total 2D spectrum shown in Fig. 5.3.11(a). The low signal strength is attributed to two factors; firstly, the E1HH1 exciton is not as strongly excited in the present experiment, leading to a weaker contribution from the E1HH1 exciton, and secondly, the larger barrier width in S1-20 should reduce the coupling strength between E1HH1 and E2HH2. A similarly weak signal is observed for the (E1LH1,E2HH2) cross-peak for the same reasons. A weak cross-peak at (E2LH2,E2HH2) is also present in the 2D spectrum due to the weak excitation of the E2LH2 exciton in this case.

With the waiting time set to 5000 fs, the SR-FWM signal and the spectrally-integrated signal from the E2HH2 exciton are shown in Fig. 5.3.10. The corresponding 2D spectra are shown in Fig. 5.3.12. The total, rephasing and non-rephasing spectra are shown in Fig. 5.3.12(a), Fig. 5.3.12(b) and Fig. 5.3.12(c), respectively. Again there is a cross-peak at (E1HH1,E2HH2) in the total 2D spectrum shown in Fig. 5.3.12(a), however, the intensity of the cross-peak does not change significantly between Fig. 5.3.11(a) and Fig. 5.3.12(a). In S1-4 and S1-6, energy transfer produced an increase in the cross-peak intensity when the waiting time was increased from 0 to 5000 fs. Assuming the exciton recombination rate does not vary from sample to sample, the rate of energy transfer to the E2HH2 exciton from the E1HH1 and E1LH1 excitons should decrease as a function of barrier width. For the same waiting time for each sample, there should be a smaller increase in the cross-peak intensity for S1-20 compared to S1-4 and S1-6. A reduced transfer rate for a larger barrier width is consistent with the data shown in this section.

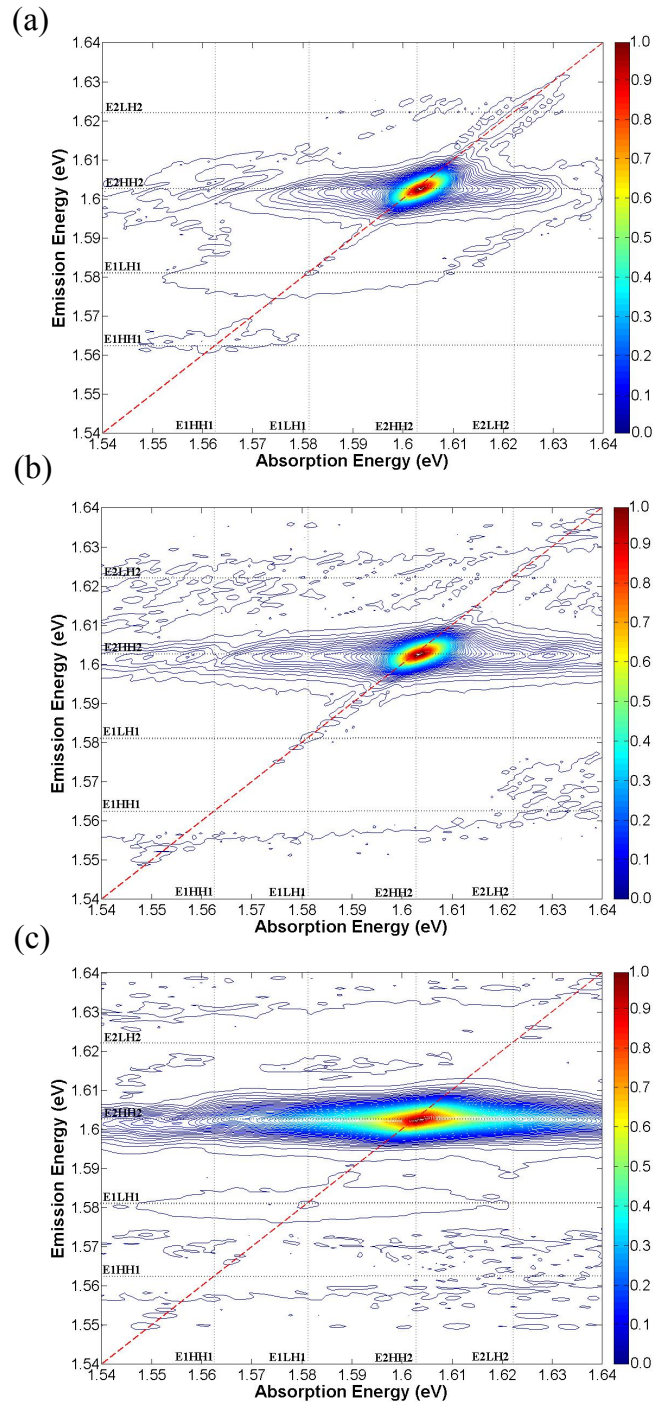


Figure 5.3.11: 2D spectra for S1-20 for $T = 0$. The total 2D spectrum is presented in (a). On-diagonal peaks are observed for the E1HH1, E1LH1, E2HH2 and E2LH2 excitons, with emission energies equal to 1.562 ± 0.001 eV, 1.581 ± 0.001 eV, 1.602 ± 0.001 eV and 1.624 ± 0.001 eV, respectively. The rephasing and non-rephasing components of the total 2D spectrum are shown in (b) and (c).

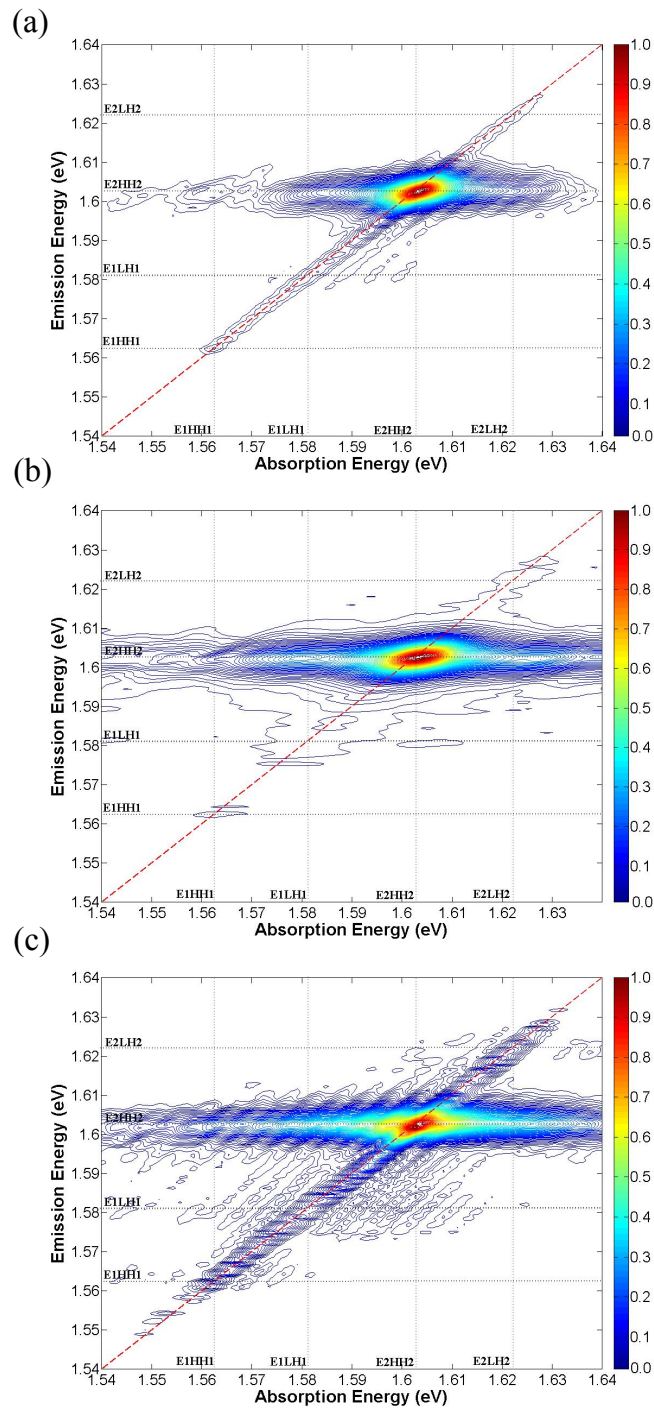


Figure 5.3.12: 2D spectra for S1-20 for $T = 5000$ fs. The total 2D spectrum is presented in (a). On-diagonal peaks are observed for the E1HH1, E1LH1, E2HH2 and E2LH2 excitons, with emission energies equal to 1.562 ± 0.0005 eV, 1.581 ± 0.0005 eV, 1.602 ± 0.0005 eV and 1.624 ± 0.001 eV, respectively. The rephasing and non-rephasing components of the total 2D spectrum are shown in (b) and (c).

5.3.2 Signal for non-rephasing pulse ordering

The signal observed for negative coherence times and 1.5 meV higher in energy than the E2HH2 exciton in S1-4 are discussed in this subsection. So far it has been shown that the strength of this signal decreases with waiting time. Furthermore, a strong barrier width dependence was also observed, suggesting a dependence on the tunnelling of the E, HH and LH wavefunctions, or for interactions which do not require wavefunction overlap, like dipole-dipole coupling, a dependence on the spatial separation of the states involved.

The tables in Appendix B, which show the calculated transition energies and integrated overlaps of the E, HH and LH state wavefunctions for each sample, may be used to estimate the transition from which the signal on the high energy side of E2HH2 originates. For S1-4, the excitons with transition energies close to the E2HH2 exciton are E2HH1, E1LH2 and E2LH1, with energy differences of -6 meV, 7.5 meV and 18 meV, respectively. Each of these excitons would show a strong dependence on barrier width since they are made up of electron and hole states localised to different QWs, and would therefore be consistent with the experimental results. There are, however, discrepancies between the measured transition energies and the calculated transition energies for the E1HH1, E1LH1, E2HH2 and E2LH2 excitons in this sample: E1HH1, E1LH1 and E2LH2 are lower than the calculated values by 5 meV, 9 meV and 6 meV, respectively, and E2HH2 is larger than the calculated energy by 4.5 meV. This would mean the energy differences given in Appendix B for E2HH1, E1LH2 and E2LH1 were not accurate, though it is possible to take these differences into account. If we assume the maximum possible variation in energy for the E1 and HH1 subbands, E2HH1 will still not have a transition energy which is larger than E2HH2 and therefore can be excluded as being the origin of the negative coherence time signal. Similarly, E2LH1 will have a transition energy which is at least 3 meV larger than the E2HH2 exciton and may also be excluded. The results therefore suggest that the signal observed 1.5 meV above the E2HH2 transition in Fig. 5.3.1 and Fig. 5.3.2 is originating from E1LH2.

Comparing the overlap of the electron and hole wavefunctions for the E2HH2 and E1LH2

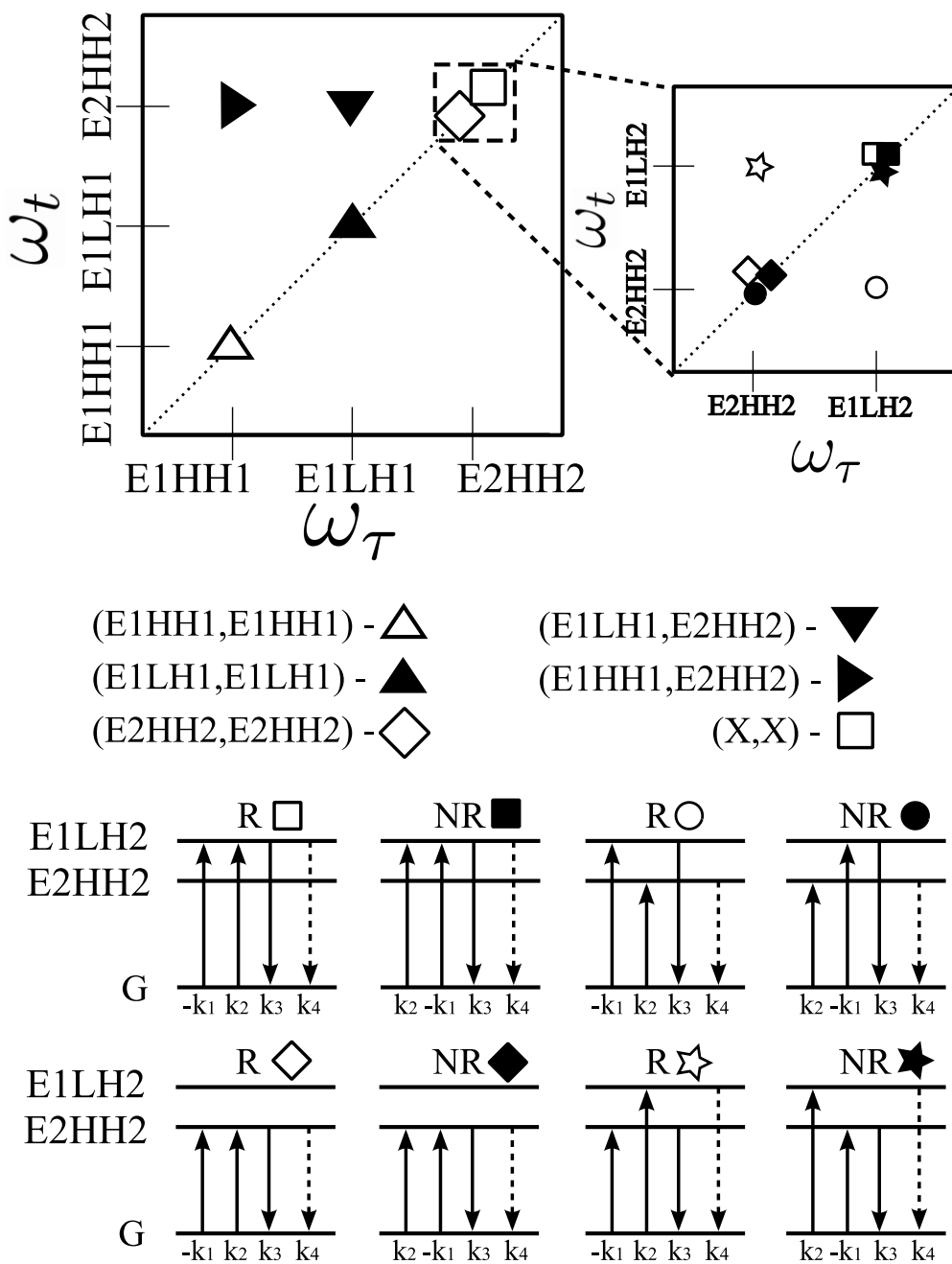


Figure 5.3.13: A schematic of the total 2DFT spectrum shown in Fig. 5.3.2. The region around the $(E2HH2, E2HH2)$ peak is magnified to show the contribution of the pathways given by \square , \blacksquare , \diamond , \blacklozenge , \circ , \bullet , \star and \blackstar to the 2DFT spectrum. R and NR refer to rephasing and non-rephasing, respectively.

transitions, which are 0.9 and 0.1, respectively, it is surprising that the FWM signal from E1LH2 in S1-4 is sufficiently intense to resolve. The presence of this signal and that it only occurs for non-rephasing pulse ordering may be explained by considering quantum pathways involving the E2HH2 and E1LH2 excitons and the expected signal strength. Figure 5.3.13 shows a schematic of the total 2DFT spectrum shown in Fig. 5.3.2(a). The region around the (E2HH2,E2HH2) peak is magnified to show where signals given by the pathways labelled \square , \blacksquare , \diamond , \blacklozenge , \circ , \bullet , \star and \blackstar are located on the 2DFT spectrum. The pathways responsible for the signals generated in the magnified region are also shown. The pathways given by \diamond and \blacklozenge will produce points on the diagonal in the 2DFT spectrum with energy equal to E2HH2 and with a signal strength proportional to $0.9^4 (\mu_{eh}^4)$, where μ_{eh} is the dipole moment of the transition, which is proportional to the overlap of the electron and hole wavefunctions). The on-diagonal peaks given by \square and \blacksquare , with energy equal to E1LH2, will have a much weaker signal strength proportional to 0.1^4 . The non-rephasing pulse ordering for a Raman-like coherence pathway shown by \bullet and \blackstar will give on-diagonal signals that are overlapped with the \diamond and \blacklozenge , and the \square and \blacksquare pathways. The \bullet and \blackstar pathways will generate a FWM signal with an intensity proportional to $\mu_{E2HH2}^2 \mu_{E1LH2}^2$, which will be ~ 81 times greater than the \square and \blacksquare pathways due to just the E1LH2 exciton. The pathway given by \bullet is overlapped with the non-rephasing signal from the E2HH2 exciton (\blacklozenge) and cannot be separated. Similarly, the pathways given by \circ and \star can't be resolved in the 2D spectra because the strength of these signals are much weaker than the on-diagonal rephasing signal from the E2HH2 exciton (\diamond).

By considering the different quantum pathways, it is suggested that the signal emitted for non-rephasing pulse ordering in S1-4 (Fig. 5.3.1) is due to the Raman-like coherence pathway given by \blackstar . This pathway gives an on-diagonal peak in the 2D spectra which will only occur for non-rephasing pulse ordering. The enhancement of the dipole moment of the E1LH2 exciton through coupling with the E2HH2 exciton allows the E1LH2 exciton to be resolved in these experiments.

5.3.3 Raman-like coherence

Raman-like coherences refer to coherently coupled states that do not have a direct transition dipole [37, 184, 185]. Without a direct transition dipole, a coherence between these states is non-radiative. An example of states which do not have a transition dipole occurs in the E, HH and LH three-level system: the E state shares a transition dipole with the HH and LH states, however, no transition dipole exists between the HH and LH states [37]. Following a second order interaction, i.e., concurrently exciting the E1HH1 and E1LH1 transitions with resonant pulses, a Raman-like coherence can be established between the HH and LH states.

In the present case we are considering E1HH1 and E2HH2, which are two two-level systems with no common state. The excitation sequences that represent Raman-like coherence pathways between E1HH1 and E2HH2 are shown in Fig. 5.3.14. The zero-exciton (ground) state is labeled G. For the purposes of this example, the excitation pulses are considered to arrive in the sequence \mathbf{k}_1 , \mathbf{k}_2 , \mathbf{k}_3 and the signal emitted in the \mathbf{k}_4 direction is detected. In the pathway shown in Fig. 5.3.14(a), the first two excitation pulses generate a coherence in each of the E1HH1 and E2HH2 excitons. The third excitation pulse, with energy equal to E1HH1, returns the three-level system to a coherence of just the E2HH2

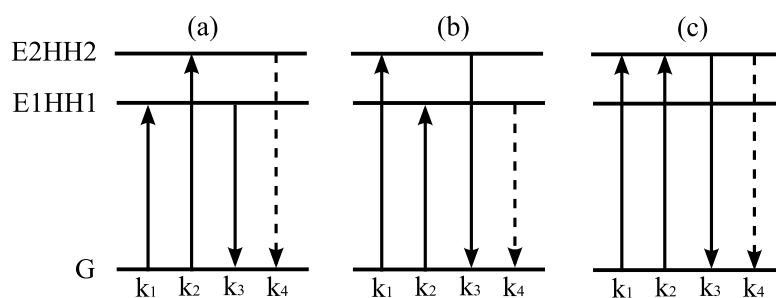


Figure 5.3.14: Quantum pathways of interest that are discussed in the text. The Raman-like coherence quantum pathways are shown in (a) and (b). The excitation pulses arrive in the sequence \mathbf{k}_1 , \mathbf{k}_2 , \mathbf{k}_3 . The first two excitation pulses generate a coherence in each of the E1HH1 and E2HH2 excitons. The third excitation pulse removes the coherence established between E1HH1 and E2HH2, and the polarisation radiates via a FPD in the \mathbf{k}_4 direction. The pathways given in (a) and (b) will generate signals at an energy equal to E1HH1 and E2HH2, respectively. In (c), the pathway that would lead to the generation of either a PE, or a transient grating signal, depending on interpulse delays, is shown.

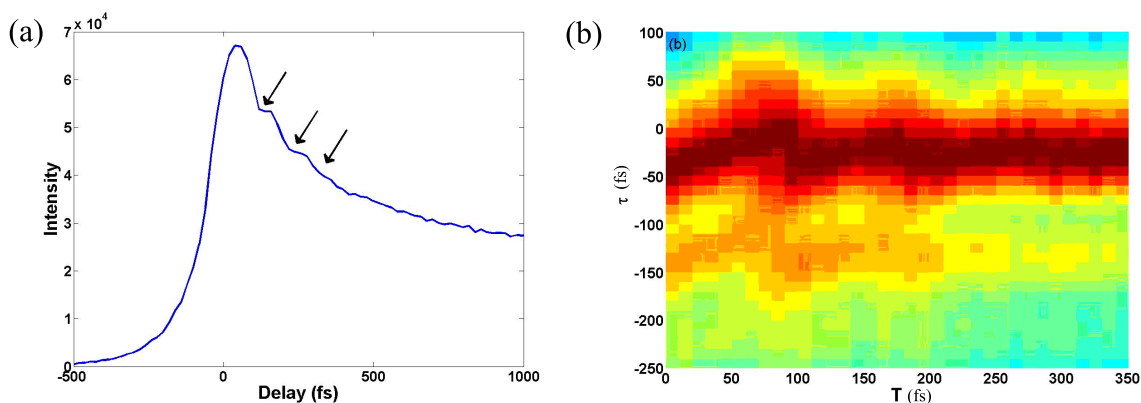


Figure 5.3.15: (a) The spectrally-integrated signal from the E2HH2 transition in sample S1-4 whilst scanning the waiting time (T) with τ fixed at 0 fs. Beating with a beat period of 85-100 fs is observed. (b) The FWM signal from E2HH2 as a function of T and τ . As the signal component corresponding to the Raman-like coherence between E1HH1 and E2HH2 decays as a function of T , the FWM signal becomes almost entirely dependent on τ from $250 \leq T \leq 350$ fs.

exciton, after which the E2HH2 exciton coherence radiates in the \mathbf{k}_4 direction. In the pathway shown in Fig. 5.3.14(b), the E2HH2 exciton is excited first, generating a signal with energy equal to E1HH1.

In the following measurement, the Raman-coherence between E1HH1 and E2HH2 is investigated by examining the time-integrated FWM signal. The observation of beating at a period equal to the energy difference between the E1HH1 and E2HH2 excitons, whilst scanning T , would indicate that a Raman-like pathway can be established between the E1HH1 and E2HH2 excitons. A plot of the spectrally-integrated signal (1.604 - 1.624 eV) from the E2HH2 transition as a function of waiting time, T , with the coherence time fixed at $\tau = 0$, is shown in Fig. 5.3.15(a). Beating with a period of approximately 85 - 100 fs is observed, suggesting a Raman-like coherence has been established between the E1HH1 and E2HH2 excitons. The beats decay within 250 fs. The beating signal occurs on top of a slowly decaying transient grating signal ($\tau = 0$) which will decay due to population relaxation and carrier diffusion. The transient grating pathway is shown in Fig. 5.3.14(c) and generates a signal with energy equal to E2HH2. As shown in Fig. 5.3.15(a), the decay of the transient grating is much longer than the coherent dynamics, and is of no interest in the

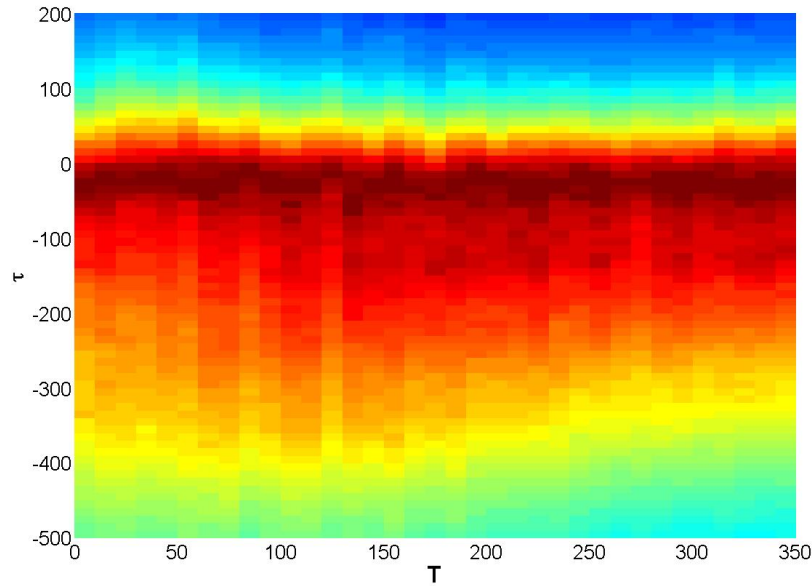


Figure 5.3.16: The spectrally-integrated E2HH2 FWM signal from S1-6, normalised and plotted as a function of T and τ . The time scales on both axis are in fs. Compared to sample S1-4 and Fig. 5.3.15, no Raman-like signal is observed in this data. The rephasing FWM signal from the E2HH2 exciton dominates.

present investigation.

The presence of beating as a function of waiting time is even clearer in Fig. 5.3.15(b), where the spectrally-integrated and normalised FWM signal from the E2HH2 exciton is plotted as a function of τ and T . Such plots are used to compare the coherent dynamics during the period τ to the coherent dynamics during the period T (see Lee et al. [186] for example). As τ and T are varied, the beat maxima shift along the anti-diagonal, indicating the beat phase is constant as a function of $\tau + T$. The shift in the beat maxima as a function of τ and T decays within 250 fs. For $250 \leq T \leq 350$ fs, the beat maxima no longer change as a function of T and remain stationary at $\tau \approx -40$ fs and $\tau \approx -140$ fs.

A similar plot for S1-6 is given in Fig. 5.3.16. Unlike for sample S1-4, no clear T dependence of the FWM signal is evident in Fig. 5.3.16. The data shown in Fig. 5.3.16 is dominated by the rephasing signal from the E2HH2 exciton, with no obvious beating as a function of T . This shows that the Raman-like coherence between E1HH1 and E2HH2

in this case is much weaker than in S1-4 and is dependent on the spatial separation of the E1HH1 and E2HH2 excitons. Experiments which can separate the Raman-like coherence and transient grating signals should be considered for making more sensitive measurements of the coherent dynamics.

5.3.4 Discussion

Prior to the present investigation, coherent coupling between excitons which do not share a common state had only been investigated by Li et al. [36]. In that investigation, asymmetric double QW samples with barrier widths of 1.7 nm and 10 nm were examined. The range in between was not investigated. In the sample with the 1.7 nm barrier, the energy difference between the HH1 and HH2 subbands was too small to accurately identify excitons which share these states (for example, E1HH1 and E1HH2). Furthermore, the congested 2D spectra for the sample with the 1.7 nm barrier made it difficult to determine which states were coherently coupled. In the present investigation, asymmetric double QW samples with barrier widths of 4 nm, 6 nm and 20 nm were examined. The energy separation between the exciton transitions is sufficiently large so that there is little ambiguity in the assignment of the signals in the experimental results. Coherent coupling was observed between the E2HH2 exciton and the E1HH1 and E1LH1 excitons, where the coupling is strongest for the 4 nm barrier and decreases as the barrier width is increased. If it could be shown that the two bright HH excitons are spatially separated in these samples, this would be the first time that coherent coupling has been demonstrated between spatially separated excitons which do not share a common state in a double QW system.

In order to determine if the excitons are localised to different QWs, and therefore if they can be considered as being spatially separated, it is necessary to show the degree of localisation of the E, HH and LH wavefunctions within the wide and narrow QWs and how the calculated wavefunctions compare the real samples. In the S1-4 in Fig. 5.2.1(b), the HH1 and HH2 wavefunctions are shown to be highly localised to opposite QWs, whilst the wavefunctions for the E1, E2, LH1 and LH2 subbands extend through the barrier

into the adjacent QW. The extent of the E wavefunctions over both QWs in S1-4 may be approximated by assuming that the HH1 and HH2 wavefunctions are completely localised to the wide and narrow QWs, respectively, and by considering the overlap of the E1 and E2 wavefunctions with the localised HH wavefunctions. It is reasonable to approximate the HH1 and HH2 wavefunctions as being completely localised to the wide and narrow QWs in S1-4 given that the integrated overlap of the two wavefunctions is 0.0072. The calculated overlap of the E1 and HH2, and the E2 and HH1 wavefunctions is roughly 0.1, indicating the localisation of the E1 and E2 wavefunctions to the wide and narrow QWs, respectively, is not as strong as for the HH wavefunctions. Using the same method to quantify the localisation of the LH1 and LH2 wavefunctions, overlap values of 0.17 and 0.20 are calculated, respectively. For sample S1-6 in Fig. 5.2.1(c), the overlap of the E1 and HH2, and the E2 and HH1 wavefunctions is calculated to be 0.027 and 0.033 respectively, indicating a significant reduction in the extension of the E1 and E2 wavefunctions into the adjacent QWs compared to S1-4. The overlap of the LH1 and HH2 wavefunctions, and the LH2 and HH1 wavefunctions, is calculated to be 0.07 and 0.09, respectively. For S1-20, the overlap of the HH wavefunctions with the E and LH wavefunctions is insignificant (< 0.001). Therefore, in S1-20, the wavefunctions for the E, HH and LH subbands may be considered to be localised to the wide and narrow QWs.

If the HH1 and HH2 wavefunctions are localised to the wide and narrow QWs, as suggested by the calculations, it may be possible that for the E2HH2 exciton, HH2 will keep its partner electron, E2, localised in the narrow QW, regardless of the extent of the E2 wavefunction in the wide QW. Similarly for the wide QW and the E1HH1 exciton, HH1 will keep its partner electron, E1, localised to the wide QW. If this is the case, then for S1-4 and subsequently S1-6, it may be reasonable to consider the E1HH1 and E2HH2 excitons as being localised to wide and narrow QWs and spatially separated. Such localisation of the E1HH1 and E2HH2 excitons to the wide and narrow QWs in the grown samples is evident in the experimental results. Recalling the SR-FWM signal for S1-4 with $T = 0$ in Fig. 5.3.1(a), an extended FWM signal is observed from the E2HH2 exciton. This is in contrast to the rapid decay of the FWM signal from the E2HH2 exciton observed in S1-2 due to interference with

the E1HH1 free-carrier continuum. The strong extended FWM signal which is observed from S1-4 and not from S1-2 suggests that in S1-4 the E2HH2 excitons are interacting very weakly, if at all, with the E1HH1 free-carrier continuum. This weak interaction suggests that the E2HH2 excitons are highly localised to the narrow QW for barrier widths ≥ 4 nm.

The localisation of the E1HH1 and E2HH2 excitons to the wide and narrow QWs, respectively, can be further investigated by looking for dephasing as the result of free-carrier scattering. To examine the localisation of the E2HH2 exciton to the narrow QW (and subsequently the localisation of the E1HH1 exciton to the wide QW), the decay time of the FWM signal from the E2HH2 exciton in S1-4 and S1-20 are compared. In S1-20, the probability of the E1 and HH1 free-carriers scattering with the E2HH2 exciton is insignificant because they will be localised to different QWs, therefore the E2HH2 exciton shouldn't experience dephasing due to scattering with E1 and HH1 free-electrons, and therefore may be used as a reference to examine this effect. For the same excitation conditions, decay times of 206 ± 30 fs and 180 ± 3 fs are measured for E2HH2 in S1-4 and S1-20, respectively, where the decay time is fit for $\tau < -700$ fs. Within the measured uncertainty the decay times match, suggesting that dephasing of the E2HH2 exciton due to scattering with free-carriers from the E1 and HH1 subbands is insignificant in S1-4. The weak interaction between the E2HH2 exciton and the E1 and HH1 free-carrier continuum provides further evidence that the E2HH2 and E1HH1 excitons are highly localised to the narrow and wide QWs, respectively. The results strongly suggest that for barrier widths ≥ 4 nm, the E1HH1 and E2HH2 excitons are spatially separated.

The localisation of the E1HH1 and E2HH2 excitons to separate QWs reduces the number of possible coupling mechanisms. In the ADQW sample with the 1.7 nm barrier that was examined by Li et al. [36], the 2DFT spectra suggested that each of the exciton states were coupled with each other. The authors suggested that the excitons were coupled through a common ground state as the result of valence band mixing. In the present experiment the experimental results show that the wavefunctions for the two lowest energy HH subbands are highly localised to adjacent QWs in each of the samples examined (S1-4, S1-6 and S1-

20), making the possibility that a common state is mediating the observed coupling in the present case unlikely.

Since the E1HH1 and E2HH2 excitons do not share a common state, the mechanism coupling them is probably a ‘ranged’ interaction, that is, not dependent on the spatial overlap of the E1HH1 and E2HH2 excitons, but dependent on the separation between them. There are several Coulomb interactions which should be discussed; these are local field effects, long-range Coulomb interactions and dipole-dipole coupling. Considering local field effects in three-pulse FWM experiments, the first excitation pulse resonantly excites an exciton transition and generates a macroscopic polarisation in the sample. The local field from the coherent excitons superimpose with the excitation electric field and generate a nonlinear component to the polarisation, or in other words, drive additional coherent interactions within the macroscopic polarisation. Doubly excited excitations, which have been excited by the excitation field and the local field, have a wavevector equal to the sum of the interacting field wavevectors [41, 42]. In the case where two coupled exciton transitions with different energy are resonantly and coherently excited by a spectrally broad pulse, the local field interaction could excite a coherence between them. In order to conserve the wavevector in the signal detection direction in a multiple pulse FWM experiment, each excitation pulse must lead to two excitations of the polarisation, one from the incident pulse and one from the local field effects. Such a quantum pathway may be expected to have a strong excitation fluence dependence, however, the local field effect interaction varies linearly with excitation fluence [12], as the excitation from each incident pulse will also generate a local field. Local field effects could lead to the generation of quantum beating between coupled states in FWM experiments, however, it is not the mechanism responsible for coupling the spatially separated excitons.

Long-range Coulomb interactions can lead to correlated motions of charged particles. The correlated motion between of the electrons and holes of excitons can produce changes in the exciton energy and the dephasing rate of the excitons. These effects are typically known as excitation induced shift (EIS) and excitation induced dephasing (EID). Recent

experiments have started to explore higher-order correlations responsible for such effects [41, 43]. The higher-order correlations examined in those experiments produced coherent signals with energy around $\times 2$ and $\times 3$ the transition energy of the excited exciton; such signals were not observed in the experiments presented this chapter. It is not immediately obvious how long-range Coulomb interactions could lead to a beating signal at the energy difference between the E1HH1 and E2HH2 excitons in the present experiment. Since the contribution of long-range Coulomb interactions to coherent dynamics are still not completely understood, the contribution of this interaction cannot be excluded.

It is well known that dipole-dipole coupling can mediate coherent coupling between spatially separated excitations. In a theoretical investigation, Batsch et al. [140] showed that dipole-dipole coupling between spatially separated excitons could produce quantum beating in FWM experiments. The strength of the coupling between two dipole-dipole coupled excitons would vary as a function of r^{-3} , where r is the distance separating the two excitons. Dipole-dipole coupling could also coherently couple HH and LH excitons, however the strength of the coupling would not be as strong as coupling between two HH excitons due the weaker dipole moment of the LH exciton. By excluding coupling through a common state and local field interactions, and given it is not apparent how long-range coulomb interactions could lead to the beating signal observed in the presented work, it is suggested that dipole-dipole coupling is the mechanism coupling the spatially separated excitons in this case.

5.3.5 Summary and Outlook

The initial intention of this investigation was to examine the dynamics of coherently coupled excitons in double QWs. In addition to this, there were also plans to investigate the effect of an LO-phonon resonance on coherently coupled excitons. In sample set 1, the energy difference between the E1HH1 and E2HH2 exciton transitions for samples S1-4, S1-6 and S1-20 were 44 meV, 42 meV and 40 meV respectively, which was larger than planned. The LO-phonon energy in GaAs is 35 meV. Given the large discrepancy between the exciton

transition energies and the LO phonon energy, it is not possible to make any comments regarding an LO phonon resonance. Nevertheless, investigation presented in this chapter on sample set 1 provides a first examination of the coherent dynamics of spatially separated excitons in ADQWs.

The 2DFT spectra and the Raman-like coherence signal suggests that the E1HH1 and E2HH2 excitons are coherently coupled. The strength of the coupling is largest for the narrowest barrier width and decreases as the barrier width is increased. The Raman-like signal was only observed in S1-4, where the coupling strength was the largest. In S1-6, the Raman-like signal was too weak to resolve on top of the transient grating signal.

The 2DFTS revealed that the E1LH1 and E2HH2 excitons were also coupled. The only evidence for this is in the 2D spectra; Beating with a beat period equal to the energy difference between the E1LH1 and E2HH2 excitons was not observed in the FWM signal and not resolved when using standard fitting techniques.

Comparisons were made between the FWM results and the calculations in order to determine whether the E1HH1 and E2HH2 excitons were localised to the wide and narrow QWs, respectively. The calculations suggested the HH1 and HH2 wavefunctions were highly localised to the wide and narrow QWs, respectively, however, the E and LH wavefunctions showed much greater extension through the barrier separating the QWs. Experimental evidence was provided to evaluate the localisation of the E1HH1 and E2HH2 excitons. The results strongly suggest that for barrier widths ≥ 4 nm, the E1HH1 and E2HH2 excitons can be considered as being spatially separated.

The mechanism responsible for coupling the excitons was also discussed. Since the excitons are considered to be spatially separated, the coupling mechanism must not be dependent on their spatial overlap. For this reason, coupling mechanisms not dependent on overlap were considered. For closely spaced excitons dipole-dipole coupling appears to be the most likely mechanism, however, other mechanisms may be responsible.

In order to definitively determine the coupling mechanism, we need to obtain a clearer

measure of the coupling strength. To aid resolving the coupling strength between spatially separated excitons, methods which could improve the signal to noise ratio in the detected FWM signal, and therefore also in the 2DFT spectra, are suggested. This is particularly important for samples with wide barriers (> 6 nm) separating the two QWs where the coupling strength is weaker. To increase the signal strength, high quality multiple QW samples should be considered. Most of the noise on the FWM signal originates from laser scatter from the front surface of the sample and small movements in the sample position whilst the FWM signal was acquired (due to vibrations within the circulating helium cryostat). An anti-reflection coating on the front surface of the sample may help to reduce the noise.

Experiments which would allow a quantitative analysis of the coupling strength would greatly assist in determining the coupling mechanism. A two-colour FWM experiment utilising the Raman-like coherence quantum pathway could unambiguously reveal coherent coupling between two excitons with different transition energy and should be the focus of future work. In experiments where spectrally broad excitation pulses are used, the signal corresponding to the Raman-like coherence pathway will be superimposed on top of a strong transient grating signal which will occur for the same pulse ordering and which is emitted in the same wavevector conserving direction. It is suggested that two-colour FWM experiments which selectively excite the quantum pathway for the Raman-like coherence would remove any population pathways from contributing to the FWM signal and would allow a quantitative analysis of the coupling strength between the E1HH1 and E2HH2 excitons. One limitation of such an experiment would be that the two exciton states of interest would need to be sufficiently well separated in energy so that the two transitions could be selectively excited.

Chapter 6

Conclusions

In this thesis, ultrafast spectroscopy was used to explore a range of dynamics in two semiconductor quantum well systems: ZnO/MgZnO quantum wells and GaAs/AlGaAs asymmetric double quantum wells. ZnO is a relatively new material system of significant interest because it has the potential to be used in blue/UV light emitting devices. This work focused on the effects of and the potential uses for the built-in electric field in ZnO/MgZnO QWs. The GaAs material system on the other hand is an established material which is well understood and the techniques used for growing GaAs/AlGaAs quantum wells are highly optimised. For these reasons GaAs/AlGaAs was chosen as the base material to construct a range of high quality asymmetric double quantum wells which were used to explore coherent coupling between spatially separated excitons. In this chapter the main conclusions are summarised.

Time-integrated photoluminescence, time-resolved photoluminescence and differential transmission pump-probe experiments were used to examine the carrier induced screening effect in ZnO/MgZnO QWs in detail. In the fluence dependent PL experiment, carrier induced screening of the internal electric field produced a blue shift of the E1-H1 transition energy due to excited carriers screening the built-in electric field. The time-resolved photoluminescence revealed a time dependent recombination lifetime, which increased from

0.18 μs to 5.8 μs , showing that the E1-H1 wavefunction overlap integral was varying as a function of the carrier density. The recombination dynamics on the ps timescale were examined using one-colour and two-colour differential transmission pump-probe experiments. In the one-colour experiment, the recombination lifetime over the first 100 ps varied from 160 to 250 ps as the excitation fluence was decreased, showing that the early time dynamics are also dependent on the carrier density. In the two-colour pump-probe experiment, where the probe had a larger photon energy than the pump, a strong absorption of the probe was observed immediately following the pump pulse, showing that the shielding of the internal electric field occurred in less than 1 ps.

The recombination dynamics were modeled by self-consistently solving the Schrödinger and the Poisson equations. The measured recombination dynamics were fit to the calculated dynamics and allowed the QW properties (transition energy, E1-H1 wavefunction overlap and carrier density) to be determined at any time following excitation. Combining the calculated and the measured dynamics revealed that for complete overlap of the E1 and H1 wavefunctions the recombination lifetime is expected to be between 1 and 2 ns. However, in the one-colour differential transmission pump-probe experiment, the recombination lifetime was shown to be much shorter than this. This result suggests that at high carrier densities the recombination lifetime no longer varies linearly with the overlap of the E1 and H1 wavefunctions, which is possibly due to some other recombination mechanism being activated at high densities. The good fit between the measured and the calculated dynamics strongly suggests that for carrier densities less than $2 \times 10^{12} \text{ cm}^{-2}$ the recombination dynamics are well described by the model used.

A range of ZnO/MgZnO QWs with graded barriers were also investigated to see if the combination of an internal electric field and graded barriers could be used to predictably control the E1-H1 transition energy and wavefunction overlap integral. The barrier designs examined in this investigation consisted of two square barrier QWs, three symmetric graded barrier QWs and two asymmetric QWs which were graded in opposite directions relative to the built-in electric field. Photoluminescence experiments showed good agreement between

the calculated and the measured interband transition energies. The two asymmetrically graded QWs had the largest difference between their calculated E1 and H1 wavefunction overlap integrals (0.25 and 0.71), therefore very different recombination lifetimes were predicted for these samples. A TRPL experiment using a streak camera provided a measure of the overlap integral for the E1 and H1 wavefunctions. The two square barrier QWs and the two asymmetrically graded barrier QWs clearly follow the same trend, where, as the calculated overlap integral for the E1 and H1 wavefunctions increased, the recombination lifetime decreased. The relationship between the E1-H1 wavefunction overlap integral and recombination lifetime for the symmetrically graded QWs deviated from the trend given by the other samples. Clear LO-phonon replicas were observed in the PL spectra for the symmetrically graded QWs, and not so for the square and asymmetrically graded QWs, which is consistent with these samples being wider than they were intended to be. Further investigation is required in order to explain these differences. Nonetheless, this work has shown that the combination of asymmetrically graded barriers and a built-in electric field can be used to predictably control the overlap integral for the E1 and H1 wavefunctions and the E1-H1 transition energy.

Four-wave mixing and two-dimensional Fourier transform spectroscopy were used to explore the coherent dynamics of excitons in asymmetric double quantum wells with an emphasis on spatially separated excitons. The 2DFT spectra suggested that the E1HH1 and E2HH2 excitons, the lowest energy heavy-hole excitons localised to opposite QWs, are coherently coupled. The strength of the coupling, which is given by the amplitude of the cross-peak in the 2DFT spectra, is largest for the narrowest barrier width and decreases as the barrier width is increased. In addition to this, a Raman-like coherence signal was observed. The Raman-like signal was only observed in S1-4, in which the coupling strength was the largest. In S1-6, the Raman-like signal was too weak to resolve on top of the transient grating signal.

The 2DFT spectra also revealed coupling between the E1LH1 and E2HH2 excitons. The only evidence for this is in the 2D spectra. Beating with a beat period equal to the energy

difference between the E1LH1 and E2HH2 excitons was not observed in the FWM signal and not resolved when using standard fitting techniques. This result clearly demonstrates the power of 2DFT spectroscopy.

The mechanism responsible for coupling the excitons was also discussed. Since the excitons are localised to spatially separated QWs, coupling mechanisms not dependent on wavefunction overlap were considered. For closely spaced excitons, dipole-dipole coupling appears to be the most likely mechanism, however, without further investigation, long-range coulomb interactions cannot be excluded.

Bibliography

- [1] J. W. Orton. *The story of semiconductors*. Oxford University Press, Oxford, 2004.
- [2] L. D. Forest. US Patent No. 879532. 1906.
- [3] Nobelprize.org - the transistor. <http://nobelprize.org/educational/physics/transistor/history/>.
- [4] M. Fox. *Optical properties of solids: Oxford master series in condensed matter physics*. Oxford University Press, Oxford, 2001.
- [5] P. Y. Yu and M. Cardona. *Fundamentals of semiconductors: Physics and materials properties*. Springer, Berlin, 2003.
- [6] M. D. Sturge. Optical absorption of gallium arsenide between 0.6 and 2.75 eV. *Physical Review*, 127(3):768–773, 1962.
- [7] M. A. Green and M. J. Keevers. Optical properties of intrinsic silicon at 300 K. *Progress in Photovoltaics*, 3(3):189–192, 1995.
- [8] S. Adachi. *GaAs and related materials: Bulk semiconducting and superlattice properties*. World Scientific, Singapore, 1994.
- [9] P. Harrison. *Quantum wells, wires, and dots: Theoretical and computational physics of semiconductor nanostructures*. Wiley, Hoboken; NJ, 2005.
- [10] J. L. M. Q. Gonzalez and D. Thompson. Getting started with Numerov’s method. *Computers in Physics*, 11:514–515, 1998.
- [11] T. Pang. *An introduction to computational physics*. Cambridge University Press, Cambridge, 1997.
- [12] J. Shah. *Ultrafast spectroscopy of semiconductors and semiconductor nanostructures*. Springer Verlag, Berlin, 1999.
- [13] D. S. Kim, J. Shah, J. E. Cunningham, T. C. Damen, W. Schafer, M. Hartmann, and S. Schmittrink. Giant excitonic resonance in time-resolved 4-wave-mixing in quantum-wells. *Physical Review Letters*, 68(7):1006–1009, 1992.

-
- [14] G. W. Hanson. *Fundamentals of nanoelectronics*. Pearson/Prentice Hall, Upper Saddle River, N.J., 2008.
- [15] H. D. Sun, T. Makino, N. T. Tuan, Y. Segawa, Z. K. Tang, G. K. L. Wong, M. Kawasaki, A. Ohtomo, K. Tamura, and H. Koinuma. Stimulated emission induced by exciton-exciton scattering in ZnO/ZnMgO multiquantum wells up to room temperature. *Applied Physics Letters*, 77(26):4250–4252, 2000.
- [16] D. M. Bagnall, Y. F. Chen, Z. Zhu, T. Yao, S. Koyama, M. Y. Shen, and T. Goto. Optically pumped lasing of ZnO at room temperature. *Applied Physics Letters*, 70(17):2230, 1997.
- [17] A. G. Thompson. MOCVD technology for semiconductors. *Materials Letters*, 30(4):255–263, 1997.
- [18] W. KAISER. *Ultrashort laser pulses and applications*. Springer-Verlag, Berlin, 1988.
- [19] G. D. Gilliland. Photoluminescence spectroscopy of crystalline semiconductors. *Materials Science and Engineering: Reports*, 18(3-6):99 – 399, 1997.
- [20] Hammamatsu. *Hammamatsu C6138(FESCA-200) Specifications Sheet*. Hammamatsu, Japan, 2010.
- [21] J. Takeda, K. Nakajima, S. Kurita, S. Tomimoto, S. Saito, and T. Suemoto. Time-resolved luminescence spectroscopy by the optical Kerr-gate method applicable to ultrafast relaxation processes. *Physical Review B*, 62(15):10083, 2000.
- [22] B. F. Feuerbacher, J. Kuhl, R. Eccleston, and K. Ploog. Quantum beats between the light and heavy hole excitons in a quantum-well. *Solid State Communications*, 74(12):1279–1283, 1990.
- [23] K. Leo, T. C. Damen, J. Shah, E. O. Gobel, and K. Kohler. Quantum beats of light hole and heavy hole excitons in quantum-wells. *Applied Physics Letters*, 57(1):19–21, 1990.
- [24] E. O. Gobel, K. Leo, T. C. Damen, J. Shah, S. Schmittrink, W. Schafer, J. F. Muller, and K. Kohler. Quantum beats of excitons in quantum-wells. *Physical Review Letters*, 64(15):1801–1804, 1990.
- [25] M. Koch, J. Feldmann, E. O. Gobel, P. Thomas, J. Shah, and K. Kohler. Coupling of exciton-transitions associated with different quantum-well islands. *Physical Review B*, 48(15):11480–11483, 1993.
- [26] D. Birkedal, V. G. Lyssenko, J. M. Hvam, and K. ElSayed. Continuum contribution to excitonic four-wave mixing due to interaction-induced nonlinearities. *Physical Review B*, 54(20):14250–14253, 1996.

- [27] S. T. Cundiff, M. Koch, W. H. Knox, J. Shah, and W. Stolz. Optical coherence in semiconductors: Strong emission mediated by nondegenerate interactions. *Physical Review Letters*, 77(6):1107–1110, 1996.
- [28] M. U. Wehner, D. Steinbach, and M. Wegener. Ultrafast coherent transients due to exciton-continuum scattering in bulk GaAs. *Physical Review B*, 54(8):R5211–R5214, 1996.
- [29] L. Allen and J. H. Eberly. *Optical resonance and two-level atoms*. Dover, New York, 1987.
- [30] C. F. Klingsirn. *Semiconductor optics*. Springer, Berlin, 2007.
- [31] W. Demtröder. *Laser spectroscopy: Basic concepts and instrumentation*. Springer, Berlin, 2002.
- [32] A. Honold, L. Schultheis, J. Kuhl, and C. W. Tu. Reflected degenerate 4-wave mixing on GaAs single quantum wells. *Applied Physics Letters*, 52(25):2105–2107, 1988.
- [33] T. Yajima and Y. Taira. Spatial optical parametric coupling of picosecond light-pulses and transverse relaxation effect in resonant media. *Journal of the physical society of Japan*, 47(5):1620–1626, 1979.
- [34] A. M. Weiner, S. De Silvestri, and E. P. Ippen. Three-pulse scattering for femtosecond dephasing studies: theory and experiment. *Journal of the Optical Society of America B*, 2(4):654–662, 1985.
- [35] D. M. Jonas. Two-dimensional femtosecond spectroscopy. *Annual review of physical chemistry*, 54:425–463, 2003.
- [36] X. Li, T. Zhang, S. Mukamel, R. P. Mirin, and S. T. Cundiff. Investigation of electronic coupling in semiconductor double quantum wells using coherent optical two-dimensional fourier transform spectroscopy. *Solid State Communications*, 149(9-10):361–366, 2009.
- [37] S. T. Cundiff. Coherent spectroscopy of semiconductors. *Optics Express*, 16(7):4639–4664, 2008.
- [38] A. D. Bristow, T. Zhang, M. E. Siemens, S. T. Cundiff, and R. P. Mirin. Separating homogeneous and inhomogeneous line widths of heavy- and light-hole excitons in weakly disordered semiconductor quantum wells. *The Journal of Physical Chemistry B*, 115(18):5365–5371, 2011.
- [39] E. Collini, C. Y. Wong, K. E. Wilk, P. M. G. Curmi, P. Brumer, and G. D. Scholes. Coherently wired light-harvesting in photosynthetic marine algae at ambient temperature. *Nature*, 463:644 – 647, 2010.

- [40] S. T. Cundiff, T. Zhang, A. D. Bristow, D. Karaickaj, and X. Dai. Optical two-dimensional Fourier transform spectroscopy of semiconductor quantum wells. *Accounts of Chemical Research*, 42(9):1423–1432, 2009.
- [41] K. W. Stone, D. B. Turner, K. Gundogdu, S. T. Cundiff, and K. A. Nelson. Exciton-exciton correlations revealed by two-quantum, two-dimensional fourier transform optical spectroscopy. *Accounts of Chemical Research*, 42(9):1452–1461, 2009.
- [42] K. W. Stone, K. Gundogdu, D. B. Turner, X. Li, S. T. Cundiff, and K. A. Nelson. Two-quantum 2d ft electronic spectroscopy of biexcitons in gaas quantum wells. *Science*, 324(5931):1169–1173, 2009.
- [43] D. B. Turner and K. A. Nelson. Coherent measurements of high-order electronic correlations in quantum wells. *Nature*, 466(7310):1089–1092, 2010.
- [44] Signatures of many-particle correlations in two-dimensional Fourier-transform spectra of semiconductor nanostructures. *Solid State Communications*, 142(3):154 – 158, 2007.
- [45] C. N. Borca, T. Zhang, X. Li, and S. T. Cundiff. Optical two-dimensional Fourier transform spectroscopy of semiconductors. *Chemical Physics Letters*, 416(4-6):311–315, 2005.
- [46] B. P. Zhang, N. T. Binh, K. Wakatsuki, C. Y. Liu, Y. Segawa, and N. Usami. Growth of ZnOMgZnO quantum wells on sapphire substrates and observation of the two-dimensional confinement effect. *Applied Physics Letters*, 86(3):1–3, 2005.
- [47] J. A. Davis, L. V. Dao, M. T. Do, P. Hannaford, K. A. Nugent, and H. M. Quiney. Noninterferometric two-dimensional fourier-transform spectroscopy of multilevel systems. *Physical Review Letters*, 100(22):227401, 2008.
- [48] K. W. DeLong, Rick Trebino, J. Hunter, and W. E. White. Frequency-resolved optical gating with the use of second-harmonic generation. *Journal of Optical Society of America B*, 11(11):2206–2215, 1994.
- [49] R. W. Gerchberg and W. O. Saxton. Practical algorithm for the determination of phase from image and diffraction plane pictures. *Optik (Stuttgart)*, 35(2):237–250, 1972.
- [50] J. A. Davis, T. R. Calhoun, K. A. Nugent, and H. M. Quiney. Ultrafast optical multidimensional spectroscopy without interferometry. *The Journal of Chemical Physics*, 134(2):024504, 2011.
- [51] Z. L. Wang. Zinc oxide nanostructures: Growth, properties and applications. *Journal of Physics Condensed Matter*, 16(25):829–858, 2004.
- [52] C. Jagadish and S. J. Pearton. *Zinc oxide bulk, thin films and nanostructures: processing, properties and applications*. Elsevier, Amsterdam; London, 2006.

- [53] H. Morkoç, S. Strite, G. B. Gao, M. E. Lin, B. Sverdlov, and M. Burns. Large-band-gap SiC, III-V nitride, and II-VI ZnSe-based semiconductor device technologies. *Journal of Applied Physics*, 76(3):1363–1398, 1994.
- [54] S. N. Mohammad, A. A. Salvador, and H. Morkoc. Emerging gallium nitride based devices. *Proceedings of the IEEE*, 83(10):1306–1355, 1995.
- [55] Leont'eva G. V. Apollonova L. A. Chilingirov R. K. Bobkov I. I. Kolesova, O. E. Therapeutic effect of the transfusion of UV-irradiated donor plasma in mechanical jaundice [lechebny ffekt transfuzii obluchenno uf-luchami donorsko plazmy pri mekhanicheskoy zheltukhe.]. *Biulleten" eksperimental'noi biologii i meditsiny*, 101(3):282–284, 1986.
- [56] J. W. Orton and C. T. Foxon. Group III nitride semiconductors for short wavelength light-emitting devices. *Reports on Progress in Physics*, 61:1–75, 1998.
- [57] U. Ozgur, D. Hofstetter, and H. Morkoc. ZnO devices and applications: A review of current status and future prospects. *Proceedings of the IEEE*, 98(7):1255–1268, 2010.
- [58] M. Hamza. Laser photoradiation therapy for neonatal jaundice. *Proceedings of SPIE - The International Society for Optical Engineering*, 737:93–97, 1987.
- [59] K. Okada, Y. Yamada, T. Taguchi, F. Sasaki, S. Kobayashi, T. Tani, S. Nakamura, and G. Shinomiya. Biexciton luminescence from GaN epitaxial layers. *Japanese Journal of Applied Physics* 2, 35(6 B):787, 1996.
- [60] D. C. Look. Recent advances in ZnO materials and devices. *Materials Science and Engineering B: Solid-State Materials for Advanced Technology*, 80(1-3):383–387, 2001.
- [61] A. Fulati, S. Usman, A., M. Riaz, G. Amin, O. Nur, and M. Willander. Miniaturized pH sensors based on zinc oxide nanotubes/nanorods. *Sensors*, 9(11):8911–8923, 2009.
- [62] B. H. Chu, B. S. Kang, F. Ren, C. Y. Chang, Y. L. Wang, S. J. Pearton, A. V. Glushakov, D. M. Dennis, J. W. Johnson, P. Rajagopal, J. C. Roberts, E. L. Piner, and K. J. Linthicum. Enzyme-based lactic acid detection using AlGaIn/GaN high electron mobility transistors with ZnO nanorods grown on the gate region, journal = Applied Physics Letters, year = 2008, volume = 93, number = 4.
- [63] Yefan Chen and D. M. Bagnall. Plasma assisted molecular beam epitaxy of ZnO on c-plane sapphire: Growth and characterization. *Journal of Applied Physics*, 84(7):3912, 1998.
- [64] Z. G. Yu, P. Wu, and H. Gong. Theoretical and experimental studies on oxygen vacancy in p-type ZnO. *Physica B: Condensed Matter*, 401-402:417–420, 2007.

- [65] J. L. Lyons, A. Janotti, and C. G. Van de Walle. Why nitrogen cannot lead to *p*-type conductivity in ZnO. *Applied Physics Letters*, 95(25), 2009.
- [66] C. Klingshirn. *Zinc oxide : From fundamental properties towards novel applications*. Springer, Heidelberg, 2010.
- [67] C. Klingshirn. ZnO: From basics towards applications. *Physica Status Solidi (B) Basic Research*, 244(9):3027–3073, 2007.
- [68] T. Makino, K. Tamura, C. H. Chia, Y. Segawa, M. Kawasaki, A. Ohtomo, and H. Koinuma. Radiative recombination of electron-hole pairs spatially separated due to quantum-confined Stark and Franz-Keldish effects in ZnO/Mg_{0.27}Zn_{0.73}O quantum wells. *Applied Physics Letters*, 81(13):2355, 2002.
- [69] T. Makino, A. Ohtomo, C. H. Chia, Y. Segawa, H. Koinuma, and M. Kawasaki. Internal electric field effect on luminescence properties of ZnO/(Mg,Zn)O quantum wells. *Physica E: Low-Dimensional Systems and Nanostructures*, 21(2-4):671–675, 2004.
- [70] C. Morhain, T. Bretagnon, P. Lefebvre, X. Tang, P. Valvin, T. Guillet, B. Gil, T. Taliercio, M. Teisseire-Doninelli, B. Vinter, and C. Deparis. Internal electric field in wurtzite ZnO Zn_{0.78}Mg_{0.22}O quantum wells. *Physical Review B*, 72(24):241305(R), 2005.
- [71] M. Yano, K. Hashimoto, K. Fujimoto, K. Koike, S. Sasa, M. Inoue, Y. Uetsuji, T. Ohnishi, and K. Inaba. Polarization-induced two-dimensional electron gas at Zn_{1-x}Mg_xO/ZnO heterointerface. *Journal of Crystal Growth*, 301-302:353–357, 2007.
- [72] M. W. Allen, P. Miller, R. J. Reeves, and S. M. Durbin. Influence of spontaneous polarization on the electrical and optical properties of bulk, single crystal ZnO. *Applied Physics Letters*, 90(6):062104, 2007.
- [73] J. A. Davis and C. Jagadish. Ultrafast spectroscopy of ZnO/ZnMgO quantum wells. *Laser & Photonics Review*, 3(1-2):85–96, 2009.
- [74] D. A. B. Miller, D. S. Chemla, T. C. Damen, A. C. Gossard, W. Wiegmann, T. H. Wood, and C. A. Burrus. Band-edge electroabsorption in quantum well structures: The quantum-confined stark effect. *Physical Review Letters*, 53(22):2173–2176, 1984.
- [75] D. A. B. Miller, D. S. Chemla, T. C. Damen, A. C. Gossard, W. Wiegmann, T. H. Wood, and C. A. Burrus. Electric field dependence of optical absorption near the band gap of quantum-well structures. *Physical Review B*, 32(2):1043–1060, 1985.
- [76] H. Brown. *Zinc oxide rediscovered*. The New Jersey Zinc Company, New York, 1957.
- [77] Tang Z. K. Wong G. K. L. Zu, P. et al. Ultraviolet spontaneous and stimulated emissions from ZnO microcrystallite thin films at room temperature. *Solid State Communications*, 103(8):459–463, 1997.

- [78] Wong G. K. L. Yu P. Tang, Z. K. et al. Room-temperature ultraviolet laser emission from self-assembled ZnO microcrystallite thin films. *Applied Physics Letters*, 72(25):3270–3272, 1998.
- [79] A. Ohtomo, M. Kawasaki, T. Koida, K. Masubuchi, H. Koinuma, Y. Sakurai, Y. Yoshida, T. Yasuda, and Y. Segawa. $Mg_xZn_{1-x}O$ as a II-VI widegap semiconductor alloy. *Applied Physics Letters*, 72(19):2466–2468, 1998.
- [80] A. Ohtomo, M. Kawasaki, I. Ohkubo, H. Koinuma, T. Yasuda, and Y. Segawa. Structure and optical properties of ZnO/ $Mg_{0.2}Zn_{0.8}O$ superlattices. *Applied Physics Letters*, 75(7):980–982, 1999.
- [81] A. Ohtomo, K. Tamura, K. Saikusa, K. Takahashi, T. Makino, Y. Segawa, H. Koinuma, and M. Kawasaki. Single crystalline ZnO films grown on lattice-matched $ScAlMgO_4(0001)$ substrates. *Applied Physics Letters*, 75(17):2635–2637, 1999.
- [82] T. Makino, C. H. Chia, N. T. Tuan, H. D. Sun, Y. Segawa, M. Kawasaki, A. Ohtomo, K. Tamura, and H. Koinuma. Room-temperature luminescence of excitons in ZnO/(Mg,Zn)O multiple quantum wells on lattice-matched substrates. *Applied Physics Letters*, 77(7):975–977, 2000.
- [83] A. Ohtomo, K. Tamura, M. Kawasaki, T. Makino, Y. Segawa, Z. K. Tang, G. K. L. Wong, Y. Matsumoto, and H. Koinuma. Room-temperature stimulated emission of excitons in ZnO/(Mg,Zn)O superlattices. *Applied Physics Letters*, 77(14):2204–2206, 2000.
- [84] L Zou, ZZ Ye, JY Huang, and BH Zhao. Structural characterization and photoluminescent properties of $Zn_{1-x}Mg_xO$ films on silicon. *Chinese Physics Letters*, 19(9):1350–1352, 2002.
- [85] P. Misra, T. K. Sharma, S. Porwal, and L. M. Kukreja. Room temperature photoluminescence from ZnO quantum wells grown on (0001) sapphire using buffer assisted pulsed laser deposition. *Applied Physics Letters*, 89(16):161912–3, 2006.
- [86] H. D. Sun, T. Makino, Y. Segawa, M. Kawasaki, A. Ohtomo, K. Tamura, and H. Koinuma. Biexciton emission from ZnO/ $Zn_{0.74}Mg_{0.26}O$ multi-quantum wells. *Applied Physics Letters*, 78(22):3385–3387, 2001.
- [87] C. H. Chia, T. Makino, K. Tamura, Y. Segawa, M. Kawasaki, A. Ohtomo, and H. Koinuma. Confinement-enhanced biexciton binding energy in ZnO/ $ZnMgO$ multiple quantum wells. *Applied Physics Letters*, 82(12):1848–1850, 2003.
- [88] J. A. Davis, L. Van Dao, X. Wen, P. Hannaford, V. A. Coleman, H. H. Tan, C. Jagadish, K. Koike, S. Sasa, M. Inoue, and M. Yano. Observation of coherent biexcitons in ZnO/ $ZnMgO$ multiple quantum wells at room temperature. *Applied Physics Letters*, 89(18), 2006.

- [89] T. Gruber, C. Kirchner, R. Kling, F. Reuss, and A. Waag. ZnMgO epilayers and ZnO-ZnMgO quantum wells for optoelectronic applications in the blue and UV spectral region. *Applied Physics Letters*, 84(26):5359–5361, 2004.
- [90] J. A. Davis, L. V. Dao, X. Wen, C. Ticknor, P. Hannaford, V. A. Coleman, H. H. Tan, C. Jagadish, K. Koike, S. Sasa, M. Inoue, and M. Yano. Suppression of the internal electric field effects in ZnO/Zn_{0.7}Mg_{0.3}O quantum wells by ion-implantation induced intermixing. *Nanotechnology*, 19(5), 2008.
- [91] T. Bretagnon, P. Lefebvre, T. Guillet, T. Taliercio, B. Gil, and C. Morhain. Barrier composition dependence of the internal electric field in ZnO Zn_{1-x} Mg_x O quantum wells. *Applied Physics Letters*, 90(20):201912, 2007.
- [92] B. P. Zhang, B. L. Liu, J. Z. Yu, Q. M. Wang, C. Y. Liu, Y. C. Liu, and Y. Segawa. Photoluminescence and built-in electric field in ZnO/Mg 0.1Zn0.9O quantum wells. *Applied Physics Letters*, 90(13), 2007.
- [93] V. A. Coleman, M. Buda, H. H. Tan, C. Jagadish, M. R. Phillips, K. Koike, S. Sasa, M. Inoue, and M. Yano. Observation of blue shifts in ZnO/ZnMgO multiple quantum well structures by ion-implantation induced intermixing. *Semiconductor Science and Technology*, 21(3), 2006.
- [94] J. M. Chauveau, C. Morhain, M. Teisseire, M. Lagt, C. Deparis, J. Zuniga-Perez, and B. Vinter. (Zn, Mg)O/ZnO-based heterostructures grown by molecular beam epitaxy on sapphire: Polar vs. non-polar. *Microelectronics Journal*, 40(3):512–516, 2009.
- [95] B. Meyer. Private communication - Materials Research Society (MRS) 2009 Fall Meeting. 2009.
- [96] J. M. Chauveau, M. Laugt, P. Venegues, M. Teisseire, B. Lo, C. Deparis, C. Morhain, and B. Vinter. Non-polar a-plane ZnMgO/ZnO quantum wells grown by molecular beam epitaxy. *Semiconductor Science and Technology*, 23(3), 2008.
- [97] X. Q. Gu, L. P. Zhu, Z. Z. Ye, H. P. He, Y. Z. Zhang, F. Huang, M. X. Qiu, Y. J. Zeng, F. Liu, and W. Jaeger. Room-temperature photoluminescence from ZnOZnMgO multiple quantum wells grown on Si(111) substrates. *Applied Physics Letters*, 91(2), 2007.
- [98] T. Makino, Y. Segawa, A. Tsukazaki, A. Ohtomo, and M. Kawasaki. Photoexcitation screening of the built-in electric field in ZnO single quantum wells. *Applied Physics Letters*, 93(12), 2008.
- [99] T. Makino, Y. Segawa, M. Kawasaki, and H. Koinuma. Optical properties of excitons in ZnO-based quantum well heterostructures. *Semiconductor Science and Technology*, 20(4), 2005.

- [100] T. Bretagnon, P. Lefebvre, P. Valvin, B. Gil, C. Morhain, and X. Tang. Time resolved photoluminescence study of ZnO/(Zn,Mg)O quantum wells. *Journal of Crystal Growth*, 287(1):12–15, 2006.
- [101] T. Guillet, T. Bretagnon, T. Taliercio, P. Lefebvre, B. Gil, C. Morhain, and X. Tang. Time-resolved spectroscopy of excitonic transitions in ZnO/(Zn, Mg)O quantum wells. *Superlattice Microst.*, 41(5-6):352–359, 2007.
- [102] A. K. Sharma, J. Narayan, J. F. Muth, C. W. Teng, C. Jin, A. Kvit, R. M. Kolbas, and O. W. Holland. Optical and structural properties of epitaxial $\text{mg}_x\text{zn}_{1-x}\text{O}$ alloys. *Applied Physics Letters*, 75(21):3327–3329, 1999.
- [103] Jepsen P.U. Monozon B.S. Koch M. Lahmann S. Rossow U. Hangleiter A. Turchinovich, D. Ultrafast polarization dynamics in biased quantum wells under strong femtosecond optical excitation. *Physical Review B*, 68(24), 2003.
- [104] Hu L. Zhang H. Huo, B. The Huang-Rhys factor and the strength of exciton-LO phonon coupling in ZnO/Mg_{0.15}Zn_{0.85}O superlattices. *Materials Science in Semiconductor Processing*, 10(6):287–290, 2007.
- [105] J. W. Sun and B. P. Zhang. Well-width dependence of exciton-longitudinal-optical-phonon coupling in MgZnO/ZnO single quantum wells. *Nanotechnology*, 19(48), 2008.
- [106] S Kalliakos, P Lefebvre, and T Taliercio. Nonlinear behavior of photoabsorption in hexagonal nitride quantum wells due to free carrier screening of the internal fields. *Physical Review B*, 67(20), 2003.
- [107] D Turchinovich, BS Monozon, and PU Jepsen. Role of dynamical screening in excitation kinetics of biased quantum wells: Nonlinear absorption and ultrabroadband terahertz emission. *Journal of Applied Physics*, 99(1), 2006.
- [108] D. Turchinovich and P. Uhd Jepsen. Nonlinear excitation kinetics of biased quantum wells: Coherent dynamical screening effect. *Physica Status Solidi C - Current Topics in Solid State Physics*, 3(7):2494–2497, 2006.
- [109] A. Pinos, S. Marcinkevicius, K. Liu, M. S. Shur, E. Kuokstis, G. Tamulaitis, R. Gaska, J. Yang, and W. Sun. Screening dynamics of intrinsic electric field in AlGa_N quantum wells. *Applied Physics Letters*, 92(6), 2008.
- [110] F. Chen, W. D. Kirkey, A. Furis, M. C. Cheung, and A. N. Cartwright. Excitonic field screening and bleaching in InGa_N/Ga_N multiple quantum wells. *Solid State Communicatons*, 125(11-12):617–622, 2003.
- [111] K. Omae, Y. Kawakami, S. Fujita, M. Yamada, Y. Narukawa, and T. Mukai. Effects of internal electric field and carrier density on transient absorption spectra in a thin Ga_N epilayer. *Physical Review B*, 65(7):073308, 2002.

- [112] K. Omae, Y. Kawakami, S. Fujita, Y. Narukawa, and T. Mukai. Effects of internal electrical field on transient absorption in $In_xGa_{1-x}N$ thin layers and quantum wells with different thickness by pump and probe spectroscopy. *Physical Review B*, 68(8):085303, 2003.
- [113] P Lefebvre, S Kalliakos, T Bretagnon, P Valvin, T Taliercio, B Gil, N Grandjean, and J Massies. Observation and modeling of the time-dependent descreening of internal electric field in a wurtzite GaN/Al_{0.15}Ga_{0.85}N quantum well after high photoexcitation. *Physical Review B*, 69(3), 2004.
- [114] G. Coli and K. K. Bajaj. Excitonic transitions in ZnO/MgZnO quantum well heterostructures. *Applied Physics Letters*, 78(19):2861–2863, 2001.
- [115] W. Chen and T. G. Andersson. Quantum-confined stark shift for differently shaped quantum wells. *Semiconductor Science and Technology*, 7(6):828–836, 1992.
- [116] K. K. Law, R. H. Yan, A. C. Gossard, and J. L. Merz. Electric field induced absorption changes in triangular quantum wells grown by pulsed beam molecular beam epitaxy technique. *Journal of Applied Physics*, 67(10):5, 1990.
- [117] P. W. Yu, D. C. Reynolds, G. D. Sanders, K. K. Bajaj, C. E. Stutz, and K. R. Evans. Electric-field effects of the excitons in asymmetric triangular Al_xGa_{1-x}As-GaAs quantum wells. *Physical Review B*, 43(5):4344, 1991.
- [118] G. D. Sanders and K. K. Bajaj. Theory of electroabsorption in asymmetric graded gap quantum wells. *Journal of Vacuum Science and Technology B*, 5(4):1295, 1987.
- [119] G. D. Sanders and K. K. Bajaj. Absorptive electrooptic spatial light modulators with different quantum well profiles. *Journal of Applied Physics*, 68(10):9, 1990.
- [120] L. Wang, R. Li, Z. Yang, D. Li, T. Yu, N. Liu, L. Liu, W. Chen, and X. Hu. High spontaneous emission rate asymmetrically graded 480 nm InGaN/GaN quantum well light-emitting diodes. *Applied Physics Letters*, 95(21):3, 2009.
- [121] J. Thalken, W. F. Li, S. Haas, and A. F. J. Levi. Adaptive design of excitonic absorption in broken-symmetry quantum wells. *Applied Physics Letters*, 85(1):121–123, 2004.
- [122] R. M. Farrell, D. F. Feezell, M. C. Schmidt, D. A. Haeger, K. M. Kelchner, K. Iso, H. Yamada, M. Saito, K. Fujito, D. A. Cohen, J. S. Speck, S. P. Denbaars, and S. Nakamura. Continuous-wave operation of AlGaIn-cladding-free nonpolar m-plane InGaIn/GaN laser diodes. *Japanese Journal of Applied Physics, Part 2: Letters*, 46(29-32), 2007.
- [123] J. Park and Y. Kawakami. Photoluminescence property of InGaIn single quantum well with embedded AlGaIn layer. *Applied Physics Letters*, 88(20), 2006.
- [124] S. H. Park, J. Park, and E. Yoon. Optical gain in InGaIn/GaN quantum well structures with embedded AlGaIn layer. *Applied Physics Letters*, 90(2), 2007.

- [125] S. H. Park, D. Ahn, and J. W. Kim. High-efficiency staggered 530 nm InGaN/InGaN/GaN quantum-well light-emitting diodes. *Applied Physics Letters*, 94(4), 2009.
- [126] S. H. Park, D. Ahn, B. H. Koo, and J. W. Kim. Electronic and optical properties of staggered InGaN/InGaN quantum-well light-emitting diodes. *Physica Status Solidi (A) Applications and Materials*, 206(11):2637–2640, 2009.
- [127] R. A. Arif, Y. K. Ee, and N. Tansu. Polarization engineering via staggered InGaN quantum wells for radiative efficiency enhancement of light emitting diodes. *Applied Physics Letters*, 91(9):3, 2007.
- [128] R. A. Arif, H. Zhao, and N. Tansu. Type-II InGaN-GaNAs quantum wells for lasers applications. *Applied Physics Letters*, 92(1), 2008.
- [129] R. A. Arif, H. P. Zhao, Y. K. Ee, and N. Tansu. Spontaneous emission and characteristics of staggered InGaN quantum-well light-emitting diodes. *IEEE Journal of Quantum Electronics*, 44(5-6):573–580, 2008.
- [130] H. Zhao, R. A. Arif, and N. Tansu. Self-consistent gain analysis of type-II 'W' InGaN-GaNAs quantum well lasers. *Journal of Applied Physics*, 104(4), 2008.
- [131] H. Zhao, R. A. Arif, Y. K. Ee, and N. Tansu. Optical gain analysis of strain-compensated InGaN-AlGaN quantum well active regions for lasers emitting at 420-500 nm. *Optical and Quantum Electronics*, 40(5-6):301–306, 2008.
- [132] H. Zhao, R. A. Arif, Y. K. E, and N. Tansu. Self-consistent analysis of strain-compensated InGaN-AlGaN quantum wells for lasers and light-emitting diodes. *IEEE Journal of Quantum Electronics*, 45(1):66–78, 2009.
- [133] H. Zhao, R. A. Arif, and N. Tansu. Design analysis of staggered InGaN quantum wells light-emitting diodes at 500-540 nm. *IEEE Journal on Selected Topics in Quantum Electronics*, 15(4):1104–1114, 2009.
- [134] H. Zhao, G. Liu, X. H. Li, G. S. Huang, J. D. Poplawsky, S. T. Penn, V. Dierolf, and N. Tansu. Growths of staggered InGaN quantum wells light-emitting diodes emitting at 520-525 nm employing graded growth-temperature profile. *Applied Physics Letters*, 95(6), 2009.
- [135] H. P. Zhao, G. Y. Liu, X. H. Li, R. A. Arif, G. S. Huang, J. D. Poplawsky, S. T. Penn, V. Dierolf, and N. Tansu. Design and characteristics of staggered InGaN quantum-well light-emitting diodes in the green spectral regime. *Optoelectronics, IET*, 3(6):283–295, 2009.
- [136] U. Ozgur, Y. I. Alivov, C. Liu, A. Teke, M. A. Reshchikov, S. Dogan, V. Avrutin, S. J. Cho, and H. Morkoc. A comprehensive review of ZnO materials and devices. *Journal of Applied Physics*, 98(4):041301, 2005.

- [137] M. Yano, K. Ogata, F. P. Yan, K. Koike, S. Sasa, and Inoue M. ZnO and ZnMgO growth by molecular beam epitaxy. *Materials Research Society Symposium Proceedings*, 744:M3.1, 2003.
- [138] V. G. Lyssenko, J. Erland, I. Balslev, K.-H. Pantke, B. S. Razbirin, and J. M. Hvam. Nature of nonlinear 4-wave-mixing beats in semiconductors. *Physical Review B*, 48(8):5720–5723, 1993.
- [139] J. Erland and I. Balslev. Theory of quantum beat and polarization interference in 4-wave-mixing. *Physical Review A*, 48(3):R1765–R1768, 1993.
- [140] M. Batsch, T. Meier, P. Thomas, M. Lindberg, S. W. Koch, and J. Shah. Dipole-dipole coupling of excitons in double-quantum wells. *Physical Review B*, 48(16):11817–11826, 1993.
- [141] M. Koch, J. Feldmann, G. von Plessen, ouml, E. O. bel, P. Thomas, and K. hler. Quantum beats versus polarization interference: An experimental distinction. *Physical Review Letters*, 69(25):3631, 1992.
- [142] A. Euteneuer, E. Finger, M. Hofmann, W. Stolz, T. Meier, P. Thomas, S. W. Koch, W. W. Rühle, R. Hey, and K. Ploog. Coherent excitation spectroscopy on inhomogeneous exciton ensembles. *Physical Review Letters*, 83(10):2073–2076, 1999.
- [143] E. Finger, S. Kraft, A. Euteneuer, M. Hofmann, W. Stolz, and W.W. Rhle. Coherent excitation spectroscopy of disordered quantum-well structures. *Physica Status Solidi (B)*, 221(1):373–378, 2000.
- [144] J. A. Davis, J. J. Wathen, V. Blanchet, and R. T. Phillips. Time-resolved four-wave-mixing spectroscopy of excitons in a single quantum well. *Physical Review B*, 75(3):035317, 2007.
- [145] J. Kasprzak, B. Patton, V. Savona, and W. Langbein. Coherent coupling between distant excitons revealed by two-dimensional nonlinear hyperspectral imaging. *Nature Photonics*, 5(1):57–63, 2010.
- [146] A. M. Fox, D. A. B. Miller, G. Livescu, J. E. Cunningham, and W. Y. Jan. Excitonic effects in coupled quantum wells. *Physical Review B*, 44(12):6231, 1991.
- [147] D. K. Kim and D. S. Citrin. Electric-field-induced strong mixing between e1-hh1 and e1-hh2 excitons in asymmetric double quantum wells. *Physical Review B*, 76(12):125305, 2007.
- [148] D. K. Kim and D. S. Citrin. Strong excitonic mixing effect in asymmetric double quantum wells: On the optimization of electroabsorption modulators. *Physica Status Solidi (C)*, 5(7):2400–2403, 2008.

- [149] S. Y. Lei, B. Shen, and G. Y. Zhang. Anticrossing gap between pairs of the subbands in $\text{Al}_x\text{Ga}_{1-x}\text{N}/\text{GaN}$ double quantum wells. *Chinese Physics Letters*, 23(2):450, 2006.
- [150] A. M. Fox, D. A. B. Miller, G. Livescu, J. E. Cunningham, J. E. Henry, and W. Y. Jan. Excitons in resonant coupling of quantum wells. *Physical Review B*, 42(3):1841, 1990.
- [151] T. Kamizato and M. Matsuura. Excitons in double quantum wells. *Physical Review B*, 40(12):8378, 1989.
- [152] H. Schneider, H. T. Grahn, K. v. Klitzing, and K. Ploog. Sequential resonant tunneling of holes in GaAs-AlAs superlattices. *Physical Review B*, 40(14):10040, 1989.
- [153] G. Livescu, A. M. Fox, D. A. B. Miller, T. Sizer, W. H. Knox, A. C. Gossard, and J. H. English. Resonantly enhanced electron tunneling rates in quantum wells. *Physical Review Letters*, 63(4):438, 1989.
- [154] P. Lawaetz. Valence-band parameters in cubic semiconductors. *Physical Review B*, 4(10):3460, 1971.
- [155] A. Raymond, J. L. Robert, and C. Bernard. Electron effective mass in heavily doped GaAs. *Journal of Physics C - Solid State Physics*, 12(12):2289–2293, 1979.
- [156] L. Pavesi and M. Guzzi. Photoluminescence of $\text{Al}_x\text{Ga}_{1-x}\text{As}$ alloys. *Journal of Applied Physics*, 75(10):4779–4842, 1994.
- [157] J. S. Blakemore. Semiconducting and other major properties of gallium-arsenide. *Journal of Applied Physics*, 53(10):R123–R181, 1982.
- [158] D. E. Aspnes. GaAs lower conduction-band minima: Ordering and properties. *Physical Review B*, 14(12):5331, 1976.
- [159] H. Okumura, S. Misawa, S. Yoshida, and S. Gonda. Determination of the conduction-band discontinuities of GaAs/ $\text{Al}_x\text{Ga}_{1-x}\text{As}$ interfaces by capacitance-voltage measurements. *Applied Physics Letters*, 46(4):377–379, 1985.
- [160] R. P. Leavitt and J. W. Little. Simple method for calculating exciton binding energies in quantum-confined semiconductor structures. *Physical Review B*, 42(18):11774, 1990.
- [161] R. L. Greene, K. K. Bajaj, and D. E. Phelps. Energy levels of wannier excitons in GaAs- $\text{Ga}_{1-x}\text{Al}_x\text{As}$ quantum-well structures. *Physical Review B*, 29(4):1807, 1984.
- [162] C. Priester, G. Allan, and M. Lannoo. Wannier excitons in GaAs/ $\text{Ga}_{1-x}\text{Al}_x\text{As}$ quantum-well structures: Influence of the effective-mass mismatch. *Physical Review B*, 30(12):7302, 1984.
- [163] A. G. Milnes. *Deep Impurities in Semiconductors*. John Wiley and Sons, New York, 1973.

- [164] D. Y. Oberli, J. Shah, T. C. Damen, C. W. Tu, T. Y. Chang, D. A. B. Miller, J. E. Henry, R. F. Kopf, N. Sauer, and A. E. DiGiovanni. Direct measurement of resonant and nonresonant tunneling times in asymmetric coupled quantum wells. *Physical Review B*, 40(5):3028, 1989.
- [165] S. Haacke, N. T. Pelekanos, H. Mariette, M. Zigone, A. P. Heberle, and W. W. Rühle. Tunneling dynamics in CdTe/(Cd,Zn)Te asymmetric double-quantum-well structures. *Physical Review B*, 47(24):16643–16646, 1993.
- [166] D. Y. Oberli, J. Shah, T. C. Damen, J. M. Kuo, J. E. Henry, J. Lary, and S. M. Goodnick. Optical phonon-assisted tunneling in double quantum-well structures. *Applied Physics Letters*, 56(13):1239–1241, 1990.
- [167] S. T. Cundiff. Effects of correlation between inhomogeneously broadened transitions on quantum beats in transient four-wave mixing. *Physical Review A*, 49(4):3114, 1994.
- [168] A. M. T. Kim, S. Hunsche, T. Dekorsy, H. Kurz, and K. Köhler. *Applied Physics Letters*, 68:2956, 1996.
- [169] K. Leo, E. O. Göbel, T. C. Damen, J. Shah, S. Schmitt-Rink, W. Schäfer, J. F. Müller, K. Köhler, and P. Ganser. Subpicosecond 4-wave-mixing in GaAs/Al_xGa_{1-x}As quantum-wells. *Physical Review B*, 44(11):5726–5737, 1991.
- [170] A. Honold, L. Schultheis, J. Kuhl, and C. W. Tu. Collision broadening of two-dimensional excitons in a GaAs single quantum well. *Physical Review B*, 40(9):6442–6445, 1989.
- [171] A. V. Gopal and A. S. Vengurlekar. Well-width dependence of light-hole exciton dephasing in GaAs quantum wells. *Physical Review B*, 62(7):4624, 2000.
- [172] J. Erland, K.-H. Pantke, V. Mizeikis, V. G. Lyssenko, and J. M. Hvam. Spectrally resolved 4-wave-mixing in semiconductors - influence of inhomogeneous broadening. *Physical Review B*, 50(20):15047–15055, 1994.
- [173] J. Erland, D. Birkedal, V. G. Lyssenko, and J. M. Hvam. Spectral signatures of excitonic four-wave mixing signals in GaAs multiple quantum wells. *Journal of the Optical Society of America B-Optical Physics*, 13(5):981–988, 1996.
- [174] J. M. Hvam, D. Birkedal, V. Mizeikis, and K. El Sayed. Interband coherence in semiconductors; Excitons and beyond. *Journal of Luminescence*, 72-4:25–28, 1997.
- [175] J. Hegarty, L. Goldner, and M. D. Sturge. “Localized and delocalized two-dimensional excitons in GaAs – AlGaAs multiple-quantum-well structures”. *Physical Review B*, 30(12):7346, 1984.
- [176] J. Hegarty and M. D. Sturge. Studies of exciton localization in quantum-well structures by nonlinear-optical techniques. *Journal of the Optical Society of America B-Optical Physics*, 2(7):1143–1154, 1985.

-
- [177] H. Wang, M. Jiang, and D. G. Steel. Measurement of phonon-assisted migration of localized excitons in GaAs/AlGaAs multiple-quantum-well structures. *Physical Review Letters*, 65(10):1255, 1990.
- [178] M. D. Webb, S. T. Cundiff, and D. G. Steel. Observation of time-resolved picosecond stimulated photon echoes and free polarization decay in GaAs/AlGaAs multiple quantum wells. *Physical Review Letters*, 66(7):934, 1991.
- [179] M. D. Webb, S. T. Cundiff, and D. G. Steel. Stimulated-picosecond-photon-echo studies of localized exciton relaxation and dephasing in GaAs/Al_xGa_{1-x}As multiple quantum wells. *Physical Review B*, 43(15):12658, 1991.
- [180] S. T. Cundiff and D. G. Steel. Coherent transient spectroscopy of excitons in gaas-algaas quantum wells. *Quantum Electronics, IEEE Journal of*, 28(10):2423–2433, 1992.
- [181] S. G. Carter, Z. Chen, and S. T. Cundiff. Echo peak-shift spectroscopy of non-Markovian exciton dynamics in quantum wells. *Physical Review B*, 76(12):4, 2007.
- [182] K. Leo, M. Wegener, J. Shah, D. S. Chemla, E. O. Göbel, T. C. Damen, S. Schmitt-Rink, and W. Schäfer. Effects of coherent polarization interactions on time-resolved degenerate four-wave mixing. *Physical Review Letters*, 65(11):1340, 1990.
- [183] A. G. V. Spivey and S. T. Cundiff. Inhomogeneous dephasing of heavy-hole and light-hole exciton coherences in GaAs quantum wells. *Journal of the Optical Society of America B*, 24(3):664–670, 2007.
- [184] K. B. Ferrio and D. G. Steel. Raman quantum beats of interacting excitons. *Physical Review Letters*, 80(4):786, 1998.
- [185] L. Yang, T. Zhang, A.D. Bristow, S.T. Cundiff, and S. Mukamel. Isolating excitonic raman coherence in semiconductors using two-dimensional correlation spectroscopy. *The Journal of Chemical Physics*, 129(23):234711, 2008.
- [186] H. Lee, Y. C. Cheng, and G. R. Fleming. Coherence dynamics in photosynthesis: Protein protection of excitonic coherence. *Science*, 316(5830):1462–1465, 2007.

Appendix A

Publications of the author

Publications:

1. C. R. Hall, L. Dao, K. Koike, S. Sasa, H. H. Tan, M. Inoue, M. Yano, P. Hannaford, C. Jagadish, and J. A. Davis. Recombination dynamics and screening of the internal electric field in ZnO/Zn_xMg_{1-x}O multiple quantum wells, *Physical Review B*, 80, 235316 (2009);
2. C. R. Hall, L. V. Dao, K. Koike, S. Sasa, H. H. Tan, M. Inoue, M. Yano, C. Jagadish and J. A. Davis. Using graded barriers to control the optical properties of ZnO/Zn_{0.7}Mg_{0.3}O quantum wells with an intrinsic internal electric field, *Applied Physics Letters*, 96, 193117 (2010);
3. C. R. Hall, L. V. Dao, K. Koike, S. Sasa, H. H. Tan, M. Inoue, M. Yano, C. Jagadish and J. A. Davis. Dynamics of Carriers and the Influence of the Quantum Confined Stark Effect in ZnO/ZnMgO Quantum Wells, *Proceedings of the international conference on ultrafast phenomena*, Snowmass Village, Colorado, 2010
4. J. A. Davis, C. R. Hall, L. V. Dao, K. A. Nugent, H. M. Quiney, H. H. Tan, and C. Jagadish. Three-Dimensional Electronic Spectroscopy of Excitons in Asymmetric Double Quantum Wells, *Submitted to the Journal of Chemical Physics*;

Conference Presentations:

1. C. R. Hall, L. V. Dao, K. Koike, S. Sasa, H. H. Tan, M. Inoue, M. Yano, C. Jagadish and J. A. Davis. Dynamics of carriers and the influence of the quantum confined stark effect in ZnO/ZnMgO quantum wells. *Conference on Optoelectronic and Microelectronic Materials and Devices (COMMAD)*, pp.45-46, 12-15 Dec. 2010
2. C. R. Hall, L.V. Dao, H.H. Tan, C. Jagadish, and J.A. Davis. Observation of spatially separated coherent coupling near the LO phonon resonance within asymmetric double quantum wells. *Conference on Optoelectronic and Microelectronic Materials and Devices (COMMAD)*, 2010 , pp.115-116, 12-15 Dec. 2010
3. C. R. Hall, L. V. Dao, K. Koike, S. Sasa, H. H. Tan, M. Inoue, M. Yano, C. Jagadish and J. A. Davis. Dynamics of carriers and the influence of the quantum confined Stark effect in ZnO/ZnMgO quantum wells. *International Conference on Ultrafast Phenomena*, OSA Technical Digest (CD) (Optical Society of America, 2010), TuE45
4. C. R. Hall, L. V. Dao, K. Koike, S. Sasa, H. H. Tan, M. Inoue, M. Yano, C. Jagadish and J. A. Davis. Dynamics of carriers and the influence of the quantum confined stark effect

in ZnO/ZnMgO quantum wells. *Australian Ultrafast Laser Users Workshop (AULUW)*, Melbourne, Feb 11-12, 2010

5. C. R. Hall, J. A. Davis, L. V. Dao, P. Hannaford, H. H. Tan, C. Jagadish, K. Koike, S. Sasa, M. Inoue and M. Yano. The Quantum Confined Stark Effect in Square and Graded Barrier ZnO/ZnMgO Quantum Wells. *The Materials Research Society - Fall Meeting*, Boston, 2009.

6. C. R. Hall, J. A. Davis, L. V. Dao, P. Hannaford, H. H. Tan, C. Jagadish, K. Koike, S. Sasa, M. Inoue and M. Yano. Study of the Quantum Confined Stark Effect in ZnO quantum wells. *Nanophotonics Down Under - Devices and Applications*, Melbourne, 2009.

Appendix B

GaAs ADQW tables

S1-2

	E1HH1	E2HH2	E1LH1	E2HH1	E1LH2	E2LH1	E2LH2	F (eV)	F - E _{x_b} (eV)	Overlap	
E1HH1	0.0	6.1	21.0	32.6	38.6	44.4	53.6	76.9	1.5822	1.5722	0.9494
E1HH2	6.1	0.0	15.0	26.5	32.6	38.3	47.5	70.9	1.5883	1.5783	0.2500
E1LH1	21.0	15.0	0.0	11.5	17.6	23.3	32.6	55.9	1.6032	1.5932	0.9911
E2HH1	32.6	26.5	11.5	0.0	6.1	11.8	21.0	44.4	1.6148	1.6048	0.2656
E2HH2	38.6	32.6	17.6	6.1	0.0	5.8	15.0	38.3	1.6208	1.6108	0.9369
E1LH2	44.4	38.3	23.3	11.8	5.8	0.0	9.2	32.6	1.6266	1.6166	0.1151
E2LH1	53.6	47.5	32.6	21.0	15.0	9.2	0.0	23.3	1.6358	1.6258	0.1150
E2LH2	76.9	70.9	55.9	44.4	38.3	32.6	23.3	0.0	1.6591	1.6491	0.9888

E_{x_b} = 0.01 eV



S1-4

	E1HH1	E1HH2	E1LH1	E2HH1	E2HH2	E1LH2	E2LH1	E2LH2	E (eV)	E - E _{x0} (eV)	Overlap
E1HH1	0.0	6.1	24.1	28.6	34.6	42.1	52.6	70.7	1.5850	1.5750	0.9810
E1HH2	6.1	0.0	18.0	22.5	28.6	36.0	46.6	64.6	1.5910	1.5810	0.0910
E1LH1	24.1	18.0	0.0	4.5	10.5	18.0	28.6	46.6	1.6090	1.5990	0.9922
E2HH1	28.6	22.5	4.5	0.0	6.1	13.5	24.1	42.1	1.6135	1.6035	0.1022
E2HH2	34.6	28.6	10.5	6.1	0.0	7.5	18.0	36.0	1.6196	1.6096	0.9704
E1LH2	42.1	36.0	18.0	13.5	7.5	0.0	10.5	28.6	1.6271	1.6171	0.1006
E2LH1	52.6	46.6	28.6	24.1	18.0	10.5	0.0	18.0	1.6376	1.6276	0.0987
E2LH2	70.7	64.6	46.6	42.1	36.0	28.6	18.0	0.0	1.6556	1.6456	0.9904

S1-6

	E1HH1	E1HH2	E1LH1	E2HH1	E2HH2	E1LH2	E2LH1	E2LH2	F (eV)	F - E _{x₀} (eV)	Overlap
E1HH1	0.0	6.1	24.6	28.2	34.2	41.6	52.8	69.8	1.5852	1.5752	0.9858
E1HH2	6.1	0.0	18.5	22.1	28.2	35.6	46.7	63.7	1.5913	1.5813	0.0275
E1LH1	24.6	18.5	0.0	3.6	9.6	17.0	28.2	45.2	1.6098	1.5998	0.9958
E2HH1	28.2	22.1	3.6	0.0	6.1	13.4	24.6	41.6	1.6134	1.6034	0.0331
E2HH2	34.2	28.2	9.6	6.1	0.0	7.4	18.5	35.6	1.6194	1.6094	0.9753
E1LH2	41.6	35.6	17.0	13.4	7.4	0.0	11.2	28.2	1.6268	1.6168	0.0534
E2LH1	52.8	46.7	28.2	24.6	18.5	11.2	0.0	17.0	1.6380	1.6280	0.0512
E2LH2	69.8	63.7	45.2	41.6	35.6	28.2	17.0	0.0	1.6550	1.6450	0.9940

S1-20

	E1HH1	E1HH2	F1LH1	E2HH1	E2HH2	E1LH2	E2LH1	E2LH2	F (eV)	E - E _b (eV)	Overlap
E1HH1	0.0	6.1	24.7	28.1	34.2	41.5	52.8	69.6	1.5852	1.5752	0.9863
E1HH2	6.1	0.0	18.6	22.1	28.1	35.5	46.8	63.6	1.5913	1.5813	-
E1LH1	24.7	18.6	0.0	3.4	9.5	16.8	28.1	44.9	1.6099	1.5999	0.9972
E2HH1	28.1	22.1	3.4	0.0	6.1	13.4	24.7	41.5	1.6134	1.6034	-
E2HH2	34.2	28.1	9.5	6.1	0.0	7.3	18.6	35.5	1.6194	1.6094	0.9759
E1LH2	41.5	35.5	16.8	13.4	7.3	0.0	11.3	28.1	1.6267	1.6167	-
E2LH1	52.8	46.8	28.1	24.7	18.6	11.3	0.0	16.8	1.6381	1.6281	-
E2LH2	69.6	63.6	44.9	41.5	35.5	28.1	16.8	0.0	1.6549	1.6449	0.9953

S2-2

	E1HH1	E1HH2	E1LH1	E2HH1	E2HH2	E1LH2	E2LH1	E2LH2	F (eV)	F - Exb (eV)	Overlap
E1HH1	0.0	3.3	23.5	26.5	29.8	45.6	50.0	72.1	1.5952	1.5852	0.8961
E1HH2	3.3	0.0	20.2	23.2	26.5	42.3	46.7	68.8	1.5985	1.5885	0.3841
E1LH1	23.5	20.2	0.0	3.0	6.3	22.1	26.5	48.6	1.6187	1.6087	0.9934
E2HH1	26.5	23.2	3.0	0.0	3.3	19.1	23.5	45.6	1.6217	1.6117	0.3972
E2HH2	29.8	26.5	6.3	3.3	0.0	15.8	20.2	42.3	1.6250	1.6150	0.8953
E1LH2	45.6	42.3	22.1	19.1	15.8	0.0	4.4	26.5	1.6408	1.6308	0.0899
E2LH1	50.0	46.7	26.5	23.5	20.2	4.4	0.0	22.1	1.6452	1.6352	0.0901
E2LH2	72.1	68.8	48.6	45.6	42.3	26.5	22.1	0.0	1.6673	1.6573	0.9910

S2-4

	E1HH1	E1HH2	E2HH1	E2HH2	E1LH1	E1LH2	E2LH1	E2LH2	F (eV)	E - Exb (eV)	Overlap
E1HH1	0.0	3.3	16.1	19.3	28.6	40.5	44.6	56.6	1.6009	1.5909	0.9494
E1HH2	3.3	0.0	12.8	16.1	25.3	37.2	41.4	53.3	1.6041	1.5941	0.2500
E2HH1	16.1	12.8	0.0	3.3	12.5	24.4	28.6	40.5	1.6169	1.6069	0.2656
E2HH2	19.3	16.1	3.3	0.0	9.3	21.2	25.3	37.2	1.6202	1.6102	0.9369
E1LH1	28.6	25.3	12.5	9.3	0.0	11.9	16.1	28.0	1.6294	1.6194	0.9911
E1LH2	40.5	37.2	24.4	21.2	11.9	0.0	4.2	16.1	1.6414	1.6314	0.1151
E2LH1	44.6	41.4	28.6	25.3	16.1	4.2	0.0	11.9	1.6455	1.6355	0.1150
E2LH2	56.6	53.3	40.5	37.2	28.0	16.1	11.9	0.0	1.6574	1.6474	0.9888

S2-6

	E1HH1	E1HH2	E2HH1	E2HH2	E1LH1	E1LH2	E2LH1	E2LH2	E (eV)	E - Exb (eV)	Overlap
E1HH1	0.0	3.3	14.7	17.9	29.9	39.1	44.6	53.7	1.6016	1.5916	0.9787
E1HH2	3.3	0.0	11.4	14.7	26.6	35.8	41.3	50.5	1.6048	1.5948	0.0683
E2HH1	14.7	11.4	0.0	3.3	15.2	24.4	29.9	39.1	1.6162	1.6062	0.0749
E2HH2	17.9	14.7	3.3	0.0	11.9	21.1	26.6	35.8	1.6195	1.6095	0.9735
E1LH1	29.9	26.6	15.2	11.9	0.0	9.2	14.7	23.9	1.6314	1.6214	0.9893
E1LH2	39.1	35.8	24.4	21.1	9.2	0.0	5.5	14.7	1.6406	1.6306	0.1174
E2LH1	44.6	41.3	29.9	26.6	14.7	5.5	0.0	9.2	1.6461	1.6361	0.1151
E2LH2	53.7	50.5	39.1	35.8	23.9	14.7	9.2	0.0	1.6553	1.6453	0.9889

S2-20

	E1HH1	E1HH2	E2HH1	E2HH2	E1LH1	E1LH2	E2LH1	E2LH2	E (eV)	E - Exb (eV)	Overlap
E1HH1	0.0	3.3	14.5	17.8	30.2	38.7	44.7	53.2	1.6016	1.5916	0.9759
E1HH2	3.3	0.0	11.3	14.5	26.9	35.5	41.5	50.0	1.6049	1.5949	-
E2HH1	14.5	11.3	0.0	3.3	15.6	24.2	30.2	38.7	1.6162	1.6062	-
E2HH2	17.8	14.5	3.3	0.0	12.4	20.9	26.9	35.5	1.6194	1.6094	0.9759
E1LH1	30.2	26.9	15.6	12.4	0.0	8.5	14.5	23.1	1.6318	1.6218	0.9953
E1LH2	38.7	35.5	24.2	20.9	8.5	0.0	6.0	14.5	1.6403	1.6303	-
E2LH1	44.7	41.5	30.2	26.9	14.5	6.0	0.0	8.5	1.6463	1.6363	-
E2LH2	53.2	50.0	38.7	35.5	23.1	14.5	8.5	0.0	1.6549	1.6449	0.9953